Late Pleistocene variability in Timor Sea hydrology: evidence from paleotemperature proxies

Dissertation

In fulfilment of the requirements for the degree “Dr. rer. nat.”

Of the Faculty of Mathematics and Natural Sciences

At Kiel University

Submitted by

Elena Lo Giudice Cappelli

Kiel, 2015

Referent: Prof. Dr. Wolfgang Kuhnt

Koreferent: Prof. Dr. Ralph Schneider

Tag der Disputation: 17th July 2015

Zum Druck genehmigt

Der Dekan: Prof. Dr. Wolfgang J. Duschl

Eidesstattliche Erklärung

Hiermit erkläre ich an Eides statt, dass die vorliegende Dissertation mit dem Titel "Late Pleistocene variability in Timor Sea hydrology: evidence from paleotemperature proxies", abgesehen von der Beratung durch meine akademischen Lehrer, in Inhalt und Form meine eigene Arbeit darstellt.

Ich habe diese Arbeit, ganz oder zum Teil, an keiner anderen Stelle im Rahmen eines Prüfungsverfahrens vorgelegt. Teile dieser Arbeit wurden zur Veröffentlichung in Fachzeitschriften eingereicht, oder sind in Vorbereitung eingereicht zu werden.

Diese Arbeit ist unter Einhaltung der Regeln guter wissenschaftlicher Praxis der Deutschen Forschungsgemeinschaft (DFG) entstanden.

Kiel, den Elena Lo Giudice Cappelli

Elena Lo Giudice Cappelli

Acknowledgements

The research presented in this thesis would not have been possible without the help and support of many people. First and foremost, I thank my PhD supervisors Professor Wolfgang Kuhnt and Dr Ann Holbourn for giving me the chance to undertake this position, and for all their efforts in guiding and advising me over these years. I truly appreciate their extensive help in reading and improving my manuscripts, and the opportunity they gave me of participating in a research cruise on the R/V Sonne in 2011. I am also grateful to Ken Johnson and Willem Renema for initiating the "Throughflow" project, the source of my PhD funding, and for the many training and networking opportunities this project offered.

All my appreciation also goes to many other scientists who have contributed and helped me in my research, in particular, Marcus Regenberg, Dörte Mikschl, Nils Andersen, Dieter Garbe-Schönberg, Ulrike Westernströer, Karen Bremer, Thomas Blanz, and Silvia Koch and furthermore I thank Professor Ralph Schneider for acting as the second referee on this thesis.

I also want to acknowledge all of the fellow PhD students in the Throughflow project, for the fieldtrips, conferences and adventures we shared together: Amanda, Anja, Bill, Emanuela, Nadia, Nathan, Nick, Simone, Sonja, Vedrana, Vibor and Viola. I wish you all good luck in the future.

A big thank you to my colleagues and friends at MiPa for the great time spent together. Nick, thanks for being so patience with me and answering all my crazy and sometime not-so-appropriate questions about your beautiful language, the *perks* of being a native English speaker, I would say. Janne, you have been my first officemate and German friend, guided me through the obscure German bureaucracy, and made my first years in Kiel memorable, for all of this *vielen Dank*! Jan, my current office and *tea*

mate, thanks for the nice scientific and non-scientific conversations, for not minding about me singing and dancing in the office and for being cool with my out-of-control Italian swearing at the computer! Sebastian and Janika, thanks for our "*frische luft pausen"* and the endless laughs we had together, those moments kept me going when I thought I had no energies left, plus the chocolate! Kevin, stop trying stealing my cigarettes, I am *not* thankful for that…Thanks to Sven for the nice chats over coffee, the useful German to English translations (*Vier*) and for showing me some cool *artial mars* moves! Karlitos, thanks for making riding a bike so sexy! Larissa, thanks for reminding me of lunchtime! To the students and Hiwis in MiPa: Dennis, L^{uk}as, Izabela, Annika, Thorsten, and Janine, thanks for your help in the lab. I wish you guys all the best.

I am especially thankful to my *Kieler family*: Yiming and Thomas, Steffi and Regina, Nina, Christa and Elfi. I will never forget our bike trips and camping holidays, the many evenings filled with wine, delicious food, brilliant conversations and music, the weddings, the goodbyes, and the new beginnings.

Special thanks goes to Angela and Eva, I honestly have no words to say how important your friendship is to me, and you know too well it is not that easy to leave me speechless…vi voglio bene, σε αγαπώ.

Ultimo ma non meno importante, voglio ringraziare la mia famiglia, Annina e Stella, senza di voi non sarei la persona che sono oggi. *Marmottina* grazie per il supporto che mi hai dato in tutti questi anni, nonostante la distanza ci sei sempre stata!

Abstract

Since the early days of paleoceanographic investigations, variations in temperature, salinity and other environmental parameters have been reconstructed based on the elemental and isotopic composition of both planktonic and benthic foraminiferal tests deposited in marine sediments. However, substantial uncertainties still exist concerning the relationships between geochemical proxies and ambient variability. In the first phase of this study, I investigated the reliability of geochemical proxies (Mg/Ca and $\delta^{18}O$) for bottom water temperature (BWT) and sea surface temperature (SST) reconstructions in a suite of core top samples from the Timor Sea and Makassar Strait. Published core top data from the global ocean were compiled with new *Cibicidoides wuellerstorfi* and *Hoeglundina elegans* Mg/Ca and Sr/Ca ratios from core top samples spanning a temperature range from 2 to 12 °C. Results show a geographical distribution of benthic Mg/Ca ratios in relation to BWT: *C. wuellerstorfi* shows Mg/Ca sensitivity to BWT of 19% increase in Mg/Ca per °C for the Atlantic Ocean, and of 16% per °C for the Indian and Pacific Oceans. *Hoeglundina elegans* shows Mg/Ca sensitivity to BWT of 14% per °C for the Indo-Pacific Ocean. To test the reliability of *C. wuellerstorfi* and *H. elegans* Mg/Ca temperature equations, calcification temperatures derived from Mg/Ca ratios were compared with estimates derived from new $\delta^{18}O$ measurements from the Timor Sea and Makassar Strait. These two independent methods yielded comparable results, providing good approximations of CTD-measured temperatures. *Cibicidoides wuellerstorfi* Sr/Ca variability appears to be driven by carbonate ion saturation, whereas *H. elegans* Sr/Ca variability is driven by BWT, most likely because Sr has a better fit than Mg in the aragonitic lattice.

Globigerinoides ruber Mg/Ca ratios, and $U^{k'}_{37}$ were also measured in core tops from the Makassar Strait and Timor Sea and were compiled with published core top

data from the Indian Ocean and South China Sea. Results indicate that the $U^{k'}_{37}$ thermometer is less sensitive to SST above > 26 °C than existing global calibration would suggest, with temperatures biased toward quiescent, low-productivity months in regions of strong seasonal temperature variability such as the Java upwelling region. In contrast, Mg/Ca ratios show a less consistent seasonally-weighted SST signal. However, significant uncertainties remain with regard to analytical procedures and post-depositional effects such as dissolution and bioturbation, which warrant further investigation in the future.

In the second phase of this study, I used a multi-proxy record of planktonic and benthic foraminiferal $\delta^{18}O$, Mg/Ca-derived surface and lower thermocline temperatures, X-ray fluorescence (XRF)-derived runoff and sediment winnowing from sediment core SO18471 to reconstruct hydrological variability in the Timor Strait for the past 130 ka. Core SO18471, retrieved from a water depth of 485 m at the southern edge of the Timor Strait close to the Sahul Shelf, sits in a strategic position to reconstruct variations in the vertical structure of the Indonesian Throughflow (ITF) as well as to investigate hydrological changes related to monsoon variability and shelf dynamics over time. Sediment winnowing demonstrates that the ITF thermocline flow intensified during MIS 5a-d and MIS 1. In contrast during MIS 5e, winnowing was reduced and terrigenous input increased suggesting intensification of the local wet monsoon and a weaker ITF. Lower thermocline warming during globally cold periods (MIS 4 – MIS 2) appears to be related to a weaker and contracted thermocline ITF and advection of warm and salty Indian Ocean waters.

Zusammenfassung

Seit den frühen Tagen der Paläozeanographie basiert die Rekonstruktion von Paläotemperaturen, -salinitäten und anderen Umweltfaktoren auf Isotopenwerten der Schalen planktonischer und benthischer Foraminiferen, welche in marinen Sedimenten abgelagert wurden. Später integrierte Elementanalysen von Foraminiferengehäuse wurden für verbesserte Klimarekonstruktionen herangezogen. Trotzdem bestehen immer noch Unsicherheiten über die Beziehungen zwischen geochemischen Proxies und Umweltfaktoren. In der ersten Phase meiner Studien untersuchte ich die Zuverlässigkeit geochemischer Proxies (Mg/Ca und $\delta^{18}O$) für die Rekonstruktion der Boden- (BWT) und Oberflächenwassertemperatur (SST) an Sedimentoberflächenproben aus der Timorsee und der Straße von Makassar. Bereits publizierte globale Daten wurden mit neuen Mg/Ca- und Sr/Ca-Messungen an *Cibicidoides wuellerstorfi* und *Hoeglundina elegans* zusammengefasst und repräsentieren nun den Temperaturbereich zwischen 2 und 12°C. Diese ergaben eine regionale Abhängigkeit des Verhältnisses zwischen Mg/Ca und BWT. Für *C. wuellerstorfi* wurde ein Anstieg des Mg/Ca-Verhältnisses um 19% pro °C im Atlantik und 16% im Indischen und Pazifischen Ozean ermittelt. Die Sensitivität von *H. elegans* gegenüber Bodenwassertemperaturänderungen beträgt 14% pro °C im Indischen und Pazifischen Ozean. Um die Präzision der Mg/Ca-Kalibrationen für *C. wuellerstorfi* und *H. elegans* zu testen, wurden so errechnete Kalzifizierungstemperaturen mit Temperaturen verglichen, welche durch neue $\delta^{18}O$ Messungen an Proben aus der Timorsee und der Straße von Makassar ermittelt wurden. Diese voneinander unabhängigen Methoden ergaben vergleichbare Resultate und korrelieren gut mit CTD-basierten Temperaturmessungen. Variationen des Sr/Ca- Verhältnisses von *C. wuellerstorfi* sind scheinbar von der Karbonationen-Sättigung abhängig, wohingegen

dieses Verhältnis in *H. elegans* von der BWT abhängig ist. Dies resultiert wahrscheinlich aus der besseren Kompatibilität von Sr mit der aragonitischen Kristallstruktur.

Ein weiterer Datensatz basiert auf neuen Messungen des Mg/Ca-Verhältnisses an *Globigerinoides ruber* und $U^{k'}_{37}$ von Sedimentoberflächenproben genommen in der Timorsee und der Straße von Makassar kombiniert mit bereits publizierten Sedimentoberflächenproben aus dem Indischen Ozean und der Südchinasee. Die Auswertung ergab eine geringere Sensitivität von $U^{k'}_{37}$ gegenüber SST für Temperaturen über 26°C als globale Kalibrationen implizieren. In Regionen mit starken saisonalen Temperaturunterschieden wie der Java-upwelling-Region spiegeln diese eher Temperaturen während Monaten mit niedriger Produktivität wieder. Das Mg/Ca-Verhältnis weist im Gegensatz hierzu eine größere Variationsbreite und dementsprechend weniger Saisonalitäts-Kontrolle auf. Allerdings bestehen weiterhin Unsicherheiten bezüglich der analytischen Methodik und post-sedimentärer Effekte wie Lösungserscheinungen und Bioturbation, welche nur durch weitere Untersuchungen geklärt werden können. In der zweiten Phase meiner Studien rekonstruierte ich Änderungen der Hydrologie in der Timorsee während der letzten 130.000 Jahre anhand des Sedimentbohrkernes SO18471. Hierzu verwandte ich $\delta^{18}O$ gemessen an planktischen und benthischen Foraminiferen, Temperaturen des Oberflächenwassers und der unteren Thermokline abgeleitet aus Mg/Ca-Messungen und Änderungen des Sedimentationsverhalten basierend auf Röntgenfluoreszensanalyse (RFA). Der Bohrkern eignete sich aufgrund seiner Position nahe des Sahul-Schelfes (Wassertiefe 485 m) in der südlichen Timorsee hervorragend für die Rekonstruktion der Variabilität der vertikalen Struktur des Indonesischen Durchstrom (IDS) und der hydrologischen Variabilität verursacht durch Variationen

des Monsuns und der Schelfdynamik. Änderungen des Sedimentationsverhaltens spiegeln eine Intensivierung des IDS in der Thermokline während MIS 5a-d und MIS 1 wieder. Im Gegensatz war der Sedimentabtransport während MIS 5e reduziert und der terrigene Eintrag erhöht, was auf eine lokale Intensivierung des Monsunregen während der Regenzeit und eine Abschwächung des IDS zurückzuführen ist. Eine verminderte Erwärmung der Thermokline während globaler Kaltzeiten (MIS 4 – MIS 2) ist vermutlich versursacht durch eine schwächere und kontrahierte Thermokline des IDS und eine Advektion von warmen, salinaren Wässern aus dem Indischen Ozean.

Table of Contents

List of Figures

Chapter 1

Chapter 2

Chapter 3

Chapter 4

List of Tables

Chapter 2

Chapter 3

Chapter 1

Introduction

1.1 Motivation and Objectives

The Indonesian Throughflow (ITF) is the only low-latitude connection between the Pacific and Indian Oceans, allowing heat and freshwater exchanges between these two ocean basins and therefore playing a crucial role in the global thermohaline circulation. Due to its importance, in the last decades several projects have been developed with the primary goal of studying circulation and water mass stratification within the Indonesian Seas, especially to determine sources, pathways, and mixing histories of the throughflow water masses (e.g.: ARLINDO and INSTANT projects). Paleoclimate studies investigating the response of global climate to orbital and millennial scale forcings are key to further understand modern climate and predict its future evolution. However, the processes and feedback mechanisms behind climate past evolution in the ITF area are still not clear due to the limited number of high-resolution paleoceanographic archives. In particular, the reconstruction of ocean intermediate circulation and of changes in source waters at higher latitudes that are transferred to the low latitudes, remain highly challenging.

The main goals of this thesis are to integrate modern core top studies with marine sediment core paleorecords to ground truth climate and paleoceanographic reconstructions in the ITF region. This thesis includes Mg/Ca, Sr/Ca and $\delta^{18}O$ measurements performed in two species of benthic foraminifera, *Hoeglundina elegans* and *Cibicidoides wuellerstorfi*, based on a suite of core top samples from the Timor Sea and Makassar Strait. The aims of this initial study are (1) to provide better-constrained temperature calibrations for intermediate to deep water masses, (2) to improve our understanding of the carbonate ion effect on benthic Mg/Ca ratios and (3) explore potential proxies to reconstruct carbonate ion saturation variability over time (**Chapter 2**). Mg/Ca measurements were also performed in the planktonic

foraminifera *Globigerinoides ruber* based on core top samples from the Makassar Strait and Timor Sea. These measurements were paired with another proxy for sea surface temperature (SST) reconstructions, the $U^{k'}_{37}$ alkenone unsaturation index, and integrated with published data to provide new insights in the relationship between SST and geochemical proxy records (**Chapter 4**).

Based on this new *H. elegans* Mg/Ca temperature calibration, the first Timor Strait record of lower thermocline temperatures spanning the last 130 ka was produced. These benthic foraminiferal Mg/Ca data from Timor Strait Core SO18471 (9° 21.9870' S, 129° 58.9830'E; 485 m water depth; 13.5 m length) were combined with a multi-proxy record of planktonic and benthic foraminiferal $\delta^{18}O$, Mg/Ca-derived surface temperature and X-ray fluorescence (XRF)-derived runoff and sediment winnowing from the same core. The main objectives of this study are (1) to reconstruct the hydrological evolution of both surface and deeper water masses in the Timor Strait over the last 130 ka, (2) to capture the variability of the ITF vertical structure and intensity over glacial – interglacial periods, (3) to monitor variations in the Indonesian-Australian Monsoon system on orbital and millennial timescales (**Chapter 3**).

1.2 Structure of the thesis

Chapter 1 summarizes current knowledge on modern and late Pleistocene climate and oceanography of the Indo Pacific Warm Pool (IPWP), with specific focus on the Indonesian Throughflow (ITF) evolution over time.

Chapter 2 is a calibration study based on benthic Mg/Ca ratios used as geochemical proxy to reconstruct bottom water temperature (BWT) variability, titled "Refining *C. wuellerstorfi* and *H. elegans* Mg/Ca temperature calibrations" by E. Lo Giudice Cappelli, M. Regenberg, A. Holbourn, W. Kuhnt, Dieter Garbe-Schönberg,

and Nils Andersen. This chapter is published in *Marine Micropaleontology* (doi: 10.1016/j.marmicro.2015.10.001).

Chapter 3 is a multi-proxy study focused on changes in climate and oceanography of the Timor Strait over the last 130 ka. This manuscript is titled "Changes in Timor Strait hydrology during the past 130 ka" by E. Lo Giudice Cappelli, A. Holbourn, W. Kuhnt, and M. Regenberg. This manuscript is currently in review in *Palaeogeography, Palaeoclimatology, Palaeoecology*.

Chapter 4 is an exploratory study of the application and limitations of two commonly used geochemical proxies of sea surface temperature in the West Pacific- the Mg/Ca ratios of planktonic foraminifera, and the coccolithophore-derived $U^{k'}_{37}$ index. It is titled "Geochemical proxies of sea surface temperature in the tropical West Pacific: insights from modern core tops".

Chapter 5 provides final conclusions of this thesis and suggestions for future work.

Appendix A. *Hoeglundina elegans* Mg/Ca ratios were measured with laser ablation in 28 selected samples of sediment core SO18471 to investigate the variability of this temperature proxy in two different morphotypes of *H. elegans*, which occur within a restricted interval (400 – 750 cm).

Appendix B. As part of the Network Training Activities of the Marie Curie Initial Training Network "Throughflow", I participated to two fieldtrips in Indonesia to gain practical experience in measuring and describing 42 stratigraphic sections in middle to upper Miocene coastal deposits from East Kalimantan and to collect samples including fossils, bulk sediments, and drilled plugs for multiple analyses. These two fieldtrips led to an extensive study on middle Miocene fossil fauna based on corals, large benthic foraminifera, coralline algae, mollusks, and bryozoan by

colleagues of the "Throughflow" network, to which I contributed with a study of benthic foraminiferal assemblages that was included in a paper titled "A diverse patch reef from turbid habitats in the Middle Miocene (East Kalimantan, Indonesia)" by N. Santodomingo, V. Novak, V. Pretković, N. Marshall, E. Di Martino, E. Lo Giudice Cappelli, A. Rösler, S. Reich, J. C. Braga, W. Renema, and K. Johnson, published in *Palaios* (doi: http://dx.doi.org/10.2110/palo.2013.047).

1.3 Regional Setting

1.3.1 Oceanography

The ITF is a complex ocean current system that transports cool and fresh waters from the Pacific Ocean to the Indian Ocean and, thus, plays an important role in modulating local and global climate (Fig. 1.1) [*Cresswell et al.*, 1993; *Gordon and Fine*, 1996*; Gordon* 2005]. It is driven across the Indonesian Archipelago by the pressure gradient between the tropical western Pacific Ocean and the Indian Ocean [*Cresswell et al.*, 1993].

Today, North Pacific surface to upper thermocline waters (~0 to 200 m) enter the Celebes Sea through a relatively shallow (<800 m) passage South of Mindanao, then flow in a southwesterly direction through the Makassar Strait, feeding the ITF (Fig. 1.1). Cool and fresh surface waters originating from the South China Sea are additionally advected via the Sulu Sea through the Sibutu Strait into the Celebes Sea, and via the Java Sea through the Karimata Strait into the southern end of the Makassar Strait (Fig. 1.1) [*Sprintall et al*., 2009; *Gordon et al.,* 2012]. From the southern end of the Makassar Strait, only a small proportion of the ITF waters, ~2.6 Sv, enters directly the Indian Ocean through the Lombok Strait, while the greater part of the ITF continues to flow eastward into the Banda Sea (western route) (Fig. 1.1)

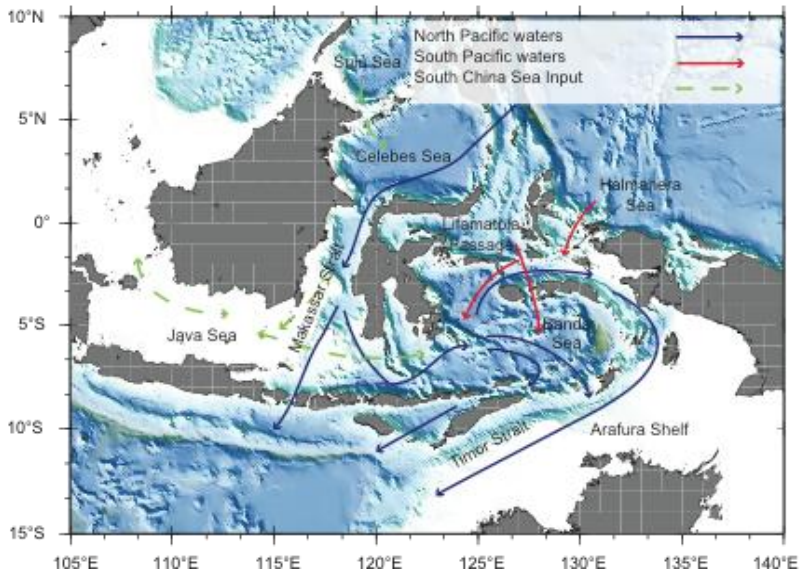

Fig. 1.1 ITF pathways [*Gordon* 2005; *Gordon et al*., 2012]

[*Sprintall et al*., 2009]. However, the Dewakang sill (650 m) at the southern end of the Makassar Strait prevents the flow of deeper waters into the Banda Sea or through the Lombok Strait [*Talley and Sprintall*, 2005]. Low-salinity North Pacific Intermediate Water characterized the ITF lower thermocline flow (~200 to 500 m) reaching the Banda Sea from the western route [*Rosenthal et al.*, 2013]. South Pacific surface waters enter the Indonesian seas through the Halmahera Sea, while lower thermocline and intermediate waters, stemming from the New Guinea Costal Undercurrent, reach the Banda Sea via the Lifamatola passage (eastern route) (Fig. 1.1) [*Talley and Sprintall*, 2005]. In the Banda Sea, North and South Pacific waters mix together and undergo tidal mixing, monsoon-driven upwelling, and air-sea exchanges resulting in the Indonesian Intermediate Water between ~450 and 1000 m [e.g.: *Gordon et al.*, 2005; *Talley and Sprintall,* 2005; *Koch-Larrouy et al*., 2010]. Indonesian Intermediate Water also carries a contribution of Antarctic Intermediate Water, stemming from the New Guinea Costal Undercurrent and entering the Banda

Sea via the Lifamatola Strait [*Zenk et al.*, 2005; *Rosenthal et al.*, 2013]. From the Banda Sea, the ITF enters the Indian Ocean through two relatively narrow passages: the Ombai Strait (~4.9 Sv, sill depth of 3250 m) and the Timor Strait (~7.5 Sv, sill depth of 1890 m), which provides the main outflow pathway into the Indian Ocean (Fig. 1.1) [*Ffield and Gordon* 1992; *Gordon and Fine* 1996; *Gordon*, 2005; *Sprintall et al.*, 2009].

Considering the topographic barriers within the Indonesian seas together with seasonal monsoonal wind reversals, the ITF transport from the Pacific to the Indian Ocean is thought to take place mainly in the thermocline layer [*Gordon et al.*, 2003a, *Gordon et al.*, 2003b; *Gordon et al*., 2008; *Sprintall et al.*, 2009]. Model studies suggested that stratification and surface heat fluxes in the Indian Ocean are significantly modified by the presence of a thermocline-dominated ITF relative to a surface-dominated ITF [*Gordon et al*., 2003b; *Song and Gordon* 2004]. A thermocline-dominated ITF would cool and freshen the tropical eastern Indian Ocean close to the Indonesian archipelago [*Gordon et al.*, 2003b; *Gordon et al.*, 2005], inducing sea surface temperature anomalies across the whole Indian basin resulting in an overall heat gain for the Indian Ocean [*Song and Gordon*, 2004; *Gordon et al*., 2005].

1.3.2 Climate

On a seasonal scale, latitudinal migrations of the Intertropical Convergence Zone (ITCZ), a narrow band of convergent surface winds close to the equator, determine the climatic patterns in the Indo Pacific Warm Pool (IPWP). The ITCZ displacement into a more southern or northern position is a response of interhemispheric temperature gradients, the most dramatic of which occurs over the

Indian Ocean and adjacent land masses, where the ITCZ position oscillates between 20° N in austral winter to 8° S in austral summer [*Schneider et al*., 2014]. The ITCZ migration is strongly correlated to seasonal rainfall variations associated to the monsoon cycle in South East Asia. Consequently, hydrographic properties and the intensity of the ITF are substantially altered following the monsoon cycle and the ITCZ seasonal displacements. During the austral summer monsoon (NW monsoon), when the ITCZ is in its southernmost position, Indonesia and NW Australia experience a warm and wet season, and the ITF is weaker as the pressure gradient between the Pacific and Indian Oceans is at its lowest (Fig. 1.2a and b). Westerly winds limit the flow of surface waters within the Makassar Strait, favoring the advection of Java Sea fresh waters at the southern end of the Makassar Strait (Fig. 1.2b) [*Gordon et al*., 2003b]. Additionally, in the Banda Sea surface water stemming from the Flores Sea sinks as a result of wind induced Ekman downwelling, and only a small amount is exported to the north via the Halmahera Strait, and to the south via the Timor Strait (Fig. 1.2a and b) [*Wyrtki*, 1958; *Gordon and Susanto*, 2001]. In contrast, during the austral winter monsoon (SE monsoon), when the ITCZ retreats northward, Indonesia and NW Australia experience a cold and dry season, and the ITF is stronger as the pressure gradient between the Pacific and Indian Oceans is at its highest (Fig. 1.2c and d). Easterly winds remove the fresh water plug at the southern end of the Makassar Strait promoting a southward surface flow (Fig. 1.2d) [*Gordon et al.*, 2003b]. In the Banda Sea, intensified surface currents towards the Indian Ocean sequestrate water from the Arafura Sea and, by compensation, Ekman upwelling occurs in this area [*Wyrtki*, 1958; *Gordon and Susanto*, 2001].

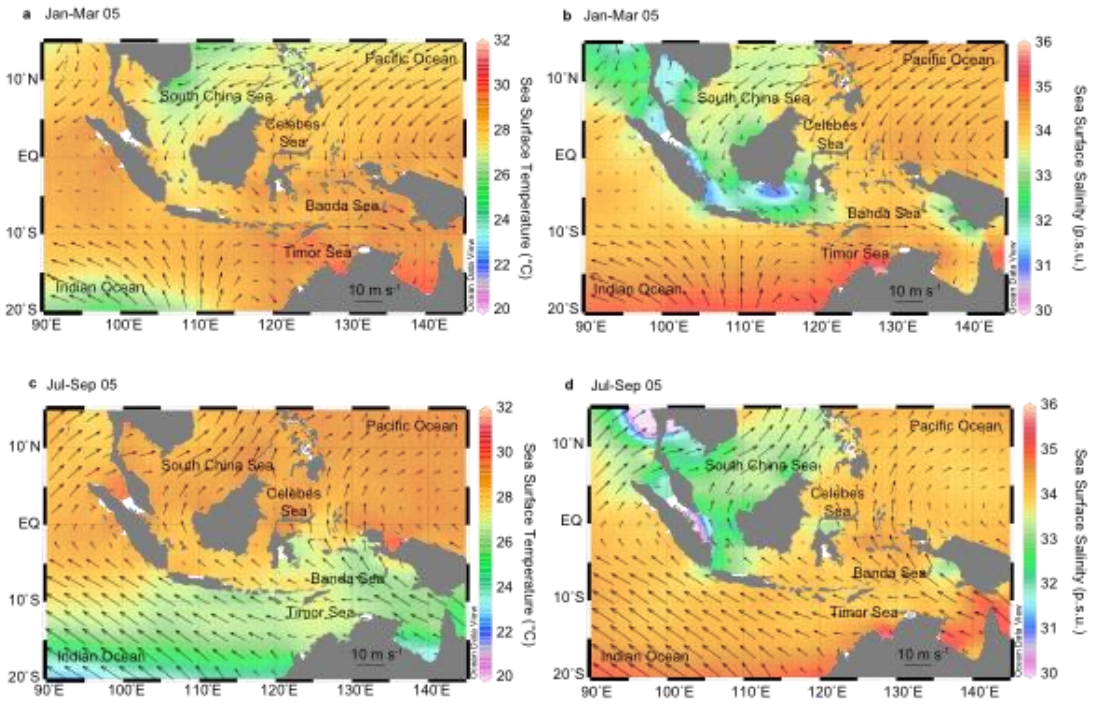

Fig. 1.2 Monsoon-induced seasonal variations in temperature, salinity and wind trajectory in the tropical Indo-Pacific plotted with Ocean Data View [*Schlitzer*, 2013]. **a)** and **b)** Austral summer (January-March) seasonal sea surface temperature (SST) and salinity variations. **c)** and **d)** Austral winter (July-September) seasonal SST and salinity variations. Temperature and salinity data are from the World Ocean Atlas 2005 [*Locarnini et al*., 2006]. Superimposed are winds trajectories (arrows) in February (**a** and **b**) and August (**c** and **d**). Wind data are monthly averages for February and August 2005 from NCEP Reanalysis Dataset (http://www.esrl.noaa.gov/psd/).

1.4 Glacial – interglacial cycles

1.4.1 Sea level

The evolution of the ITF over longer timescales, such as glacial – interglacial cycles, is still poorly understood, as only a handful of records spans longer timescales. Most of these paleoclimate studies focused on sea surface temperature and salinity reconstructions [*Visser et al*., 2003; *Spooner et al*., 2005; *Xu et al*., 2008; *Holbourn et al*., 2011; *Gibbons et al*., 2014], whereas only a limited number of records extended to reconstructions of the ITF upper thermocline variability during the past ~140-160 ka [*Xu et al*., 2008; *Holbourn et al*., 2011]. No record of intermediate water for the ITF area extends past the Holocene, precluding understanding of the wider spectrum of variability on glacial – interglacial timescales, when relationships to past climatic

boundary conditions (e.g., ice volume, sea level, seaway geometry, interhemispheric thermal gradient) fundamentally differed from the present day.

Sea level reconstructions from the Sunda Shelf reported exposure of wide areas of the shelf, and a reduction in size of the adjacent South China Sea, during the Last Glacial Maximum (LGM, 21-19 ka; Fig. 1.3) [*Hanebuth et al*., 2000 and 2009].

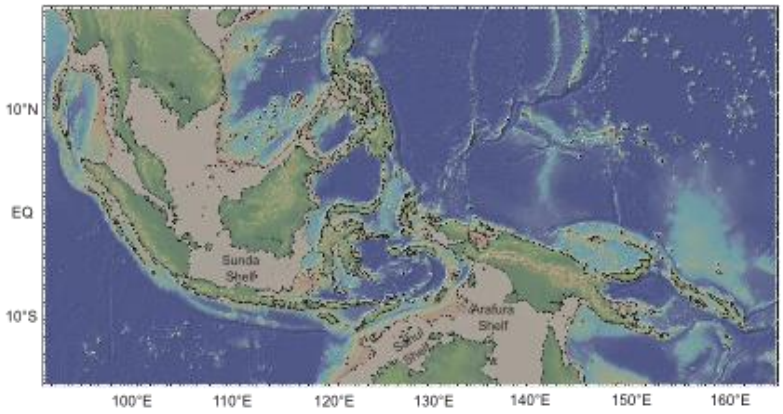

Fig. 1.3 Black contour lines show differences in topography and bathymetry in the Indo-Pacific between present day and LGM, when sea level was ~120 m lower. Basemap was generated with GeoMapApp (http://www.geomapapp.org) using the Global Multi-Resolution Topography synthesis database [*Ryan et al*., 2009].

Similarly, micropaleontological evidence from the Bonaparte Gulf (Timor Sea) [*Yokoyama et al.,* 2000 and 2001; *De Deckker and Yokoyama* 2009; *Ishiwa et al*., 2015] indicated brackish to marginal sea conditions just prior and during the LGM, when sea level was at its lowest, being between ~125-120 m lower than today (Fig. 1.3). At ~19 ka, records from both the Sunda Shelf and the Bonaparte Gulf together with compilations of global sea level data [e.g.: *Lambeck et al.*, 2002] show an increase in sea level and transgression to marine conditions, marking the end of the LGM (Fig. 1.3). Additionally, a dramatic and rapid sea level increase between 14.6 and 14.3 ka marks the meltwater pulse (MWP) 1A, a major melting event in the polar region [*Hanebuth et al.,* 2000].

Paired surface and upper thermocline temperature and salinity records from the Timor Sea suggested the presence of a surface-dominated ITF during periods of lowered sea level, when the Sunda Shelf was exposed (sill depth of ~40 m) [*Xu et al*., 2006 and 2008; *Holbourn et al*., 2011]. At this time, no connection between the South China Sea and the Java Sea implied no advection of Java Sea fresh water at the southern end of the Makassar Strait, favoring the ITF surface to flow eastward into the Banda Sea. Conversely, during sea level highstands, cooling and freshening of the ITF upper thermocline were interpreted as a strengthening of the thermocline-dominated ITF, following the opening of the shallow connection between the South China Sea and the Java Sea. At this time, fresh water stemming from the Java Sea may have created a plug at the southern end of the Makassar Strait limiting the ITF surface flow [*Xu et al*., 2006 and 2008; *Holbourn et al*., 2011]. In contrast, a more recent study [*Rosenthal et al*., 2013] proposed an alternative interpretation for temperature changes in intermediate waters at low latitudes. These authors related early Holocene warming of intermediate waters in the Makassar Strait and Flores Sea to variations in the temperature of source waters at higher latitudes. However this hypothesis has not been tested on longer timescales, when sea level changes would have dramatically affected global circulation.

1.4.2 The monsoon system

During the last glacial cycle, sea surface temperatures (SST) were generally lower during glacial stages in both hemispheres. On the Ontong Java Plateau (0° 19’ 6.6’’ N, 159° 21’ 39.6’’ E), SSTs were ~3°C lower during Marine Isotope Stage (MIS) 2 and 6 (glacials) than during interglacials (MIS 1 and 5e) [*Lea et al.*, 2000]. In the Makassar Strait (4° 41.33’ S, 117° 54.17’ E), SSTs were 3.7 °C lower during MIS

2 than MIS 1, and 5.3 °C lower during MIS 6 than MIS 5e [*Visser et al.,* 2003]. In the Timor Sea (13° 4.95' S, 121° 47.27' E), SSTs were 3.2 °C lower during MIS 2 than MIS 1, and 4.0 °C lower during MIS 6 than MIS 5e [*Xu et al.,* 2008]. These lowered SSTs, and a possibly reduced Indo Pacific Warm Pool (IPWP) [*De Deckker and Yokoyama,* 2009], limited heat and vapor supply from sea to the atmosphere resulting in generally lower monsoonal precipitations and runoff [*Wang et al.,* 1999].

In contrast, during glacial terminations, Northern Hemisphere warming and consequent ice sheet melting promoted a slowdown in the Meridional Overturning Circulation, which in turn generated cold anomalies in the North Atlantic [*Cheng et al.,* 2009; *Denton et al.,* 2010; *Clark et al.,* 2012]. This may have resulted in a southern displacement of the ITCZ [*Wang et al*., 2004; *Chiang et al.,* 2005; *Denton et al.,* 2010; *Muller et al*., 2008; *Mohtadi et al*., 2011] and consequent warming of the Southern Hemisphere and Antarctica [*Petit et al*., 1999; *Shakun et al*., 2012], possibly enhancing monsoonal forcing by increasing the heat and vapor supply to the atmosphere. Borneo speleothem $\delta^{18}O$ records [*Carolin et al.,* 2013] and multi-proxy data from marine sediment cores from the Sulu Sea [*Rosenthal et al*., 2003] and off south Java [*Mohtadi et al.,* 2011] captured North Atlantic cold events corresponding to drier conditions in these areas, possibly implicating a migration of the ITCZ and the rain belt further south (Fig. 1.4). Speleothem $\delta^{18}O$ records from Flores [*Griffiths et al.,* 2009; *Ayliffe et al*., 2013] and NW Australia [*Denniston et al.,* 2013], and multi-proxy data from marine sediment cores from the Timor Sea [*Kuhnt et al.,* 2015] and the western Banda Sea [*Muller et al*., 2012] support a southern displacement of

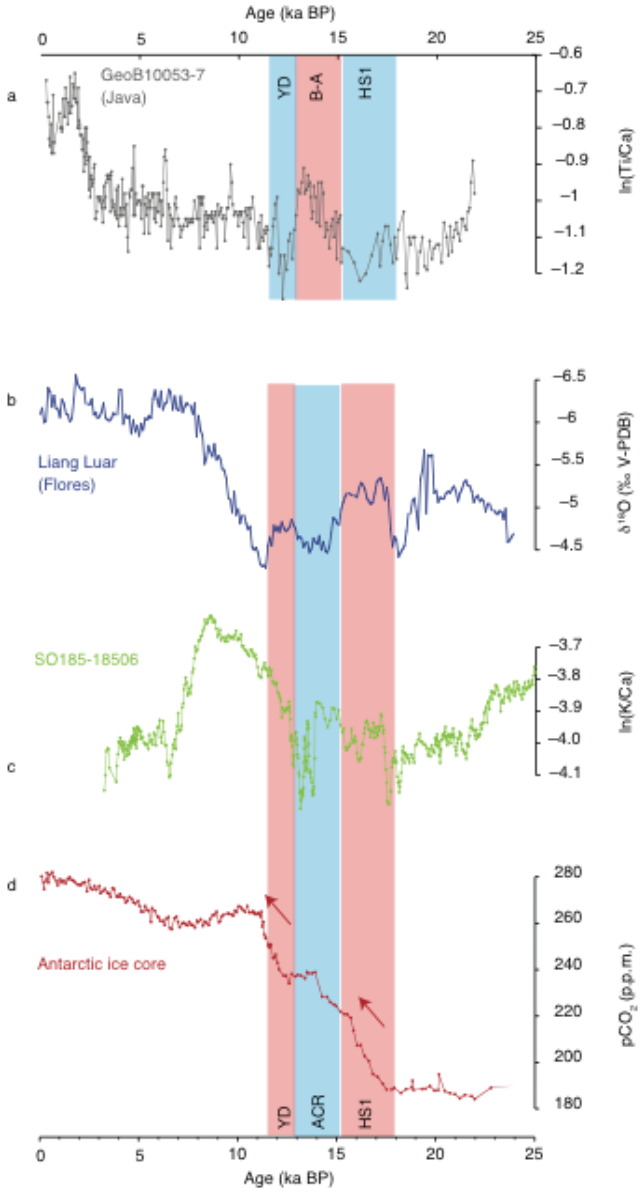

Fig. 1.4 a) Marine sediment core from off Java [*Mohtadi et al.*, 2011] captures Northern Hemisphere high latitudes abrupt climate changes. **b)** and **c)** Flores speleothem [*Ayliffe et al.*, 2013] and marine sediment core from the Timor Sea [*Kuhnt et al.*, 2015] record abrupt climate changes in Antarctica. **d)** Antarctic Ice Core (Dome Concordia) pCO_2 record [*Monin et al.*, 2001], red arrows indicate main warming phases. YD: Younger Dryas, ACR: Antarctic Cold Reversal; HS1: Heinrich Stadial 1; B-A: Bølling-Allerød. Red shadings mark warming phases in both hemispheres; blue shadings mark cold phases. (Figure modified from *Kuhnt et al.* [2015]).

the ITCZ during North Hemisphere cooling, as wet conditions were documented in these locations synchronous with warming in Antarctica (Fig. 1.4). However, whereas marine sediment cores from the Sulu Sea [*Rosenthal et al.*, 2003] and off south Java [*Mohtadi et al.*, 2011] recorded more humid conditions during warm events in the Northern Hemisphere high latitudes (Fig. 1.4), no evidence were found in the Borneo

speleothem $\delta^{18}O$ records [*Carolin et al.,* 2013], suggesting that other mechanisms, such as changes in atmospheric circulation and exposure of vast land masses (Sunda and Sahul shelves), played an important role in driving hydrological changes in the IPWP by modulating moisture and heat supply to the atmosphere.

References

Ayliffe, L. K., M. K. Gagan, J. Zhao, R. N. Drysdale, J. C. Hellstrom, W. S. Hantoro, M. L. Griffiths, H. Scott-Gagan, E. St Pierre, J. A. Cowley, and B. W. Suwargadi (2013), Rapid interhemispheric climate links via the Australasian monsoon during the last deglaciation, *Nature communications*, 4, 2908, doi: 10.1038/ncomms3908.

Carolin, S. A., K. M. Cobb, J. F. Adkins, B. Clark, J. L. Conroy, S. Lejau, J. Malang, and A. Tuen (2013), Varied response of western Pacific hydrology to climate forcings over the last glacial period, *Science*, 340, 1564-1567, doi: 10.1026/science.1233797.

Cheng, H., L. Edwards, W. S. Broecker, G. H. Denton, X. Kong, Y. Wang, R. Zhang, and X. Wang (2009), Ice age terminations, *Science, 326*, 5950, 248-252, doi: 10.1126/science.1177840

Chiang, J. C. H., and C. M. Bitz (2005), Influence of high latitude ice cover on the marine Intertropical Convergence Zone, *Climate Dynamics*, 25, 5, 477-496, doi: 10.1007/s00382-005-0040-5

Clark, P. U., J. D. Shakun et al. (2012), Global climate evolution during the last deglaciation, *Proceedings of the National Academy of Sciences of the United States of America*, *109* (19), 1134-1142, doi: 10,1073/pnas.1116619109.

Cresswell, G., A. Frische, J. Peterson, and D. Quadfasel (1993), Circulation in the Timor Sea, *Journal of Geophysical Research*, *98*(C8), 14379-14389, doi: 10.1029/93JC00317.

De Deckker, P., and Y. Yokoyama (2009), Micropaleontological evidence for Late Quaternary sea-level changes in Bonaparte Gulf, Australia, *Global and Planetary Change*, 66, 85-22, doi:10.1016/j.gloplacha.2008.03.012.

Denniston, R. F., K-H. Wyrwoll, Y. Asmerom, V. J. Polyak, W. F. Humphreys, J. Cugley, D. Woods, Z. LaPointe, J. Peota, and E. Greaves (2013), North Atlantic forcing of millennial-scale Indo-Australian monsoon dynamics during the Last Glacial period, *Quaternary Science Reviews*, 72, 159-168, doi: 10.1016/j.quascirev.2013.04.012.

Denton, G. H., R. F. Andersen, J. R. Toggweiler, R. L. Edwards, J. M. Schaefer, and A. E. Putnam (2010), The last glacial termination, *Science, 328*, 1652, doi: 10.1126/science.1184119.

Ffield, A. L., and A. L. Gordon (1992), Vertical Mixing in the Indonesian Thermocline, *Journal of Physical Oceanography*, *22*(2), 184-195.

Gibbons, F. T., D. W. Oppo, M. Mothadi, Y. Rosenthal, J. Cheng, Z. Liu, B. K. Linsley (2014), Deglacial $\delta^{18}O$ and hydrological variability in the tropical Pacific and Indian Ocean, *Earth and Planetary Science Letters*, 387, 240-251, http://dx.doi.org/10.1016/j.epsl.2013.11.032.

Gordon, A. L., and R. A. Fine (1996), Pathway of water between the Pacific and Indian oceans in the Indonesian seas, *Nature*, *379*, 146-149, doi: 10.1038/379146a0.

Gordon, A. L., and R. D. Susanto (2001), Banda Sea surface-layer divergence, *Ocean Dynamics*, 52, 2-10, doi: 10.1007/s10236-001-8172-6.

Gordon, A. L., C. F. Giulivi, and A. Gani Ilahude (2003a), Deep topographic barriers within the Indonesian seas, *Deep-Sea Research II*, 50, 2205-2228, doi: 10.1016/S0967-0645(03)00053-5.

Gordon, A. L., R. D. Susanto, and K. Vranes (2003b), Cool Indonesian throughflow as a consequence of a restricted surface layer flow, *Nature*, *425*, 824-828, doi: 10.1038/nature02038.

Gordon, A. L. (2005), Oceanography of the Indonesian seas and their throughflow, *Oceanography*, *18*(4), 14-27, http://dx.doi.org/10.5670/oceanog.2005.01.

Gordon, A. L., R. D. Susanto, A. Ffield, B. A. Huber, W. Pranowo, and S. Wirasantosa (2008), Makassar Strait throughflow, 2004 to 2006, *Geophysical Research Letters*, 35, L24605, doi: 10.1029/2008GL036372.

Gordon, A. L., B. A. Huber, E. J. Metzger, R. D. Susanto, H. E. Hurlburt, and T. R. Adi (2012), South China Sea throughflow impact on the Indonesian throughflow, *Geophysical Research Letters*, 39, L11602, doi: 10.1029/2012GL052021.

Griffiths, M. L., R. N. Drysdale, M. K. Gagan, J.-x. Zhao, L. K. Ayliffe, J. C. Hellstrom, W. S. Hantoro, S. Frisia, Y.-x. Feng, I. Cartwright, E. St Pierre, M. J. Fischer, and B. W. Suwargadi (2009), Increaseing Australian-Indonesian monsoon rainfall linked to early Holocene sea-level rise, *Nature Geoscience*, 2, 636-639 doi: 10.1038/NGEO605.

Hanebuth, T., K. Stattegger, and P. Grootes (2000), Rapid flooding of the Sunda Shelf: a late-glacial se-level record, *Science*, 288, 1033-1036, doi: 10.1026/science.288.5468.1033.

Hanebuth, T., K. Stattegger, and A. Bojanowski (2009), Termination of the Last Glacial Maximum sea-level lowstand: the Sunda Shelf data revised, *Global and Planetary Change*, 66, 76-84, doi:10.1016/j.gloplacha.2008.03.011

Holbourn, A., W. Kuhnt, and J. Xu (2011), Indonesian Throughflow variability during the last 130 ka: the Timor Sea outflow, The SE Asian gateway: history and tectonics of Australia-Asia collision, Geological Society, London, Special Publications, *355*, 283-303, doi: 10.1144/SP355.14.

Ishiwa, T., Y. Yokoyama, Y. Miyairi, S. Obrochta, T. Sasaki, A. Kitamura, A. Suzuki, M. Ikehara, K. Ikehara, K. Kimoto, J. Bourget, and H. Matsuzaki (2015), Reapprisal of sea-level lowstand during the Last Glacial Maximum observed in the Bonaparte Gulf sediments, northwestern Australia, *Quaternary International* (in press).

Koch-Larrouy, A., M. Lengaigne, P. Terray, G. Madec, and S. Masson (2010), Tidal mixing in the Indonesian Seas and its effect on the tropical climate system, *Climate Dynamics*, *34*, 891-904, doi: 10.1007/s00382-009-0642-4.

Kuhnt, W., A. Holbourn, J. Xu, B. Opdyke, P. De Deckker, U. Röhl, and M. Mudelsee (2015), Southern Hemisphere control on Australian monsoon variability during the late deglaciation and Holocene, *Nature Communications*, 6, 5916-5922, doi: 10.1038/ncomms6916.

Lambeck, K., Y. Yokoyama, and T. Purcell (2002), Into and out of the Last Glacial Maximum: sea-level change during Oxygen Isotope Stages 3 and 2, Quaternary Science Reviews, 21, 343-360, doi:10.1016/S0277-3791(01)00071-3.

Laskar, J., P. Robutel, F. Joutel, M. Gastineau, A C. M. Correeia, and B. Levrard (2004), A long-term numerical solution for the insolation quantities of the Earth, *Astronomy and Astrophysics*, 428, 261-285, doi: 10.1051/0004-6361:20041335.

Lea, D. W., D. K. Pak, and H. J. Spero (2000), Climate Impact of Late Quaternary equatorial Pacific sea surface temperature variations, *Science, 289*, 1719, doi: 10.1126/science.289.5485.1719.

Locarnini, R. A., A. V. Mishonov, J. I. Antonov, T. P. Boyer, and H. E. Garcia (2006), World Ocean Atlas 2005, Volume 1: temperature. *In*: Levitus S. (ED.) *NOAA Atlas NESDIS61*. U.S. Government Printing Office, Washington, DC, 182.

Mohtadi, M., D. W. Oppo, S. Steinke, J-B W. Stuut, R. De Pol-Holz, D. Hebbeln, and A. Lückge (2011), Glacial to Holocene swings of the Australian-Indonesian monsoon, *Nature Geoscience*, 4, 540-544, doi: 10.1038/NGEO1209.

Muller, J., M. Kylander, R. A. J. Wüst, D. Weiss, A. Martinez-Cortizas, A. N. LeGrande, T. Jennerjahn, H. Behling, W. T. Anderson, and G. Jacobson (2008), Possible evidence for ert Heinrich phases in tropical NE Australia: the Lynch's Crater deposit, *Quaternary Science Reviews*, 27, 468-475, doi:10.1016/j.quascirev.2007.11.006.

Muller, J., J. F. McManus, D. W. Oppo, and R. Francois (2012), Strengthening of the Northeast Monsoon over the Flores Sea, Indonesia, at the time of Heinrich event 1, *Geology*, 40, 635-638, doi: 10.1130/G32878.1.

Petit, J. R., J. Jouzel, D. Raynaud, N. I., Barkov, J.-M. Barnola, I. Basile, M. Bender, J. Chappellaz, M. Davis, G. Delaygue, M. Delmotte, V. M. Kotlyakov, M. Legrand, V. Y. Lipenkov, C. Lorius, L. Pépin, C. Ritz, E. Saltzman, and M. Stievenard (1999), Climate and atmospheric history of the past 420,000 years from the Vostock ice core, Antarctica, *Nature, 399*, 429-436, doi:10.1038/20859.

Rosenthal, Y., D. W. Oppo, and B. K. Linsley (2003), The amplitude and phasing of climate change during the last deglaciation in the Sulu Sea, western equatorial Pacific, *Geophysical Research Letters*, 30, 8, 1428-1431, doi: 10.1029/2002GL016612.

Rosenthal, Y., B. K. Linsley, D. W. Oppo (2013), Pacific ocean heat content during the past 10,000 years, *Science*, *342*, 617, doi: 10.1126/science.1240837.

Ryan, W. B. F., et al. (2009), Global Multi-Resolution Topography synthesis, *Geochemistry Geophysics Geosystems, 10, Q03014, doi: 10.1029/2008GC002332.*

Schlitzer, R., Ocean Data View, http://odv.awi.de, 2013.

Schneider, T., T. Bischoff, and G. H. Haug (2014), Migrations and dynamics of the intertropical convergence zone, *Nature*, 513, 45-53, doi: 10.1038/nature13636.

Shakun, J. D., P. U. Clark, F. He, S. A. Marcott, A. C. Mix, Z. Liu, B. Otto-Bliesner, A. Schmittner, and E. Bard (2012), Global warming preceded by increasing carbon dioxide concentrations during the last deglaciation, *Nature*, 484, 49-54, doi: 10.1038/natture10915.

Song, Q., and A. L. Gordon (2004), Significance of the vertical profile of the Indonesian Throughflow transport to the Indian Ocean, *Geophysical Research Letters*, *31*, L16307, doi: 10.1029/2004GL020360.

Spooner, M. I., T. T. Barrows, P. De Deckker, and M. Paterne (2005), Paleoceanography of the Banda Sea, and Late Pleistocene initiation of the Northwest Monsoon, *Global and Planetary Change*, *49*, 28-46, doi: 10.1016/j.gloplacha.2005.05.002.

Sprintall, J., S. E. Wijffels, R. Molcard, and I. Jaya (2009), Direct estimates of the Indonesian Throughflow entering the Indian Ocean: 2004-2006, *Journal of Geophysical Research*, *114*, C07001, doi: 10.1029/2008JC005257.

Talley, L. D., and J. Sprintall (2005), Deep expression of the Indonesian Throughflow: Indonesian Intermediate Water in the South Equatorial Current, *Journal of Geophysical Research*, *110*, C10009, doi: 10.1029/2004JC002826.

Visser, K., R. Thunell, and L. Stott (2003), Magnitude and timing of temperature change in the Indo-Pacific warm pool during deglaciation, *Nature*, 421, 152-155, doi:10.1038/nature01297.

Wang, P. (1999), Response of Western Pacific marginal seas to glacial cycles: paleoceanographic and sedimentological features, *Marine Geology*, *156*, 5-39.

Wang, X., A. S. Auler, R. L. Edwards, H. Cheng, P. S. Cristalli, P. L. Smart, D. A. Richards, and C-C Shen (2004), Wet periods in northeastern Brazil over the past 210 kyr linked to distant climate anomalies, *Nature*, 432, doi:10.1038/nature03067

Wyrtki, K. (1958) The water exchange between the Pacific and the Indian Oceans in relation to upwelling process. Proceedings of the Ninth Pacific Science Congress, Inst Mar Res, Djakarta, Indonesia, 16: 61-65.

Xu, J., W. Kuhnt, A. Holbourn, N. Andersen, and G. Bartoli (2006), Changes in the vertical profile of the Indonesian Throughflow during Termination II: evidence from the Timor Sea, *Paleoceanography*, *21*, PA4202, doi: 10.1029/2006PA001278.

Xu, J., A. Holbourn, W. Kuhnt, Z. Jian, and H. Kawamura (2008), Changes in the thermocline structure of the Indonesian outflow during Terminations I and II, *Earth and Planetary Science Letters*, *273*, 152-162, doi: 10.1016/j.epsl.2008.06.029.

Yokoyama, Y., K. Lambeck, P. De Deckker, P. Johnston, and K. Fiffield (2000), Timing of the Last Glacial Maximum from observed sea-level minima, *Nature*, 406, 713-716 doi:10.1038/35021035.

Yokoyama, Y., P. De Deckker, K. Lambeck P. Johnston, and K. Fiffield (2001), Sea-level at the Last Glacial Maximum: evidence from northwestern Australia to constrain ice volumes fro oxygen isotope stage 2, *Palaeogeography, Palaeoclimatology, Palaeoecology*, 165, 281-297, doi:10.1016/S0031-0182(00)00164-4.

Zenk, W., G. Siedler, A. Ishida, J. Holfort, Y. Kashino, Y. Kuroda, T. Miyama, T. J. Müller (2005), Pathways and variability of the Antarctic Intermediate Water in the western equatorial Pacific Ocean, *Progress in Oceanography*, 67, 245-281, doi: 10.1016/j.pocean.2005.05.003.

Chapter 2

Refining *C. wuellerstorfi* and *H. elegans* Mg/Ca temperature calibrations

Elena Lo Giudice Cappelli, Marcus Regenberg, Ann Holbourn, Wolfgang Kuhnt, Dieter Garbe-Schönberg, and Nils Andersen

Published in *Marine Micropaleontology* (doi: 10.1016/j.marmicro.2015.10.001)

Abstract

We present core top Mg/Ca, Sr/Ca and $\delta^{18}O$ measurements for *Cibicidoides wuellerstorfi* and *Hoeglundina elegans* from the Timor Sea and the Makassar Strait, which span a bottom water temperature (BWT) range from 2 to 18 °C. In both species Mg/Ca ratios are positively and significantly correlated with BWT, while $\delta^{18}O$ measurements are significantly anti-correlated with BWT. Comparison of calcification temperatures derived from Mg/Ca ratios and $\delta^{18}O$ measurements yield comparable results and closely match CTD-measured temperatures. We integrate our results with previously published data sets from the Atlantic, Indian and Pacific Oceans and provide temperature calibration equations over the temperature range from 2 to 12 °C for *H. elegans* and from 0 to 10 °C for *C. wuellerstorfi.* We found geographical differences in the relation of benthic Mg/Ca ratios to BWT: *C. wuellerstorfi* shows Mg/Ca sensitivity to BWT of 19% increase in Mg/Ca per °C for the Atlantic Ocean and of 15% per °C for the Indian and Pacific Oceans. *Hoeglundina elegans* shows Mg/Ca sensitivity to BWT of 16% increase in Mg/Ca per °C for the Atlantic Ocean and of 14% per °C for the Indian and Pacific Oceans. *Cibicidoides wuellerstorfi* Sr/Ca variability appears to be driven by carbonate ion saturation, whereas *H. elegans* Sr/Ca variability is closely linked to BWT in the compiled data sets from the Atlantic, Indian and Pacific Oceans.

2.1. Introduction

The recognition that substitution of magnesium for calcium in both planktonic and benthic foraminiferal tests occurs as a temperature-controlled process [*Savin and Douglas*, 1973; *Bender at al.*, 1975] led to the development of Mg/Ca ratios as a proxy for paleotemperature reconstructions [e.g.: *Russell et al.*, 1994; *Nürnberg et al.*,

1996; *Rosenthal et al*., 1997; *Rathburn and De Deckker* 1997; *Lea et al.*, 1999; *Reichart et al.*, 2003; *Regenberg et al.,* 2009]. However, the degree of Mg^{2+} substitution in benthic foraminiferal tests varies from species to species, depending on biological controls during the biomineralization process (vital effects) [*Erez* 2003; *Bentov and Erez,* 2005 and 2006; *de Nooijer et al.*, 2014]. Therefore, species-specific Mg/Ca calibrations are needed to reliably reconstruct BWT variability over time [*Rosenthal et al.,* 1997; *Lear et al.,* 2002; *Elderfield et al*., 2006; *Healey et al.*, 2008; *Raitzsch et al.*, 2008].

The relationship between benthic Mg/Ca ratios and BWT remains controversial. Previously published benthic Mg/Ca-BWT calibrations, covering a wide BWT range (from -1 to 18 °C), were based on multiple species of the genus *Cibicidoides*, such as *C. wuellerstorfi, C. pachyderma, C. compressa, C. kullenbergi* and *wuellerstorfi*-like *Cibicidoides* [*Lear et al.*, 2002; *Martin et al*., 2002; *Elderfield et al.*, 2006]. In these studies, the colder part of the *Cibicidoides* spp. BWT calibration was characterized by Mg/Ca measurements of *C. wuellerstorfi*, as this species was the most abundant below 5 °C. In contrast, the warmer part of the calibration represented the relationship between *C. pachyderma* Mg/Ca ratios and BWT, as this species was dominant above 5 °C [*Lear et al*., 2002; *Martin et al.*, 2002; *Elderfield et al.*, 2006]. As samples from lower BWT fell along a steeper trend than that described by the *Cibicidoides* spp. calibration, *Martin et al.* [2002] and *Elderfield et al.* [2006] suggested that other factors (e.g., dissolution, carbonate ion effect) may exert a second-order control on Mg/Ca variability at low BWT.

To resolve this issue, recent studies focused on species-specific calibrations, based on *C. wuellerstorfi* Mg/Ca ratios covering the colder part of the BWT calibration range (<6 °C) [*Healey et al*., 2008; *Raitzsch et al*., 2008; *Yu and Elderfield*

2008; *Tisserand et al.*, 2013]. These studies found that the slope of the *C. wuellerstorfi* Mg/Ca-BWT relationship is steeper than previously published *Cibicidoides* spp. calibrations. However, this difference was considered too large to be exclusively ascribed to species-specific vital effects on Mg^{2+} uptake into foraminiferal tests. It was, thus, suggested that low carbonate ion saturation inhibits Mg^{2+} uptake into *C. wuellerstorfi* tests (carbonate ion effect) [*Elderfield et al*., 2006; *Healey et al*., 2008; *Raitzsch et al*., 2008; *Yu and Elderfield* 2008; *Tisserand et al.*, 2013]. In addition, four published *Hoeglundina elegans* Mg/Ca temperature calibrations, covering a temperature range between 2 and 19 °C, reported very different rates of Mg/Ca increase in relation to BWT: ~3% per 1°C increase in BWT [*Rosenthal et al.*, 2006; *Bryan and Marchitto* 2008], ~7% [*Rosenthal et al.*, 2006] and ~16% per °C [*Ní Fhlaithearta et al.*, 2010]. This also led to the suggestion that changes in bottom water carbonate ion saturation ($\Delta[CO_3^{2-}]$), rather than BWT, might control Mg/Ca variability in *H. elegans* [*Rosenthal et al.*, 2006, *Bryan and Marchitto* 2008].

The carbonate ion effect is thought to become significant in bottom waters, where $\Delta[CO_3^{2-}]_{calcite}$ <25 μmol kg^{-1} or temperature is lower than 3 °C for *C. wuellerstorfi* [*Elderfield et al*., 2006; *Healey et al*., 2008; *Raitzsch et al*., 2008; *Yu and Elderfield* 2008] and where $\Delta[CO_3^{2-}]_{aragonite}$ <15 μmol kg^{-1} for *H. elegans* [*Rosenthal et al*., 2006]. *Elderfield et al.* [2006] first quantified the effect of $\Delta[CO_3^{2-}]_{calcite}$ in *C. wuellerstorfi* Mg/Ca ratios and proposed Mg/Ca sensitivity to $\Delta[CO_3^{2-}]_{calcite}$ of 0.0086 mmol mol^{-1} per μmol kg^{-1}. *Healey et al*. [2008] reported a similar value, while *Raitzsch et al*. [2008] and *Yu and Elderfield* [2008] proposed a value of ~0.01 mmol mol^{-1} per μmol kg^{-1}. At present, it is unclear to what extent Mg/Ca ratios in *C. wuellerstorfi* and *H. elegans* can be reliably used for paleotemperature

reconstructions, as it remains a challenge to distinguish between temperature and carbonate ion effect on benthic Mg/Ca ratios. In a recent study, *Yu et al.* [2014] found that $\Delta[CO_3^{2-}]_{calcite}$ exerts a significant control on modern *C. wuellerstorfi* Sr/Ca ratios and used this relationship to track past changes in deep water carbonate ion saturation. Paired measurements of Mg/Ca and Sr/Ca ratios in the same foraminiferal samples can, thus, provide a valuable tool to better evaluate the relationship between carbonate ion saturation and element to calcium ratios in benthic foraminifera.

We present new *C. wuellerstorfi* and *H. elegans* Mg/Ca, $\delta^{18}O$, and Sr/Ca measurements from core tops retrieved from the Timor Sea and the Makassar Strait (Indonesia), which span BWT between 2 and 18 °C, $\Delta[CO_3^{2-}]_{calcite}$ between 14 and 41 μmol kg^{-1} and $\Delta[CO_3^{2-}]_{aragonite}$ between -23 and 100 μmol kg^{-1} (Fig. 2.1 and Tab. 2.1). In this region, *C. wuellerstorfi* is found in relatively shallow waters depths (~300–1000 m), thus in warmer BWT than the deeper/bathyal and abyssal specimens previously studied. These new Mg/Ca measurements provide an opportunity to expand the data sets of previously published calibrations for *C. wuellerstorfi* and *H. elegans* and to discuss regional differences in benthic Mg/Ca ratios in relation to BWT. New Sr/Ca ratios contribute to improve our understanding of changes in deep water $\Delta[CO_3^{2-}]$ and to better define the geochemical characteristics of different ocean basins.

2.2. Material and Methods

2.2.1 Sampling strategy

We analyzed Mg/Ca, Sr/Ca and $\delta^{18}O$ in the benthic foraminifera *C. wuellerstorfi* and *H. elegans* in 19 core tops (0 – 1 cm slice) from multicores retrieved

in the Timor Sea during the Sonne-185 "VITAL" Cruise [*Kuhnt et al*., 2005] and in 16 core tops (0 – 1 cm slice) from the Makassar Strait collected during the Sonne-217 "MAJA" Cruise [*Kuhnt et al*., 2011] (Fig. 2.1 and Tab. 2.1). *Cibicidoides wuellerstorfi* is an epifaunal species, which lives in middle to lower bathyal and abyssal depths [*Holbourn et al*., 2013] and has been commonly used to reconstruct BWT [*Lear et al.*, 2002; *Elderfield et al.*, 2006]. *Hoeglundina elegans* lives at or close to the sediment-water interface and has an aragonitic, glassy test that is less susceptible to diagenetic overgrowth than calcitic specimens [*Boyle et al.*, 1995; *Schönfeld*, 2001; *Fontanier et al*., 2002; *Reichart et al.*, 2003; *Rosenthal et al*., 2006].

Table 2.1. Core Top Locations

Core	Latitude, S	Longitude, E	Water Depth, m	BWT, °C
		Timor Sea		
18454	9° 46.201'	131° 14.105'	131	18.3
18503	15° 18.861'	121° 05.007'	354	9.95
18489	13° 03.016'	122° 56.016'	431	9.01
18488	12° 53.529'	122° 45.353'	555	7.82
18493	13° 25.160'	122° 05.061'	599	7.23
18469	9° 14.395'	129° 38.549'	704	6.25
18501	15° 08.503'	120° 47.010'	742	6.13
18468	9° 11.982'	129° 31.939'	803	5.80
18467	9° 10.429'	129° 27.928'	899	4.99
18466	9° 09.383'	129° 25.008'	1004	4.62
18465	9° 08.683'	129° 23.405'	1082	4.61
18500	14° 58.833'	120° 41.852'	1167	4.1
18464	9° 07.264'	129° 19.286'	1203	4.26
18463	9° 06.231'	129° 16.682'	1311	4.18
18499	14° 54.500'	120° 33.989'	1383	3.51
18462	9° 05.324'	129° 14.220'	1422	4.26
18478	11° 00.974'	120° 05.016'	1769	3.56
18506	15° 18.652'	119° 30.089'	2410	2.17
18507	13° 50.993'	120° 00.008'	2450	2.00
		Makassar Strait		
18534	7°30.618'	116°15.804'	563	6.90
18518	4°31.490'	118°56.510'	620	6.43
18532	5°55.849'	116°49.300'	629	6.60
18517	1°32.210'	117°33.792'	699	6.14
18545	5°5.315'	118°43.333'	707	6.07
18541	6°46.302'	119°23.928'	739	5.75
18536	7°28.130'	118°13.948'	836	5.65
18530	5°14.459'	117°20.348'	876	5.31
18537	7°35.595'	118°14.644'	929	5.38
18522	1°24.120'N	119°4.758'	974	4.67
18531	5°10.129'	117°27.918'	1086	4.50
18540	6°52.405'	119°34.997'	1200	4.09
18526	3°36.860'	118°10.058'	1538	3.95
18527	3°57.844'	117°49.161'	1615	3.61
18528	4°45.331'	117°53.369'	1785	3.47
18525	2°32.754'	118°38.128'	1822	3.52

Conductivity-temperature-depth (CTD) casts were deployed at the multicore locations during the two cruises to measure *in situ* temperature (Tab. 2.1).

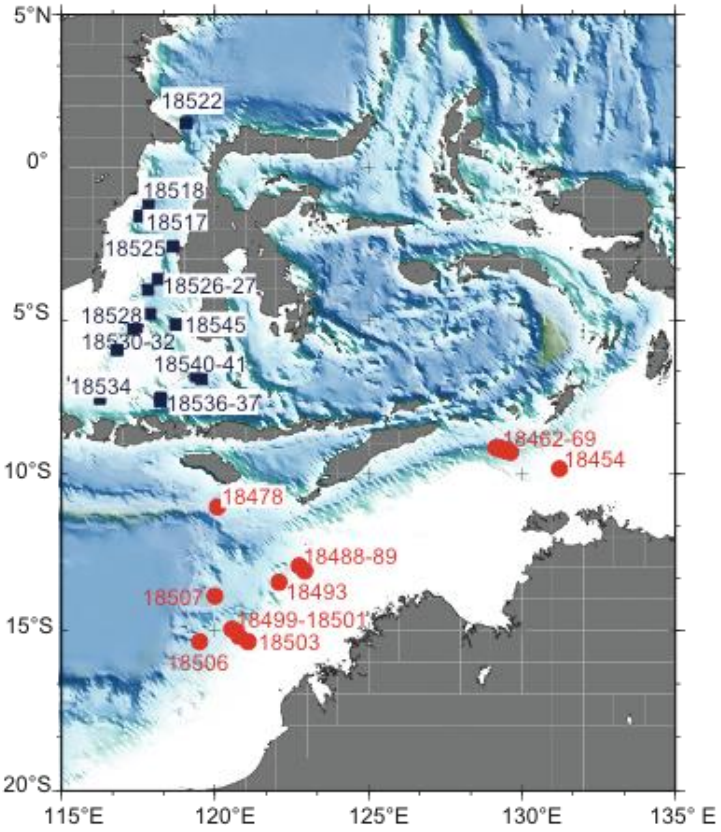

Fig. 2.1. a) Bathymetric chart with location of multicores referred to in this work. Red circles indicate multicores retrieved from the Timor Sea in a water depth range from 130 to 2500 m, blue squares indicate multicores retrieved from the Makassar Strait in a water depth range from 350 to 1800 m.

Five multicore stations in the Timor Sea and eight in the Makassar Strait were not paired with CTD measurements; therefore we derived *in situ* temperature by linear interpolation from the closest stations available. Timor Sea core top samples from water depths between 130 and 2500 m correspond to CTD-derived BWT between 2 and 18 °C; Makassar samples from water depths between 550 and 1800 m correspond to CTD-derived BWT between 3.5 and 7 °C (Tab. 2.1 and Fig. 2.1). Most core top samples were retrieved in areas where sedimentation rates are higher than ~10 cm per kyr [*Kuhnt et al.*, 2005, 2011]. Additionally, all core top samples contained rose-Bengal stained specimens of benthic foraminifers indicative of well-preserved sediment surfaces.

Water samples were collected at different water depths in six stations in the Timor Strait and in 17 stations in the Makassar Strait using a CTD-Rosette. Aliquots

of seawater from the CTD-Rosette were sampled for seawater stable oxygen isotope ($\delta^{18}O_{sw}$) measurements (Auxiliary Tabs. 2.1 and 2.2). When water samples were not available, $\delta^{18}O_{sw}$ values were estimated by linear interpolation from the next CTD station that reached deeper water depth.

2.2.2 Mg/Ca and Sr/Ca measurements of benthic foraminiferal tests

Between 5 and 30 tests of *H. elegans* and *C. wuellerstorfi* were selected for Mg/Ca, Sr/Ca and $\delta^{18}O$ analysis from the > 250 μm size fraction. All tests were checked under the microscope for cement encrustations and infillings before being broken into large fragments. After crushing, foraminiferal samples were split into sub-samples for Mg/Ca and Sr/Ca analyses (2/3 of the total sample) and $\delta^{18}O$ analyses (remaining 1/3). Mg/Ca and Sr/Ca samples were cleaned of the contaminant phases using the cleaning procedure with reductive step detailed in *Martin and Lea* [2002], without the alkaline chelation step. Samples were analyzed by ICP-OES (Inductively Coupled Plasma-Optical Emission Spectrometer) using a Spectro Ciros SOP instrument with cooled cyclonic spraychamber and microconcentric nebulization (200 μl min^{-1}) at the Institute of Geosciences, University of Kiel. Intensity ratio calibration followed the method of *de Villiers et al.* [2002] and internal analytical precision was 0.1 – 0.2% RSD. For external normalization and drift control, the certified reference material ECRM 752-1 (limestone) was measured after every sixth foraminiferal sample. The differences between the expected Mg/Ca ratio of 3.821 mmol mol^{-1} and Sr/Ca of 0.18 mmol mol^{-1} [*Greaves et al.*, 2008; not centrifuged] and the measured values were used to correct foraminiferal Mg/Ca and Sr/Ca ratios incrementally for offset and instrument drift.

In samples containing sufficient numbers of specimens, duplicates were measured (Auxiliary Tabs. 2.1 and 2.2). Twenty-two paired analyses of *H. elegans* Mg/Ca ratios gave a reproducibility of ±0.10 mmol mol^{-1} (standard deviation) corresponding to an overall average precision of 5.6% (pooled relative standard deviation). Foraminiferal Fe/Ca, Al/Ca and Mn/Ca ratios were additionally checked to monitor cleaning efficacy and no correlation with Mg/Ca ratios was found. Four *C. wuellerstorfi* samples from the Timor Sea and four *H. elegans* samples from the Makassar Strait, which showed Al/Ca ratios higher than 1 mmol mol^{-1}, indicative of sample contamination, were not included in the calibration study (Auxiliary Tabs. 2.1 and 2.2). Additionally, one *H. elegans* Mg/Ca measurement from the Makassar Strait (sample 18534; Mg/Ca = 2.45 mmol mol^{-1}), was discarded as it substantially diverged from its replicates (~1.6 mmol mol^{-1}, equivalent to ~7 °C), pointing to a problem either during cleaning or measuring the sample (Auxiliary Tab. 2.2).

2.2.3 $\delta^{18}O$ analyses in *H. elegans* tests and $\delta^{18}O_{sw}$ measurements

Foraminiferal samples for stable isotopes analysis were cleaned in absolute ethanol in an ultrasonic bath, dried at 40 °C and measured with a Finnigan MAT 253 mass spectrometer at the Leibniz Laboratory for Radiometric Dating and Isotope Research (Leibniz Laboratory), University of Kiel. The instrument is coupled on-line to a Carbo-Kiel Device (Type IV) for automated CO_2 preparation from carbonate samples for isotopic analysis. On the basis of the performance of international and lab-internal standard carbonates, the precision is better than ±0.09‰. Results were calibrated using the NIST (National Institute of Standard and Technology, Gaithersburg, Maryland) carbonate isotope standard and NBS (National Bureau of Standard) 19 and in addition NBS 20, and are reported on the Vienna PeeDee

Belemnite (V-PDB) scale. We integrated the new *C. wuellerstorfi* $\delta^{18}O$ measurements with previously published measurements from the same Timor Sea core top samples [*Holbourn et al.*, 2011].

$\delta^{18}O_{sw}$ was measured at the Leibniz Laboratory, University of Kiel, on a Thermo Finnigan DeltaPlusXL mass spectrometer connected to a Gasbench II device. The oxygen isotopic composition of water is analyzed by a so-called carbon dioxide-water equilibration method: not water, but carbon dioxide equilibrated with water is actually measured in the mass spectrometer. $\delta^{18}O_{sw}$ was measured relative to Vienna Standard Mean Ocean Water (V-SMOW) and internal lab standard. Measurements reproducibility is ±0.06‰ (standard deviation) based on multiple analyses performed on the same water samples.

Since the isotopic fractionation between seawater and $CaCO_3$ is a temperature dependent process, calcite $\delta^{18}O$ and $\delta^{18}O_{sw}$ can be used as a temperature proxy [e.g.: *Urey*, 1947; *Shackleton*, 1974]. However, as benthic $\delta^{18}O$ was measured relative to the V-PDB standard, and $\delta^{18}O_{sw}$ was referenced to V-SMOW, it was necessary to convert the V-SMOW scale to the V-PDB scale before generating a temperature calibration. We used the correction factor of 0.27‰ following *Hut* [1987].

2.2.4 Carbonate ion concentration and saturation

The degree of carbonate ion saturation ($\Delta[CO_3^{2-}]$) is the key parameter when evaluating carbonate ion control on benthic Mg/Ca ratios [*Rosenthal et al*., 2006; *Elderfield et al.*, 2006]. We used carbonate ion saturation with respect to aragonite ($\Delta[CO_3^{2-}]_{aragonite}$) to assess the carbonate ion effect on *H. elegans* Mg/Ca ratios and carbonate ion saturation with respect to calcite ($\Delta[CO_3^{2-}]_{calcite}$) to evaluate the

carbonate ion effect on *C. wuellerstorfi* Mg/Ca ratios. To estimate carbonate ion concentration ($[CO_3^{2-}]_{in\ situ}$), $\Delta[CO_3^{2-}]_{aragonite}$ and $\Delta[CO_3^{2-}]_{calcite}$ in the Timor Sea and Makassar Strait core tops, we used data from *Rosenthal et al*. [2006]. These authors measured total dissolved inorganic carbon and total alkalinity in water samples collected in the Makassar Strait and entered these parameters together with temperature and salinity measurements from the CTD into the co2sys program [*Lewis and Wallace*, 1998] to obtain $[CO_3^{2-}]_{in\ situ}$. For this study, we re-calculated carbonate ion saturation ($[CO_3^{2-}]_{saturation}$) after *Jansen et al.* [2002] for aragonite and calcite. The degree of saturation with respect to aragonite and calcite was then calculated using the following equation and the appropriate $[CO_3^{2-}]_{saturation}$ value:

$$\Delta[CO_3^{2-}] = [CO_3^{2-}]_{in\ situ} - [CO_3^{2-}]_{saturation} \quad (1)$$

For previous studies, we used published carbonate ion concentration and saturation data [*Elderfield et al.*, 2006; *Raitzsch et al*., 2008; *Yu and Elderfield* 2008; *Tisserand et al.*, 2013; *Kubota et al*., 2015]. When not available, we used data from the nearest GEOSECS stations for each core location following the approach described above [i.e. in *Martin et al*., 2002, and *Lear et al.*, 2002; *Reichart et al.*, 2003; *Healey et al.*, 2008]. For the *H. elegans* samples of *Reichart et al*. [2003] from the Bay of Biscay, it was not possible to estimate $\Delta[CO_3^{2-}]_{aragonite}$ as there is no GEOSECS station in close proximity.

2.2.5 Compilation of benthic Mg/Ca measurements from different ocean basins

Combination of our data with previously published *C. wuellerstorfi* and *H. elegans* Mg/Ca ratios is complicated by the usage of different cleaning techniques (i.e., oxidative vs. reductive cleaning) or instruments (i.e., ICP-OES, ICP-MS and

Laser Ablation ICP-MS) in previous studies, which may lead to systematic offsets (Tab. 2.2). The *C. wuellerstorfi* Mg/Ca measurements of *Tisserand et al.* [2013] did not include a reductive step in the cleaning procedure, whereas the measurements of *Reichart et al.* [2003] and *Raitzsch et al.* [2008] were performed with laser ablation. All other studies [*Martin et al.*, 2002; *Lear et al*., 2002; *Elderfield et al*., 2006; *Rosenthal et al.*, 2006; *Yu and Elderfield* 2008; *Kubota et al*., 2015] used a cleaning protocol similar to ours, including a reductive step.

Table 2.2. Published Mg/Ca temperature calibrations referred to in this study

Reference	Species	Cleaning Method	Calibration equation	Temperature range (°C)
Martin et al. [2002]	*Cibicidoides* spp.	Reductive	Mg/Ca = 1.22 exp(0.109 BWT)	-1.1 - 18
Lear et al. [2002]	*Cibicidoides* spp.	Reductive	Mg/Ca = 0.867 exp(0.109 BWT)	0.8 - 18.4
Elderfield et al. [2006]	*Cibicidoides* spp.	Reductive	Mg/Ca=0.90 exp(0.11 BWT)	-1.1 - 18
Raitzsch et al. [2008]	*C. wuellerstorfi*	Laser Ablation	Mg/Ca = 0.83 exp(0.145 BWT)	0.39 - 3.88
Healey et al. [2008]	*C. wuellerstorfi*	Reductive	Mg/Ca = 0.78 exp(0.23 BWT)	0.8 - 3.8
Yu and Elderfield [2008]	*C. wuellerstorfi*	Reductive	Mg/Ca = 0.59 exp(0.28 BWT) without carbonate ion saturation correction	0.98 - 4.26
Tisserand et al. [2013]	*C. wuellerstorfi*	Oxidative	Mg/Ca = 0.82 exp(0.19 BWT)	0 - 6
Reichart et al. [2003]	*H. elegans*	Laser Ablation	Mg/Ca = 0.39 exp (0.16 BWT)	2.5 - 13
Rosenthal et al. [2006]	*H. elegans*	Reductive	Mg/Ca = 0.96+0.0034 BWT (Atlantic)	4.2 - 18.4
Rosenthal et al. [2006]	*H. elegans*	Reductive	Mg/Ca = 0.248+0.0071 BWT (Pacific; without carbonate ion saturation correction)	1.7 - 17
Bryan and Marchitto [2008]	*H. elegans*	Reductive	Mg/Ca = 1.01+0.030 BWT	1.7 - 19
Ni Fhlaithearta et al. [2010]	*H. elegans*	Laser Ablation	Mg/C a= 0.39 exp(0.156 BWT)	2 - 16

Elderfield et al. [2006] proposed an offset of 0.2 mmol mol^{-1} between paired *C. wuellerstorfi* samples from the same core top measured with oxidative and reductive cleaning, which we used as a correction factor ($Mg/Ca_{Tisserand} - 0.2$) for the dataset of *Tisserand et al.* [2013]. No offset is apparent, when Mg/Ca measurements obtained with laser ablation [*Reichart et al.*, 2003; *Raitzsch et al.*, 2008] are plotted together with Mg/Ca ratios measured with wet chemistry (Figs. 2.5a and 2.6a). As the calibration equations of *Martin et al.* [2002], *Lear et al*. [2002] and *Elderfield et al*. [2006] were based on Mg/Ca measurements performed in multiple species of the genus *Cibicidoides*, we selected the *C. wuellerstorfi* measurements from their studies to generate new species-specific *C. wuellerstorfi* Mg/Ca temperature calibrations.

Hoeglundina elegans samples retrieved from Little Bahama Banks [*Rosenthal et al*., 2006] are not included in this calibration study, as *Curry and Marchitto* [2008] found that foraminiferal samples are diagenetically overprinted by high-Mg overgrowth in these shallow, carbonate-rich sediments, resulting in anomalously high Mg/Ca ratios.

2.3. Results

2.3.1 Benthic Mg/Ca-temperature relationships for the Timor Sea and Makassar Strait

Core top Mg/Ca ratios in *C. wuellerstorfi* range from 0.90 to 4.15 mmol mol^{-1}, corresponding to CTD-measured BWT from 2 to 10°C (Auxiliary Tab. 2.1). Mg/Ca ratios in *H. elegans* vary between 0.33 and 1.84 mmol mol^{-1}, corresponding to CTD-measured BWT from 2 to 18°C (Auxiliary Tab. 2.2). In both species, Mg/Ca ratios decrease with increasing water depth (Figs. 2a and 3a), showing good agreement with *in situ* BWT measurements (Figs. 2b and c, 3b and c). Linear and exponential regressions show positive correlation between benthic Mg/Ca ratios and BWT, described by the following equations (Figs. 2d and 3d):

Cibicidoides wuellerstorfi

$$Mg/Ca = (0.57 \pm 0.21) + (0.23 \pm 0.04)\ BWT \quad (2)$$

($R^2 = 0.56$; n = 30; $p<0.0001$)

$$Mg/Ca = (0.91 \pm 0.10)\ exp^{(0.12 \pm 0.02)\ BWT} \quad (3)$$

($R^2 = 0.65$; n = 30; $p<0.0001$)

Hoeglundina elegans:

$$Mg/Ca = (0.36 \pm 0.04) + (0.07 \pm 0.006)\ BWT \quad (4)$$

(R^2 = 0.65; n = 74; p<0.0001)

$$Mg/Ca = (0.47 \pm 0.06)\ exp^{(0.08 \pm 0.009)\ BWT} \quad (5)$$

(R^2 = 0.56; n = 74; p<0.0001)

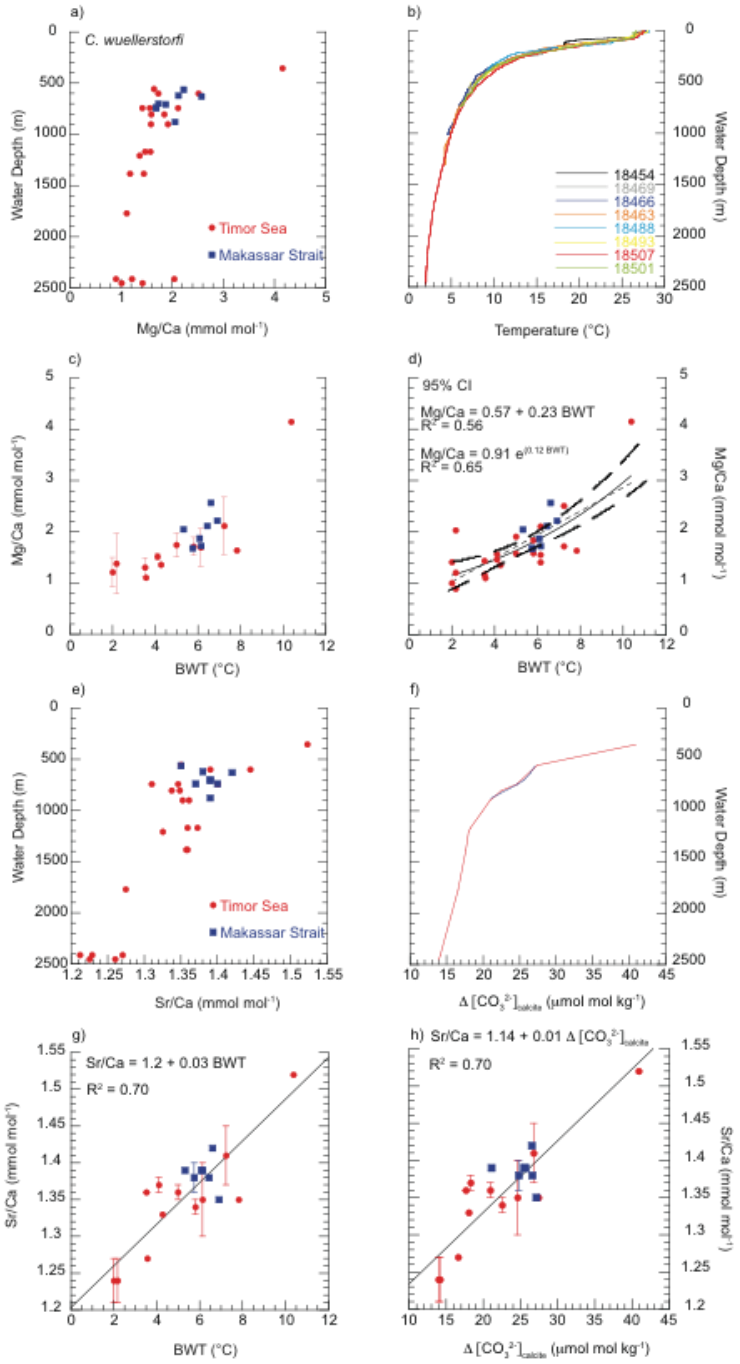

Fig. 2.2. a) *Cibicidoides wuellerstorfi* Mg/Ca versus water depth. **b)** CTD-measured temperature profiles. **c)** *Cibicidoides wuellerstorfi* Mg/Ca ratios versus CTD-derived bottom water temperatures; replicate samples were averaged and error bars represent their standard deviation. **d)** Calibration of *C. wuellerstorfi* Mg/Ca ratios versus CTD-derived BWT; solid line represents exponential fit, finely dashed line represents linear fit, black dashed lines mark the 95% confidence interval. **e)** *Cibicidoides wuellerstorfi* Sr/Ca versus water depth. **f)** Carbonate ion saturation profile with respect to calcite. **g)** *Cibicidoides wuellerstorfi* Sr/Ca ratios versus CTD-derived BWT. **h)** *Cibicidoides wuellerstorfi* Sr/Ca ratios versus $\Delta[CO_3^{2-}]_{calcite}$.

2.3.2 Benthic Sr/Ca-temperature and Sr/Ca-$\Delta[CO_3^{2-}]$ relationships for the Timor Sea and Makassar Strait

Core top Sr/Ca ratios in *C. wuellerstorfi* range from 1.21 to 1.52 mmol mol^{-1}, corresponding to $\Delta[CO_3^{2-}]_{calcite}$ values between 14 and 41 μmol kg^{-1} (Figs. 2e and f). Sr/Ca ratios in *H. elegans* vary between 0.44 to 3.26 mmol mol^{-1}, corresponding to $\Delta[CO_3^{2-}]_{aragonite}$ values between -23 and 100 μmol kg^{-1} (Figs. 3e and f). In both species, Sr/Ca ratios decrease with increasing water depth (Figs. 2e and 3e). Linear regressions best describe relationships between benthic Sr/Ca ratios and BWT (Figs. 2g and 3g) and between benthic Sr/Ca ratios and $\Delta[CO_3^{2-}]$ (Figs. 2h and 3h):

Cibicidoides wuellerstorfi

$$Sr/Ca = (1.2 \pm 0.02) + (0.03 \pm 0.003)\ BWT \quad (6)$$

($R^2 = 0.70$; n = 30; $p<0.0001$)

$$Sr/Ca = (1.14 \pm 0.03) + (0.01 \pm 0.001)\ \Delta[CO_3^{2-}]_{calcite} \quad (7)$$

($R^2 = 0.70$; n = 30; $p<0.0001$)

Hoeglundina elegans:

$$Sr/Ca = (0.19 \pm 0.07) + (0.19 \pm 0.01)\ BWT \quad (8)$$

($R^2 = 0.82$; n = 74; $p<0.0001$)

$$Sr/Ca = (1.4 \pm 0.04) + (0.023 \pm 0.002)\ \Delta[CO_3^{2-}]_{aragonite} \quad (9)$$

($R^2 = 0.64$; n = 74; $p=0.06$)

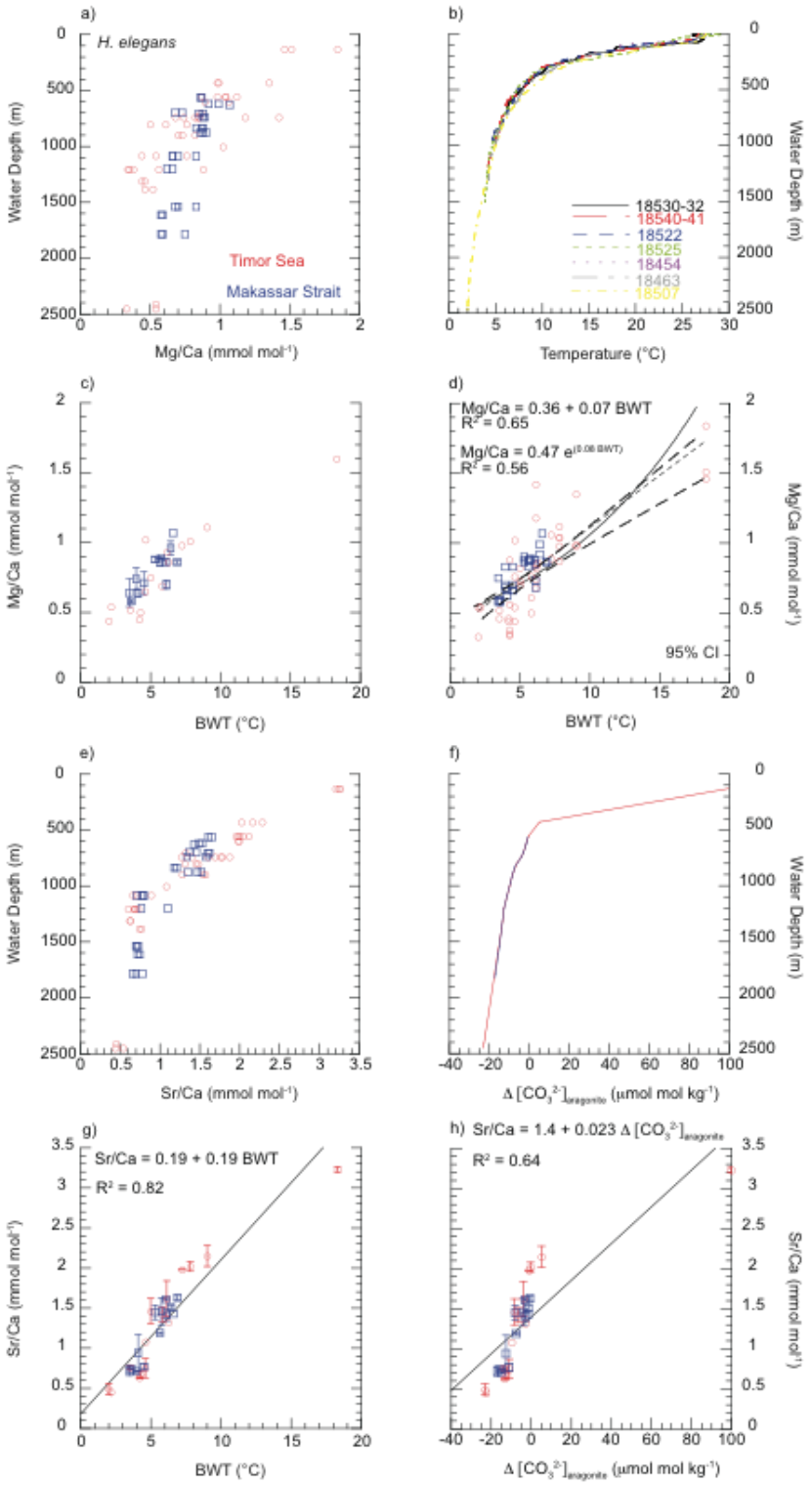

Fig. 2.3. a) *Hoeglundina elegans* Mg/Ca versus water depth. **b)** CTD-measured temperature profiles. **c)** *Hoeglundina elegans* Mg/Ca ratios versus CTD-derived BWT; replicate samples were averaged and error bars represent their standard deviation. **d)** Calibration of *H. elegans* Mg/Ca ratios versus CTD-derived BWT; solid line represents exponential fit, finely dashed line represents linear fit, thicker dashed lines mark the 95% confidence interval. **e)** *Hoeglundina elegans* Sr/Ca versus water depth. **f)** Carbonate ion saturation profile with respect to aragonite. **g)** *Hoeglundina elegans* Sr/Ca ratios versus CTD-derived BWT. **h)** *Hoeglundina elegans* Sr/Ca ratios versus $\Delta[CO_3^{2-}]_{aragonite}$.

2.3.3 Benthic $\delta^{18}O$ – temperature relationship for the Timor Sea and Makassar Strait

In the Timor Sea, *C. wuellerstorfi* $\delta^{18}O$ values range between 0.67 and 2.74‰, while *H. elegans* $\delta^{18}O$ values vary between -0.20 and 4.21‰, both exhibiting consistent increases with water depth (Figs. 4a and d). In the Makassar Strait, *C. wuellerstorfi* $\delta^{18}O$ values fluctuate between 1.77 and 2.20‰ and *H. elegans* $\delta^{18}O$ values between 2.88 and 3.60‰ (Figs. 4a and d). Benthic $\delta^{18}O$ is strongly anti-correlated with CTD-measured BWT (R^2 >0.8) (Figs. 4b and e) and linear regressions best describe the relationship between BWT and benthic $\delta^{18}O$ measurements corrected for $\delta^{18}O_{sw}$ ($\delta^{18}O - \delta^{18}O_{sw} + 0.27$) (Figs. 4c and f):

C. wuellerstorfi

$$(\delta^{18}O_{C.wuellerstorfi} - \delta^{18}O_{sw} + 0.27) = (3.6 \pm 0.07) - (0.22 \pm 0.013)\ BWT \quad (10)$$

($R^2 = 0.84$; n = 57; $p<0.0001$)

H. elegans

$$(\delta^{18}O_{H.elegans} - \delta^{18}O_{sw} + 0.27) = (5.2 \pm 0.1) - (0.26 \pm 0.016)\ BWT \quad (11)$$

($R^2 = 0.89$; n = 35; $p=0.004$)

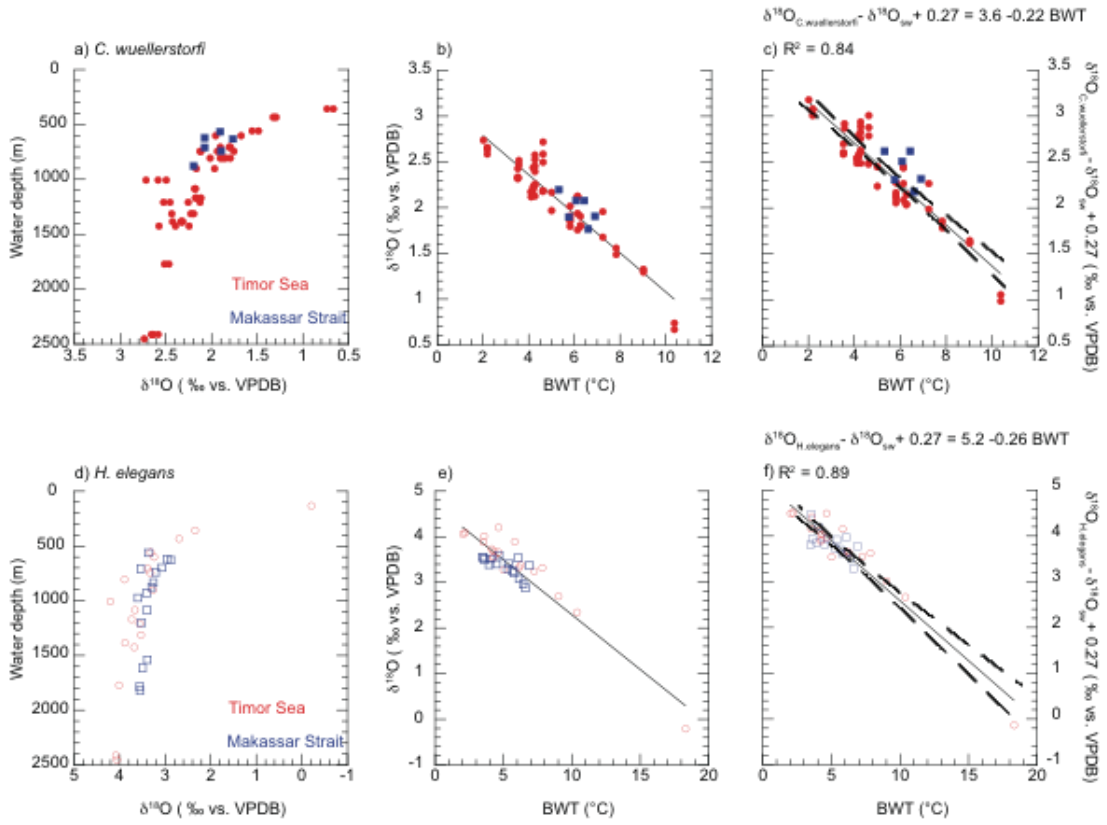

Fig. 2.4. a) *Cibicidoides wuellerstorfi* $\delta^{18}O$ versus water depth. **b)** *Cibicidoides wuellerstorfi* $\delta^{18}O$ versus BWT. **c)** Corrected *C. wuellerstorfi* $\delta^{18}O$ versus BWT. Dashed lines represent 95% confidence interval. **d)** *Hoeglundina elegans* $\delta^{18}O$ versus water depth. **b)** *Hoeglundina elegans* $\delta^{18}O$ versus BWT. **c)** Corrected *H. elegans* $\delta^{18}O$ versus BWT. Dashed lines mark the 95% confidence interval.

2.4. Discussion

2.4.1 *Cibicidoides wuellerstorfi*

2.4.1.1 Comparison to published data

We plotted published *C. wuellerstorfi* Mg/Ca ratios from BWT ranging between -1 and 16 °C together with new Mg/Ca data from the Timor Sea and Makassar Strait covering the 2 to 10 °C temperature range (compiled dataset) (Fig. 2.5a). Core top samples include samples from the Atlantic Ocean [*Lear et al.*, 2002; *Martin et al.*, 2002; *Elderfield et al.*, 2006; *Healey et al.*, 2008; *Raitzsch et al.*, 2008; *Yu and Elderfield* 2008], samples from the Brazilian margin, where $\Delta[CO_3^{2-}]_{calcite}$ is

almost constant [*Tisserand et al*., 2013], samples from the Norwegian Sea, where BWT changes are minimal [*Elderfield et al.,* 2006; *Yu and Elderfield* 2008], samples from the Pacific Ocean [*Lear et al.,* 2002; *Martin et al*., 2002; *Elderfield et al.,* 2006; *Yu and Elderfield* 2008; *Kubota et al*., 2015] and from the Indian Ocean [*Elderfield et al.,* 2006; *Healey et al.*, 2008; *Yu and Elderfield* 2008] (Supplementary Fig. 2.1). Previous works showed that Mg/Ca variability in samples from the Norwegian Sea is not driven by temperature [*Elderfield et al*., 2006; *Yu and Elderfield,* 2008], as relatively high Mg/Ca ratios correspond to almost uniform and generally low BWT (Fig. 2.5a). *Kubota et al*. [2015] reported Mg depletion in samples where $\Delta[CO_3^{2-}]_{calcite} > 80$ μmol kg^{-1} (Figs. 5a and d), as benthic foraminifera tend to uptake less Mg^{2+} when calcifying in highly supersaturated conditions [*Marchitto et al*., 2007; *Bryan and Marchitto*, 2008]. We did not include these data, as the aim of this study is to provide Mg/Ca temperature calibrations, where BWT is the main driver of Mg/Ca variability and $\Delta[CO_3^{2-}]_{calcite}$ exerts a minimal influence on Mg/Ca ratios. Our Timor Sea and Makassar Strait *C. wuellerstorfi* Mg/Ca ratios are interspersed with measurements from the Pacific and Indian Oceans (Fig. 2.5a), in contrast to samples from the Atlantic Ocean which show higher Mg/Ca ratios over the same BWT range (Fig. 2.5a), suggesting a possible geographical trend in the distribution of Mg/Ca ratios in relation to BWT.

To further investigate inter-basinal differences, we divided the compiled dataset between Atlantic and Indian + Pacific (Ind+Pac) samples and recalculated the relationship between *C. wuellerstorfi* Mg/Ca ratios and BWT. We obtained Mg/Ca sensitivity to BWT of 0.19 ± 0.009 mmol mol^{-1} per °C for the Atlantic Ocean and of 0.15 ± 0.01 mmol mol^{-1} per °C for the Ind+Pac samples (Fig. 2.5b and c). Post-depositional alteration can be likely excluded as only pristine foraminiferal tests were

selected for Mg/Ca analyses. The different sensitivities may be related to differences in seasonality of primary production and food supply [*Reygondeau et al*., 2013, *Burkett et al.*, 2015], considering that 99 out of 180 Atlantic samples come from high latitudes (north of 30 °N, and south of 30 °S), whereas only 32 out of 128 Ind+Pac samples come from high latitudes (Auxiliary Material Fig. 2.1). Another consideration is that *C. wuellerstorfi* has a characteristic upper depth limit at ~1000 m in the Atlantic [*Altenbach et al.,* 1999], whereas it commonly occurs between 1000 and 300 m in the South China Sea, eastern Indian Ocean and Pacific Ocean [*Kuhnt et al*., 1999; *Kubota et al*., 2015]. This difference in depth distribution may be related to food availability and microhabitat for the epifaunal, suspension-feeding *C. wuellerstorfi*. At shallower water depths and in areas with reduced bottom currents such as the South China Sea and eastern Indian Ocean, *C. wuellerstorfi* may live and calcify more commonly within a layer of phytodetritus fluff above the sediment surface [*Kuhnt et al*., 1999], which is characterized by lower pH and lower carbonate ion concentrations than clear ocean bottom waters.

2.4.1.2 Carbonate ion effect on *C. wuellerstorfi* Mg/Ca ratios

Several authors suggested that the carbonate ion effect instead of BWT is the main driver of *C. wuellerstorfi* Mg/Ca variability at temperatures below 3 °C [*Martin et al.,* 2002; *Elderfield et al.*, 2006; *Yu and Elderfield*, 2008] and recommended separation of temperature and $\Delta[CO_3^{2-}]_{calcite}$ signals. *Elderfield et al.* [2006, ref. Fig. 6] found that above 3 °C the sensitivity of $\Delta[CO_3^{2-}]_{calcite}$ to BWT is ~3 μmol kg^{-1} per °C, whereas below 3 °C the sensitivity is ten times higher. Thus, these authors identified a threshold at 3 °C, below which *C. wuellerstorfi* Mg/Ca ratios are controlled by $\Delta[CO_3^{2-}]_{calcite}$ and not BWT. In our compiled dataset, we found $\Delta[CO_3^{2-}]_{calcite}$

sensitivity to BWT of ~15 μmol kg^{-1} per °C for the Atlantic Ocean, and of ~19 μmol kg^{-1} per °C for the Ind+Pac data below 3 °C (Fig. 2.5d). This agrees with previous studies that described waters of the Indian and Pacific Oceans as more corrosive than Atlantic Ocean waters [e.g.: *Yu et al.*, 2014]. We found no correlation between $\Delta[CO_3^{2-}]_{calcite}$ and BWT in the Atlantic Ocean above 3 °C, and $\Delta[CO_3^{2-}]_{calcite}$ sensitivity to BWT of ~4 μmol kg^{-1} per °C for the Ind+Pac dataset for the BWT range from 3 to 10 °C (Fig. 2.5d), confirming that the carbonate ion effect on *C. wuellerstorfi* Mg/Ca ratios is negligible for the selected data. Samples from the Norwegian Sea and from highly supersaturated waters ($\Delta[CO_3^{2-}]_{calcite}$>80 μmol kg^{-1}) fall on different trends (Fig. 2.5d) confirming that BWT is not the main driver of Mg/Ca variability for these samples [*Elderfield et al*., 2006; *Yu and Elderfield*, 2008; *Kubota et al*., 2015]. We thus excluded these samples from the discussion of the relationship between Mg/Ca and BWT.

To further investigate the relationship between *C. wuellerstorfi* Mg/Ca ratios and $\Delta[CO_3^{2-}]_{calcite}$, we attempted to separate the effect of $\Delta[CO_3^{2-}]_{calcite}$ on Mg/Ca ratios from the temperature signal following the approach detailed in *Elderfield et al.* [2006]. This requires a temperature calibration where *C. wuellerstorfi* Mg/Ca variability is only driven by BWT, which is the case for the compiled dataset between 3 and 10 °C (Fig. 2.5d). We therefore recalculated the relationship between *C. wuellerstorfi* Mg/Ca ratios and BWT (3 - 10 °C) and obtained the following equations (Figs. 5b and c):

Atlantic Ocean

$$Mg/Ca = (0.73 \pm 0.06)\ exp^{(0.21 \pm 0.01\ BWT)} \quad (12)$$

($R^2 = 0.73$; n = 67; $p<0.0001$)

Ind+Pac samples

$$Mg/Ca = (0.72 \pm 0.13) \exp^{(0.145 \pm 0.02\ BWT)} \quad (13)$$

($R^2 = 0.62$; n = 35; $p<0.0001$)

We estimated Mg/Ca ratios using published BWT and exponential equations (12) and (13) and calculated the difference between measured and estimated Mg/Ca ratios ($\Delta Mg/Ca = Mg/Ca_{measured} - Mg/Ca_{estimated}$) to subtract the temperature component from the measured Mg/Ca ratios over the BWT range from 0 to 3°C (Fig. 2.5e) and from 3 to 10 °C (Fig. 2.5f). ΔMg/Ca represents the Mg/Ca component that is not explained by temperature. In the selected Atlantic Ocean dataset, low correlation (R^2 <0.2) between ΔMg/Ca and $\Delta[CO_3^{2-}]_{calcite}$ suggests that the carbonate ion effect on *C. wuellerstorfi* Mg/Ca ratios is negligible over the temperature range from 0 to 6 °C (Figs. 5e and f). This likely reflects the fact that 130 out of 180 samples come from waters where $\Delta[CO_3^{2-}]_{calcite}$ >25 µmol kg^{-1}, the threshold proposed by *Yu and Elderfield* [2008] above which Mg/Ca variability is driven by BWT and 175 out of 180 samples come from supersaturated waters with respect to calcite ($\Delta[CO_3^{2-}]_{calcite}$ >0 µmol kg^{-1}) (Figs. 5e and f).

We extended the temperature range of equation (12) down to 0 °C, and obtained the following exponential equation (Fig. 2.5b):

Atlantic Ocean

$$Mg/Ca = (0.80 \pm 0.03) \exp^{(0.19 \pm 0.009\ BWT)} \quad (14)$$

($R^2 = 0.74$; n = 180; $p<0.0001$)

The consistent distribution of *C. wuellerstorfi* Mg/Ca ratios along calibration equation (14) and high correlation coefficient ($R^2 = 0.74$) also suggest that temperature rather than $\Delta[CO_3^{2-}]_{calcite}$ controls *C. wuellerstorfi* Mg/Ca variability in the selected Atlantic Ocean dataset (0 to 6 °C) (Fig. 2.5b). Additionally equation (12) lies within the 95% confidence interval of equation (14) (Fig. 2.5b).

In the selected Indian and Pacific dataset, only 11 out of 128 samples come from waters where $\Delta[CO_3^{2-}]_{calcite}$ is >25 µmol kg^{-1} and 80 out of 128 samples come from supersaturated waters with respect to calcite ($\Delta[CO_3^{2-}]_{calcite}$ >0 µmol kg^{-1}) (Figs. 5e and f). Low correlation (R^2 <0.2) between ΔMg/Ca and $\Delta[CO_3^{2-}]_{calcite}$ is found from 0 to 3°C (Fig. 2.5e) and from 3 to 10 °C (Fig. 2.5f). The standard deviation of the difference between the calculated and measured temperature is relatively high (±1.5 °C) for equation (13) used to calculate ΔMg/Ca and it may account for the relatively high scatter of the data (Figs. 5e and f). Therefore, it remains unclear to what extent the carbonate ion effect influences *C. wuellerstorfi* Mg/Ca ratios for the Indian and Pacific dataset.

We extended the temperature range of equation (13) down to 0 °C, and obtained the following exponential equation (Fig. 2.5c):

Ind+Pac samples

$$Mg/Ca = (0.71 \pm 0.04)\ exp^{(0.15 \pm 0.01\ BWT)} \quad (15)$$

($R^2 = 0.68$; n = 128; p<0.0001)

The consistent distribution of *C. wuellerstorfi* Mg/Ca ratios along calibration equation (15) and good correlation (R^2 = 0.68) suggest that temperature rather than $\Delta[CO_3^{2-}]_{calcite}$ controls *C. wuellerstorfi* Mg/Ca variability in the selected Ind+Pac dataset (0 to 10 °C) (Fig. 2.5c). Additionally equation (15) lies within the 95% confidence interval of equation (13) (Fig. 2.5c).

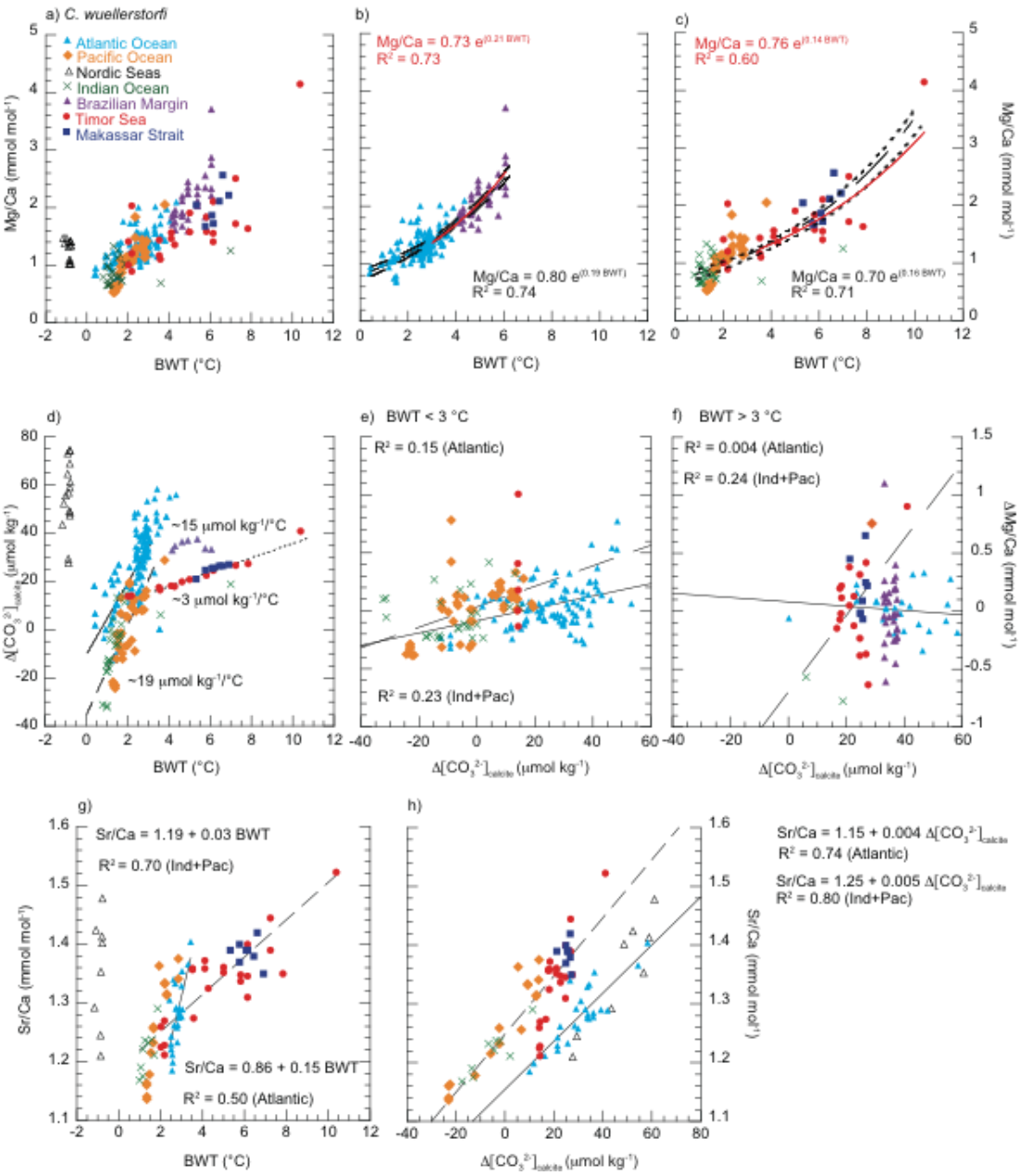

Fig. 2.5. a) Comparison between published and new *C. wuellerstorfi* Mg/Ca measurements, spanning the BWT range from -1 to 10 °C. An offset is evident between samples from the Atlantic Ocean, and samples from the Indian and Pacific Oceans. **b)** *Cibicidoides wuellerstorfi* Mg/Ca ratios versus BWT for the Atlantic Ocean. Solid black curve represents *C. wuellerstorfi* Mg/Ca temperature calibration for the BWT range from 0 to 6 °C; dashed black lines mark the 95% confidence interval. Red curve represents the temperature equation for the BWT range from 3 to 6 °C. **c)** *Cibicidoides wuellerstorfi* Mg/Ca ratios versus BWT for the Indian and Pacific Oceans. Black dashed curve represents the *C. wuellerstorfi* Mg/Ca temperature calibration for the BWT range from 1 to 10 °C; finely dashed lines mark the 95% confidence interval. Red curve represents the temperature equation for the BWT range from 3 to 10 °C. **d** $\Delta[CO_3^{2-}]_{calcite}$ sensitivity to BWT. Solid black line represents the relationship for the Atlantic Ocean below 3 °C; dashed black line represents the relationship for the Ind+Pac data below 3 °C; finely dashed black line represents the relationship for the Ind+Pac data above 3 °C **e)** *Cibicidoides wuellerstorfi* Mg/Ca sensitivity to $\Delta[CO_3^{2-}]_{calcite}$ below 3 °C. No correlation indicates negligible carbonate ion effect on *C. wuellerstorfi* Mg/Ca ratios for the selected data sets. **f)** *Cibicidoides wuellerstorfi* Mg/Ca sensitivity to $\Delta[CO_3^{2-}]_{calcite}$ above 3 °C. No correlation indicates negligible carbonate ion effect on *C. wuellerstorfi* Mg/Ca ratios for the selected data sets. **g)** *Cibicidoides wuellerstorfi* Sr/Ca sensitivity to BWT. **h)** *Cibicidoides wuellerstorfi* Sr/Ca sensitivity to $\Delta[CO_3^{2-}]_{calcite}$.

2.4.1.3 Controls on *C. wuellerstorfi* Sr/Ca variability

We plotted published *C. wuellerstorfi* Sr/Ca ratios [*Yu et al.,* 2014] together with new Sr/Ca measurements versus BWT (Fig. 2.5g). Once again, Sr/Ca ratios of samples from the Nordic seas, which lie on a different trend compared to samples from the Atlantic and Ind+Pac regions (Fig. 2.5g), were excluded. The relationship between *C. wuellerstorfi* Sr/Ca ratios and BWT is best described by the following linear equations (Fig 5g):

Atlantic Ocean

$$Sr/Ca = (0.86 \pm 0.09) + (0.15 \pm 0.03)\ BWT \quad (16)$$

($R^2 = 0.5$; n = 26; $p<0.0001$)

Ind+Pac samples

$$Sr/Ca = (1.19 \pm 0.01) + (0.03 \pm 0.003)\ BWT \quad (17)$$

($R^2 = 0.7$; n = 59; $p<0.0001$)

We found a correlation between Sr/Ca and temperature of $R^2 = 0.5$ in the Atlantic data set and of 0.7 in the Ind+Pac data set. In the Atlantic Ocean *C. wuellerstorfi* Sr/Ca sensitivity to BWT is ~0.15 mmol mol^{-1} per °C, whereas in the Ind+Pac samples sensitivity is ~0.03 mmol mol^{-1} per °C (Fig. 2.5g). Interestingly, a change in the slope of the relationship between *C. wuellerstorfi* Sr/Ca ratios and BWT is evident at ~3 °C in the Ind+Pac data (Fig. 2.5g). At BWT lower than 3 °C, Sr/Ca ratios fall on a steeper trend than at higher temperatures, possibly reflecting a carbonate ion effect on *C. wuellerstorfi* Sr/Ca ratios in deeper waters. Due to the limited number of Sr/Ca measurements above 3 °C in the Atlantic Ocean, we cannot evaluate whether a similar trend occurs in this basin (Fig. 2.5g). On account of the low sensitivity, we speculate that the influence of BWT on *C. wuellerstorfi* Sr/Ca variability is negligible above 3 °C in the Atlantic and Ind+Pac regions. In contrast,

below 3 °C, the higher Sr/Ca sensitivity to temperature may reflect a carbonate ion effect on *C. wuellerstorfi* Sr/Ca ratios (Fig. 2.5g).

We next plotted published *C. wuellerstorfi* Sr/Ca ratios [*Yu et al.*, 2014] together with our Sr/Ca measurements against $\Delta[CO_3^{2-}]_{calcite}$ to evaluate the carbonate ion effect on *C. wuellerstorfi* Sr/Ca variability (Fig. 2.5h). Our Sr/Ca measurements from the Timor Sea and Makassar Strait are interspersed with the Ind+Pac Sr/Ca ratios, whereas a clear offset is shown between Atlantic and Ind+Pac samples (Fig. 2.5h), in agreement with *Yu et al.* [2014]. The following linear equations best describe the relationship between Sr/Ca ratios and $\Delta[CO_3^{2-}]_{calcite}$ (Fig. 2.5h):

Atlantic Ocean:

$$Sr/Ca = (1.15 \pm 0.016) + (0.004 \pm 0.0005)\ \Delta[CO_3^{2-}]_{calcite} \quad (18)$$

($R^2 = 0.74$; n = 26; $p<0.0001$)

Ind+Pac samples:

$$Sr/Ca = (1.25 \pm 0.007) + (0.005 \pm 0.0003)\ \Delta[CO_3^{2-}]_{calcite} \quad (19)$$

($R^2 = 0.80$; n = 59; $p<0.0001$)

The high correlation (R^2 >0.74) between *C. wuellerstorfi* Sr/Ca ratios and $\Delta[CO_3^{2-}]_{calcite}$ for both ocean basins and no discernible change in the slope of this relationship between saturated and undersaturated ($\Delta[CO_3^{2-}]_{calcite}$ <0 μmol kg^{-1}) waters (Fig. 2.5h) suggest that $\Delta[CO_3^{2-}]_{calcite}$ exerts the main control on Sr/Ca variability. These results support the findings of *Yu et al.* [2014], who suggested using this ratio as an auxiliary proxy to monitor past changes in $\Delta[CO_3^{2-}]_{calcite}$ in deeper waters, given that seawater Sr/Ca remained stable over time. *Dawber and Tripati* [2012] also found a significant and positive correlation between *Oridorsalis umbonatus* Sr/Ca and $\Delta[CO_3^{2-}]_{calcite}$ and suggested that this dependence may be related to the carbonate ion effect on the amount of calcium remaining in the "internal biomineralization pool"

after calcite precipitation, and consequently on the fractionation of Sr (Rayleigh fractionation, *Erez* [2003]; *de Nooijer et al*. [2014]).

2.4.2 *Hoeglundina elegans*

2.4.2.1 Comparison to published data

Our *H. elegans* Mg/Ca measurements from the Timor Sea and Makassar Strait are interspersed with published measurements of *Rosenthal et al.* [2006] from Hawaii and the Makassar Strait and of *Reichart et al.* [2003] from the Arabian Sea (Indo+Pacific samples) (Fig. 2.6a). In contrast, samples from the Bay of Biscay (Atlantic Ocean) show higher Mg/Ca ratios for the same BWT range (Fig. 2.6a), pointing to a geographical trend, as we noted for *C. wuellerstorfi* Mg/Ca ratios. By dividing the compiled dataset between samples from the Atlantic and Indo+Pacific Oceans, we obtained the following exponential equations (Fig. 2.6b and c):

Atlantic Ocean

$$Mg/Ca = (0.4 \pm 0.18)\ exp^{(0.16 \pm 0.02\ BWT)} \quad (20)$$

($R^2 = 0.83$; n = 9; $p<0.0001$)

Indo+Pacific Ocean

$$Mg/Ca = (0.405 \pm 0.05)\ exp^{(0.09 \pm 0.007\ BWT)} \quad (21)$$

($R^2 = 0.51$; n = 138; $p<0.0001$)

Interestingly, the three Indo+Pacific samples from shallow locations (samples MC047 from Hawaii, MC037 from Indonesia, and 18454 from the Timor Sea) depart from the main trend towards lower Mg/Ca ratios, despite the high BWT (>15 °C) of ambient waters (Fig. 2.6c). In contrast, samples from the Bay of Biscay, covering a

temperature range between 2.5 and 13 °C, do not show Mg^{2+} depletion at higher temperatures (Fig. 2.6b).

2.4.2.2 Carbonate ion effect on *H. elegans* Mg/Ca ratios

Rosenthal et al. [2006] found a threshold at 15 μmol kg^{-1} below which *H. elegans* Mg/Ca variability appears to depend on the combined effects of temperature and $\Delta[CO_3^{2-}]_{aragonite}$. Following the approach in section 4.1.2 and detailed in *Elderfield et al.* [2006], we plotted BWT against $\Delta[CO_3^{2-}]_{aragonite}$ and found $\Delta[CO_3^{2-}]_{aragonite}$ sensitivity to BWT of ~5 μmol kg^{-1} $°C^{-1}$ below 15 μmol kg^{-1}, and of ~9 μmol kg^{-1} $°C^{-1}$ above 15 μmol kg^{-1} for the Indo+Pacific Ocean (Fig. 2.6d), which differs from *Rosenthal et al.* [2006]. The sensitivity of $\Delta[CO_3^{2-}]_{aragonite}$ to BWT of 5-9 μmol kg^{-1} $°C^{-1}$ is lower than the sensitivity of $\Delta[CO_3^{2-}]_{calcite}$ to BWT of ~30 μmol kg^{-1} $°C^{-1}$ (below 3 °C) identified by *Elderfield et al.* [2006], as the threshold below which the carbonate ion effect on *C. wuellerstorfi* Mg/Ca ratios becomes significant. No $\Delta[CO_3^{2-}]_{aragonite}$ measurements are available for the Atlantic Ocean dataset.

As for *C. wuellerstorfi* (section 4.1.2), we attempted to separate the effects of temperature and carbonate ion saturation on *H. elegans* Mg/Ca ratios, following *Elderfield et al.* [2006]. In equation (20), the consistent distribution of *H. elegans* Mg/Ca ratios along the calibration equation together with the high correlation coefficient (R^2 >0.8) suggest that temperature rather than carbonate ion saturation is the main control on Mg/Ca variability (Fig. 2.6b). However, we do not have $\Delta[CO_3^{2-}]_{aragonite}$ estimates for the Atlantic Ocean, and cannot quantify the carbonate ion effect on *H. elegans* Mg/Ca ratios for this region. For the Indo+Pacific dataset (equation (21)), the three samples showing Mg depletion at higher BWT (>15 °C) (Fig. 2.6c)

come from highly supersaturated waters where $\Delta[CO_3^{2-}]_{aragonite}$ > 70 μmol kg^{-1} (Fig. 2.6d) and, as for *C. wuellerstorfi*, were not included in the following discussion as the aim of this study is to provide Mg/Ca temperature calibrations where BWT is the main driver of Mg/Ca variability and $\Delta[CO_3^{2-}]_{aragonite}$ exerts a minimal influence on Mg/Ca ratios. We also did not consider 20 samples corresponding to BWT <3 °C, as the carbonate ion effect on *H. elegans* Mg/Ca ratios below 3 °C is unclear. We therefore recalculated equation (21) for the BWT range from 3 to 12 °C and obtained the following exponential equation (Fig. 2.6c):

Indo+Pacific Ocean

$$Mg/Ca = (0.43 \pm 0.07) \exp^{(0.1 \pm 0.01\ BWT)} \quad (22)$$

(R^2 = 0.42; n = 110; p<0.0001)

We calculated ΔMg/Ca based on published BWT and equation (22) over the whole temperature range from 2 to 12 °C and found low correlation (R^2 < 0.2) between ΔMg/Ca and $\Delta[CO_3^{2-}]_{aragonite}$ below or above 15 μmol kg^{-1} (Fig. 2.6e), or below or above 3 °C (Fig. 2.6f). This may reflect that $\Delta[CO_3^{2-}]_{aragonite}$ sensitivity to BWT is generally low (Fig. 2.6d) and/or may be biased by the fact that below 3 °C *H. elegans* Mg/Ca measurements are scarce (Fig. 2.6c). However, the standard deviation of the difference between the calculated and measured temperature is relatively high (±2.2 °C) for equation (22) used to calculate ΔMg/Ca.

When we extend the temperature range of equation (22) down to 2 °C, we obtain the following exponential equation (Fig. 2.6c):

Indo+Pacific

$$Mg/Ca = (0.31 \pm 0.06) \exp^{(0.14 \pm 0.01\ BWT)} \quad (23)$$

(R^2 = 0.61; n = 130; p<0.0001)

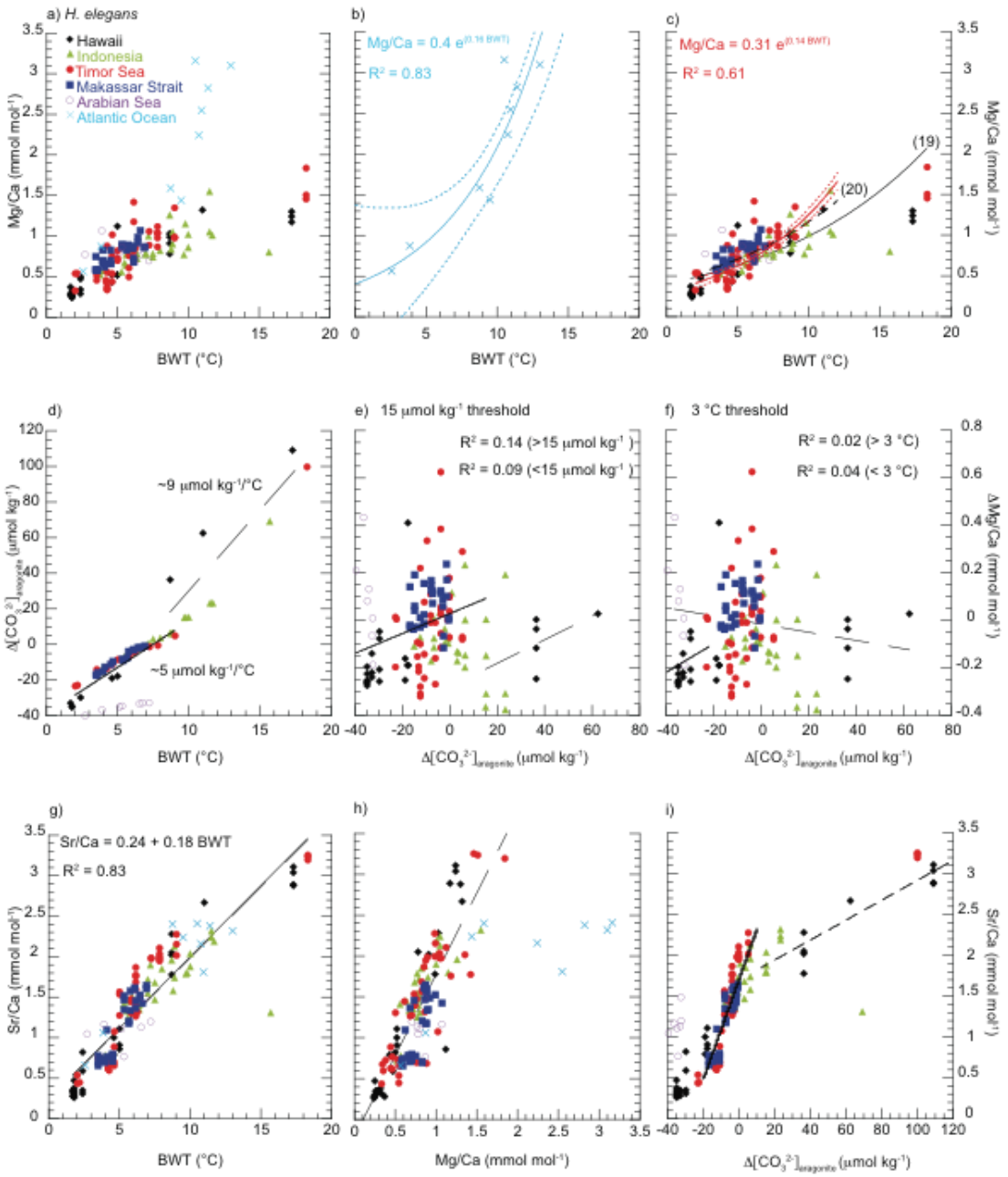

Fig. 2.6. a) Comparison between published and new *H. elegans* Mg/Ca measurements, spanning the BWT range from 2 to 18 °C. An offset is evident between samples from the Atlantic Ocean and samples from the Indian and Pacific Oceans. **b)** Calibration of *H. elegans* Mg/Ca ratios versus BWT for the Atlantic Ocean (solid blue curve). Dashed lines mark the 95% confidence interval. **c)** *Hoeglundina elegans* Mg/Ca ratios versus BWT for the Indian and Pacific Oceans. Red curve represents *H. elegans* Mg/Ca temperature calibration for the BWT range from 2 to 12 °C; dashed red lines mark the 95% confidence interval. Black and dashed black curves represent equations (19) and (20), respectively. **d)** $\Delta[CO_3^{2-}]_{aragonite}$ sensitivity to BWT. Solid black line represents the relationship for the Indo-Pacific data below 15 µmol kg^{-1}; dashed black line represents the relationship for the Indo-Pacific data above 15 µmol kg^{-1}. No data are available for the Atlantic Ocean. **e)** *Hoeglundina elegans* Mg/Ca sensitivity to $\Delta[CO_3^{2-}]_{aragonite}$. No correlation above or below 15 µmol kg^{-1} indicates negligible carbonate ion effect on *H. elegans* Mg/Ca ratios for the selected dataset. **f)** *Hoeglundina elegans* Mg/Ca sensitivity to $\Delta[CO_3^{2-}]_{aragonite}$. No correlation above or below 3 °C indicates negligible carbonate ion effect on *H. elegans* Mg/Ca ratios for the selected dataset. **g)** *Hoeglundina elegans* Sr/Ca sensitivity to BWT; solid black line represents the relationship between Sr/Ca ratios and BWT for the compiled set of data, while the dashed black line represents the same relationship for the Indo-Pacific samples only. **h)** *Hoeglundina elegans* Sr/Ca versus Mg/Ca ratios. Variations in Mg/Ca and Sr/Ca ratios are positively correlated in the Indo-Pacific Ocean (dashed line), suggesting that BWT controls both Mg and Sr uptake in *H. elegans* tests. It is unclear why Sr/Ca ratios in the Atlantic Ocean do not increase with increasing Mg/Ca ratios at higher BWT. **i)** *Hoeglundina elegans* Sr/Ca sensitivity to $\Delta[CO_3^{2-}]_{aragonite}$.

The consistent distribution of *H. elegans* Mg/Ca ratios along calibration equation (23) and significant correlation (R^2 = 0.61; p<0.0001) suggest temperature exerts a main control on *H. elegans* Mg/Ca variability (Fig. 2.6c). Applying equation (22) or (23) to estimate BWT leads to similar results, with a small offset of ±0.65 °C, above 3 °C. However, the offset between BWT estimates increases up to 3 °C below 3 °C.

2.4.2.3 Controls on *H. elegans* Sr/Ca variability

We calculated the relationship between *H. elegans* Sr/Ca ratios and BWT for the compiled dataset without discriminating between sample provenance (on account of the limited number of measurements in the Atlantic Ocean) and obtained the following linear equation (Fig 6g):

Compiled dataset

$$Sr/Ca = (0.24 \pm 0.05) + (0.18 \pm 0.007)\ BWT \quad (24)$$

(R^2 = 0.83; n = 147; p<0.0001)

We found high correlation (R^2 >0.8) between Sr/Ca and BWT, most likely due to the aragonitic mineralogy of *H. elegans* tests, since Sr^{2+} has a better fit in the aragonitic lattice than in the calcitic one [e.g.: *Rosenthal et al.,* 2006]. Additionally, no change in the slope of the relationship between *H. elegans* Sr/Ca ratios and BWT over the temperature range from 2 to 18 °C (Fig. 2.6g) suggests that BWT drives Sr/Ca variability in *H. elegans* tests. Only the shallow sample from Indonesia (MC037, *Rosenthal et al.* [2006]) departs from the main trend. Furthermore, *H. elegans* Mg/Ca and Sr/Ca ratios are positively and significantly correlated (R^2 = 0.74) for the Indo+Pacific samples, suggesting that BWT controls the variability of both parameters (Fig. 2.6h). In contrast, in the Atlantic Ocean, Mg/Ca and Sr/Ca ratios are positively correlated at lower BWT, fitting together with the Indo+Pacific samples,

whereas at higher BWT *H. elegans* Sr/Ca ratios do not increase with Mg/Ca ratios (Fig. 2.6h). The reason for this discrepancy is unclear and more measurements from the Atlantic Ocean are needed to better define the relationship between *H. elegans* Mg/Ca, Sr/Ca and BWT. We additionally examined the relationship between $\Delta[CO_3^{2-}]_{aragonite}$ and *H. elegans* Sr/Ca ratios (Fig. 2.6i). Changes in the slope of this relationship suggest that $\Delta[CO_3^{2-}]_{aragonite}$ does not drive *H. elegans* Sr/Ca variability (Fig. 2.6i). Below -20 μmol kg^{-1}, we found no correlation between *H. elegans* Sr/Ca ratios and $\Delta[CO_3^{2-}]_{aragonite}$, although different sensitivities of *H. elegans* Sr/Ca ratios to $\Delta[CO_3^{2-}]_{aragonite}$ are found between -20 and 15 μmol kg^{-1} and above 15 μmol kg^{-1} (Fig. 2.6i).

2.4.3 Robustness of paleotemperature proxies: benthic $\delta^{18}O$ versus benthic Mg/Ca ratios

To test the reliability of Mg/Ca temperature equations, we compared calcification temperatures derived from Mg/Ca ratios with those derived from $\delta^{18}O$ measurements. These two independent methods yielded comparable results, providing good approximations of CTD-measured temperatures (Fig. 2.7a and b). For *C. wuellerstorfi*, the difference between CTD-measured and $\delta^{18}O$-derived temperature (equation (10)) (ΔT = CTD-measured BWT – $\delta^{18}O$-derived temperature) shows a standard error of ± 0.83 °C in the Timor Sea and Makassar Strait. In contrast, the difference between CTD-measured and Mg/Ca-based temperatures shows a standard error of ± 0.77 °C for the Atlantic Ocean (equation (14)), and of ± 1.5 °C for the Ind+Pac area (equation (15)) (Fig. 2.7a). The higher standard error found for Ind+Pac BWT estimates probably relates to the scarcity of Mg/Ca measurements above 2 °C,

as 58 Mg/Ca samples were measured for the temperature range from 0.8 to 2 °C and 70 cover the whole range from 2 to 10 °C (Fig. 2.5c).

For *H. elegans*, the difference between CTD-measured and $\delta^{18}O$-derived temperatures (equation (11)) shows a standard error of ± 1 °C, whereas the difference with Mg/Ca-based temperatures shows a standard error of ± 1.1 °C for the Atlantic Ocean (equation (20)), and a standard error of ± 1.9 °C for the Indo+Pacific Ocean (equation (23)) (Fig. 2.7b). The higher standard error found for Indo+Pacific BWT estimates is most likely due to the high number of Mg/Ca measurements and their associated natural variability (n = 130) compared to the limited number of samples for the Atlantic Ocean (n = 9), and the Timor Sea and Makassar Strait (n = 35).

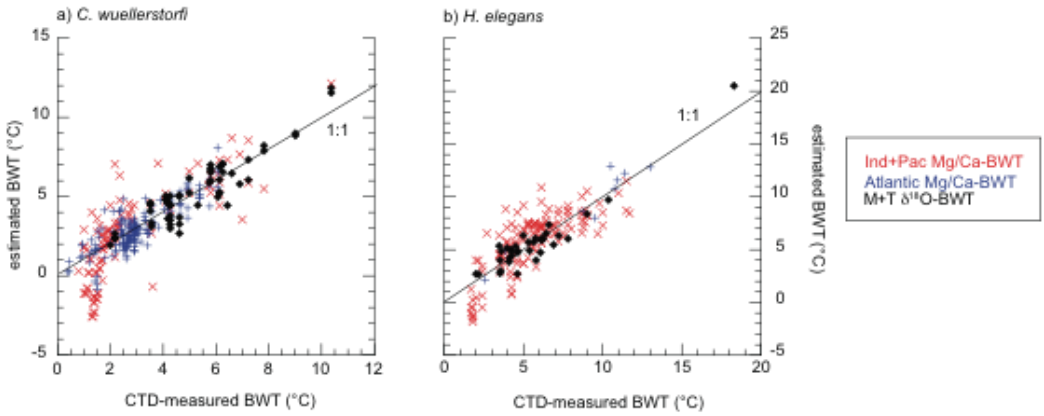

Fig. 2.7. a) CTD-measured BWT versus BWT estimates based on *C. wuellerstorfi* Mg/Ca ratios (red crosses Ind+Pac data, blue crosses Atlantic data), and $\delta^{18}O$ measurements (black diamonds). **b)** CTD-measured BWT versus BWT estimates based on *H. elegans* Mg/Ca ratios (red crosses Indo-Pacific data, blue crosses Atlantic data), and $\delta^{18}O$ measurements (black diamonds).

2.5. Conclusion

Compiling new *C. wuellerstorfi* Mg/Ca measurements with published data, we extended the Mg/Ca temperature calibration for this species to 10 °C. Exponential equations (14) and (15) best describe the relationship between temperature and *C. wuellerstorfi* Mg/Ca ratios for the Atlantic Ocean and for the Indian and Pacific

Oceans, respectively. Our study indicates that temperature rather than $\Delta[CO_3^{2-}]_{calcite}$ controls *C. wuellerstorfi* Mg/Ca variability in the selected Atlantic Ocean dataset (0 to 6 °C) and Ind+Pac dataset (0 to 10 °C). *Cibicidoides wuellerstorfi* Sr/Ca ratios show high potential to record past changes in carbonate ion saturation, as $\Delta[CO_3^{2-}]_{calcite}$ appears to drive *C. wuellerstorfi* Sr/Ca variability. Distinct *C. wuellerstorfi* Sr/Ca-$\Delta[CO_3^{2-}]_{calcite}$ relationships are found for the different ocean basins, which may be due to the higher "corrosiveness" of Indian and Pacific waters.

Combining new *H. elegans* Mg/Ca measurements with published data, we provided temperature calibration equations over the temperature range from 2 to 12 °C. Exponential equations (20) and (23) best describe the relationship between *H. elegans* Mg/Ca ratios and BWT for the Atlantic Ocean and the Indo+Pacific Ocean, respectively. In highly supersaturated waters with respect to aragonite ($\Delta[CO_3^{2-}]_{aragonite}$ > 70 μmol kg^{-1}), Mg/Ca depletion in *H. elegans* tests was observed. *Hoeglundina elegans* Sr/Ca variability appears to be driven by BWT, most likely because of the aragonitic mineralogy of this benthic foraminiferal species, since Sr^{2+} has a better fit in the aragonitic lattice than in the calcitic one. No geographical trend in the distribution of Sr/Ca ratios in relation to BWT is apparent between the Atlantic and Indo+Pacific Oceans, possibly because Sr/Ca ratios in the Atlantic Ocean do not increase with increasing Mg/Ca ratios at higher BWT.

Acknowledgements

We are grateful to Karen Bremer for ICP-OES measurements and the crew of the R/V *Sonne* for all their efforts during the SO-185 VITAL and SO-217 MAJA cruises. Funding for this research was provided by the Marie Curie Action Plan,

Seventh Framework Program (Grant n°237922) and BMBF Grants 03G0217A (MAJA) and 03G0185A (VITAL).

Appendix. Taxonomic Information

Cibicidoides wuellerstorfi (Schwager), 1866

Original Designation: *Anomalina wuellerstorfi* Schwager, 1866, p. 258, pl.7, figs. 105-107.

Hoeglundina elegans (d'Orbigny), 1826

Original designation: *Rotalia (Turbinulina) elegans* d'Orbigny, 1826, p. 276, Model No. 54, illustrated in Parker et al., 1871, pl. 12, fig. 142.

References

Altenbach, A. V., U. Pflaumann, R. Schiebel, A. Thies, S. Timm, and M. Trauth (1999), Scaling percentages and distributional patterns of benthic foraminifera with flux rates of organic carbon, *Journal of Foraminiferal Research*, 29, 3, 173-185,

Bender, M.L., R.B. Lorens, and F.D. Williams (1975), Sodium, magnesium, and strontium in the tests of planktonic foraminifera, *Micropaleontology*, 21, 448-459, doi: 10.2307/1485293.

Bentov, S., and J. Erez (2005), Novel observations on biomineralization processes in foraminifera and implications for Mg/Ca ratio in the shells, *Geology*, *33 (11)*, 841–844; doi: 10.1130/G21800.1.

Bentov, S., and J. Erez (2006), Impact of biomineralization process on the Mg content of foraminiferal shells: A biological perspective, *Geochemistry, Geophysics, Geosystems, 7*, Q01P08, doi: 10.1029/2005GC001015.

Boyle, E.A., L. Labeyrie, and J.C. Duplessly (1995), Calcitic foraminiferal data confirmed by cadmium in aragonitic *Hoeglundina*: Application to the Last Glacial Maximum in the northern Indian Ocean, *Paleoceanography, 10*, 881-900, doi:10.1029/95PA01625.

Bryan, S.P., and T.M. Marchitto (2008), Mg/Ca-temperature proxy in benthic foraminifera: New calibrations from the Florida Straits and a hypothesis regarding Mg/Li, *Paleoceanography*, *23*, PA2220, doi: 10.1029/2007PA001553.

Burkett, A., A. Rathburn, R. Venturelli, M. Perez, L. Levin, and N. Spendal (2015), Phylogenetic placement of Cibicidoides wuellerstorfi (Schwager, 1866) from methane seeps and non-seep habitats on the Pacific margin, *Geobiology*, 13, 44-52, doi: 10.1111/gbi.12118.

Curry, W. B., T.M. Marchitto (2008), A secondary ionization mass spectrometry calibration of *Cibicidoides pachyderma* Mg/Ca with temperature, *Geochemistry, Geophysics, Geosystems*, *9*(4), Q04009, doi: 10.1029/2007GC001620.

Dawber, C. F., and A. Tripati (2012), Relationships between bottom water carbonate saturation and element/Ca ratios in coretop samples of the benthic foraminifera Oridorsalis umbonatus, *Biogeosciences*, 9, 3029-3045, doi: 10.5194/bg-9-3029-2012.

de Villiers, S., M. Greaves, and H. Elderfield (2002), An intensity ratio calibration method for accurate determination of Mg/Ca and Sr/Ca of marine carbonates by ICP-AES, *Geochemistry, Geophysics, Geosystems*, *3*(1), 1001, doi: 10.1029/2001GC000169.

Elderfield, H., M. Cooper, and G. Ganssen (2000), Sr/Ca in multiple species of planktonic foraminifera: implications for reconstructions of seawater Sr/Ca, *Geochemistry, Geophysics, Geosystems*, 1, 1999GC000031.

Elderfield, H., J. Yu, P. Anand, T. Kiefer, and B. Nyland (2006), Calibrations for benthic foraminiferal Mg/Ca paleothermometry and the carbonate ion hypothesis, *Earth and Planetary Science Letters*, *250*, 633-649, doi: 10.1016/j.epsl.2006.07.041.

Elmore, A., S. Sosdian, Y. Rosenthal, and J.D. Wright (2012), A global evaluation of temperature and carbonate ion control on Mg/Ca ratios of ostracoda genus *Krithe*, *Geochemistry, Geophysics, Geosystems*, *13*, Q09003, doi:10.1029/2012GC004073.

Erez, J., (2003), The Source of Ions for Biomineralization in Foraminifera and Their Implications for Paleoceanographic Proxies, *Reviews in Mineralogy and Geochemistry*, *54*, 115–149, doi: 10.2113/0540115.

Fontanier, C., F.J. Jorissen, L. Licari, A. Alexandre, P. Anschutz, and P. Carbonel (2002), Live benthic foraminiferal faunas from the Bay of Biscay: Faunal density, composition, and microhabitats, *Deep Sea Research, Part I*, *49*, 751-785,

doi:10.1016/SO967-0637(01)00078-4.

Healey, S., R. Thunell, and B.H. Corliss (2008), The Mg/Ca-temperature relationship of benthic foraminifera calcite: New core-top calibrations in the <4 °C temperature range, *Earth and Planetary Science Letters*, *272*, 523-530, doi: 10.1016/j.epsl.2008.05.023.

Hodell, D. A., C. D. Charles, and F. J. Sierro (2001), Late Pleistocene evolution of the ocean's carbonate system, *Earth and Planetary Science Letters*, 192 (2), 109-124, doi:10.1016/S0012-821X(01)00430-7.

Jansen, H., R.E. Zeebe, and D.A. Wolf-Gladrow (2002), Modeling the dissolution of settling $CaCO_3$ in the ocean, *Global Biogeochemical Cycles*, 16, doi: 10.1029/2000GB001279.

Kuhnt, W., S. Hess, and Z. Jian (1999), Quantitative composition of benthic foraminiferal assemblages as a proxy indicator for organic carbon flux rates in the South China Sea, Marine Geology, 156, 123-157, doi:10.1016/S0025-3227(98)00176-5

Kuhnt, W., et al. (2005), Cruise report SONNE-185 "Variability of the Indonesian Throughflow and Australasian climate history of the last 150000 years (VITAL)", Report, Institut für Geowissenschaften der Christian-Albrechts-Universität zu Kiel, Germany, 304 pp., doi: 10.2312/cr_so217.

Kuhnt, W. et al. (2011), Cruise report SONNE-217 "Variability of the Indonesian Throughflow within the Makassar-Java passage (MAJA)", Report, Institut für Geowissenschaften der Christian-Albrechts-Universität zu Kiel, Germany, 195 pp., doi: 10.2312/cr_so185.

Lea, D. W., T. A. Mashiotta, and H. Spero (1999), Controls on magnesium and strontium uptake in planktonic foraminifera determined by live culturing, *Geochimica et Cosmochimica Acta*, *63*, 2369-2380, doi: 10.1016/S0016-7037(99)00197-0.

Lear, C., Y. Rosenthal, and N. Slowey (2002), Benthic foraminiferal Mg/Ca paleothermometry: A revised core-top calibration, *Geochimica et Cosmochimica Acta*, *66*, 3375-3387, doi: 10.1016/S0016-7037(02)00941-9.

Lewis, E., and D. Wallace (1998), Program developed for CO2 system calculations. *Rep. ORNL/CDIAC-105*, Carbon Dioxide Inf. Anal. Cent., Oak Ridge, Tenn. (Available at http://cdiac.esd.ornl.gov/oceans/co2rprt.html).

Martin, P.A., and D. Lea (2002), A simple evaluation of cleaning procedures on fossil benthic foraminiferal Mg/Ca, *Geochemistry, Geophysics, Geosystems*, *3*(10), 8401, doi: 10.1029/2001GC000280.

Martin, P.A., D.W. Lea, Y. Rosenthal, N.J. Shackleton, M. Sarnthein, and T. Papenfuss (2002), Quaternary deep sea temperature histories derived from benthic foraminiferal Mg/Ca, *Earth and Planetary Science Letters*, *198*, 193-209, doi: 10.1016/S0012-821X(02)00472-7.

Ní Fhlaithearta, S., G. Reichart, F. J. Jorissen, C. Fontanier, E.J. Rohling, J. Thomson, and G.J. de Lange (2010), Reconstructing the seafloor environment during sapropel formation using benthic foraminiferal trace metals, stable isotopes, and sediment composition. *Paleoceanography*, *25*, PA4225, doi: 10.1029/2009PA001869.

Nürnberg, D., J. Bijma, and C. Hemleben (1996), Assessing the reliability of magnesium in foraminiferal calcite as a proxy for water mass temperatures, *Geochimica et Cosmochimica Acta*, *60*, 803-814, doi: 10.1016/0016-7037(95)00446-7.

Raitzsch, M., H. Kuhnert, J. Groeneveld, and T. Bickert (2008), Benthic Mg/Ca anomalies in South Atlantic core top sediments and their implications for paleothermometry, *Geochemistry, Geophysiscs, Geosystems*, *9*, Q05010, doi: 10.1029/2007GC001788.

Rathburn, A.E., and P. De Deckker (1997), Magnesium and strontium composition of recent benthic foraminifera from the Coral Sea, Australia and Prydz Bay, Antarctica, *Marine Micropaleontology*, *32*, 231-248, doi: 10.1016/S0377-8398(97)00028-5.

Regenberg, M., S. Steph, D. Nürnberg, R. Tiedemann, and D. Garbe-Schönberg (2009), Calibrating Mg/Ca ratios of multiple planktonic foraminiferal species with δ^{18}O-calcification temperatures: Paleothermometry for the upper water column, *Earth and Planetary Science Letters*, *278*, 324-336, doi: 10.1016/j.epsl.2008.12.019

Reichart, G.J., F. Jorissen, P. Anschutz, and P.R.D. Mason (2003), Single foraminiferal test chemistry records the marine environment, *Geology, 31*, 355-358, doi: 10.1130/0091-7613(2003)031.

Reygondeau, G., A. Longhurst, E. Martinez, G. Beaugrand, D. Antoine, and O. Maury (2013), Dynamic biogeochemical provinces in the global ocean, *Global Biogeochemical Cycles*, 27, 1046-1058, doi: 10.1002/gbc.20089.

Rosenthal, Y., E.A. Boyle, and N. Slowey (1997), Temperature control on the incorporation of magnesium, strontium, fluorine, and cadmium into benthic foraminiferal shells from Little Bahama Bank: Prospects for thermocline paleoceanography, *Geochimica et Cosmochimica Acta, 61(17)*, 3633-3643, doi: 10.1016/S0016-7037(97)00181-6.

Rosenthal, Y., C.H. Lear, D.W. Oppo, and B.K. Linsley (2006), Temperature and carbonate ion effects on Mg/Ca and Sr/Ca ratios in benthic foraminifera: Aragonitic species *Hoeglundina elegans*, *Paleoceanography*, *21*, PA1007, doi: 10.1029/2005PA001158.

Russell, A.D., S. Emerson, B.K. Nelson, J. Erez, and D.W. Lea (1994), Uranium in foraminiferal calcite as a recorder of seawater uranium concentration, *Geochimica et Cosmochimica Acta, 58(2)*, 671-681, doi: 10.1016/0016-7037(94)90497-9.

Savin, S.M., and R.G. Douglas (1973), Stable isotope and magnesium geochemistry of recent planktonic foraminifera from the South Pacific, *Geological Society of*

America Bulletin, *84*, 2327-2342, doi: 10.1130/0016-7606(1973)84 <2327:SIAMGO> 2.0.CO;2.

Schönfeld, J. (2001), Benthic foraminifera and pore-water oxygen profiles: A re-assessment of species boundary conditions at the western Iberian margin, *Journal of Foraminiferal Research*, 31(2), 86-107, doi:10.2113/0310086.

Stoll, H. M., and D. P. Schrag (1998), Effects of Quaternary sea level cycles on strontium in seawater, *Geochimica et Cosmochimica Acta*, 62, 1107-1118.

Stoll, H. M., D. P. Schrag, and S. C. Clemens (1999), Are seawater Sr/Ca variations preserved in Quaternary foraminifera? *Geochimica et Cosmochimica Acta*, 63(21), 3535-3547.

Tisserand, A.A., T. M. Dokken, C. Waelbroeck, J. M. Gherardi, V. Scao, C. Fontanier, and F. Jorissen (2013), Refining benthic foraminiferal Mg/Ca-temperature calibration using core-tops from the western tropical Atlantic: Implication for paleotemperature estimation, *Geochemistry, Geophysics, Geosystems*, *14*(4), 929-946, doi: 10.1002/ggge.20043.

Yu, J., and H. Elderfield (2008), Mg/Ca in the benthic foraminifera *Cibicidoides wuellerstorfi* and *Cibicidoides mundulus*: Temperature versus carbonate ion saturation, *Earth and Planetary Science Letters*, *276*, 129-139, doi: 10.1016/j.epsl.2008.09.015.

2.6 Auxiliary Material

Auxiliary Table 2.1. *C. wuellerstorfi* results

Station	Water Depth, m	BWT, °C	$\Delta[CO_3]_{calcite}$ µmol kg^{-1}	$\delta^{18}O_{sw}$ vs SMOW	*C. wuellerstorfi* Mg/Ca, mmol mol^{-1}	*C. wuellerstorfi* Sr/Ca, mmol mol^{-1}	*C. wuellerstorfi* $\delta^{18}O$ vs VPDB	*C. wuellerstorfi* $\delta^{18}O - \delta^{18}O_{sw}$ vs VPDB
				Timor Sea				
18503	354	10.37	40.89	-0.05	4.15	1.52	0.67	0.99
18503	354	10.37	40.89	-0.05			0.74	1.06
18489	431	9.01	32.31	-0.05			1.3	1.62
18489	431	9.01	32.31	-0.05			1.33	1.65
18488	555	7.82	27.40	-0.03	1.64	1.35	1.49	1.79
18488	555	7.82	27.40	-0.03	3.96	1.33	1.56	1.86
18493	599	7.23	26.75	-0.04	2.51	1.44	1.68	1.99
18493	599	7.23	26.75	-0.04	1.72	1.39	1.96	2.27
18469	704	6.25	25.42	0.03			1.91	2.15
18469	704	6.25	25.42	0.03			1.81	2.05
18469	704	6.25	25.42	0.03			1.8	2.04
18501	742	6.13	24.59	-0.06	2.11	1.35	2.12	2.44
18501	742	6.13	24.59	-0.06	1.56	1.40	2.13	2.45
18501	742	6.13	24.59	-0.06	1.41	1.31	1.94	2.27
18501	742	6.13	24.59	-0.06	2.23	1.43	1.76	2.09
18468	803	5.80	22.52	0.01	1.84	1.35	2.02	2.28
18468	803	5.80	22.52	0.01	1.59	1.34	1.8	2.06
18468	803	5.80	22.52	0.01			1.91	2.17
18468	803	5.80	22.52	0.01			1.88	2.14
18468	803	5.80	22.52	0.01			1.85	2.11
18467	899	4.99	20.93	0.00	1.91	1.35	2.17	2.45
18467	899	4.99	20.93	0.00	1.58	1.36	1.97	2.24

Auxiliary Table 2.1. (continued)

Station	Water Depth, m	BWT, °C	$\Delta[CO_3]_{calcite}$ µmol kg^{-1}	$\delta^{18}O_{sw}$ vs SMOW	*C. wuellerstorfi* Mg/Ca, mmol mol^{-1}	*C. wuellerstorfi* Sr/Ca, mmol mol^{-1}	*C. wuellerstorfi* $\delta^{18}O$ vs VPDB	*C. wuellerstorfi* $\delta^{18}O$ - $\delta^{18}O_{sw}$ vs VPDB
18466	1004	4.62	19.91	-0.02	2.20	1.41	2.5	2.79
18466	1004	4.62	19.91	-0.02			2.72	3.01
18466	1004	4.62	19.91	-0.02			2.59	2.88
18465	1082	4.61	19.13	-0.03			2.19	2.49
18465	1082	4.61	19.13	-0.03			2.18	2.48
18500	1167	4.10	18.28	-0.10	1.57	1.37	2.17	2.54
18500	1167	4.10	18.28	-0.10	1.47	1.36	2.18	2.55
18500	1167	4.10	18.28	-0.10			2.12	2.49
18464	1206	4.26	18.02	-0.09	1.36	1.33	2.46	2.83
18464	1206	4.26	18.02	-0.09			2.26	2.63
18464	1206	4.26	18.02	-0.09			2.13	2.49
18464	1206	4.26	18.02	-0.09			2.53	2.89
18463	1311	4.18	17.80	-0.09			2.44	2.80
18463	1311	4.18	17.80	-0.09			2.2	2.56
18463	1311	4.18	17.80	-0.09			2.23	2.59
18499	1383	3.51	17.64	0.00	1.44	1.36	2.43	2.70
18499	1383	3.51	17.64	0.00	1.17	1.36	2.34	2.61
18499	1383	3.51	17.64	0.00			2.32	2.59
18499	1383	3.51	17.64	0.00			2.33	2.60
18462	1422	4.26	17.55	-0.09			2.58	2.94
18462	1422	4.26	17.55	-0.09			2.4	2.76
18462	1422	4.26	17.55	-0.09			2.25	2.61
18478	1769	3.56	16.60	-0.13	1.11	1.27	2.52	2.92

Auxiliary Table 2.1. (continued)

Station	Water Depth, m	BWT, °C	$\Delta[CO_3]_{calcite}$ µmol kg^{-1}	$\delta^{18}O_{sw}$ vs SMOW	*C. wuellerstorfi* Mg/Ca, mmol mol^{-1}	*C. wuellerstorfi* Sr/Ca, mmol mol^{-1}	*C. wuellerstorfi* $\delta^{18}O$ vs VPDB	*C. wuellerstorfi* $\delta^{18}O - \delta^{18}O_{sw}$ vs VPDB
18478	1769	3.56	16.60	-0.13			2.47	2.87
18506	2410	2.17	14.14	-0.15	2.04	1.21	2.65	3.08
18506	2410	2.17	14.14	-0.15	1.21	1.23	2.66	3.08
18506	2410	2.17	14.14	-0.15	0.90	1.27	2.65	3.07
18506	2410	2.17	14.14	-0.15			2.59	3.01
18507	2450	2.00	13.96	-0.16	1.42	1.23	2.74	3.18
18507	2450	2.00	13.96	-0.16	1.01	1.26		
18507	2450	2.00	13.96	-0.16	1.12	1.23		
				Makassar Strait				
18534	563	6.90	27.11	-0.14	2.22	1.35	1.91	2.32
18518	620	6.43	26.55	-0.27	2.12	1.38	2.08	2.62
18532	629	6.60	26.51	-0.14	2.57	1.42	1.77	2.18
18517	699	6.14	25.63	-0.28	1.73	1.39		
18545	707	6.07	25.47	-0.16	1.87	1.39	2.08	2.51
18541	739	5.75	24.74	-0.14	1.68	1.40	1.90	2.31
18541	739	5.75	24.74	-0.14	1.69	1.37		
18530	876	5.31	21.09	-0.15	2.05	1.39	2.20	2.62

Red values represent samples not included in this study

Auxiliary Table 2.2. *H. elegans* results

Station	Water Depth, m	BWT, °C	$\Delta[CO_3]_{aragonite}$ µmol kg^{-1}	$\delta^{18}O_{sw}$ vs SMOW	*H. elegans* Mg/Ca, mmol mol^{-1}	*H. elegans* Sr/Ca, mmol mol^{-1}	*H. elegans* $\delta^{18}O$ vs VPDB	*H. elegans* $\delta^{18}O$ - $\delta^{18}O_{sw}$ vs VPDB
				Timor Sea				
18454	131	18.30	99.83	0.20	1.84	3.20	-0.20	-0.13
18454	131	18.30	99.83	0.20	1.51	3.24		
18454	131	18.30	99.83	0.20	1.46	3.26		
18503	354	10.37	13.98	-0.05			2.35	2.67
18489	431	9.01	5.08	-0.05	1.35	2.02	2.70	3.02
18489	431	9.01	5.08	-0.05	0.98	2.28		
18489	431	9.01	5.08	-0.05	0.99	2.16		
18488	555	7.82	-0.36	-0.03	0.87	1.95	3.33	3.63
18488	555	7.82	-0.36	-0.03	1.12	2.11		
18488	555	7.82	-0.36	-0.03	1.04	2.04		
18488	555	7.82	-0.36	-0.03	0.98	2.00		
18488	555	7.82	-0.36	-0.03	1.04	1.98		
18493	599	7.23	-1.2	-0.04	1.06	1.98	3.25	3.56
18493	599	7.23	-1.2	-0.04	0.89	1.99		
18469	704	6.25	-2.97	0.03	0.86	1.32	3.39	3.63
18469	704	6.25	-2.97	0.03				
18501	742	6.13	-3.97	-0.06	1.42	1.78	3.34	3.67
18501	742	6.13	-3.97	-0.06	0.85	1.87		
18501	742	6.13	-3.97	-0.06	0.68	1.27		
18501	742	6.13	-3.97	-0.06	0.74	1.40		
18501	742	6.13	-3.97	-0.06	0.84	1.60		
18501	742	6.13	-3.97	-0.06	0.82	1.69		

Auxiliary Table 2.2. (continued)

Station	Water Depth, m	BWT, °C	$\Delta[CO_3]_{aragonite}$ µmol kg^{-1}	$\delta^{18}O_{sw}$ vs SMOW	*H. elegans* Mg/Ca, mmol mol^{-1}	*H. elegans* Sr/Ca, mmol mol^{-1}	*H. elegans* $\delta^{18}O$ vs VPDB	*H. elegans* $\delta^{18}O$ - $\delta^{18}O_{sw}$ vs VPDB
18501	742	6.13	-3.97	-0.06	1.18	1.76		
18468	803	5.80	-6.31	0.01	0.61	1.45	3.90	4.16
18468	803	5.80	-6.31	0.01	0.76	1.48		
18468	803	5.80	-6.31	0.01	0.5	1.31		
18467	899	4.99	-8.33	0.00	0.7	1.28	3.28	3.55
18467	899	4.99	-8.33	0.00	0.82	1.57		
18467	899	4.99	-8.33	0.00	0.73	1.54		
18466	1004	4.62	-9.82	-0.02	1.02	1.08	4.21	4.50
18466	1004	4.62	-9.82	-0.02				
18466	1004	4.62	-9.82	-0.02				
18465	1082	4.61	-10.96	-0.03	0.76	0.7	3.67	3.97
18465	1082	4.61	-10.96	-0.03	0.54	0.66		
18465	1082	4.61	-10.96	-0.03	0.44	0.89		
18500	1167	4.10	-12.21	-0.10			3.74	4.11
18500	1167	4.10	-12.21	-0.10				
18464	1206	4.26	-12.65	-0.09	0.88	0.69	3.57	3.93
18464	1206	4.26	-12.65	-0.09	0.56	0.67		
18464	1206	4.26	-12.65	-0.09	0.34	0.68		
18464	1206	4.26	-12.65	-0.09	0.38	0.73		
18464	1206	4.26	-12.65	-0.09	0.35	0.60		
18463	1311	4.18	-13.36	-0.09	0.46	0.62	3.54	3.90
18463	1311	4.18	-13.36	-0.09	0.44	0.63		
18499	1383	3.51	-13.87	0.00	0.52	0.74	3.89	4.16

Auxiliary Table 2.2. (continued)

Station	Water Depth, m	BWT, °C	$\Delta[CO_3]_{aragonite}$ µmol kg^{-1}	$\delta^{18}O_{sw}$ vs SMOW	*H. elegans* Mg/Ca, mmol mol^{-1}	*H. elegans* Sr/Ca, mmol mol^{-1}	*H. elegans* $\delta^{18}O$ vs VPDB	*H. elegans* $\delta^{18}O$ - $\delta^{18}O_{sw}$ vs VPDB
18499	1383	3.51	-13.87	0.00	0.46	0.77		
18462	1422	4.26	-14.15	-0.09			3.69	4.05
18462	1422	4.26	-14.15	-0.09				
18478	1769	3.56	-16.82	-0.13			4.02	4.42
18506	2410	2.17	-22.71	-0.15	0.54	0.45	4.09	4.51
18506	2410	2.17	-22.71	-0.15				
18506	2410	2.17	-22.71	-0.15				
18507	2450	2.00	-23.12	-0.16	0.54	0.54	4.07	4.50
18507	2450	2.00	-23.12	-0.16	0.33	0.44		
18507	2450	2.00	-23.12	-0.16				
				Makassar Strait				
18534	563	6.90	-0.66	-0.14	2.45	1.09	3.37	3.78
18534	563	6.90	-0.66		0.87	1.65		
18534	563	6.90	-0.66		0.86	1.61		
18518	620	6.43	-1.48	-0.27	0.99	1.53	2.96	3.50
18518	620	6.43	-1.48		0.92	1.49		
18532	629	6.60	-1.6	-0.14	1.07	1.43	2.88	3.29
18517	699	6.14	-2.84	-0.28	0.68	1.37	3.08	3.63
18517	699	6.14	-2.84		0.73	1.46		
18545	707	6.07	-3.05	-0.16	0.88	1.60	3.54	3.97
18545	707	6.07	-3.05		0.85	1.62		
18541	739	5.75	-3.89	-0.14	0.89	1.34	3.21	3.62
18541	739	5.75	-3.89		0.88	1.58		

Auxiliary Table 2.2. (continued)

Station	Water Depth, m	BWT, °C	$\Delta[CO_3]_{aragonite}$ µmol kg^{-1}	$\delta^{18}O_{sw}$ vs SMOW	*H. elegans* Mg/Ca, mmol mol^{-1}	*H. elegans* Sr/Ca, mmol mol^{-1}	*H. elegans* $\delta^{18}O$ vs VPDB	*H. elegans* $\delta^{18}O$ - $\delta^{18}O_{sw}$ vs VPDB
18536	836	5.65	-7.44	-0.18	0.83	1.21	3.26	3.71
18536	836	5.65	-7.44		0.87	1.18		
18536	836	5.65	-7.44		0.88	1.18		
18530	876	5.31	-8	-0.15	0.9	1.35	3.30	3.72
18530	876	5.31	-8		0.86	1.47		
18530	876	5.31	-8		0.88	1.52		
18537	929	5.38	-8.75	-0.24	0.83	1.20	3.41	3.92
18522	974	4.67	-9.39	-0.07	0.9	1.50	3.60	3.94
18531	1086	4.50	-11.01	-0.15	0.7	0.80	3.40	3.82
18531	1086	4.50	-11.01		0.66	0.79		
18531	1086	4.50	-11.01		0.83	0.71		
18531	1086	4.50	-11.01		0.66	0.77		
18540	1200	4.09	-12.61	-0.41	0.66	0.77	3.52	4.20
18540	1200	4.09	-12.61		0.62	1.10		
18526	1538	3.95	-15	-0.20	0.83	0.70	3.39	3.86
18526	1538	3.95	-15		0.68	0.71		
18526	1538	3.95	-15		0.7	0.73		
18527	1615	3.61	-15.59	-0.17	0.69	0.64	3.50	3.94
18527	1615	3.61	-15.59		0.58	0.72		
18527	1615	3.61	-15.59		0.59	0.75		
18528	1785	3.47	-16.96	0.02	0.58	0.70	3.56	3.81
18528	1785	3.47	-16.96		0.59	0.66		
18528	1785	3.47	-16.96		0.75	0.78		
18525	1822	3.52	-17.26	-0.66	0.5	0.73	3.55	4.48

Red values represent samples not included in this study

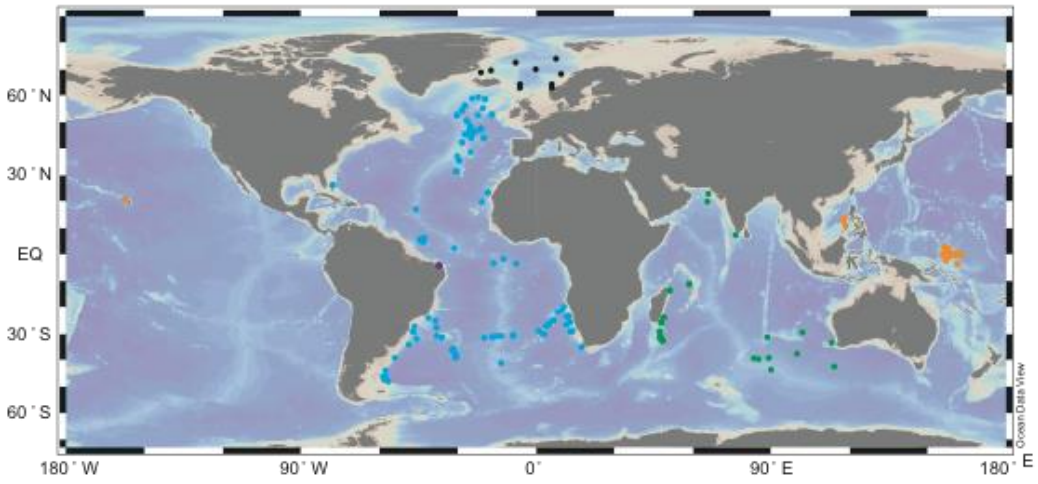

Auxiliary Figure 2.1. Locations of published core top samples

Chapter 3

Changes in Timor Strait hydrology during the past 130 ka

Elena Lo Giudice Cappelli, Ann Holbourn, Wolfgang Kuhnt, and Marcus Regenberg

In Review in *Palaeogeography, Palaeoclimatology, Palaeoecology*

Abstract

Paleostudies of the Indonesian Throughflow (ITF) are largely based on temperature and salinity reconstructions of its near surface component, whereas the variability of its lower thermocline flow has rarely been investigated. We present a multi-proxy record of planktonic and benthic foraminiferal $\delta^{18}O$, Mg/Ca-derived surface and lower thermocline temperatures, X-ray fluorescence (XRF)-derived runoff and sediment winnowing for the past 130 ka in marine sediment core SO18471. Core SO18471, retrieved from a water depth of 485 m at the southern edge of the Timor Strait close to the Sahul Shelf, sits in a strategic position to reconstruct variations in both the ITF surface and lower thermocline flow as well as to investigate hydrological changes related to monsoon variability and shelf dynamics over time. Sediment winnowing demonstrates that the ITF thermocline flow intensified during MIS 5d-a and MIS 1. In contrast during MIS 5e, winnowing was reduced and terrigenous input increased suggesting intensification of the local wet monsoon and a weaker ITF. Lower thermocline warming during globally cold periods (MIS 4 – MIS 2) appears to be related to a weaker and contracted thermocline ITF and advection of warm and salty Indian Ocean waters.

3.1. Introduction

The Indonesian Throughflow (ITF) is a complex ocean current system that transports cool and fresh waters from the Pacific Ocean to the Indian Ocean and, thus, plays an important role in modulating local and global climate [*Cresswell et al.*, 1993; *Gordon and Fine*, 1996*; Gordon* 2005; *Oppo and Rosenthal* 2010]. The Timor Strait

provides the main exit path for the ITF, as about half of the total transport (~7.5 Sv) takes place through this passage [*Sprintall et al.,* 2009]. To date, our understanding of the past evolution of the ITF remains largely based on temperature and salinity reconstructions of its near surface component, down to ~200 m, whereas the variability of the lower thermocline component along the ITF pathway has rarely been investigated. The scarcity of investigations addressing past variability of intermediate and deep waters reflects to a large extent the difficulties in developing sensitive proxy recorders of temperature for the deeper ocean, where variations are generally more muted than at or close to the surface. Based on a new Mg/Ca paleothermometry calibration study [*Lo Giudice Cappelli et al.*, 2015], we present the first Timor Strait record of lower thermocline temperatures spanning the last ~130 ka. We combine this benthic foraminiferal Mg/Ca data set from Core SO18471 with a multi-proxy record of planktonic and benthic foraminiferal $\delta^{18}O$, Mg/Ca-derived surface temperature and X-ray fluorescence (XRF)-derived runoff and sediment winnowing from the same core. The location of core SO18471 is strategic to reconstruct the variability of the ITF vertical structure over time, as it sits in a relatively shallow location, in a water depth of 485 m corresponding to the ITF lower thermocline flow, which allows to reconstruct the hydrological evolution of both surface and deeper water masses (Fig. 3.1). In addition, the proximity of core SO18471 to the Sahul Shelf allows to monitor changes in sediment discharge and winnowing related to variations in the Indonesian-Australian Monsoon system and shelf dynamics over time. We compare our results with published isotope ($\delta^{18}O$) and Mg/Ca data from the Timor Sea to explore the regional variability in temperature and water mass properties and to assess the impact of glacial – deglacial sea level changes on regional hydrography.

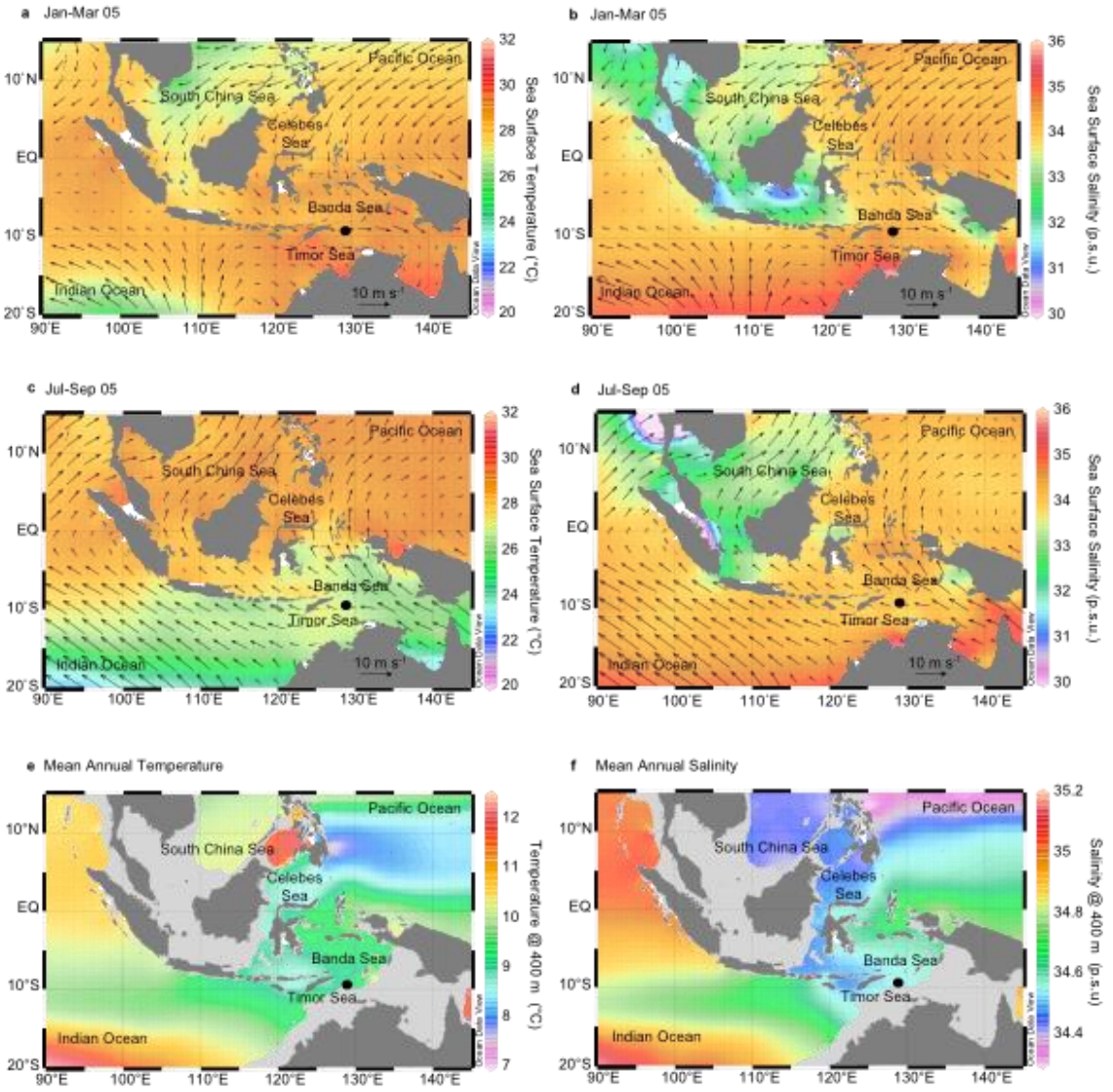

Fig. 3.1. Monsoon-induced seasonal variations in temperature, salinity and wind trajectory in the tropical Indo-Pacific plotted with Ocean Data View [*Schlitzer*, 2013]. **a)** and **b)** Austral summer (January-March) seasonal SST and salinity variations. **c)** and **d)** Austral winter (July-September) seasonal SST and salinity variations. **e)** and **f)** Mean annual temperature and salinity at 400 m. Temperature and salinity data are from the World Ocean Atlas 2005 [*Locarnini et al*., 2006]. Superimposed are winds trajectories (arrows) in February (**a** and **b**) and August (**c** and **d**). Wind data are monthly averages for February and August 2005 from NCEP Reanalysis Dataset (http://www.esrl.noaa.gov/psd/). Black circle indicates location of core SO18471.

3.2. Regional oceanography and climate dynamics

The Timor Sea encompasses the Timor Strait to the north and the Sahul Shelf to the south [*Cresswell et al.,* 1993]. The Timor Strait is dominated by the year-round southwestward flow of the ITF, while circulation on the Sahul Shelf strongly depends on the monsoon cycle [*Cresswell et al*., 1993; *Sprintall et al.*, 2009; *Schiller et al.,* 2011]. The ITF is driven across the Indonesian Archipelago by the pressure gradient between the tropical western Pacific and the Indian Ocean [*Cresswell et al.,* 1993] and consists of surface to upper thermocline waters stemming from the North Pacific, and lower thermocline and intermediate waters of South Pacific origin [*Gordon and Fine,* 1996*; Talley and Sprintall,* 2005; *Sprintall et al*., 2009]. On their way to the Timor Strait, these water masses are intensely modified by tidal mixing [*Egbert and Ray,* 2001; *Ray et al.*, 2005; *Koch-Larrouy et al*., 2010], monsoon-driven upwelling [*Moore et al.,* 2003], and air-sea exchanges [*Wijffels et al.*, 2008] in the Banda Sea (Fig. 3.1) before entering the Indian Ocean [*Ffield and Gordon,* 1992; *Gordon and Susanto,* 2001; *Sprintall et al*., 2009].

Seasonal wind reversals linked to the Indonesian-Australian Monsoon system influence the circulation in the Timor Sea. During the austral summer monsoon (NW monsoon), the ITF and northeast currents on the Sahul Shelf are weaker because the pressure gradient between the Pacific and Indian Oceans is at its lowest [*Cresswell et al.,* 1993; *Sprintall et al*., 2009; *Schiller et al*., 2011]. As the Intertropical Convergence Zone (ITCZ) is in its southernmost position, Indonesia and NW Australia experience a warm and wet season (Fig. 3.1a and b). Freshwater and terrigenous material reach the Sahul Shelf from the Victoria, Daly and Adelaide rivers (NW Australia), and variations in their load depend on the strength of the NW monsoon (Fig. 3.2) [*Alongi et al.*, 2013].

However, most terrigenous material is not of Australian but of Indonesian origin, as about 30 rivers in the western part of New Guinea represent a significant source of sediments for the Arafura and Timor Sea due to the steep topography of New Guinea, promoting intense discharge (Fig. 3.2) [*Alongi et al.*, 2013]. In contrast, during the austral winter monsoon (SE monsoon), both the ITF and the Sahul Shelf currents flow to the southwest and are intensified, as the pressure gradient between the Pacific and Indian Oceans is at its highest [*Cresswell et al.,* 1993; *Sprintall et al*., 2009; *Schiller et al*., 2011]. The ITCZ retreats northward, and Indonesia and NW Australia experience a cold and dry season (Fig. 3.1c and d). Additionally, sea surface salinity increases toward the inner part of the Sahul Shelf owing excess of evaporation over precipitation leading to local evaporative dense water formation (Fig. 3.1d) [*Cresswell et al.*, 1993]. Evaporative dense water formation also occurs during austral winter on the inner NW Australian shelf (Fig. 3.1d) and denser water are transported at intermediate depth offshore, either via eddy transport or by transport in the boundary layers [*Brink and Sherman* 2006; *Brink et al*., 2007; *Shearman and Brink* 2010].

During periods of lowered sea level, the exposure of vast shelf areas in the western Pacific, such as the Sahul Shelf, the Arafura Shelf and Gulf of Carpentaria, drastically changed local circulation and sedimentation due to changes in the geometry of the pathways connecting local seas as well as displacement of depositional basins (Fig. 3.2) [*Wang et al.*, 1999; *Reeves et al*., 2008]. Paleoclimate records of surface temperature and salinity indicated that the ITF varied considerably during the last glacial cycle due to sea level-driven alterations in the influx of cooler and fresher waters into the Indonesian seas and to variations in monsoon activity modulated by insolation changes [e.g.: *Lea et*

al., 2000; *Visser et al.*, 2003; *Spooner et al.*, 2005; *Beaufort et al.*, 2010; *Linsley et al*., 2010]. In the Timor Sea, paired records of surface and upper thermocline temperature and salinity spanning the last glacial cycle indicated that the upper thermocline showed higher variability than the surface flow [e.g. *Xu et al.*, 2006, 2008; *Holbourn et al.*, 2011; *Ding et al.*, 2013]. These studies revealed cooling and freshening of the upper thermocline during sea level highstands, which was interpreted as an intensification of the ITF thermocline flow. A weaker and more surface-dominated glacial ITF was also proposed by *Žuvela-Aloise* [2005], based on numerical circulation models. Only one recent study [*Rosenthal et al*., 2013] focused on temperature and salinity reconstructions of the deeper component of the ITF. This work, based on a suite of sediment cores retrieved from the Makassar Strait and Flores Sea, revealed a distinct warming of intermediate waters during the early Holocene maximum in Northern Hemisphere summer insolation [*Rosenthal et al*., 2013]. These authors suggested that warming of the ITF source water at higher latitudes controls intermediate water temperature variability in the Indonesian seas [*Rosenthal et al*., 2013]. However, this study does not allow to assess the wider spectrum of variability on glacial – interglacial timescale and to explore potential relationships to past climatic boundary conditions (e.g., ice volume, sea level, seaway geometry, interhemispheric thermal gradient), which fundamentally differed from the present day.

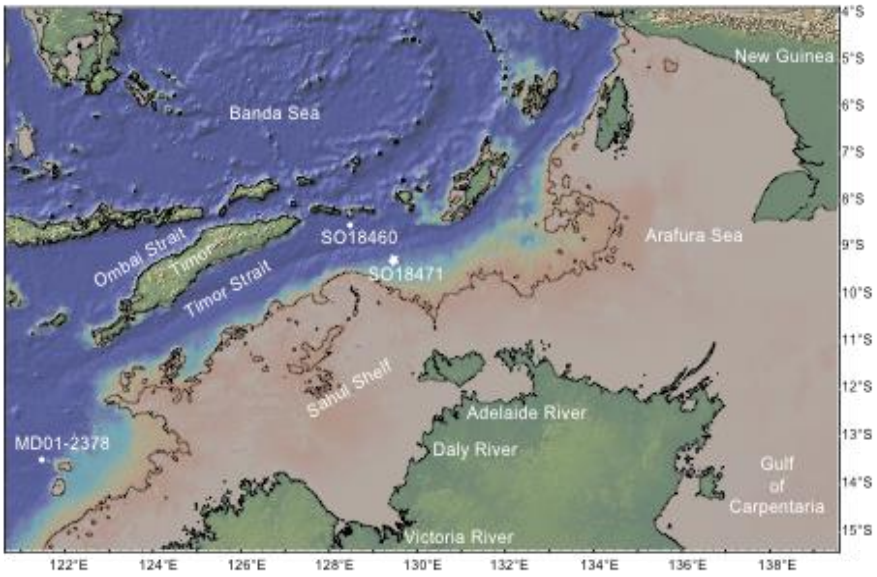

Fig. 3.2. Local map showing position of core SO18471 (this study) and cores SO18460 and MD01-2378 [*Holbourn et al*., 2011] and locations referred to in this study. Black contour lines show differences in topography and bathymetry between present day and LGM, when sea level was ~120 m lower. Basemap was generated with GeoMapApp (http://www.geomapapp.org) using the Global Multi-Resolution Topography synthesis database [*Ryan et al*., 2009].

3.3. Material and methods

3.3.1 Sampling strategy

During the Sonne-185 "VITAL" Cruise [*Kuhnt et al*., 2005], piston-core SO18471 (9° 21.987' S, 129° 58.983'E; 485 m water depth; 13.5 m length) was retrieved at the southern edge of the Timor Strait, close to the Sahul Shelf as part of a NE-SW transect across the Timor Sea (Fig. 3.1). The sediment consists of hemipelagic foraminiferal ooze and bioturbation is common throughout the record. A total of 134 sediment samples (1 cm thick sediment slices) were taken in 10 cm intervals between 0 and 1330 cm (0-133 ka), corresponding approximately to 1 kyr time resolution. In the intervals between 0 and

120 cm and between 400 and 750 cm, additional samples were taken in 5 cm intervals to increase the temporal resolution.

3.3.2 Proportion of coarse fraction (>63 μm)

Sediment samples were oven-dried below 40 °C, weighed, disaggregated by soaking in water and wet sieved over a 63 μm screen. Residues were dried on a sheet of filter paper below 40 °C, then weighed and sieved into 63-150 μm, 150-250 μm, 250-315 μm, >315 μm fractions. The proportion of coarse fraction (>63 μm) was calculated as the ratio between residue weight and total dry weight.

3.3.3 Accelerator mass spectrometry ^{14}C dating

For accelerator mass spectrometry (AMS) ^{14}C dating, approximately 800 well preserved tests of *Globigerinoides ruber* were picked from the >250 μm fraction in six samples from core SO18471. *Globigerinoides sacculifer* tests were additionally picked in two samples due to the scarcity of *G. ruber* (Table 1). Conventional ^{14}C ages were determined at the Leibniz Laboratory for Radiometric Dating and Isotope Research (Leibniz Laboratory), University of Kiel, using standard methods described by *Nadeau et al.* [1997] and *Grootes et al*. [2004]. Conventional AMS ^{14}C ages were converted into calendar ages using the radiocarbon calibration program CALIB REV7.1.0 [*Stuiver and Reimer*, 1993] and the calibration data set IntCal13 [*Reimer et al.*, 2013]. A reservoir correction of 475 years was applied following *Southon et al*. [2002].

Table 1. AMS ^{14}C dates and $\delta^{18}O$ events between sediment core SO18471 and the EDML-1 ice core (AICC2012)*

Analysis	Sample (core SO18471)	Conventional ^{14}C age, ka	Tie point	Calendar Age, ka	Species analyzed
AMS ^{14}C date	section I; 0-1 cm	1.745±25		1.4960**	*G.ruber*
AMS ^{14}C date	sectionI; 44-45 cm	12.280±80		13.950**	*G.ruber, G. sacculifer*
AMS ^{14}C date	section II; 100-101 cm	16.760±90		20.011**	*G.ruber*
AMS ^{14}C date	section II; 144-145 cm	20.790±180		24.816**	*G.ruber; G. sacculifer*
AMS ^{14}C date	section III; 200-201 cm	25.320±220		29.18**	*G.ruber*
AMS ^{14}C date	section III; 250-251 cm	29.560±420		33.525**	*G.ruber*
Foraminiferal $\delta^{18}O$	section IV; 320-321 cm		lowest $\delta^{18}O$ value of A1	39.181*	*G.ruber ; H. elegans; Uvigerina* spp.
Foraminiferal $\delta^{18}O$	section VIII; 710-711 cm		lowest $\delta^{18}O$ value of A4	59.748*	*G.ruber ; H. elegans; Uvigerina* spp.
Foraminiferal $\delta^{18}O$	section X; 900-901 cm		lowest $\delta^{18}O$ value of MIS 5a	73.334*	*G.ruber ; H. elegans; Uvigerina* spp.
Foraminiferal $\delta^{18}O$	section XII; 1092-1093 cm		peak of MIS 5d	107.69*	*G.ruber ; H. elegans; Uvigerina* spp.
Foraminiferal $\delta^{18}O$	section XII; 1142-1143 cm		end of MIS 5e $\delta^{18}O$ plateau	117.49*	*G.ruber ; H. elegans; Uvigerina* spp.
Foraminiferal $\delta^{18}O$	section XIII; 1222-1223 cm		onset of MIS 5e $\delta^{18}O$ plateau	129.46*	*G.ruber ; H. elegans; Uvigerina* spp.
Foraminiferal $\delta^{18}O$	section XIV; 1312-1313 cm		midpoint of Termination II	132.93*	*G.ruber ; H. elegans; Uvigerina* spp.

*Veres *et al.*. (2013)

**Calibration version for ^{14}C dates: IntCal13

3.3.4 Stable isotope analysis

Between 15 and 30 tests of *Hoeglundina elegans* and *Uvigerina* spp. were selected for stable isotope and Mg/Ca analysis from the >250 µm size fraction and ~30 tests of *G. ruber* were picked from the size fraction 250-315 µm. Tests were checked under the microscope for cement encrustations and infillings before being broken into large fragments. After crushing, foraminiferal samples were split into Mg/Ca sub-samples (2/3 of the total sample) and $\delta^{18}O$ sub-samples (remaining 1/3) to obtain more homogeneous and representative material for measurement. The split samples for stable isotope analysis were cleaned in ethanol in an ultrasonic bath and dried at 40 °C. Stable isotopes were measured with a Finnigan MAT 253 mass spectrometer at the Leibniz Laboratory, University of Kiel. The instrument is coupled on-line to a Carbo-Kiel Device (Type IV) for automated CO_2 preparation from carbonate samples for isotopic analysis. On the basis of the performance of international and lab-internal standard carbonates, the precision is better than ±0.09‰. Results were calibrated using the NIST (National Institute of Standard and Technology, Gaithersburg, Maryland) carbonate isotope

standard and NBS (National Bureau of Standard) 19 and in addition NBS 20, and are reported on the Vienna PeeDee Belemnite (VPDB) scale. Replicate measurements on twenty-five pairs of *H. elegans* indicate a mean reproducibility of ±0.09‰ for $\delta^{18}O$, 34 replicate samples of *Uvigerina* spp. a mean reproducibility of ±0.08‰ for $\delta^{18}O$; 62 replicate samples of *G. ruber* a mean reproducibility of ±0.10‰ for $\delta^{18}O$.

3.3.5 X-ray fluorescence core scanning

The archive half of core SO18471 was scanned for major elements intensities in 1 cm resolution at the Institute of Geosciences, University of Kiel, using the second generation Avaatech X-ray fluorescence core scanner. The core was covered with a 4 μm-thin SPEXCerti Prep Ultralene1 foil to avoid contamination of the XRF measurement unit and desiccation of the sediment. Intensities of elements common in continental siliciclastic rocks (e.g. Fe, Ti, Al, Si, K) are used as qualitative proxies for terrigenous input, normalized against calcium derived from biogenic carbonate and reported as log ratios to reduce the risk of measurement artifacts from variable signal intensities and matrix effects [*Weltje and Tjallingii*, 2008; *Kuhnt et al.,* 2015]. The log ratio of Zr/Rb is used as a grain size proxy, as Zirconium tends to be associated with coarser particles than Rubidium [e.g.: *Calvert and Pedersen,* 2007]. Zirconium is one of the main components of heavy minerals, such as zircon, which is subject to sorting and preferential settling on the continental shelf [*Lourens et al.,* 2001; *Kuhnt et al.,* 2015].

3.3.6 Carbonate content

Carbonate content was measured on dried and crushed bulk sediments by full reaction with 6 N HCl, using a "carbonate bomb" device [*Müller and Gastner*, 1971] at the Institute of Geosciences, University of Kiel. In intervals where prominent changes in the XRF-derived terrigenous input record occurred, carbonate content was measured with a resolution of approximately 50 cm. Standard error of the carbonate bomb device is ±1%.

3.3.7 Mg/Ca temperature estimates

Sea surface temperatures (SST) and bottom water temperatures (BWT) were estimated from Mg/Ca ratios of *G. ruber* and *H. elegans*, respectively. Samples were cleaned of the contaminant phases using the cleaning procedure with reductive step detailed in *Martin and Lea* [2002] and were analyzed with the ICP-OES (Inductively Coupled Plasma-Optical Emission Spectrometer) (Spectro Ciros SOP) with cooled cyclonic spraychamber and microconcentric nebulization (200 µl min^{-1}) at the Institute of Geosciences, University of Kiel. Intensity ratio calibration followed the method of *de Villiers et al.* [2002] and internal analytical precision was 0.1-0.2%. A dissolution-induced decrease of Mg/Ca, usually occurring in bottom waters with calcite-saturation states ($\Delta[CO_3^{2-}]_{calcite}$) below 21 µmol kg^{-1}, can be neglected, as core SO18471 has a modern bottom water $\Delta[CO_3^{2-}]_{calcite}$ of ~38 µmol kg^{-1}, well above the Mg/Ca lysocline [*Regenberg et al.*, 2014].

We converted *G. ruber* Mg/Ca ratios into temperatures using the calibration: Mg/Ca = 0.38±0.02 exp (0.09±0.003) SST from *Anand et al.* [2003]. For *H. elegans*, we

used the equation: Mg/Ca = 0.31±0.06 exp (0.14±0.01) BWT from *Lo Giudice Cappelli et al.* [2015]. Errors in SST and BWT reconstructions were calculated by propagating the errors introduced by Mg/Ca measurements and the Mg/Ca temperature calibrations mentioned above, following the approach described in *Mohtadi et al.* [2014]. Potential effects of glacial - interglacial sea level changes on BWT are discussed in the Supplementary Material.

Replicate measurements on 27 pairs of *H. elegans* gave a reproducibility of ±0.19 mmol mol^{-1} (standard deviation), corresponding to a temperature difference of ±1.2 °C. No duplicate measurements of *G. ruber* were performed. However according to *Xu et al.* [2006], who applied the same cleaning procedure and used the same analytical setup, sample reproducibility in *G. ruber* for a nearby core in the Timor Sea is ±0.7 °C, based on the calibration of *Anand et al.* [2003] for 24 replicate samples. Foraminiferal Fe/Ca, Al/Ca and Mn/Ca ratios were additionally used to monitor cleaning efficacy and no correlation with Mg/Ca ratios was found. However, one *G. ruber* and 9 *H. elegans* samples were not included in this study, as they showed high trace elements ratios indicative of contamination. Additionally, five *H. elegans* samples did not have enough material for measurement. From 1142 cm to the base of the core, the cleaning procedure was affected by the higher pyrite content of the samples and an additional 11 samples were rejected.

3.3.8 Sea water $\delta^{18}O$ ($\delta^{18}O_{sw}$) reconstructions

We calculated seawater $\delta^{18}O$ ($\delta^{18}O_{sw}$) from $\delta^{18}O$ of the foraminiferal calcite

($\delta^{18}O_{foram}$) and Mg/Ca-based temperature estimates for both surface and lower thermocline waters in core SO18471. We applied the equation: SST = (16.5 ± 0.2) – (4.80 ± 0.16) ($\delta^{18}O_{G.ruber}$ - $\delta^{18}O_{sw}$ + 0.27) from *Bemis et al.* [1998] to calculate $\delta^{18}O_{sw}$ in surface waters, and the equation: $\delta^{18}O_{sw}$ = 0.27 + $\delta^{18}O_{H.elegans}$+ (0.237 ± 0.003) BWT - (4.75 ± 0.04) from *Marchitto et al.* [2014] to calculate $\delta^{18}O_{sw}$ in bottom waters. In both cases, we corrected $\delta^{18}O_{sw}$ for ice volume using the sea level curve of *Waelbroeck et al.* [2002] adjusted to the chronology of core SO18471. Errors in $\delta^{18}O_{sw}$ reconstructions were calculated by propagating the errors introduced by $\delta^{18}O_{foram}$ measurements and the $\delta^{18}O$ temperature calibrations of *Bemis et al.* [1998] and *Marchitto et al.* [2014], following the approach described in *Mohtadi et al.* [2014].

3.4. Results

3.4.1 Chronology

The age model for the last 35 ka is based on six AMS ^{14}C dates in the upper 250 cm of the core (Table 1). Between 250 and 1242 cm, we correlated the *Uvigerina* spp., the *H. elegans* and the *G. ruber* $\delta^{18}O$ curves with the EDML-1 Antarctica ice core record (AICC2012) [*Veres et al*., 2013], using seven tie points (Table 1 and Fig. 3.3). The final age model was generated by linear interpolation between AMS ^{14}C ages and tie points (Fig. 3.3e). *Uvigerina* spp. and *H. elegans* $\delta^{18}O$ values recorded at the base of core SO18471 are between ~0.6 and 0.4‰ lower than during Marine Isotope Stage (MIS) 2, and between ~0.3 and 0.2‰ lower than during MIS 4, indicating that the base of the core

is still within Termination II, well above the MIS 6 $\delta^{18}O$ maximum at 138 ka (Fig. 3.3). A marked glacial-interglacial contrast is evident in the sedimentation rate, which is ~6 cm kyr^{-1} during MIS 5 and ~3 cm kyr^{-1} during the Holocene and fluctuates between ~9 and ~17 cm kyr^{-1} from MIS 4 to MIS 2 (Fig. 3.3f).

3.4.2 Terrigenous discharge/ river runoff

We used log((Fe+Ti+Al+Si+K)/Ca) and carbonate content as proxies for terrigenous discharge/river runoff, where higher log((Fe+Ti+Al+Si+K)/Ca) ratios and lower carbonate content indicate dominance of terrigenous-derived sediments. Fluctuations in both parameters generally follow glacial – interglacial cycles, with increased terrigenous input during periods of low sea level, and reduced terrigenous input during periods of high sea level (Fig. 3.4d and e). However, during MIS 5e, when sea level was at its highest, terrigenous input was higher than during MIS 1 (Fig. 3.4d and e).

3.4.3 Grain size and heavy minerals

We used the proportion of coarse fraction (>63 μm) (Fig. 3.4c) and log(Zr/Rb) (Fig. 3.4b) as a qualitative measure of sediment grain size. Both proxies follow the same glacial – interglacial trend, with higher values during sea level highstands and lower values during sea level lowstands (Fig. 3.4). As for the terrigenous proxy data, an exception to this trend is evident, however, during MIS 5e, when low values were recorded despite the highest sea level (Fig. 3.4).

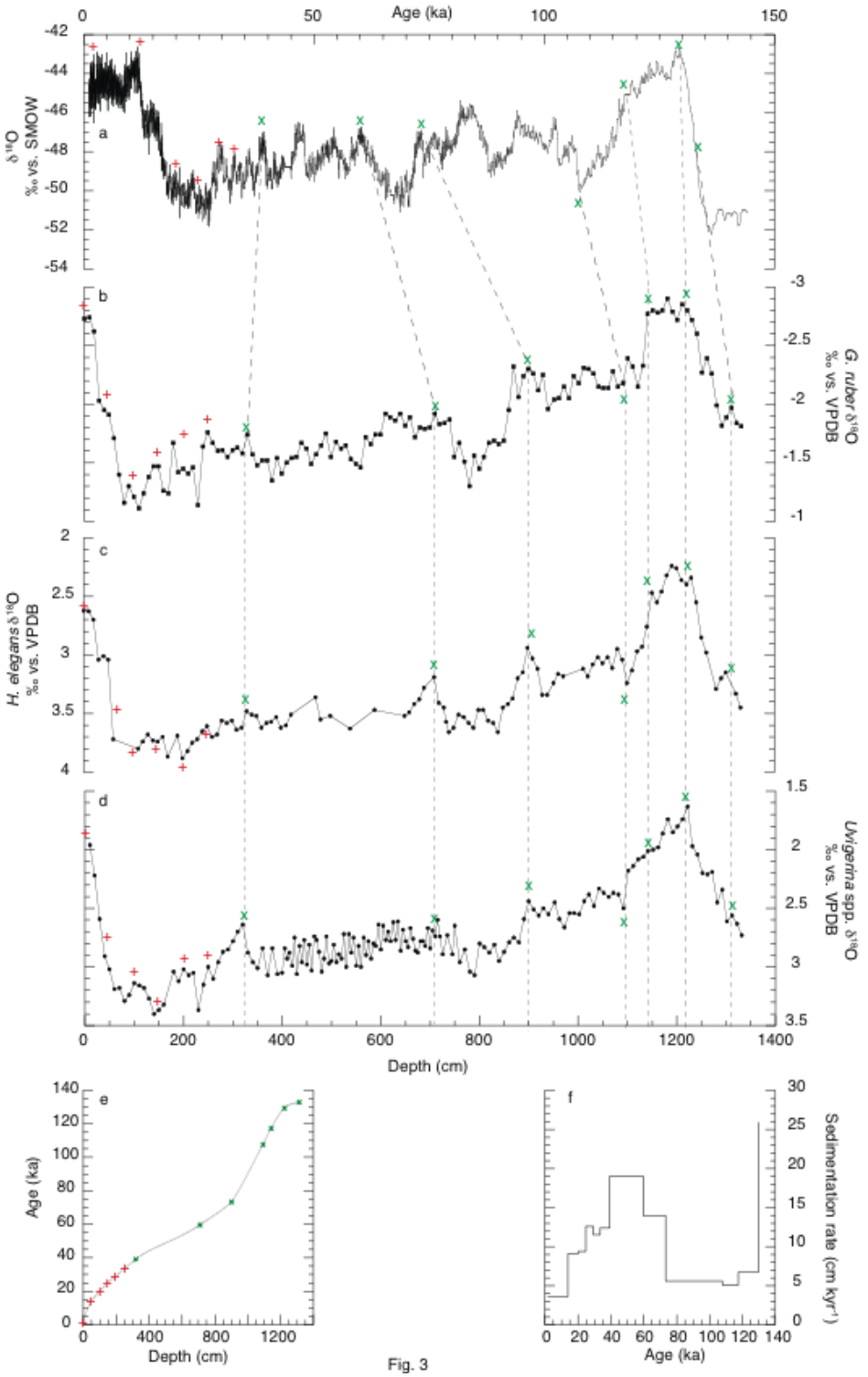

Fig. 3

Fig. 3.3. a) EDML-1 ice core $\delta^{18}O$ curve [*Veres et al*., 2013]. **b)** Core SO18471 *G. ruber* $\delta^{18}O$ record. c) Core SO18471 *H. elegans* $\delta^{18}O$ curve **d)** Core SO18471 *Uvigerina* spp. $\delta^{18}O$ record. **e)** Linear interpolation between AMS ^{14}C dates (red crosses) and $\delta^{18}O$ events used as tie points (green crosses). **d)** Changes in sedimentation rate over the last 133 ka.

3.4.4. Stable isotopes

Due to the scarcity of *H. elegans* and the occurrence of two different morphotypes in one interval of core SO18471 (Supplementary Fig. 3.2), we additionally measured *Uvigerina* spp. to obtain a higher resolution $\delta^{18}O$ record (Figs. 6a and b). *Hoeglundina elegans* $\delta^{18}O$ varies between 2.24 and 3.88‰, whereas *Uvigerina* spp. $\delta^{18}O$ ranges from 1.63 to 3.40‰ (Figs. 6a and b). We measured $\delta^{18}O$ in 103 paired-samples of *H. elegans* and *Uvigerina* spp. to calculate the $\delta^{18}O$ offset between the two species ($\Delta\delta^{18}O = \delta^{18}O_{H.elegans}-\delta^{18}O_{Uvigerina\ spp} = 0.62‰$, on average). The offset is quite consistent over the entire core (standard deviation 0.17‰) and can be used to produce an intercalibrated benthic $\delta^{18}O$ curve by adding 0.62‰ to the $\delta^{18}O$ values of *Uvigerina* spp. (Supplementary Fig. 3.3).

The *Uvigerina* spp. and *H. elegans* $\delta^{18}O$ records show a well-defined glacial – interglacial variability (Figs. 6a and b). The lowest *Uvigerina* spp. $\delta^{18}O$ value (1.63‰) is detected during MIS 5e (~129 ka) and the highest (3.40‰) occurs during MIS 2 (~24 ka) (Fig. 3.6a). Similarly, the lowest *H. elegans* $\delta^{18}O$ value (2.24‰) is detected during MIS 5e (~125 ka) and the highest (3.87‰) occurs during MIS 2 (~26 ka) (Fig. 3.6b). The glacial - interglacial $\delta^{18}O$ contrast between MIS 2 and the Holocene is 1.3‰ for *H. elegans* and 1.4‰ for *Uvigerina* spp. Between MIS 5e and the base of the record (~133 ka) the difference is only 1.2‰ for *H. elegans* and 1.1‰ for *Uvigerina* spp., implying that the base of the core extends to Termination II and does not reach MIS 6 (Figs. 6a and b).

The *G. ruber* $\delta^{18}O$ record also displays a strong glacial – interglacial signal (Fig. 3.5a), with values oscillating between -2.90 and -1.10‰. During MIS 5, *G. ruber* $\delta^{18}O$ values varied between -2.90 and -1.96‰, increasing to a maximum of -1.30‰ during MIS 4. During MIS 3, $\delta^{18}O$ values fluctuated between -1.92 and -1.14‰, then decreased rapidly from -1.11 to -2.62‰ between 21.1 and 7.9 ka. The difference between glacial and interglacial *G. ruber* $\delta^{18}O$ is 1.63‰ between MIS 2 and the Holocene and 1.10‰ between MIS 5e and the base of the record (Fig. 3.5a).

3.4.5 Sea surface temperature

Mg/Ca ratios in *G. ruber* vary between 3.23 and 5.39 mmol mol^{-1}, corresponding to SSTs ranging from 23.8 to 29.5 °C, in comparison to a modern annual average SST of 28.4 °C (*World Ocean Atlas 2005* data [*Locarnini et al.,* 2006]) (Fig. 3.5b). During austral summer (January-March), modern SST is on average 29 °C, while during austral winter (July-September) it is 26.8 °C (Fig. 3.1a and c).

Mean SSTs were ~28 °C during MIS 5, close to the modern day average, with the warmest SSTs (~29 °C) recorded during MIS 5e. In contrast, during the globally cold period from MIS 4 to MIS 2, SSTs were on average 25.8 °C, about 2.6 °C lower than today. However, SSTs were ~1°C warmer during MIS 4 in comparison to MIS2. During Termination I, SST displays a steady rise, reaching 28°C in the Holocene, which is ~1 °C lower than during MIS 5e (Fig. 3.5b).

3.4.6 Bottom water temperature

Mg/Ca ratios in *H. elegans* vary between 0.73 and 2.01 mmol mol^{-1} corresponding to BWTs between 6.1 and 13.3 °C, in comparison to a modern annual average of 8.1 °C at 500 m (*World Ocean Atlas 2005* data [*Locarnini et al.,* 2006]) (Figs. 1e and 6c). Between 130 and 125 ka, BWTs were ~3 °C higher than today, fluctuating around 11 °C (Fig. 3.6c). In the late part of MIS 5e and through MIS 5, an overall cooling trend is detected: from 11.2 °C at 125.7 ka to 8.4 °C at 71.4 ka. The beginning of the cooling is marked by a sharp drop of ~3 °C in BWT between 125 and 115 ka (Fig. 3.6c). Relatively high BWTs (~9.5 °C) are recorded during the cold period from MIS 4 to MIS 2. The most conspicuous increase appears to occur during the early part of MIS 3 between ~56 and 52 ka, when BWT increased from 7.9 °C to 13.3 °C (Fig. 3.6c). However, as a thin-walled morphotype of *H. elegans* preferentially occurs (Supplementary Fig. 3.2) and the overall abundance of this species is low within this interval, it is difficult to assess if these higher Mg/Ca ratios reflect an actual increase in BWT or rather are biased by a possible different chemical composition of the two *H. elegans* morphotypes. As we do not know whether or not these measurements are representative, we did not connect these higher values to the rest of the temperature record (Fig. 3.6c). During Termination I and throughout the Holocene, BWT decreased from 11 °C at 15 ka to 8.6 °C at 1.5 ka, with a sharp transient increase to 10 °C centered at 10.6 ka (Fig. 3.6c).

3.4.7 $\delta^{18}O_{sw}$ reconstructions

$\delta^{18}O_{sw}$ was calculated from $\delta^{18}O_{G.ruber}$ and $\delta^{18}O_{H.elegans}$ and corrected for

temperature and ice volume effects for surface and lower thermocline reconstructions, respectively. Surface $\delta^{18}O_{sw}$ values range between -0.47 and 0.56‰ with generally higher values during MIS 5 (on average of ~0.14‰) and low values between MIS 4 and MIS 2 (on average ~-0.08‰) (Fig. 3.5c). In contrast, lower thermocline $\delta^{18}O_{sw}$ values fluctuate between -0.30 and 1.41‰ with overall low values during MIS 5 (on average ~0.37‰) and high values between MIS 4 and MIS 2 (on average ~0.74‰).

3.5. Discussion

3.5.1 Sedimentation dynamics in the Timor Strait over the last 130 ka

During glacial periods, the most striking change in the geomorphology of Australasia was the exposure of vast shelf areas, such as the Sahul Shelf, the Arafura Shelf and the Gulf of Carpentaria [*Wang et al.*, 1999]. Marginal seas, such as the Timor and Arafura seas, were very sensitive to glacial sea level lowering, as changes in the proximity to exposed shelves affected local sedimentation and circulation [*Wang et al.*, 1999]. During sea level lowstands, core SO18471 was deeply influenced by the proximity of the exposed Sahul Shelf, resulting in generally higher terrigenous input (higher log(Fe+Ti+Al+Si+K/Ca) values) and lower carbonate content due to erosion of the emerged shelf during dry periods and increased discharge during humid periods, depending on the monsoon cycle (Figs. 4d and e). During sea level highstands, the location of core SO18471 was more distal from land and terrigenous input to the core location was more muted and dependent on the intensity of regional monsoonal rainfall

and river runoff. Furthermore, the marked glacial – interglacial contrast in sedimentation rate in core SO18471 over the last ~130 ka (3-6 cm ky^{-1} during MIS 5 and the Holocene in contrast to 11-17 cm ky^{-1} between MIS 4 and 2) (Fig. 3.3f) supports a decrease in terrigenous input during sea level highstands.

An exception to this glacial – interglacial trend is evident during MIS 5e, when higher terrigenous input and sedimentation rate in comparison to the Holocene suggest that the regional monsoon signal overrides the sea level effect (Figs. 3f and 4d). At this time Northern Hemisphere summer insolation was high (Fig. 3.6e) causing melting of northern ice sheets and consequently promoting slowdown in the Meridional Overturning Circulation, which in turn generated cold anomalies in the North Atlantic [*Broecker et al.*, 1985; *McManus et al.*, 1999; *Cheng et al.*, 2009]. This may have resulted in a southern displacement of the ITCZ [*Wang et al*., 2004; *Chiang et al.*, 2005; *Broccoli et al.*, 2006; *Mohtadi et al*., 2011; *Carolin et al*., 2013; *Huang et al*., 2015] and warming of the Southern Hemisphere and Antarctica [*Petit et al*., 1999; *Pépin et al.*, 2001]. Warmer Southern Hemisphere and Antarctica may have amplified local monsoon forcing [*Petit et al.*, 1999; *Pépin et al.*, 2001] by increasing heat and moisture supply to the atmosphere, eventually resulting in wet conditions and thus higher terrigenous input at the core location during MIS 5e (Fig. 3.4d). This is in agreement with a recent study proposing increased rainfall over southern Indonesia and northern Australia during Termination II [*Huang et al.*, 2015].

3.5.2 Variations in the ITF intensity over the last 130 ka

Both grain size proxies records, the log(Zr/Rb) and proportion of coarse (>63μm) material, show a strong glacial – interglacial trend, which mirrors the terrigenous input record (Fig. 3.4). Coarser material prevailed during sea level highstands (MIS 5 and 1), when core SO18471 was in a more distal location from land, and finer sediments dominated during sea level lowstands (MIS 4 and 2) (Figs. 4b, c and e). This unusual pattern likely reflects the effect of sediment winnowing by intensified bottom currents during sea level highstands, whereas at times of low sea level weaker bottom currents were unable to transport clays away (Figs. 4b, c and e). Given the location and relatively shallow water depth of core SO18471, these variations in bottom current activity are plausibly related to changes in ITF intensity. Slight discrepancies between the two grain size proxies records during MIS 5b and MIS 5a (Figs. 4b and c) may reflect changes in the abundance of shell bearing organisms, which are not expressed in the log(Zr/Rb). An exception to this glacial – interglacial trend is evident during MIS 5e, when both grain size proxies records captured low values, comparable with low sea level rather than high sea level values (Figs. 4b, c and e). A possible explanation is that the local monsoon signal overrides the sea level effect, as seen for the terrigenous input record (Fig. 3.4d). It is possible that an intensification of the local monsoon led to a strong increase in riverine discharge of clay minerals (Fig. 3.4d) and decreased proportion of coarse material (low log(Zr/Rb)) at the location of core SO18471 (Figs. 4b and c).

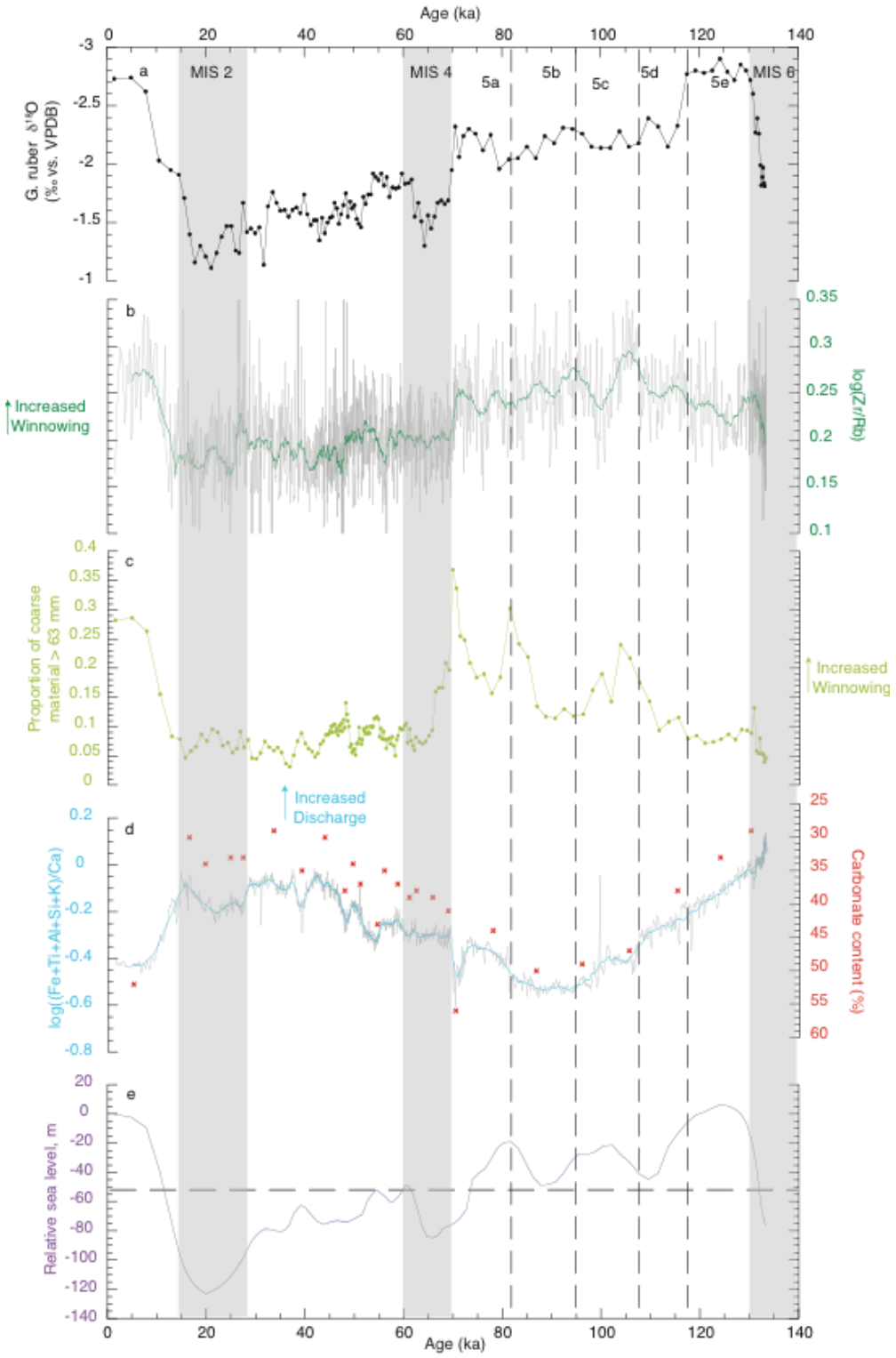

Fig. 3.4. a) *G. ruber* $\delta^{18}O$ record in core SO18471. **b)** XRF-derived grain size record. **c)** Proportion of coarse fraction >63µm. **d)** XRF-derived terrigenous input record (light blue curve); red crosses indicate measured carbonate content. **e)** Sea level curve from *Waelbroeck et al.* [2002] adjusted to chronology of core SO18471; dashed line at -53 m indicates depth of Arafura Sill. Gray shadings mark glacial periods MIS 6, 4 and 2; dashed black lines mark onset of MIS 5 sub-stages.

3.5.3 Hydrological variability during the last glacial cycle

3.5.3.1 Long-term variability

Surface and lower thermocline temperature and $\delta^{18}O_{sw}$ records show a glacial – interglacial trend: the surface is generally warmer (on average by ~2 °C) and saltier during globally warm periods (MIS 5a-d and 1), whereas the lower thermocline is generally cooler (on average by ~1.4 °C) and fresher than during globally cold periods (from MIS 4 to MIS 2) (Figs. 5 and 6). This most likely reflects the intensification and expansion of a cool and fresh thermocline ITF during sea level highstands (Figs. 4b and c), resulting in generally cool and fresh bottom waters at the core location (Figs. 6c and d). In contrast, the thermocline shoaled between MIS 4 and 2, when bottom waters became warmer and saltier at the location of core SO18471 (Figs. 6c and d). However, early MIS 5e exhibits relatively warm lower thermocline temperatures (~11 °C) and no clear freshening signal in the benthic $\delta^{18}O_{sw}$ (Figs. 6c and d), indicating a more contracted thermocline ITF (Figs. 4b and c).

Sprintall et al. [2009] highlighted the importance of the contribution of warm and salty Indian Ocean waters, reaching the Banda Sea via the Ombai and Timor straits, in participating in the formation of the modern ITF outflow into the Indian Ocean. *Holbourn et al.* [2011] tracked the evolution of water masses in the Timor Sea over the past 140 ka and found that during globally cold periods the deeper, cool and fresh, ITF outflow in the Timor Sea was reduced and the influence of warm and salty Indian Ocean water became

increasingly dominant. In core SO18471, we found a warmer and saltier lower thermocline flow (Fig. 3.6c and d) synchronous with periods of reduced ITF intensity (Figs. 4b and c), supporting advection of warmer and saltier Indian Ocean waters at the core location.

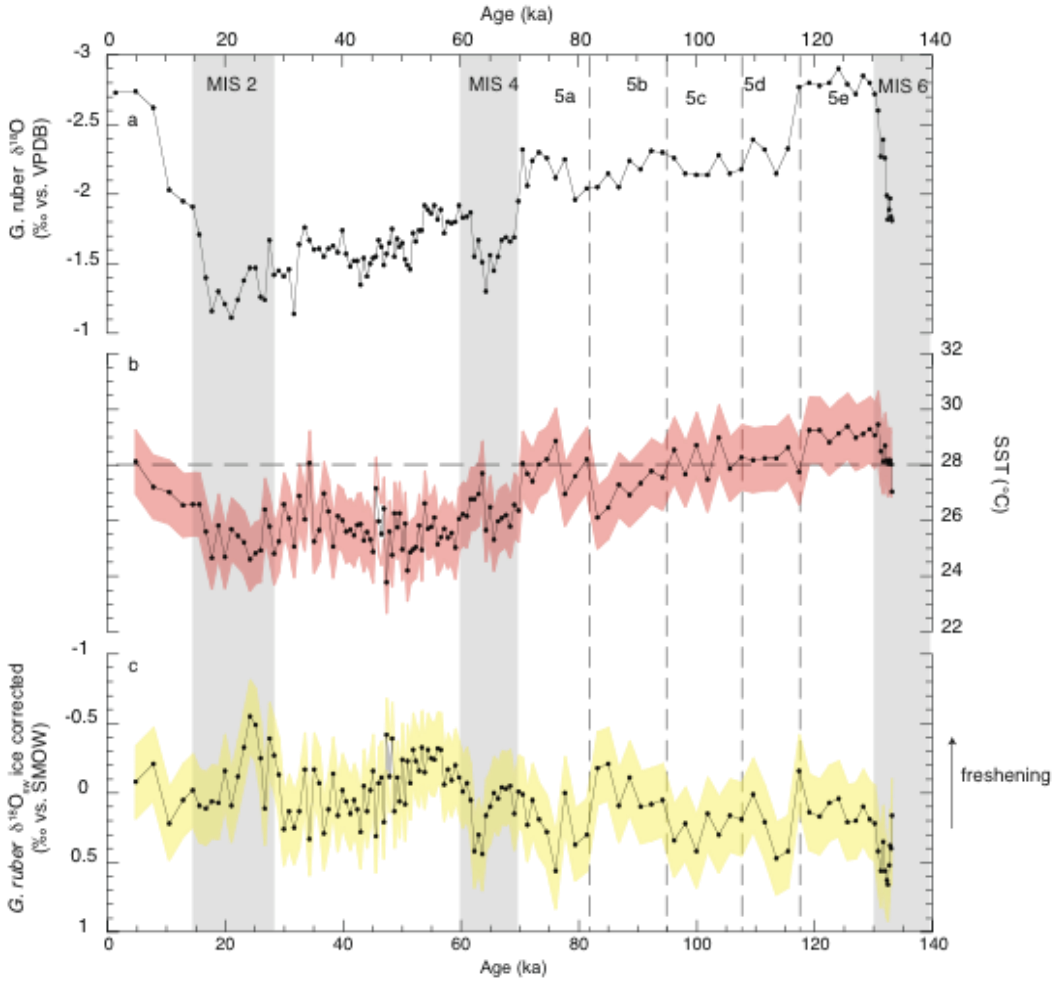

Fig. 3.5. a) *G. ruber* $\delta^{18}O$ record. **b)** *G. ruber* Mg/Ca-derived sea surface temperature in core SO18471 (black curve); dashed line indicates modern sea surface temperature [*Locarnini et al*., 2006]. **c)** *G. ruber* $\delta^{18}O_{sw}$ record. Gray shadings mark glacial periods MIS 6, 4 and 2; dashed black lines mark onset of MIS 5 sub-stages.

3.5.3.2 Summer monsoon intensification during MIS 3 and MIS 2?

The substantial freshening of surface water at 56-50 ka and 28-23 ka during the early part of MIS 3 and MIS 2 (Fig. 3.5c) suggests transient intensifications of the austral summer monsoon. This was a period of globally cold SSTs with a significant reduction in the extension of the Indo Pacific Warm Pool (IPWP) and in the heat and vapor supply from the sea to the atmosphere [*De Deckker and Yokoyama*, 2009; *Wang et al.*, 1999]. During the LGM, SSTs were ~3 to 4 °C colder than during the Holocene on the Ontong Java Plateau [*Lea et al*., 2000], in the Makassar Strait [*Visser et al*., 2003], in the Timor Sea [*Xu et al*., 2008] and at the core location (Fig. 3.5b). However, speleothem records from Flores and NW Australia [*Lewis et al.*, 2011; *Ayliffe et al.*, 2013; *Denniston et al*., 2013] and marine sediment records from the Timor Sea and the western Banda Sea [*Muller et al*., 2008; *Kuhnt et al*., 2015] support a southern displacement of the ITCZ during the early part of MIS 2 that would account for freshening of surface waters at the location of core SO18471 (Fig. 3.5c) and relatively wet conditions in the southern tropics [*Reeves et al.*, 2013]. Increased precipitation might have resulted in more stratified waters, with a freshwater cap at the core location (Fig. 3.5c), and in alteration of the vertical structure of the ITF (Figs. 6c and d).

An alternative view is that surface freshening during the early part of MIS 3 and MIS 2 in the Timor Strait may be related to regional hydrological changes. In the IPWP, *G. ruber* $\delta^{18}O_{sw}$ has been interpreted as a proxy for large-scale oceanic variations in vapor supply to the atmosphere and excess precipitation over evaporation [e.g.: *Oppo et al*., 2007; *Gibbons et al.*, 2014; *Fraser et al.*, 2014]. However, the comparison of core SO18471, retrieved in proximity of the Sahul Shelf, with two Timor Sea records from more distal locations (cores SO18460 and MD01-2378, Fig. 3.2) [*Holbourn et al.*, 2011]

suggests that local forcings drive SST and salinity variability at location of core SO18471 (Supplementary Figs. 3.4a and b).

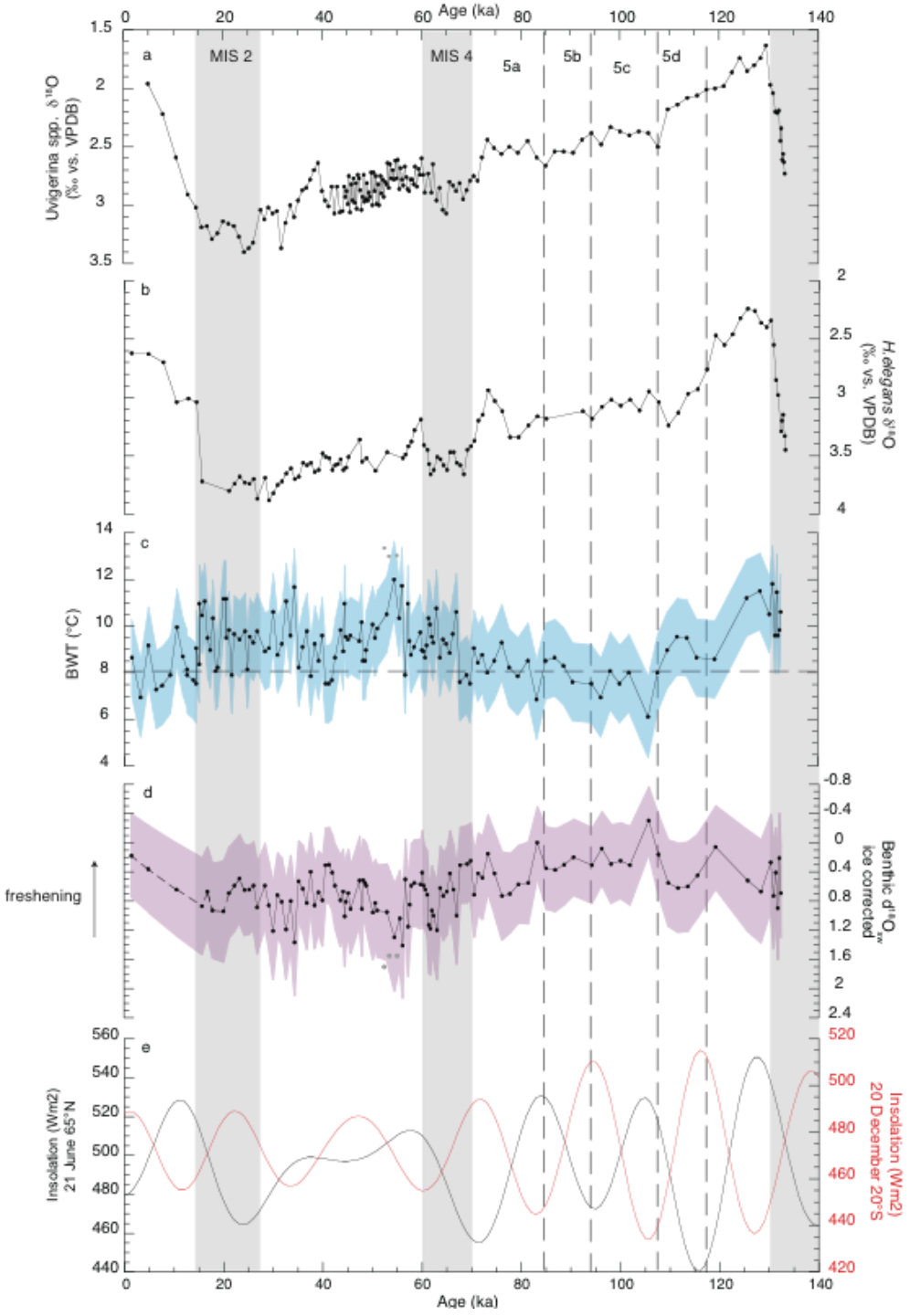

Fig. 3.6. a) *Uvigerina* spp. $\delta^{18}O$ record in core SO18471. **b)** *H. elegans* $\delta^{18}O$ record. **c)** *H. elegans* Mg/Ca-derived bottom water temperature; dashed line indicates modern temperature at 500 m [*Locarnini et al*., 2006]. **d)** Benthic $\delta^{18}O_{sw}$ record in core SO18471. **e)** Summer solstice insolation at 65°N (black line) and 20°S (red line) [*Laskar et al.*, 2004]. Gray shadings mark glacial periods MIS 6, 4 and 2; dashed black lines mark onset of MIS 5 sub-stages.

3.5.3.3 Influence of far-field high-latitude climate events

To explain the warming of intermediate water in the Makassar Strait and Flores Sea during the early Holocene maximum in Northern Hemisphere summer insolation (~10 ka), *Rosenthal et al*. [2013] hypothesized that warming in the ITF source waters at higher latitudes is transferred at intermediate depth in the tropics. Thermocline warming at ~10 ka is also recorded in upper and lower thermocline records in the Timor Sea (Fig. 3.6c and Supplementary Fig. 3.4c). Warming of the upper and lower thermocline during the early part of MIS 5e (Fig. 3.6c and Supplementary Fig. 3.4c) also coincides with the highest Northern Hemisphere summer insolation of the past 140 kyr (Fig. 3.6e). However, BWTs are higher during early MIS 5e (~11 °C) than the early Holocene (~10 °C) (Fig. 3.6c), most likely due to the higher Northern Hemisphere summer insolation during MIS 5e (Fig. 3.6e). Additionally, a temporal shutdown in the formation of Antarctic bottom water between 128 and 125 ka [*Hayes et al.*, 2014] may have contributed to warming of the lower thermocline in core SO18471 during MIS 5e and to the thermal contrast between the early MIS 5e and early Holocene (Fig. 3.6c).

3.6. Conclusion

Our records from sediment core SO18471, retrieved at the southern edge of the Timor Strait, close to the Sahul Shelf, provide new insights into local hydrological changes

related to ITF variations, changes in the local monsoon system and shelf dynamics during the last 130 ka. Our results indicate that sediment winnowing and terrigenous discharge were largely controlled by glacial – interglacial sea level changes, with reduced discharge and strong bottom currents (ITF) during sea level highstands. However, increased terrigenous input together with weakening and warming of the ITF lower thermocline flow suggest intensification of the local wet monsoon during MIS 5e. The warmer and saltier thermocline between MIS 4 and MIS 2 indicates weakening and contraction of the cool and fresh thermocline ITF and advection of warm and salty Indian Ocean waters into the Timor Strait. High Northern Hemisphere summer insolation during the early MIS 5e and early Holocene additionally appears to have influenced thermocline temperature in the Timor Strait through warming of ITF source waters at higher latitudes.

Acknowledgements

We are grateful to Dieter Garbe-Schönberg for ICP-OES measurements and Nils Andersen for stable isotopes analyses. We thank Yiming Wang for stimulating discussions and constructive suggestions. We also gratefully acknowledge the crew of the R/V *Sonne* for all their efforts during the SO-185 VITAL cruise. Funding for this research was provided by the Marie Curie Action Plan, Seventh Framework Program (Grant n° 237922) and BMBF Grant 03G0185A (VITAL). Data presented in this paper are archived and available at www.pangaea.de.

References

Alongi, D. M., M. da Silva, R. J. Wasson, and S. Wirasantosa (2013), Sediment discharge and export of fluvial carbon and nutrients into the Arafura and Timor Seas: a regional synthesis, *Marine Geology*, *343*, 146-158, doi: 10.1016/j.margeo.2013.07.004.

Anand, P., H. Elderfield, and M.H. Conte (2003), Calibration of Mg/Ca thermometry in planktonic foraminifera from sediment trap time series, *Paleoceanography*, *18*(2), 1050, doi: 10.1029/2002PA000846.

Ayliffe, L. K., M. K. Gagan, J. Zhao, R. N. Drysdale, J. C. Hellstrom, W. S. Hantoro, M. L. Griffiths, H. Scott-Gagan, E. St Pierre, J. A. Cowley, and B. W. Suwargadi (2013), Rapid interhemispheric climate links via the Australasian monsoon during the last deglaciation, *Nature communications*, 4, 2908, doi: 10.1038/ncomms3908.

Beaufort, L., S. van der Kaars, F. C. Bassinot, and V. Moron (2010), Past dynamics of the Australian monsoon: precession, phase and links to the global monsoon concept, *Climate of the Past*, *6*, 695-706, doi: 10.5194/cp-6-695-2010.

Bemis, B. E., H. J. Spero, J. Bijma, and D. W. Lea (1998), Reevaluation of the oxygen isotopic composition of planktonic foraminifera: Experimental results and revised paleotemperature equations, *Paleoceanography*, *13*(2), 150-160, doi: 10.1029/98PA00070.

Brink, K. H., and R. K. Shearman (2006), Bottom boundary layer flow and salt injection from the continental shelf to slope, *Geophysical Research Letters*, *33*, L13608, doi: 10.1029/2006GL026311.

Brink, K. H., F. Bahr, and R. K. Shearman (2007), Alongshore currents and mesoscale variability near the shelf edge off northwestern Australia, *Journal of Geophysical Research, 112*, C05013, doi: 10.1029/2006JC003725.

Broccoli, A.J., K.A. Dahl, and R.J. Stouffer (2006), Response of the ITCZ to Northern Hemisphere cooling, *Geophysical Research Letters*, 33, L01702, doi: 10.1029/2005GL024546.

Broecker, W.S., D.M. Peteet, and D. Rind (1985), Does the ocean-atmosphere system have moree than one stable mode of operation?, *Nature*, 315, 21-26.

Calvert, E., and T. Pedersen (2007), Elemental proxies for palaeoclimatic and palaeoceanographic variability in marine sediments: interpretation and application, C. Hillaire-Marcel, A.D. Vernal (Eds.), *Proxies in Late Cenozoic Paleoceanography*, Elsevier, Amsterdam, pp. 567–644, doi: 10.1016/S1572-5480(07)01019-6.

Carolin, S. A., K. M. Cobb, J. F. Adkins, B. Clark, J. L. Conroy, S. Lejau, J. Malang, and A. Tuen (2013), Varied response of western Pacific hydrology to climate forcings over

the last glacial period, *Science*, 340, 1564-1567, doi: 10.1026/science.1233797.

Cheng, H., L. Edwards, W. S. Broecker, G. H. Denton, X. Kong, Y. Wang, R. Zhang, and X. Wang (2009), Ice age terminations, *Science*, *326*, 5950, 248-252, doi: 10.1126/science.1177840

Chiang, J. C. H., and C. M. Bitz (2005), Influence of high latitude ice cover on the marine Intertropical Convergence Zone, *Climate Dynamics*, 25, 5, 477-496, doi: 10.1007/s00382-005-0040-5.

Cresswell, G., A. Frische, J. Peterson, and D. Quadfasel (1993), Circulation in the Timor Sea, *Journal of Geophysical Research*, *98*(C8), 14379-14389, doi: 10.1029/93JC00317.

De Deckker, P., and Y. Yokoyama (2009), Micropaleontological evidence for Late Quaternary sea-level changes in Bonaparte Gulf, Australia, *Global and Planetary Change*, 66, 85-22, doi:10.1016/j.gloplacha.2008.03.012.

Denniston, R. F., K-H. Wyrwoll, Y. Asmerom, V. J. Polyak, W. F. Humphreys, J. Cugley, D. Woods, Z. LaPointe, J. Peota, and E. Greaves (2013), North Atlantic forcing of millennial-scale Indo-Australian monsoon dynamics during the Last Glacial period, *Quaternary Science Reviews*, 72, 159-168, doi: 10.1016/j.quascirev.2013.04.012.

de Villiers, S., M. Greaves, and H. Elderfield (2002), An intensity ratio calibration

method for accurate determination of Mg/Ca and Sr/Ca of marine carbonates by ICP-AES, *Geochemistry, Geophysics, Geosystems*, *3*(1), 1001, doi: 10.1029/2001GC000169.

Ding, X., F. Bassinot, F. Guichard, and N. Q. Fang (2013), Indonesian Throughflow and monsoon activity records in the Timor Sea since the last glacial maximum, *Marine Micropaleontology, 101*, 115-126, doi: 10.1016/j.marmicro.2013.02.003.

Egbert, G. D., R. D. Ray (2001), Estimates of M_2 tidal energy dissipation from TOPEX/Poseidon altimeter data, *Journal of Geophysical Research*, 106(C10), 22475-22502, doi: 10.1029/2000JC000699.

Ffield, A. L., and A. L. Gordon (1992), Vertical Mixing in the Indonesian Thermocline, *Journal of Physical Oceanography*, *22*(2), 184-195.

Fraser, N., W. Kuhnt, A. Holbourn, T. Bolliet, N. Andersen, T. Blanz, and L. Beaufort (2014), Precipitation variability within the West Pacific Warm Pool over the past 120 ka: evidence from the Davao Gulf, southern Philippines, *Paleoceanography*, 29, doi: 10.1002/2013PA002599.

Gibbons, F. T., D. W. Oppo, M. Mothadi, Y. Rosenthal, J. Cheng, Z. Liu, B. K. Linsley (2014), Deglacial $\delta^{18}O$ and hydrological variability in the tropical Pacific and Indian Ocean, *Earth and Planetary Science Letters*, 387, 240-251, http://dx.doi.org/10.1016/j.epsl.2013.11.032.

Gordon, A. L., and R. A. Fine (1996), Pathway of water between the Pacific and Indian oceans in the Indonesian seas, *Nature, 379*, 146-149, doi: 10.1038/379146a0.

Gordon, A. L., and R. D. Susanto (2001), Banda Sea surface-layer divergence, *Ocean Dynamics*, 52, 2-10, doi: 10.1007/s10236-001-8172-6.

Gordon, A. L. (2005), Oceanography of the Indonesian seas and their throughflow, *Oceanography*, *18*(4), 14-27, http://dx.doi.org/10.5670/oceanog.2005.01.

Grootes, P.M., M.-J. Nadeau, A. Rieck (2004), ^{14}C-AMS at the Leibniz-Labor: radiometric dating and isotope research, *Nuclear Instruments and Methods in Physics Research B, 223-224*, 55-61.

Hautala, S.L., J.L. Reid, and N. Bray (1996), The distribution and mixing of Pacific water masses in the Indonesian Seas, *Journal of Geophysical Research*, 101,C5, 12375-12389, doi: 10.1029/96JC00037.

Hayes, C. T., A. Martínez-García, A. P. Hasenfratz, S. L. Jaccard, D. A. Hodell; D. M. Sigman, G. H. Hang, R. F. Anderson (2014), A stagnation event in the deep South Atlantic during the last interglacial period, *Science, 346,* 1514, doi: 10.1126/science.1256620.

Holbourn, A., W. Kuhnt, and J. Xu (2011), Indonesian Throughflow variability during the last 130 ka: the Timor Sea outflow, The SE Asian gateway: history and tectonics of Australia-Asia collision, Geological Society, London, Special Publications, *355*, 283-303, doi: 10.1144/SP355.14.

Huang, E., J. Tian, and J. Liu (2015), Dynamics of the Australian-Indonesian monsoon across Termination II: implications of molecular biomarker reconstructions from the Timor Sea, *Palaeogeography, Palaeoclimatology, Palaeoecology*, 423, 32-43, doi: 10.1016/j.palaeo.2015.01.027.

Koch-Larrouy, A., M. Lengaigne, P. Terray, G. Madec, and S. Masson (2010), Tidal mixing in the Indonesian Seas and its effect on the tropical climate system, *Climate Dynamics, 34*, 891-904, doi: 10.1007/s00382-009-0642-4.

Kuhnt, W., et al. (2005), Cruise report SONNE-185 "Variability of the Indonesian Throughflow and Australasian climate history of the last 150000 years (VITAL)", report, Institut für Geowissenschaften, Christian-Albrechts-Universität zu Kiel, Kiel, Germany.

Kuhnt, W., A. Holbourn, J. Xu, B. Opdyke, P. De Deckker, U. Röhl, and M. Mudelsee (2015), Southern Hemisphere control on Australian monsoon variability during the late deglaciation and Holocene, Nature Communications, *6*, 5916, doi: 10.1038/ncomms6916.

Laskar, J., P. Robutel, F. Joutel, M. Gastineau, A C. M. Correeia, and B. Levrard (2004),

A long-term numerical solution for the insolation quantities of the Earth, *Astronomy and Astrophysics*, 428, 261-285, doi: 10.1051/0004-6361:20041335.

Lea, D. W., D. K. Pak, and H. J. Spero (2000), Climate Impact of Late Quaternary equatorial Pacific sea surface temperature variations, *Science, 289*, 1719, doi: 10.1126/science.289.5485.1719.

Lewis, S.C., M.K. Gagan, L.K. Ayliffe, J-X. Zhao, W.S. Hantoro, P.C. Treble, J.C. Hellstrom, A.N. LeGrande, M. Kelley, G.A. Schmidt, and B.W. Suwargadi (2011), High-resolution stalagmite reconstructions of Australian-Indonesian monsoon rainfall variability during Heinrich stadial 3 and Greenland interstadial 4, *Earth and Planetary Science Letters*, 303, 133-142, doi: 10.1016/j.epsl.2010.12.048.

Linsley, B.K., Y. Rosenthal, and D.W. Oppo (2010), Holocene evolution of the Indonesian throughflow and the western Pacific warm pool, *Nature Geoscience, 3*, 578-583, doi: 10.1038/NGEO920.

Locarnini, R. A., A. V. Mishonov, J. I. Antonov, T. P. Boyer, and H. E. Garcia (2006), World Ocean Atlas 2005, Volume 1: temperature. *In*: Levitus S. (ED.) *NOAA Atlas NESDIS61*. U.S. Government Printing Office, Washington, DC, 182.

Lo Giudice Cappelli, E., M. Regenberg, A. Holbourn, W. Kuhnt, D. Garbe-Schönberg, and N. Andersen (2015), Refining *C. wuellerstorfi* and *H. elegans* Mg/Ca temperature

calibrations, *Marine Micropaleontology*, 121, 70-84, doi: 10.1016/j.marmicro.2015.10.001.

Lourens, L. J., R. Wehausen, H. J. Brumsack (2001), Geological constraints on tidal dissipation and dynamical ellipticity of the Earth over the past three million years, *Nature, 409,* 1029–1033, doi:10.1038/35059062.

Marchitto, T.M., W.B. Curry, J. Lynch-Stieglitz, S.P. Bryan, K.M. Cobb, and D.C. Lund (2014), Improved oxygen isotope temperature calibrations for cosmopolitan benthic foraminifera, *Geochimica et Cosmochimica Acta, 130*, 1-11, doi: 10.1016/j.gca.2013.12.034.

Martin, P.A., and D. Lea (2002), A simple evaluation of cleaning procedures on fossil benthic foraminiferal Mg/Ca, *Geochemistry, Geophysics, Geosystems, 3*(10), 8401, doi: 10.1029/2001GC000280.

McManus, J.F., D.W. Oppo, and J.L. Cullen (1999), A 0.5-million-year record of millennial-scale climate variability in the North Atlantic, *Science*, 283, 5404, 971-975, doi: 10.1126/science.283.5404.971.

Mohtadi, M., D. W. Oppo, S. Steinke, J-B W. Stuut, R. De Pol-Holz, D. Hebbeln, and A. Lückge (2011), Glacial to Holocene swings of the Australian-Indonesian monsoon, *Nature Geoscience*, 4, 540-544, doi: 10.1038/NGEO1209.

Mohtadi, M., M. Prange, D. W. Oppo, R. De Pol-Holz, U. Merkel, X. Zhang, S. Steinke, and A. Lückge (2014), North Atlantic forcing of tropical Indian Ocean climate, *Nature*, *509*, 76-80, doi: 10.1038/nature13196.

Moore, T. S., J. Marra, and A. Alkatari (2003), Response of the Banda Sea to the southeast monsoon, *Inter-Research Marine Ecology Progress Series*, 261, 41-49, doi: 10.3354/meps261041.

Müller, G., and M. Gastner (1971), The "Karbonat-Bombe", a simple device for the determination of carbonate content in sediments, soils, and other materials, *Neues Jahrbuch für Mineralogie – Monatshefte*, *10*, 466-469.

Muller, J., M. Kylander, R. A. J. Wüst, D. Weiss, A. Martinez-Cortizas, A. N. LeGrande, T. Jennerjahn, H. Behling, W. T. Anderson, and G. Jacobson (2008), Possible evidence for wet Heinrich phases in tropical NE Australia: the Lynch's Crater deposit, *Quaternary Science Reviews*, 27, 468-475, doi:10.1016/j.quascirev.2007.11.006.

Nadeau, M.-J., M. Schleicher, P.M. Grootes, H. Erlenkeuser, A. Gottdang, D.J.W. Mous, J.M. Sarnthein, and H. Willkomm (1997), The Leibniz-Labor AMS facility at the Christian-Albrechts University, Kiel, Germany, *Nuclear Instruments and Methods in Physics Research B*, *123*, 22-30.

Oppo, D. W., G.A. Schmidt, and A.N. LeGrande (2007), Seawater isotope constrains on tropical hydrology during the Holocene, *Geophysical Research Letters*, 34, L13701, doi: 10.1029/2007GL030017.

Oppo, D.W., and Y. Rosenthal (2010), The Great Indo-Pacific Communicator, *Science*, *328*, 1492-1494, doi: 10.1126/science.1187273.

Pépin, L., D. Raynaud, J-M. Barnola, and M. F. Loutre (2001), Hemispheric roles of climate forcings during glacial-interglacial transitions as deduced from the Vostock record and LLN-sD model experiments, *Journal of Geophysical Research*, 106(23), 31885-31892, doi: 10.1029/2001JD900117.

Petit, J. R., J. Jouzel, D. Raynaud, N. I., Barkov, J.-M. Barnola, I. Basile, M. Bender, J. Chappellaz, M. Davis, G. Delaygue, M. Delmotte, V. M. Kotlyakov, M. Legrand, V. Y. Lipenkov, C. Lorius, L. Pépin, C. Ritz, E. Saltzman, and M. Stievenard (1999), Climate and atmospheric history of the past 420,000 years from the Vostock ice core, Antarctica, *Nature, 399*, 429-436, doi:10.1038/20859.

Ray, R. D., G. D. Egbert, and S. Y. Erofeeva (2005), A brief overview of tides in the Indonesian seas, *Oceanography*, *18*(4), 74-79,http://dx.doi.org/10.5670/oceanog.2005.07.

Reeves, J. M., A. R. Chivas, A. García, S. Holt, M. J. J. Couapel, B. G. Jones, D. I. Cendón, and D. Fink (2008), The sedimentary record of palaeoenvironments and sea-

level change in the Gulf of Carpentaria, Australia, through the last glacial cycle, *Quaternary International, 183,* 3-22, doi: 10.1016/j.quaint.2007.11.019.

Reeves, J.M., H.C. Bostock, L.K. Ayliffe et al. (2013), Palaeoenvironmental change in tropical Australasia over the last 30,000 years – a synthesis by the OZ-INTIMATE group, *Quaternary Science Reviews,* 74, 97-114, doi: 10.1016/j.quascirev.2012.11.027.

Regenberg M., A. Regenberg, D. Garbe-Schönberg, and D. W. Lea (2014), Global dissolution effects on planktonic foraminiferal Mg/Ca ratios controlled by the calcite-saturation state of bottom waters, *Paleoceanography,* 29, 127-142, doi: 10.1002/2013PA002429.

Reimer, P. J., et al. (2013), IntCal13 and Marine13 radiocarbon age calibration curves 0-50,000 years cal BP, *Radiocarbon,* 55, 1869-1887, doi: 10.2458/azu_js_rc.55.16947.

Rosenthal, Y., B. K. Linsley, D. W. Oppo (2013), Pacific ocean heat content during the past 10,000 years, *Science, 342,* 617, doi: 10.1126/science.1240837.

Ryan, W. B. F., et al. (2009), Global Multi-Resolution Topography synthesis, *Geochemistry Geophysics Geosystems, 10,* Q03014, doi: 10.1029/2008GC002332.

Shearman, R. K., and K. H. Brink (2010), Evaporative dense water formation and cross-shelf exchange over the northwest Australian inner shelf, *Journal of Geophysical*

Research, 115, C06027, doi: 10.1029/2009JC005931.

Schiller, A. (2011), Ocean Circulation on the North Australian Shelf, *Continental Shelf Research, 31*, 1087-1095, doi: 10.1016/j.csr.2011.03.013.

Schlitzer, R., Ocean Data View, http://odv.awi.de, 2013.

Southon, J., M. Kashgarin, M. Fontugne, B. Metivier, and W. W-S. Yim (2002), Marine reservoir corrections for the Indian Ocean and Southeast Asia, *Radiocarbon*, 44, 167-180.

Spooner, M. I., T. T. Barrows, P. De Deckker, and M. Paterne (2005), Paleoceanography of the Banda Sea, and Late Pleistocene initiation of the Northwest Monsoon, *Global and Planetary Change*, *49*, 28-46, doi: 10.1016/j.gloplacha.2005.05.002.

Sprintall, J., S. E. Wijffels, R. Molcard, and I. Jaya (2009), Direct estimates of the Indonesian Throughflow entering the Indian Ocean: 2004-2006, *Journal of Geophysical Research, 114*, C07001, doi: 10.1029/2008JC005257.

Stuiver, M., and P. J. Reimer (1993), Extended 14C database and revised CALIB radiocarbon calibration program, *Radiocarbon*, 35, 215-230.

Talley, L. D., and J. Sprintall (2005), Deep expression of the Indonesian Throughflow: Indonesian Intermediate Water in the South Equatorial Current, *Journal of Geophysical*

Research, 110, C10009, doi: 10.1029/2004JC002826.

Veres, D., et al. (2013), The Antarctic ice core chronology (AICC2012): an optimized multi-parameter and multi-site dating approach for the last 120 thousand years, *Climate of the Past*, 9, 1733-1748, doi: 10.5194/cp-9-1733-2013.

Visser, K., R. Thunell, and L. Stott (2003), Magnitude and timing of temperature change in the Indo-Pacific warm pool during deglaciation, *Nature*, 421, 152-155, doi:10.1038/nature01297.

Waelbroeck, C., L. Labeyrie, E. Michel, J. C. Duplessy, J. F. McManus, K. Lambeck, E. Balbon, and M. Labracherie (2002), Sea-level and deep water temperature changes derived from benthic foraminifera isotopic record, *Quaternary Science Reviews, 21*, 295-305, http://dx.doi.org/10.1016/S0277-3791(01)00101-9.

Wang, P. (1999), Response of Western Pacific marginal seas to glacial cycles: paleoceanographic and sedimentological features, *Marine Geology, 156*, 5-39.

Wang, X., A. S. Auler, R. L. Edwards, H. Cheng, P. S. Cristalli, P. L. Smart, D. A. Richards, and C-C Shen (2004), Wet periods in northeastern Brazil over the past 210 kyr linked to distant climate anomalies, *Nature*, 432, doi:10.1038/nature03067.

Weltje, G. J., and R. Tjallingii (2008), Calibration of XRF core scanners for quantitative

geochemical logging of sediment cores: theory and application, *Earth and Planetary Science Letters, 274*(3), 423-438, doi: 10.1016/j.epsl.2008.07.054.

Wijffels, S. E., G. Meyers, J. S. Godfrey (2008), A 20-Yr Average of the Indonesian Throughflow: Regional Currents and the Interbasin Exchange, *Journal of Physical Oceanography*, 38, 1965-1978, doi: 10.1175/2008JPO3987.1.

Xu, J., W. Kuhnt, A. Holbourn, N. Andersen, and G. Bartoli (2006), Changes in the vertical profile of the Indonesian Throughflow during Termination II: evidence from the Timor Sea, *Paleoceanography, 21*, PA4202, doi: 10.1029/2006PA001278.

Xu, J., A. Holbourn, W. Kuhnt, Z. Jian, and H. Kawamura (2008), Changes in the thermocline structure of the Indonesian outflow during Terminations I and II, *Earth and Planetary Science Letters, 273*, 152-162, doi: 10.1016/j.epsl.2008.06.029.

Žuvela-Aloise, M. (2005), Modelling of the Indonesian Throughflow on glacial-interglacial timescales, Ph.D thesis, Mathematisch-Naturwissenschaftliche Fakultät, Christian-Albrechts-Universität zu Kiel, Germany.

3.7 Supplementary Material

Bottom water temperature correction for glacial – interglacial sea level changes

When reconstructing BWT over time, it is important to consider to what extent variations in sea level would affect temperature estimations. The water depth of sediment core SO18471 substantially changed between glacial and interglacial periods, being ~365 m during the LGM (against a modern day water depth of 485 m), following the sea level curve of *Waelbroeck et al.* [2002]. Based on the present day difference of ~1 °C between *in situ* CTD-measured BWT at 365 m and at 485 m, we assumed that a decrease of 120 m in sea level during the LGM would result in a 1 °C increase in bottom water temperature at the core location (Supplementary Fig. 3.1). Thus, the sea level effect on BWT reconstruction is relatively small, within the temperature calibration error. However, this estimate is based on the unrealistic assumption that water masses are stable through time and that the present gradient of 1 °C between BWT at 365 and 485 m remained unchanged over time.

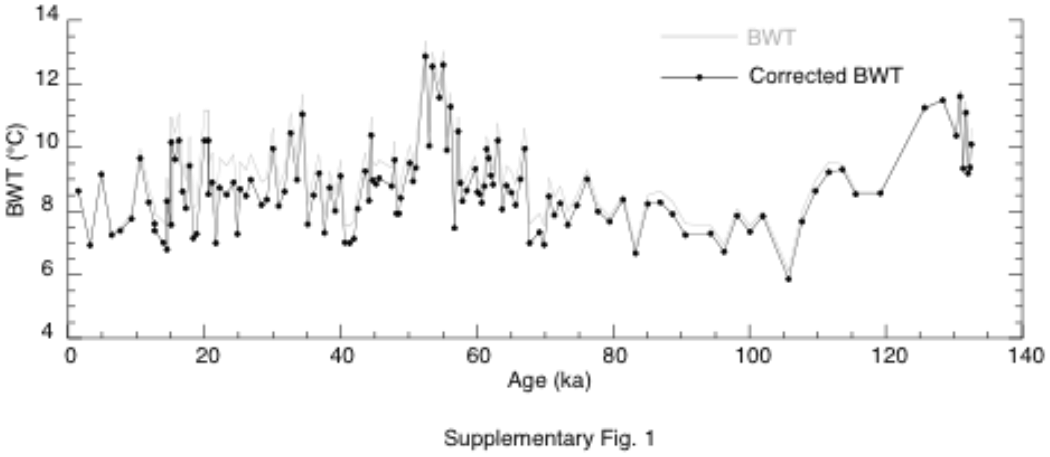

Supplementary Fig. 3.1. Mg/Ca derived bottom water temperatures (gray line) and BWT corrected for glacial – deglacial sea level changes (black line). Following the sea level curve of *Waelbroeck et al.* [2002], we estimated that the water depth of core SO18471 was ~365 m during the LGM in contrast to the modern water depth of 485 m. As the difference between CTD-measured BWT at 365 m and at 485 m is ~1°C, a decrease of 120 m in sea level during the LGM would result in a 1°C increase in temperature at the seafloor.

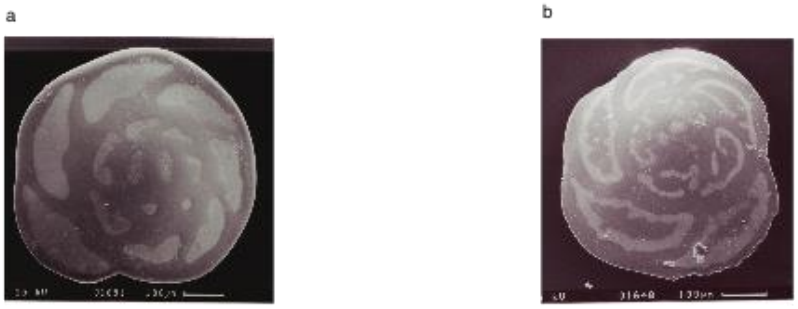

Supplementary Fig. 3.2. a) Well preserved *H. elegans*, representative of the majority of specimens in core SO18471. **b)** Thin-walled morphotype of *H. elegans* found in one interval of core SO18471, where the overall abundance of *H. elegans* was low.

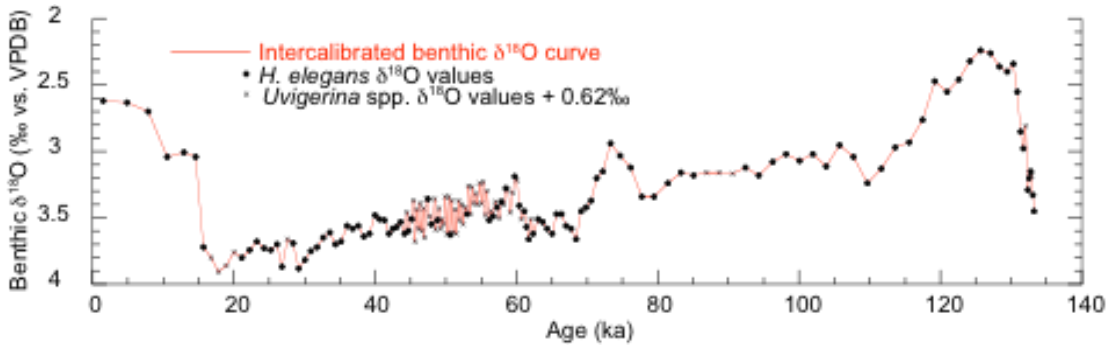

Supplementary Fig. 3.3. Intercalibrated benthic $\delta^{18}O$ record (red curve) based on the analysis of *Uvigerina* spp. and *Hoeglundina elegans* in core SO18471. Solid black circles indicate *H. elegans* $\delta^{18}O$ measurements while black crosses indicate *Uvigerina* $\delta^{18}O$ measurements corrected by +0.62‰.

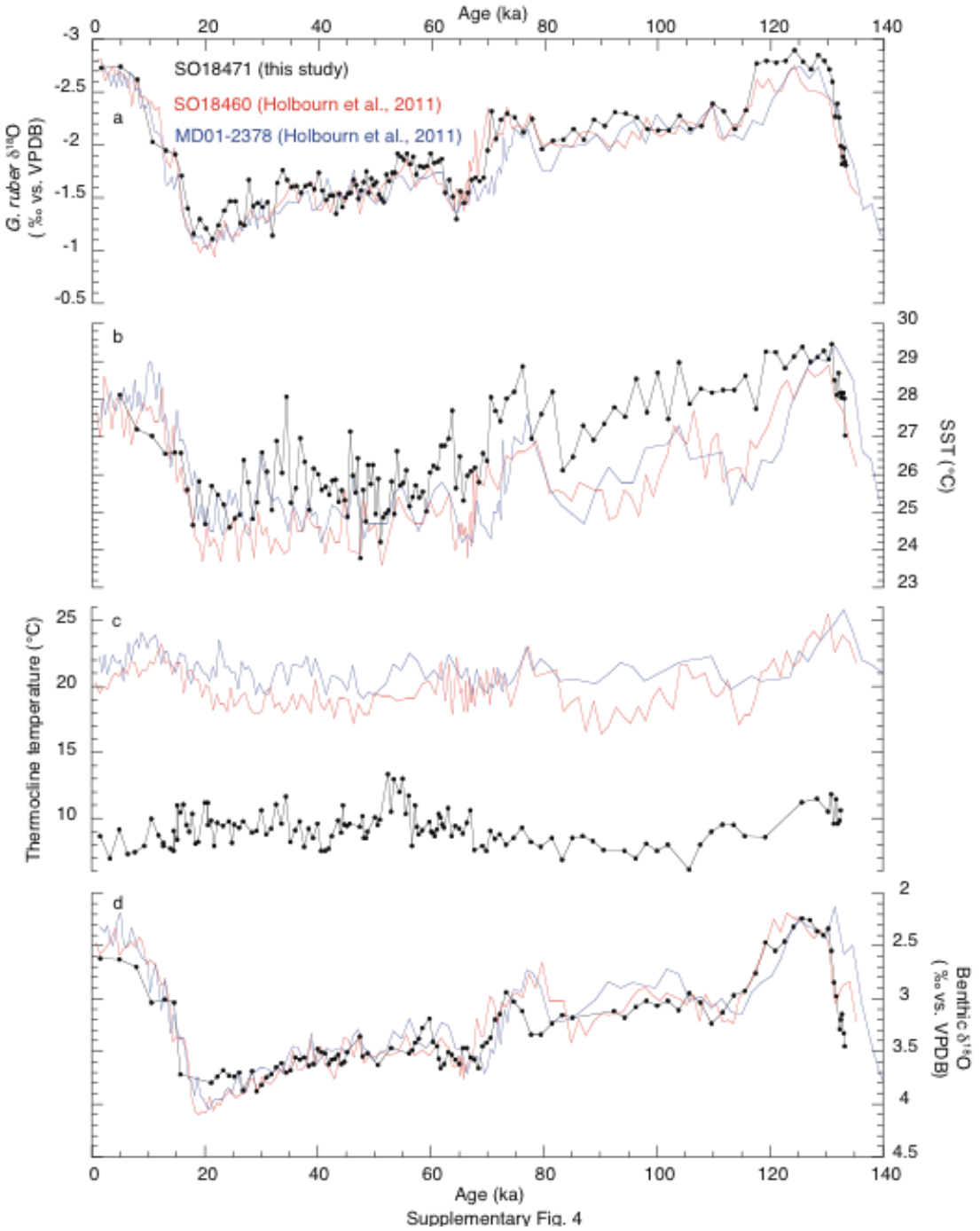

Supplementary Fig. 3.4. Core SO18471 was retrieved at the northern edge of the Timor Strait close to the Sahul Shelf; core SO18460 is located within the ITF outflow in the Timor Strait and core MD01-2378 is situated in the southwestern Timor Sea within the mixing zone with Indian Ocean thermocline waters. **a)** *Globigerinoides ruber* $\delta^{18}O$

records in cores SO18471, SO18460 and MD01-2378. **b)** Sea surface temperatures. **c)** Upper and lower thermocline temperatures. **d)** Benthic $\delta^{18}O$ records.

References

Waelbroeck, C., L. Labeyrie, E. Michel, J. C. Duplessy, J. F. McManus, K. Lambeck, E. Balbon, and M. Labracherie (2002), Sea-level and deep water temperature changes derived from benthic foraminifera isotopic record, *Quaternary Science Reviews, 21*, 295-305, http://dx.doi.org/10.1016/S0277-3791(01)00101-9.

Chapter 4

Geochemical proxies of sea surface temperature in the tropical West Pacific: insights from modern core tops

Nicholas Fraser, **Elena Lo Giudice Cappelli**, Marcus Regenberg, Wolfgang Kuhnt, Ann Holbourn, Thomas Blanz.

Abstract

Precise quantification of past changes in sea surface temperature (SST) in tropical regions is hampered by uncertainties in the relationship between SST and geochemical proxy records. In this study, we compile new and previously published core top measurements of two commonly used proxies of SST, the Mg/Ca ratio of the planktonic foraminifera *Globigerinoides ruber* (n = 146), and the $U^{K'}_{37}$ alkenone unsaturation index (n = 107), from the South China Sea, Makassar Strait, Java Sea, Timor Sea and eastern Indian Ocean. Measurements were compared with modern satellite-derived temperature and productivity data to gain insights into their modern relationships with SST, with a particular focus on seasonal bias recorded by the two proxies. $U^{K'}_{37}$ measurements show an expected positive correlation with mean annual sea surface temperatures (maSST) ($U^{K'}_{37}$ = 0.322 + 0.022maSST, R^2 = 0.55), but a lower sensitivity to temperature than has been documented in global core-cop calibrations, consistent with a 'flattening' of the $U^{K'}_{37}$-SST relationship at temperatures exceeding 24 °C. Raw Mg/Ca measurements show a higher sensitivity to maSST (Mg/Ca = $0.111e^{0.131T}$, R^2 = 0.54) than previous calibrations would suggest, although the sensitivity is reduced when samples are corrected for variable inter-laboratory cleaning procedures (Mg/Ca_{cor} = $0.335e^{0.091T}$, R^2 = 0.45), highlighting the uncertainties associated with analytical procedures of Mg/Ca-based SST reconstructions. Regressions of both Mg/Ca and $U^{K'}_{37}$ measurements with monthly satellite-derived SSTs document stronger correlations of both proxies with winter and spring SSTs, although correlations are not statistically stronger than with maSST. Analysis of residual SST patterns show that $U^{K'}_{37}$ SST estimates over-estimate maSST in regions of strong seasonal temperature variability, such as in the Java

upwelling region and Timor Sea. Mg/Ca residual SST patterns show a less clear seasonal pattern, and are likely influenced significantly by secondary effects, including carbonate ion saturation states and salinity. Mg/Ca SST estimates from the South China Sea in particular tend to under-estimate SST, in response to calcite undersaturation in this region.

4.1 Introduction

Paleoclimate records of sea surface temperature (SST) are commonly reconstructed from the use of the coccolithophore-based alkenone unsaturation index, $U^{K'}_{37}$, or the Mg/Ca ratio of the surface-dwelling planktonic foraminifera *Globigerinoides ruber*. However, the use of these proxies relies on the understanding of a number of processes which may bias reconstructed SST records towards warmer or cooler temperatures, including (but not limited to): (1) The preferential growth of foraminifera or coccolithophores in a particular season/period of the year. (2) Variability in depth habitats of foraminifera or coccolithophores. (3) Mixing of proxy signals via lateral advection of particles or bioturbation of deposited sediment. (4) Diagenetic alteration of signals during post-depositional processes (e.g. carbonate dissolution). (5) Biological inclusion of $U^{K'}_{37}$ and Mg/Ca signals into coccolithophores and foraminifera, including species-specific (and inter-species) variability. Thus, attributing a proxy measurement to a specific temperature signal requires careful consideration of these effects, including potential spatial and temporal variability.

The $U^{K'}_{37}$ paleothermometer is an organic biomarker proxy, based upon the proportions of the di- and tri-unsaturated C_{37} methyl alkenones produced in the

surface ocean by coccolithophores, principally *Emiliania huxleyi* and *Gephyrocapsa oceanica* [*Brassell et al.,* 1986], where the $C_{37:2}$ alkenone is favorably produced at high temperatures. Modern calibrations of $U^{K'}_{37}$ to SST have been made through comparison of core top and sediment trap measurements with modern surface-water properties derived from climatological atlases [e.g. *Sonzogni et al.,* 1997a, b; *Pelejero and Grimalt,* 1997; *Müller et al*., 1998; *Conte et al.,* 2006], and through laboratory culture experiments [e.g. *Prahl and Wakeham*, 1987; *Prahl et al*., 1988]. In recent paleoclimate studies, the most widely applied $U^{K'}_{37}$ calibrations are the global linear core top calibration of *Müller et al*. [1998], and the polynomial calibration of *Conte et al.* [2006] which attempts to account for the potential 'flattening' of the $U^{K'}_{37}$-T relationship at warm (>24 °C) and cool (<10 °C) temperatures. At the warm end of the calibration spectrum (24 - 30 °C), both of these core top calibrations are indistinguishable, within error ranges, from the culture-derived regressions of *Prahl et al.* [1988].

These existing $U^{K'}_{37}$ core top calibrations are typically made through direct correlation between measured $U^{K'}_{37}$ values and mean annual SST (maSST) at various water depths, and exhibit a decrease in correlation coefficients below 50 m water depth, suggesting that alkenone-producers are limited to the photic zone [*Müller et al*., 1998; *Pelejero and Grimalt,* 1997; *Kienast et al.,* 2012]. Other calibrations have attempted to weight the observed temperature signal to a seasonal preference through the preferential weighting of SST towards months of higher productivity, which is assumed to correlate to the months of dominant alkenone-producing coccolithophore blooms [e.g. *Sonzogni et al*., 1997b]. However, more recent studies in regions of highly variable productivity regimes along the West Coast of North and South

America observe that SSTs recorded in coretop-$U^{K'}_{37}$ samples are biased towards the months of weak upwelling and low nutrient availability [*Prahl et al.*, 2010; *Kienast et al.*, 2012]. Thus, a seasonal weighting of SST towards months of high productivity may not be suitable for calibration purposes. Furthermore, a recent global compilation of alkenone fluxes in sediment traps reveals no statistical difference in the $U^{K'}_{37}$ calibration slope when using flux-weighted SSTs versus maSSTs [*Rosell-Melé and Prahl*, 2013].

The basis for the use of Mg/Ca ratios as a paleotemperature proxy relies upon the thermodynamically favorable substitution of Mg^{2+} for Ca^{2+} in the calcium carbonate shells of planktonic foraminifera at higher temperatures. As with the $U^{K'}_{37}$ index, a range of modern calibrations have been made via measurements of foraminifera from core tops, sediment traps and culture experiments, which provide a range of sensitivities of foraminiferal Mg/Ca to temperature [*Nürnberg et al*., 1996; *Lea et al.*, 1999; *Lea et al.*, 2000; *Dekens et al.*, 2002; *Anand et al.*, 2003; *Regenberg et al.*, 2009]. The exact mechanisms responsible for differences in Mg/Ca calibrations is still controversial, but recent studies have proposed that alteration of foraminiferal Mg/Ca can occur through the variable effects of salinity [*Hönisch et al.*, 2013], pH [*Kisakürek et al.*, 2008] and postdepositional dissolution driven by ($[CO_3^{2-}]$) concentrations [*Regenberg et al.*, 2006, 2014]. A potential advantage of the Mg/Ca paleothermometer is that measurements can be paired with oxygen isotope ($\delta^{18}O$) measurements on the same foraminiferal samples, which may give further insights into the regional habitat depths and seasonality of individual species [e.g. *Regenberg et al.*, 2006; *Steph et al.*, 2009; *Mohtadi et al.*, 2011]. However, differing $\delta^{18}O$-temperature and $\delta^{18}O$-salinity relationships used in deriving expected equilibrium

calcite $\delta^{18}O$ values can induce considerable uncertainty into these methods, which are further compounded by low-quality salinity and seawater $\delta^{18}O$ ($\delta^{18}O_{sw}$) data in some regions. Such a problem is particularly prevalent in the tropical West Pacific. Consequently, the most reliable method of determining the seasonal patterns of foraminiferal growth in this region remains through the use of sediment traps [e.g. *Wiesner et al*., 1996; *Kawahata et al.,* 2002; *Mohtadi et al.,* 2009], though these are also only sparsely distributed.

The importance of understanding different seasonal signals recorded in proxies has been underlined by several studies comparing $U^{K'}_{37}$ and Mg/Ca-derived SST trends over the last deglacial period and Holocene [e.g. *Mix et al.,* 2006; *Steinke et al*., 2008; *Saher et al.,* 2009; *Schneider et al.,* 2010; *Wang et al*., 2013; *Laepple et al.,* 2013; *Timmermann et al.,* 2014]. In the tropical West Pacific, both $U^{K'}_{37}$ and Mg/Ca reconstructions show reasonable agreement on the magnitude of deglacial warming between 2 and 4 ° C [e.g. *Pelejero et al.,* 1999; *Kienast et al*., 2001; *Stott et al.,* 2002, 2007; *Rosenthal et al*., 2003; *Visser et al*., 2003; *Steinke et al*., 2008; *Fraser et al.,* 2014], with lower sensitivity (1 - 1.5 °C) recorded in one $U^{K'}_{37}$ record located close to Papua New Guinea [*De Garidel-Thoron et al.,* 2007]. However, more significant differences in the timing and evolution of deglacial SST change have been noted between the two proxies. SST records derived from Mg/Ca typically begin to rise in concert with southern hemisphere warming between 17 and 18 ka, with a relatively uninterrupted trend to a peak warmth at ~8 ka, and a cooling trend (by 0.5 to 1 °C) through the Holocene. In contrast, $U^{K'}_{37}$ SST records suggest the onset of warming occurred later, between 15 and 16 ka, and are interrupted by a SST plateau or slight cooling during the Bølling-Allerød (BA) and Younger Dryas (YD) periods.

From the end of the YD, $U^{K'}_{37}$ records document a relatively steadily increasing SST trend through the Holocene, in contrast to Mg/Ca records. A recent proxy-model comparison of East and West Pacific deglacial SST trends finds support for the effect of different seasonal sensitivities, and past changes in the strength of the seasonal cycle, in driving these proxy mismatches [*Timmermann et al.*, 2014]. Increasing our understanding of the modern day production of coccolithophores and foraminifera, and the potential temperature bias this may induce, is therefore an important step in assessing how these relationships may have changed in the past.

In this study, we attempt to provide insights into factors affecting the $U^{K'}_{37}$ index and Mg/Ca ratios of *G. ruber* in the tropical West Pacific. In the first part of our following discussion, we take a first-order approach to reconstructing seasonality of proxy recorders, by comparing measured $U^{K'}_{37}$ and Mg/Ca values to satellite-derived SST and net primary productivity (NPP) climatologies. In the second part of our discussion, we investigate additional factors that may affect proxy records of SST in this region. Lastly, we discuss the potential impacts these results have on existing paleotemperature records from the West Pacific, and make recommendations for future investigations.

4.2 Study area and modern climatology

This study focuses on core top measurements from the South China Sea [*Pelejero and Grimalt*, 1997; *Regenberg et al*., 2014], the Eastern Indian Ocean including the west coast of Sumatra and south coast of Java [*Mohtadi et al.*, 2011], and the Makassar, Java and Timor Seas (new measurements of this study).

Seasonality of SSTs in this region is broadly characterized by the latitudinal variations in the insolation cycle, i.e. samples in the northern hemisphere are characterized by warmer SSTs during boreal summer, and vice versa in the southern hemisphere (Figure 4.1). More central regions that lie within a few degrees of the equator (e.g. the Makassar Strait, and western Sumatra in this study) generally show a weaker seasonal SST cycle than those at higher latitudes (< 5 °N). These seasonal SST patterns drive associated wind and precipitation changes, which also have an influence on NPP (Figure 4.1). Whilst the West Pacific is generally characterized by oligotrophic conditions, in some areas such as southern Java, the eastern Timor Sea and the northern South China Sea, seasonal wind directions induce upwelling resulting in a stronger seasonal cycle of SST and NPP.

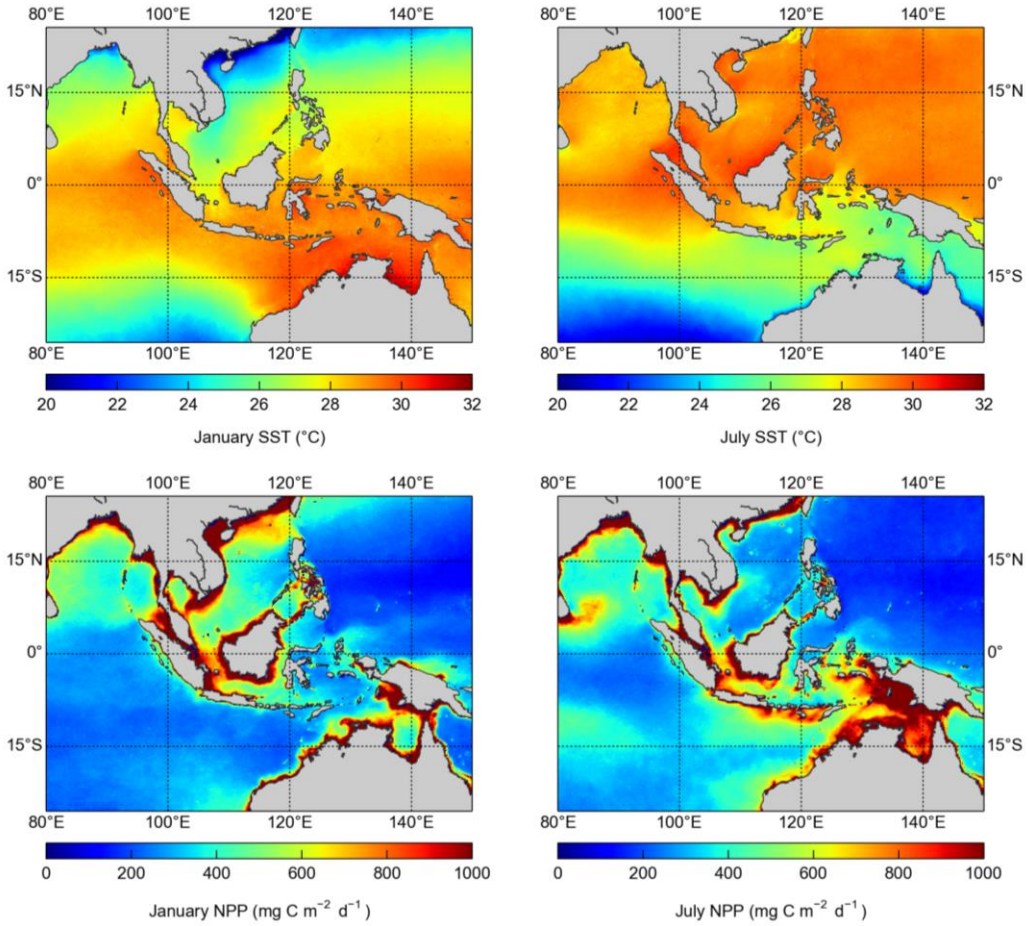

Figure 4.1 - (top) SST derived from the Advanced Very High Resolution Radiometer (AVHRR) satellite climatology [*Reynolds et al.*, 2007] during January (left) and July (right). (bottom) NPP calculated from the Vertically Generalized Production Model (VPGM) using the Sea-viewing Wide Field-of-View Season (SeaWiFS) chlorophyll product [*Behrenfeld et al.*, 2006] during January (left) and July (right).

Attempts to quantify the modern seasonal export fluxes of coccolithophores and foraminifera in the West Pacific have been made through a handful of sediment trap studies. In the northern South China Sea, coccolithophores show the highest flux rates during the boreal winter and spring, where assemblages are dominated by the alkenone-producing species *E. huxleyi* and *G. oceanica* [*Wiesner et al.*, 1996; *Chen et al.*, 2007], whilst the central South China Sea is characterized by maximum coccolithophore fluxes in late boreal spring and summer [*Wiesner et al.*, 1996]. Maximum fluxes of *G. ruber* in the South China Sea occurred at similar times as

coccolithophore maxima, with maximum fluxes in the north during boreal winter, and in the central basin during late boreal summer [*Wiesner et al*., 1996]. Sediment traps in the West Caroline Basin, to the north of New Guinea in the open West Pacific, show maximum coccolithophore fluxes during the boreal fall and winter, though the seasonal variability is markedly weaker than in the South China Sea [*Tanaka and Kawahata*, 2001]. However, anti-phased signals of *E. huxleyi*, which shows maximum abundances in boreal winter, and *G. oceanica*, which shows maximum abundances in boreal summer, mean that the seasonal export pattern of alkenones is unclear. At the same location in the West Caroline Basin, the largest fluxes of *G. ruber* are observed between August and October [*Kawahata et al.*, 2002]. A similar pattern of *G. ruber* fluxes is also noted in the Java upwelling zone, with peak abundances occurring between July and November during the main upwelling season [*Mohtadi et al*., 2011], which may indicate a cold-bias in SST recorded by *G. ruber* in this region.

4.3 Data and Methods

4.3.1 Materials and sampling strategy

New $U^{K'}_{37}$ and Mg/Ca measurements in this study were made on multi-cores and piston cores gathered on two cruises - the Sonne-185 'VITAL' cruise in the Timor Sea which took place in September and October 2005 [*Kuhnt et al.*, 2005], and the Sonne-217 'MAJA' cruise in the Makassar Strait and Java Sea which took place in July and August 2011 [*Kuhnt et al*., 2011] (Figure 4.2). Mg/Ca measurements were made on core top (0-1 cm) samples from multi-cores retrieved at a range of depths between ~300 m and ~2500 m. Due to the procedure of storing multi-core samples in

Rose Bengal and ethanol solution, these core tops were unsuitable for $U^{K'}_{37}$ analyses, which were instead made on core tops (0-1 cm) from piston cores.

4.3.2 Age control

Age control of existing core top datasets compiled here are documented fully in their respective publications. Samples from the Eastern Indian Ocean are assumed to be predominantly of a modern age, on the basis of the presence of an intact organic fluff layer on most multicore samples [*Mohtadi et al*., 2011]. Those samples that did not have such a layer were submitted for AMS ^{14}C dating, which recorded modern calendar ages (>1950 AD) in all but four samples, the oldest of which recorded an age of ~830 BP. These older ages are attributed to lower sedimentation rates on the outer slope, and stronger bioturbation on the shelf. Core top samples from the South China Sea are assumed to be of a late Holocene age, on the basis of high sedimentation rates (>5 cm/kyr) and the presence of stained benthic foraminifera [*Pelejero and Grimalt*, 1997; *Regenberg et al*., 2010, 2014].

New core top samples derived from multicores in the Timor Sea, Makassar Strait and Java Sea are assumed to represent modern to late Holocene ages, based upon the presence of stained benthic foraminifera and an organic fluff layer on a number of samples [*Kuhnt et al.*, 2011]. Samples derived from piston cores could potentially sample a different time period than multi-core samples, due to disturbance of the upper sediment layer caused by the piston coring system. However, several published and unpublished down-core records based upon these samples document high sedimentation rates (>10 cm/kyr) [e.g *Xu et al*., 2010; *Holbourn et al*., 2011, and references therein] and thus we expect that core top samples from piston cores

document late-Holocene sediments nonetheless.

4.3.3 Mg/Ca

A total of 146 core top Mg/Ca measurements on the planktonic foraminifera *G. ruber* were compiled, from previous core top studies in the South China Sea [*Regenberg et al*., 2014, n = 22], the eastern Indian Ocean [*Mohtadi et al*., 2011, n = 61] and from new measurements made in the Makassar Strait, Java Sea and Timor Sea (n = 63) (Figure 4.2). Analytical methods of previous studies are documented in their respective publications. For new measurements made here, approximately 30 tests of the planktonic foraminifera *G. ruber* were picked from core top (0-1 cm) samples, crushed into fragments under a microscope and checked for potential contaminants. Samples were subsequently cleaned following the established protocol of *Martin and Lea* [2002], including the reductive cleaning step. Samples were analyzed with the ICP-OES (Inductively Coupled Plasma-Optical Emission Spectrometer) (Spectro Ciros SOP) with cooled cyclonic spraychamber and microconcentric nebulization (200 µl min^{-1}) at the Institute of Geosciences, University of Kiel. Intensity ratio calibration followed the method of *de Villiers et al.* [2002] and internal analytical precision was 0.1 - 0.2 %. 24 duplicate measurements give a mean reproducibility of ±0.15 mmol/mol (± ~0.3 °C).

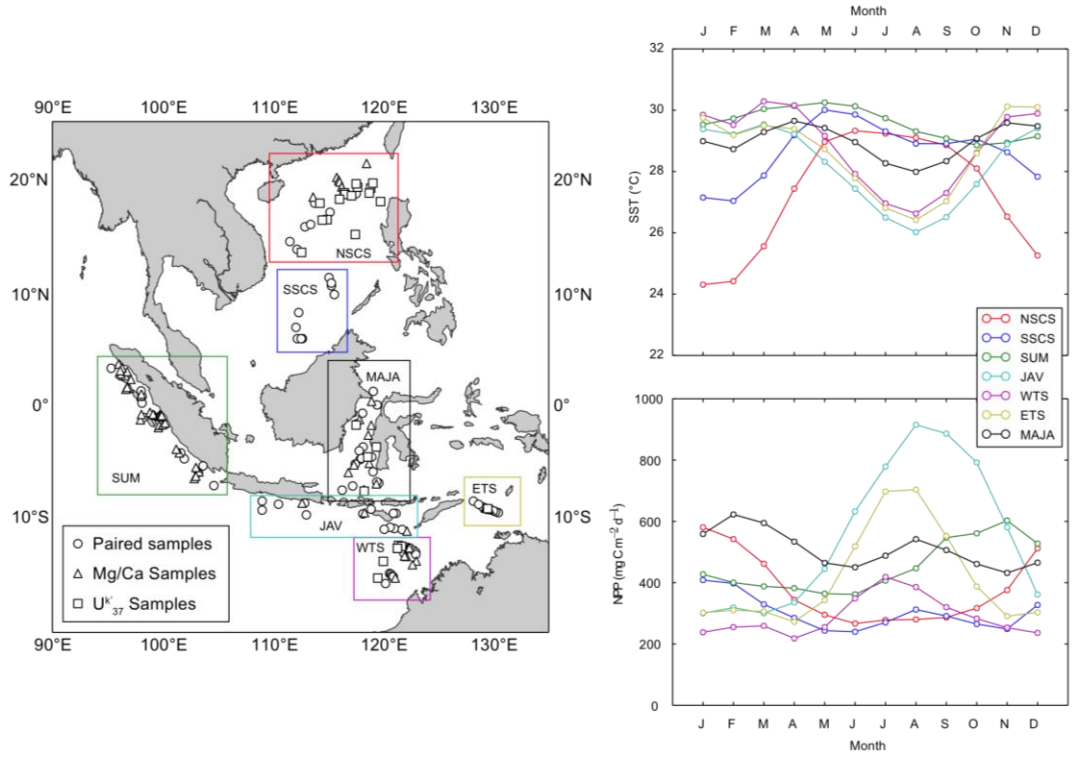

Figure 4.2 - (left) Distribution of Mg/Ca and $U^{K'}_{37}$ measurements compiled from new and existing datasets in this study. Circles represent 'paired' samples where $U^{K'}_{37}$ and Mg/Ca measurements are made at the same location, whilst triangles and squares represent locations where only Mg/Ca or $U^{K'}_{37}$ measurements are made, respectively. Colored boxes represent regions with similar hydrographic properties, abbreviated by: SUM = Coastal Sumatra, JAV = Java Upwelling Zone, WTS = Western Timor Sea, ETS = Eastern Timor Sea, MAJA = Makassar Strait and Java Sea, SSCS = Southern South China Sea, NSCS = Northern South China Sea. (right) Satellite derived monthly SST (top) and NPP (bottom) climatologies for different regions defined on map.

From the South China Sea, we only included measurements from the 300 - 350 µm size fraction (defined as 'Group III' in *Regenberg et al.*, 2014), whilst in the eastern Indian Ocean measurements were from the 250 - 355 µm size fraction [*Mohtadi et al.*, 2011]. For new measurements made in this study, we picked and analysed *G. ruber* from the 250 - 315 µm size fraction. Mg/Ca ratios in *G. ruber* have been suggested to show systematic increases with increasing shell size, as a result of changing habitats during their lifecycle. However, *Elderfield et al.* [2002] show that Mg/Ca differences between the 250 - 300 µm and 300 - 350 µm size fraction are on the order of ~0.1 mmol/mol (equivalent to a change of ~0.2 °C), whilst other studies have found no

significant increases in the Mg/Ca sensitivity of *G. ruber* with increasing size [*Ni et al.,* 2007; *Xu et al.,* 2010]. This likely results from the small amount of Mg/Ca-rich gametogenic calcite added to *G. ruber* tests, in comparison to other planktonic species that add a larger gametogenic crust and show a more pronounced increase in Mg/Ca with increasing test size [e.g. *Globigerinoides sacculifer*, *Ni et al.,* 2007]. Thus, for the purposes of this study we assume that the minor differences in size fractions have no bearing on measured Mg/Ca values.

More pronounced variability in Mg/Ca can result from different analytical methods, particularly with regard to the method of Mg/Ca cleaning used. *Rosenthal et al.* [2004] showed that cleaning samples using the 'reductive step' resulted in a 15% loss of Mg (equivalent to ~1.6 °C cooler temperatures) compared to those cleaned without the reductive step. In core tops compiled in this study, Mg/Ca measurements from the South China Sea, Makassar Strait, Java Sea and Timor Sea were made on reductively cleaned samples. In contrast, samples from the eastern Indian Ocean (i.e. those from the study of *Mohtadi et al.,* 2011) were not reductively cleaned. Thus, we shall also investigate the applicability of such a correction to non-reductively cleaned Mg/Ca samples.

4.3.4 $U^{K'}_{37}$

A total of 107 $U^{K'}_{37}$ measurements were compiled from the same regions as Mg/Ca measurements (South China Sea - *Pelejero and Grimalt* [1997], n = 31; eastern Indian Ocean - *Mohtadi et al.* [2011] n= 26; Makassar Strait, Java and Timor Sea - This study, n = 50) (Figure 4.2). Analytical methods for previously measured $U^{K'}_{37}$ samples are documented in their respective publications [*Pelejero and Grimalt,*

1997; *Mohtadi et al.*, 2011]. New $U^{K'}_{37}$ measurements were made on approximately ~1 g of freeze-dried sediments at the University of Kiel, Germany. The full methodology for sample extraction and measurement is documented in *Rincón-Martínez et al.* [2010]. Analytical precision is better than 0.02 $U^{K'}_{37}$ units (~0.6 °C). The $U^{K'}_{37}$ index was calculated using the ratio of di- and tri-unsaturated C_{37} methyl alkenones, with the formula:

$$U_{37}^{K'} = \frac{C_{37:2}}{C_{37:2} + C_{37:3}}$$

4.3.5 Climatological datasets

Climatologies of SST are obtained from the Advanced Very High Resolution Radiometer (AVHRR), which averages SST measurements over the period January 1985 to December 2002 [*Reynolds et al.*, 2007] on a 4096 by 2048 pixel grid (~9 km resolution at the equator). NPP climatologies are derived from a monthly NPP dataset calculated from the Vertically Generalized Production Model (VPGM) using the Sea-viewing Wide Field-of-View Season (SeaWiFS) chlorophyll product [*Behrenfeld et al.*, 2006], and is averaged over the period September 1997 to August 2006 on a 2160 by 1080 pixel grid (~18 km resolution at the equator). This approach differs from other Mg/Ca and $U^{K'}_{37}$ calibration studies, which typically use climatological data derived from the World Ocean Atlas (WOA) [*Locarnini et al.*, 2013]. However, the resolution of *in situ* SST measurements used to derive WOA climatologies in the West Pacific is poor, and does not resolve shelf and shelf-edge dynamics as well as satellite climatologies (Figure 4.3).

4.4 Results and Discussion

4.4.1 Mg/Ca and $U^{K'}_{37}$ in surface sediments of the West Pacific

New Mg/Ca measurements of *G. ruber* show values ranging from 4.26 to 5.50 mmol/mol (see Supplementary Information). When combined with existing datasets from the South China Sea and eastern Indian Ocean, raw Mg/Ca values show a positive correlation with maSST ($Mg/Ca = 0.111e^{0.131T}$, $R^2 = 0.54$, $p < 0.01$). This temperature sensitivity of ~13% is somewhat higher than has been reported in other Mg/Ca calibration studies, which have sensitivities in the range of 9 to 11 % (Figure

-

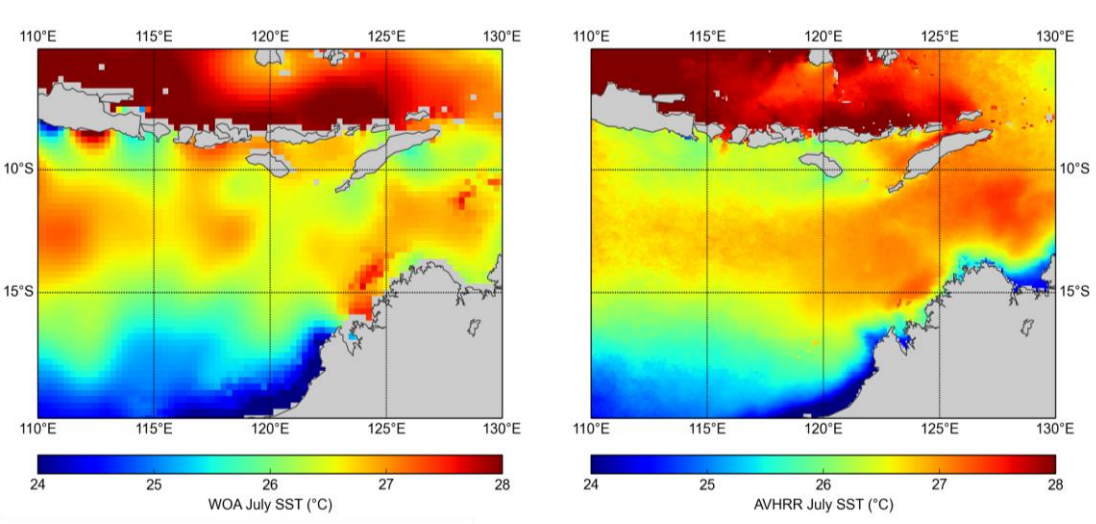

Figure 4.3 - Example of small-scale SST structure captured for a one-month (July) climatology by the World Ocean Atlas (left) [*Locarnini et al.*, 2013] compared AVHRR satellite measurements (right) [*Reynolds et al.*, 2007].

4.4) [*Lea et al.*, 2000; *Dekens et al.*, 2002; *Regenberg et al.*, 2009]. However, correcting Mg/Ca values from the eastern Indian Ocean to account for differences in

cleaning methodology (following the 15 % reduction in Mg/Ca of *Rosenthal et al.* [2004]) results in a lower temperature sensitivity of ~9 % ($Mg/Ca_{cor} = 0.335e^{0.091T}$, $R^2 = 0.45$, $p < 0.01$) (Figure 4.4).

This sensitivity is almost identical to that reported by *Dekens et al.* [2002] and *Lea et al.* [2000], although the two calibrations differ by more than 3 °C in their absolute temperature estimations, whilst our relationship falls between the two. For the remainder of this study, we therefore discuss Mg/Ca in terms of its cleaning-corrected values (Mg/Ca_{cor}), except where it becomes appropriate to discuss the difference between the two datasets. The lowest Mg/Ca_{cor} values are recorded in the South China Sea, with another group of low Mg/Ca_{cor} values observed in the Java upwelling region. In the Makassar Strait, Java Sea, Timor Sea and coastal Sumatra, Mg/Ca values are generally higher but demonstrate significant scatter (upwards of 1 mmol/mol), in excess of the range expected from analytical uncertainty (~0.3 mmol/mol) or intra-region climate variability (typically <1 °C).

New measurements of $U^{K'}_{37}$ range between 0.933 and 0.989 $U^{K'}_{37}$ units (See Supplementary Information). Compiled new and existing $U^{K'}_{37}$ measurements also show a positive correlation with maSST ($U^{K'}_{37} = 0.322 + 0.022$maSST, $R^2 = 0.55$, $p < 0.01$) (Figure 4.5). This relationship has a similar sensitivity to temperature (0.022 units/ °C) as documented in a productivity-weighted calibration from the Indian Ocean (0.023 units/°C - *Sonzogni et al*., [1997b]), and lower sensitivity than documented in

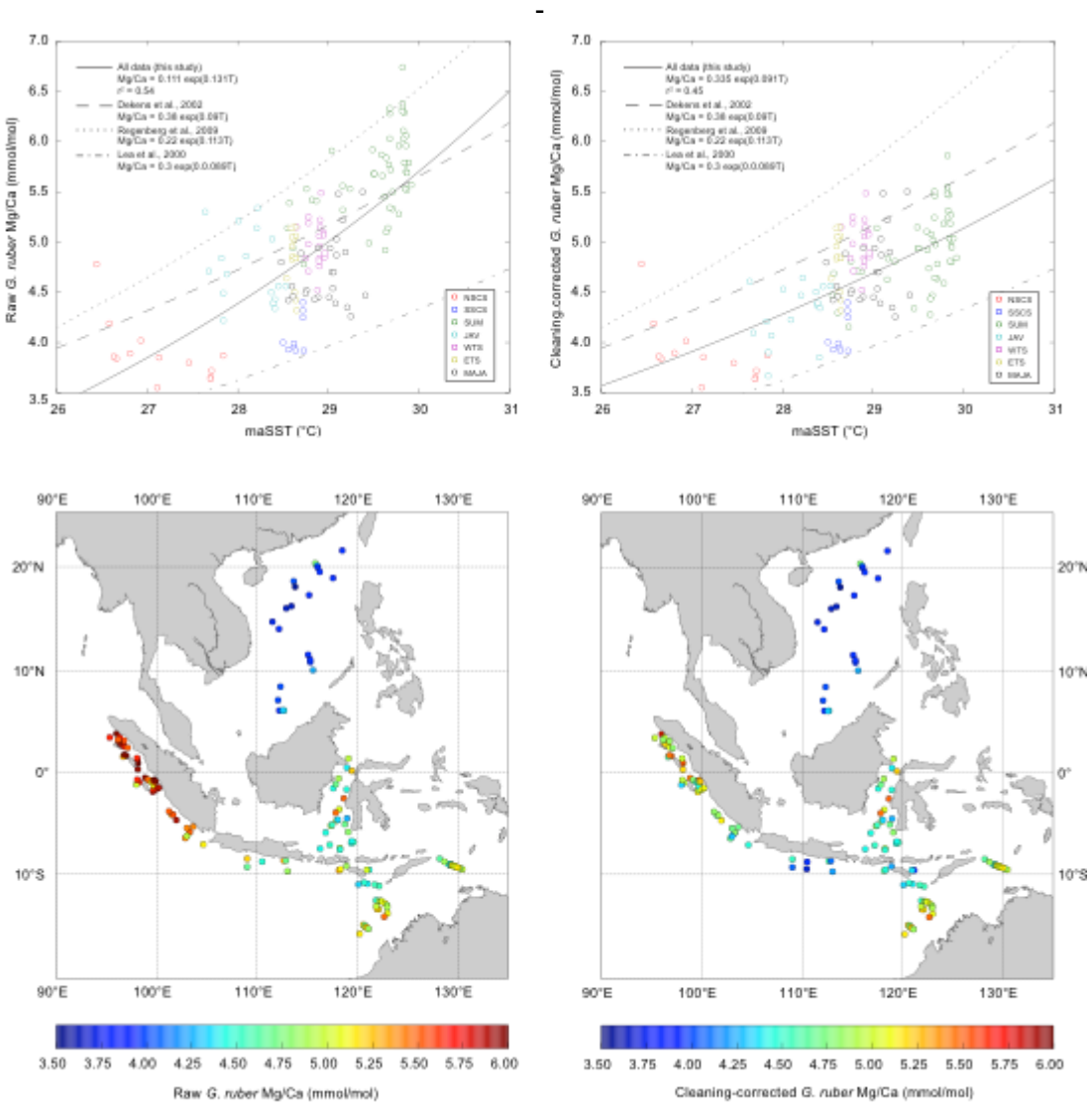

Figure 4.4 - (top) Mg/Ca measurements from compiled datasets versus AVHRR maSST estimates. Raw measurements are shown on the left, and cleaning-corrected measurements on the right. Samples are color-coded based upon regions, following the scheme shown in Figure 5.2. Additional Mg/Ca calibrations are additionally plotted. (bottom) Spatial distribution of raw (left) and cleaning-corrected (right) Mg/Ca measurements.

the two most commonly used global calibrations [*Müller et al.*, 1998; *Conte et al.*, 2006], which both have sensitivities greater than 0.03 units/°C in the warm end of the temperature spectrum. With the exception of several samples from the Java upwelling region, all samples record lower $U^{K'}_{37}$ values than would be predicted using these

global calibrations and maSSTs.

-

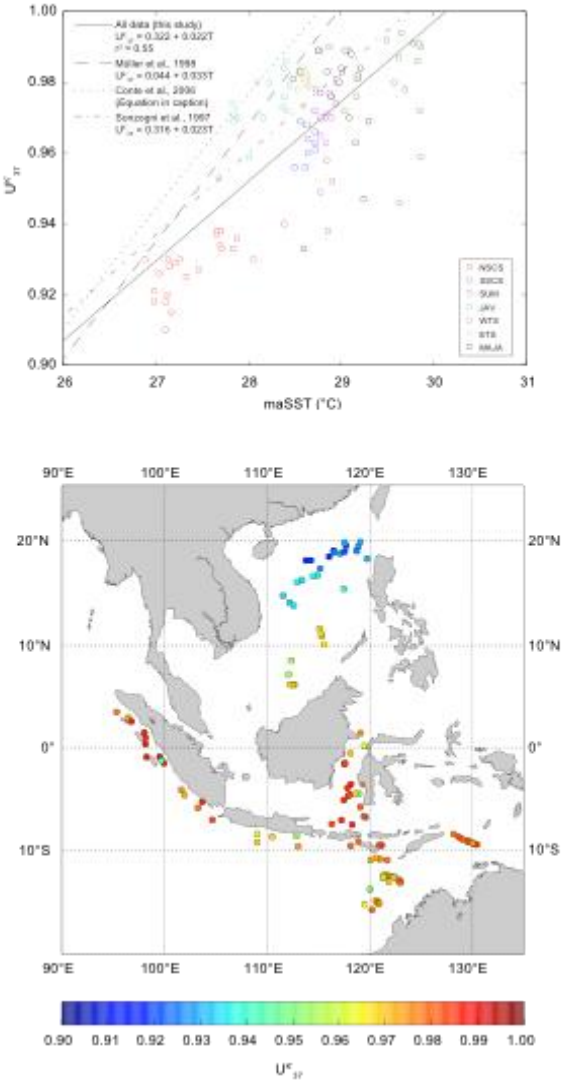

Figure 4.5 - (top) $U^{K'}_{37}$ measurements from compiled datasets versus AVHRR maSST estimates. Samples are color-coded based upon regions, following the scheme shown in Figure 5.2. Additional $U^{K'}_{37}$ calibrations are additionally plotted. (bottom) Spatial distribution of $U^{K'}_{37}$ measurements.

Whilst there are some similarities between the overall spatial distribution of $U^{K'}_{37}$ and Mg/Ca_{cor}, for example generally lower values in the South China Sea, and higher values in the Makassar Strait and coastal Sumatra, there are also some distinct differences between the two sets of measurements. In the South China Sea, Mg/Ca_{cor}

exhibits a relatively uniform spatial SST pattern, whilst $U^{K'}_{37}$ shows a zonal gradient from values of ~0.96 $U^{K'}_{37}$ units in the south, to ~0.91 $U^{K'}_{37}$ units in the north, equivalent to a SST gradient of ~2.0 °C. Additionally, $U^{K'}_{37}$ measurements do not show such prominently low values in the Java upwelling region as seen in Mg/Ca_{cor}, where values are as low as those in the South China Sea. The southern Makassar Strait is also characterized by high $U^{K'}_{37}$ values, which are greater than those in the Timor Sea, whilst Mg/Ca_{cor} indicates the opposite trend of relatively low values in the southern Makassar Strait, and slightly higher values in the Timor Sea.

4.4.2 Seasonal relationships of SST proxies

Figure 4.6 shows derived correlation coefficients of $U^{K'}_{37}$ and Mg/Ca_{cor} when regressed against the SST average of each month, as well as against annual SST (maSST), annual minimum SST (minSST), annual maximum SST (maxSST) and a productivity-weighted SST (nppSST), which is defined by the equation [following *Sonzogni et al.*, 1997b]:

$$nppSST = \frac{\sum_{i=1}^{12} SST_i \cdot NPP_i}{\sum_{i=1}^{12} SST_i}$$

where SST_i and NPP_i are the temperature and net primary productivity of each month, respectively.

Correlation coefficients >0.75 are found for $U^{K'}_{37}$ between November and April, whilst between May and October correlation coefficients are <0.25. Such a strong seasonal pattern is surprising, since a similar approach based upon core tops from the

eastern equatorial Pacific found correlations >0.79 for all months of the year [*Timmermann et al.*, 2014]. However, the correlation between $U^{K'}_{37}$ and maSST (0.74) is not significantly weaker than monthly coefficients found between November and April, and thus the pattern of $U^{K'}_{37}$ could be equally interpreted as a reflection of maSST rather than a monthly or seasonal preference. Despite the division of our samples between the northern and southern hemispheres, and the antiphase-SST relationship observed between the hemispheres, correlation coefficients for $U^{K'}_{37}$ versus minSST or maxSST do

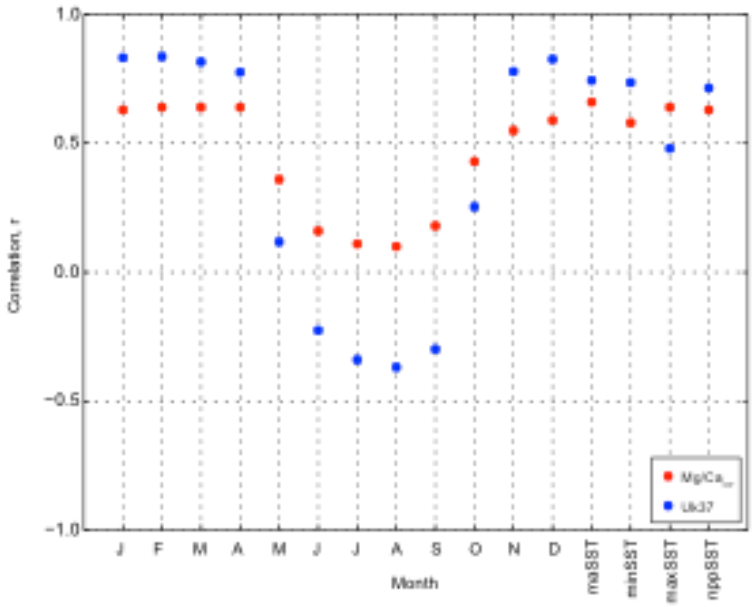

Figure 4.6 - Spatial correlations of $U^{K'}_{37}$ and Mg/Ca_{cor} versus monthly SST, mean annual SST (maSST), annual minimum SST (minSST), annual maximum SST (maxSST) and net primary productivity weighted SST (nppSST).

not exceed coefficients for maSST, which suggests that growth patterns of alkenone producers are not a function of the annual temperature cycle. Productivity weighted SST (nppSST) also shows no improvement in correlation when compared to maSST, indicating that annual growth and export rates of alkenones are not well represented

by a simple linear function of overall surface productivity.

Mg/Ca_{cor} shows a similar correlation pattern to $U^{K'}_{37}$, with the highest correlation coefficients between November and April, and lower coefficients between May and October. However, Mg/Ca_{cor} correlation coefficients show a less pronounced seasonal pattern, with lower values than their $U^{K'}_{37}$ counterparts between November and April (>0.64) and higher between May and October (<0.43), which may indicate a lower sensitivity of Mg/Ca to seasonal temperature variability than $U^{K'}_{37}$. As with $U^{K'}_{37}$, no improvement in correlation coefficients of Mg/Ca are noted with minSST, maxSST or nppSST versus maSST.

4.4.3 Residual patterns of $U^{K'}_{37}$ and Mg/Ca SST

To investigate spatial patterns of SST variability recorded in proxies we calculate the residual temperature at each site, which is the difference between the expected SST from calibration equations, and the satellite-derived maSST estimate (Figure 4.7). For $U^{K'}_{37}$, we calculate residuals using the calibration equation of *Müller et al.* [1998] ($U^{K'}_{37} = 0.044 + 0.033T$), which is statistically identical (within our temperature range) to another global calibration of *Conte et al.* [2006], and the culture-derived regression of *Prahl et al.* [1988]. For Mg/Ca, we use the calibration of *Dekens et al.* [2002] ($Mg/Ca = 0.38e^{0.09T}$), which has identical temperature sensitivity to the calibration of *Lea et al.* [2000]. We additionally investigated the effect of using different calibration equations for both $U^{K'}_{37}$ and Mg/Ca_{cor} to calculate SST residuals (not shown), and found that although the magnitude of SST residuals varies, the spatial pattern is relatively robust to the calibration chosen. Since we primarily assess the spatial variability of SST residuals, rather than offsets occurring as a result of

differing calibrations, we furthermore normalize our residual SST estimates by the respective means and standard deviations of each variable. Positive residuals indicate regions where the estimated SST from proxy measurements overestimates maSST, and vice versa.

Spatial patterns of $U^{K'}_{37}$ SST residuals are characterized by several groups of positive residuals in the Java upwelling region, the southern Makassar Strait, the eastern Timor Sea and a smaller cluster in the northern South China Sea. These regions, with the exception of the Makassar Strait, are characterized by strong seasonal cycles of NPP in antiphase with the seasonal SST cycle (Figure 4.2). Positive residuals are consistent with the growth of alkenone-producing coccolithophores during low-productivity, low-nutrient months, a finding that has been replicated in the eastern Pacific [*Prahl et al.,* 2010; *Kienast et al.,* 2012], meaning that calibrations using productivity-weighted SST are not appropriate for these regions [e.g. *Sonzogni et al.,* 1997b].

The cluster of positive $U^{K'}_{37}$ residuals in the northern South China Sea appear to be at odds with sediment trap studies, which found a strong seasonal cycle of coccolithophore production peaking in boreal spring and winter, when SSTs are at their minimum [*Wiesner et al.,* 1996; *Chen et al.,* 2007]. However, water samples from the northernmost

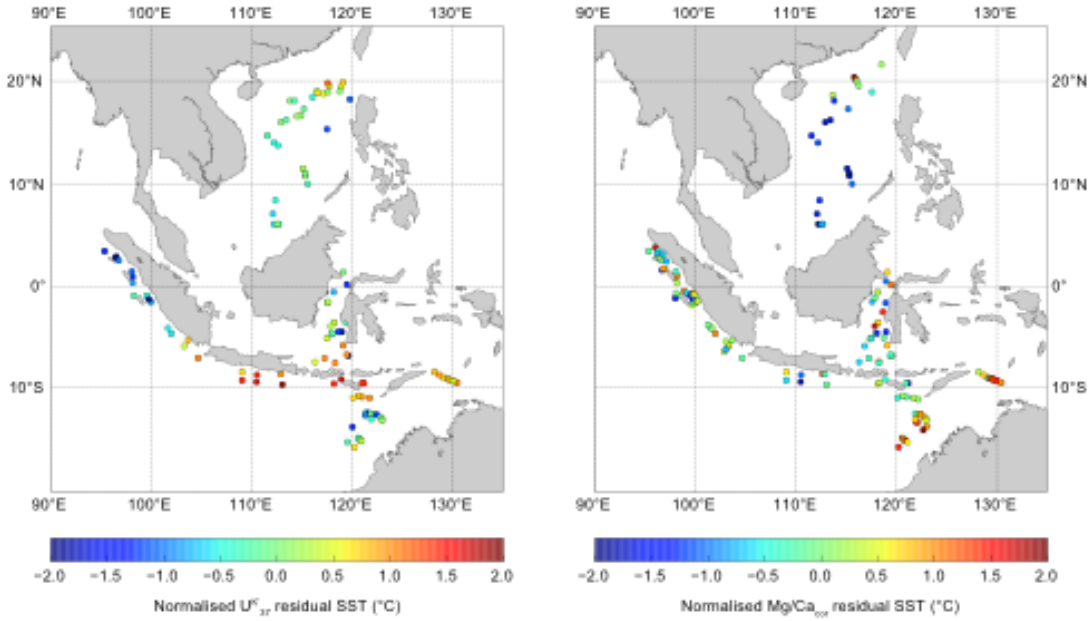

Figure 4.7 - Normalized residual SST for $U^{K'}_{37}$ calculated with the calibration of *Müller et al.* [1998] (left) and Mg/Ca_{cor} calculated with the calibration of *Dekens et al.* [2002] (right).

shelf area found larger abundances of *E. huxleyi* and *G. oceanica* during boreal summer and autumn [*Chen et al.*, 2007], suggesting that growth patterns in shelf areas may differ from the more central regions. *Rosell-Melé et al.* [2013] also documented non-linear relationships between $U^{K'}_{37}$ measurements and alkenone fluxes from a global compilation of sediment trap studies, which suggests that $U^{K'}_{37}$ signals can be attenuated by complex sedimentation processes, especially in regions of high productivity. We therefore propose that the northernmost South China Sea samples were influenced by advection or resuspension of alkenones from the high-productivity shelf environment, which may record a different $U^{K'}_{37}$ signal to the more central basin regions.

The small group of positive residuals in the southern Makassar Strait is also not well explained by seasonality of NPP as this region has a relatively weak annual

NPP cycle. However, during the boreal winter and spring (when SSTs are at their warmest) westerly winds drive fresh surface waters from the Java Sea into the Makassar Strait, providing well-stratified, low-nutrient waters that are favorable conditions for the growth of alkenone producing coccolithophores [*Tyrell and Merico*, 2004]. In contrast, groups of negative residuals are found in the western Timor Sea, coastal Sumatra and in the southern South China Sea, where the seasonal cycles of SST and NPP are generally weaker and the temperature signal may therefore be more representative of an annual average.

Mg/Ca_{cor} residual SSTs present a widely different pattern to $U^{K'}_{37}$. The most negative residuals are observed in the South China Sea, where sediment traps suggest that *G. ruber* grows preferentially during late boreal summer and early fall [*Wiesner et al.*, 1996], i.e. during the warmest months of the year, and thus we should expect the inverse residual behavior to what we observe. This may hint at a secondary control, for example calcite undersaturation, in driving low residual SSTs in this location. It is also surprising to note that residual SSTs in the Java upwelling region are not significantly offset from values from the Makassar Strait or coastal Sumatra, given that sediment traps predict the highest fluxes of *G. ruber* during the peak upwelling season, which should induce cooler SSTs [*Mohtadi et al*., 2009]. However, residual Mg/Ca SSTs in the Sumatra and Java upwelling region are based upon Mg/Ca measurements that have been corrected for different cleaning methodologies. In this study we have used a Mg/Ca correction factor of 15 % for non-reductively cleaned samples, following the recommendation of *Rosenthal et al*. [2004], though other studies have suggested that a lower Mg/Ca correction may be appropriate (e.g. 6.6% in *Xu et al.* [2010]). Without paired samples of both reductively- and non-

reductively-cleaned samples, we are unable to make predictions as to whether the correction factor is at the high or low end of these estimations, and thus our residual patterns in these regions cannot be robustly constrained. In any case, Mg/Ca residuals from these regions are imprinted by significantly more scatter than their $U^{K'}_{37}$ counterparts, which is suggestive of secondary mechanisms unrelated to seasonal temperature influences on *G. ruber* Mg/Ca.

4.4.4 Analytical concerns for the $U^{K'}_{37}$ 'warm-end'

An inherent problem of the $U^{K'}_{37}$ paleothermometer at the 'warm end' (>24 °C) of the calibration spectrum, where the $U^{K'}_{37}$ value approaches unity, is that concentrations of $C_{37:3}$ alkenones are eventually reduced towards zero. At these low concentrations, which approach the detection limits of modern analytical methods, minor analytical errors can result in non-trivial (>2 °C) errors in temperature estimations, typically towards warmer temperatures due to the preferential absorption of the $C_{37:3}$ versus the $C_{37:2}$ alkenone in the chromatographic system [*Grimalt et al.*, 2001; *Pelejero and Calvo*, 2003]. *Bentaleb et al.* [2002] further suggested, based upon a transect of water samples and *in situ* temperature measurements in the West Pacific, that the limit of $U^{K'}_{37}$ lies at 26.4 °C with saturated values occurring above this limit. However, this appears to be a pessimistic estimate given the number of high-temperature modern and paleotemperature records which are able to resolve SST variability exceeding this value [e.g. *Pelejero and Grimalt*, 1997; *Sonzogni et al.*, 1997a,b, *Kienast et al.*, 2012; *de Garidel-Thoron et al.*, 2007; *Wang et al.*, 2013; *Fraser et al.*, 2014].

We make an assessment of this phenomenon in our study by comparing

alkenone concentrations of new $U^{K'}_{37}$ measurements with residual SSTs, with the expectation that SST residuals are skewed to positive values at low concentrations. In contrast to this expectation, our results document the opposite relationship, with the data skewed towards the most negative residuals at lowest concentrations (Figure 4.8). A map of the distribution of alkenone concentrations in these samples (Figure 4.8) shows that the majority of these low-concentration samples are clustered in the western Timor Sea. It is therefore unclear whether the relationship between alkenone concentrations and residual SSTs is causative or a coincidence of sample distribution, but there is little evidence for a signal biased by limited detection of $C_{37:3}$ alkenones. Further consideration must be given to the wider compiled dataset, where analytical differences between studies may result in different responses to low-concentration samples. At the time of writing no specific alkenone concentration data was available from these studies, although the authors of *Pelejero and Grimalt* [1997] note that 'total C_{37} abundances range between 200 and 1000 ng/g', which gives concentrations sufficiently above threshold limits for detection [*Villanueva and Grimalt*, 1996].

For high-temperature paleoclimate reconstructions, the question of whether there exists an upper-limit to the $U^{K'}_{37}$ thermometer remains unanswered [c.f. *Pelejero and Calvo*, 2003]. If we consider the linear calibrations of *Müller et al.* [1998] ($U^{K'}_{37}$ = 0.044 + 0.033T) or *Sonzogni et al*. [1997b] ($U^{K'}_{37}$ = 0.316 + 0.023T), then we would assume an upper-limit to $U^{K'}_{37}$ temperatures (i.e. when $U^{K'}_{37}$ = 1) of 29.0 °C or 29.9 °C, respectively.

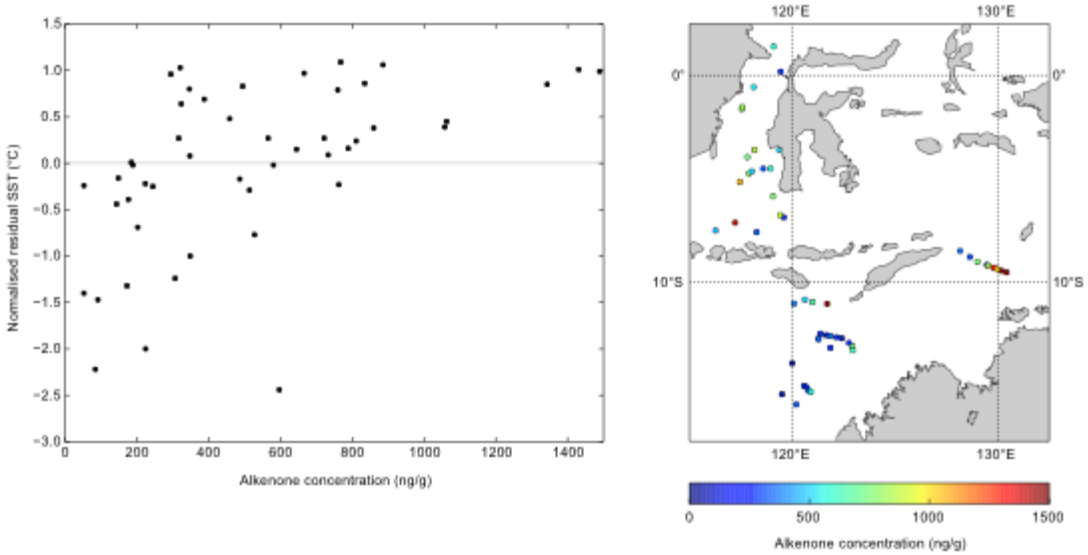

Figure 4.8 - (left) Alknone concentrations (ng/g) versus $U^{K'}_{37}$ normalized SST residuals calculated from the equation of *Müller et al.* [1998] and AVHRR maSST estimates. (right) Spatial distribution of alkenone concentrations in the Makassar Strait, Java Sea and Timor Sea.

This has clear implications in that regions where SSTs exceed 29.0 °C or 29.9 °C, a $U^{K'}_{37}$ value of 1 will be recorded, and thus a bias to low $U^{K'}_{37}$ values will always be recorded in regions where all, or part, of the seasonal SST cycle exceeds this limit. Other studies have suggested that the $U^{K'}_{37}$ curve approaches an asymptote at high temperatures [e.g. *Sikes and Volkman*, 1993; *Goni et al.*, 2001], but in the absence of high-precision measurements where $U^{K'}_{37} > 0.95$, the exact shape of such a curve is not clear. For samples compiled here, we observe a lower sensitivity to temperature than suggested by global calibrations, consistent with a flattening of the curve at the warm end of the $U^{K'}_{37}$ spectrum. A logarithmic regression fit yields no significantly better correlation ($R^2 = 0.56$) than a linear fit ($R^2 = 0.55$) meaning that it is unclear whether the relationship trends towards an asymptote or whether there exists a definitive limit where $U^{K'}_{37} = 1$. However, it is interesting to note that no values reach the limit of detection (i.e. $U^{K'}_{37} = 1$) in these datasets despite some regions where annual minimum SSTs are in excess of 29.5 °C.

4.4.5 Secondary influences on foraminiferal Mg/Ca

Carbonate ion ($[CO_3^{2-}]$) effects have been posited as an important control on Mg/Ca recorded in foraminifera, with increasing water depths and reduced calcite-saturation states resulting in a progressive decrease in Mg/Ca [*Rosenthal and Lohmann,* 2002; *Dekens et al*., 2002; *Regenberg et al*., 2006; 2014]. This may be important in the West Pacific due to the relatively shallow depth of the calcite-saturation horizon, in particular in the South China Sea. We compared our measured Mg/Ca_{cor} ratios, and residual Mg/Ca_{cor} SSTs, to depth profiles of calcite-saturation states ($\Delta[CO_3^{2-}]$) (Figure 4.9). $\Delta[CO_3^{2-}]$ was calculated by subtracting $[CO_3^{2-}]$ at saturation (based on *Jansen et al.* [2002]) from in situ $[CO_3^{2-}]$. In situ $[CO_3^{2-}]$ was derived in the South China Sea from the SouthEast Asian Time-series Study (SEATS) [*Chou et al.,* 2007], whilst in the Makassar Strait, Timor Sea and eastern Indian Ocean, in situ $[CO_3^{2-}]$ was calculated from closely located World Ocean Circulation Experiment (WOCE) water-column measurements, using with the program co2sys [*Lewis and Wallace,* 1998].

Mg/Ca_{cor} and $\Delta[CO_3^{2-}]$ show a weak positive correlation (R^2 = 0.30), suggesting a limited control of $\Delta[CO_3^{2-}]$ on Mg/Ca in this region (Figure 4.9). Other studies have suggested the existence of a threshold below which Mg/Ca ratios become affected by $\Delta[CO_3^{2-}]$ (e.g. below $\Delta[CO_3^{2-}]$ values of 21.3 ± 6.6 µmol/kg in *Regenberg et al.,* [2014]). Whilst samples below this threshold show on average lower Mg/Ca_{cor} values than those above (Figure 4.9), there is no significantly better correlation (R^2 = 0.31) for these limited samples than when considering the entire dataset, thus the effect of the threshold is unclear. The most significant problem with this methodology

likely lies in the geographic distribution of samples. The lowest Mg/Ca_{cor} ratios are found in the South China Sea, which is to be expected given the lowest maSSTs in this region. Yet the South China Sea is also the most calcite-undersaturated of all regions in this study, and therefore the low $\Delta[CO_3^{2-}]$ - low Mg/Ca_{cor} relationship observed could purely be an artifact of the data distribution. A more suitable approach is therefore to compare the residual SST estimates with $\Delta[CO_3^{2-}]$, as this eliminates potential bias' resulting from geographic and climatic variability (Figure 4.9). This relationship shows a weaker correlation than using Mg/Ca_{cor} values (R^2 = 0.16), although we note that the group of lowest residuals (< -1 °C) in the South China Sea are all found at $\Delta[CO_3^{2-}]$ values of < 21.3 µmol/kg. The dominant factor of residual SST distribution appears, therefore, to not be controlled to first order by the calcite-saturation state, although it may have a more significant influence on low-$\Delta[CO_3^{2-}]$ (< 21.3 µmol/kg) sites.

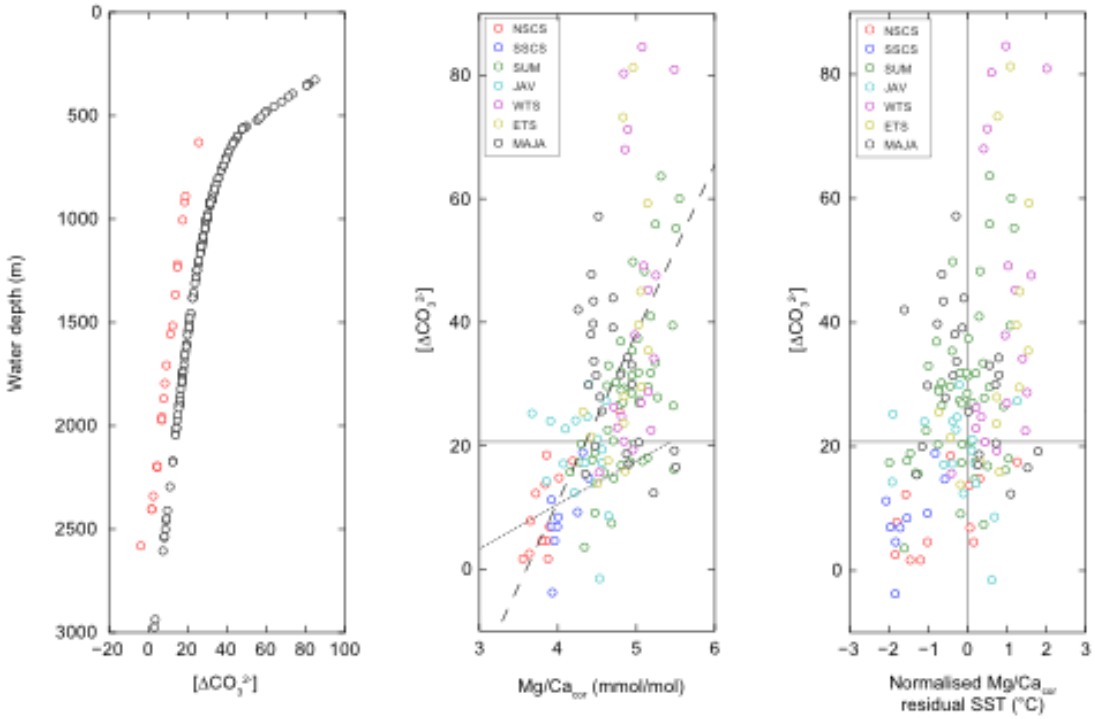

Figure 4.9 - (left) Carbonate ion saturation states ($\Delta[CO_3^{2-}]$) versus water depth for sites with Mg/Ca measurements. Red circles represent sites in the South China Sea, where $\Delta[CO_3^{2-}]$ is derived from SouthEast Asian Time Series (SEATS) stations [*Chou et al.*, 2007], whilst black circles represent sites in the Makassar Strait, Timor Sea and Eastern Indian Ocean where $\Delta[CO_3^{2-}]$ is derived from World Ocean Circulation Experiment (WOCE) stations. (middle) Mg/Ca_{cor} versus $\Delta[CO_3^{2-}]$. Sites are color-coded by region following the scheme from Figure 5.2. Dashed line represents the regression for the entire dataset (r^2 = 0.30) whilst the dotted line represents the regression for sites below a critical $\Delta[CO_3^{2-}]$ threshold of 21.3 µmol/kg (r^2 = 0.31), following *Regenberg et al.*, [2014] (horizontal grey line). (right) Normalized Mg/Ca_{cor} residual SSTs calculated from the equation of *Dekens et al.* [2002] versus $\Delta[CO_3^{2-}]$.

In addition to $[CO_3^{2-}]$ effects, salinity variability may also have an effect on the Mg/Ca paleothermometer. *Arbuszewski et al.* [2010] documented a ~27 % sensitivity of *G. ruber* Mg/Ca per salinity increase unit, based upon a core top transect from the Atlantic Ocean. However, this estimate was likely affected by carbonate dissolution [*Hönisch et al.*, 2013; *Regenberg et al.*, 2014], and more recent studies have indicated a sensitivity in the range of 3-4 % per salinity unit [*Hönisch et al.*, 2013]. Correcting Mg/Ca variability for salinity provides a challenge in the West Pacific, as the seasonal

cycle of temperature, precipitation and winds related to the Asian Monsoon systems drive strong salinity changes throughout the year (which could result in SST uncertainties upwards of 1 °C with a 4 % sensitivity). Thus, corrections for salinity also rely heavily on high-quality climatological data (e.g. satellite or *in situ* measurements) and knowledge of ecological preferences of foraminifera, in terms of both their seasonal and depth distributions. Some attempts to quantify the latter have been made based upon paired $\delta^{18}O$ and Mg/Ca measurements in this region [e.g. *Mohtadi et al.,* 2011], by comparisons of measured $\delta^{18}O$ with expected equilibrium $\delta^{18}O$ of calcite. This approach is however hampered by low quality water-column data and uncertainty in $\delta^{18}O$/salinity relationships, which are based upon relatively few $\delta^{18}O$ measurements made on corals and sclerosponges [e.g. *Morimoto et al.,* 2002; *Grottoli et al.,* 2010]. In addition, the amplitude of the seasonal cycle of salinity and temperature often outweighs depth-related variability within the mixed layer in the West Pacific, thus the depth and seasonal distributions of *G. ruber* cannot be considered separately. Future studies may therefore incorporate more robust statistical approaches that consider variability of both Mg/Ca and $\delta^{18}O$ in both the depth and time domain.

4.5 Conclusions and Recommendations

Understanding the underlying causes of divergence among different proxy records of SST is important in understanding the past climate response to external forcings. In this study we have shown that spatial patterns of $U^{K'}_{37}$ core top SST estimates in the West Pacific can be related to seasonal production variability, for

example regions with strong cycles of NPP and SST, such as the Java upwelling region, are biased towards temperatures of low-productivity months, consistent with similar relationships documented in the East Pacific [*Prahl et al.*, 2010; *Kienast et al.*, 2012]. However, we cannot rule out additional influences such as lateral advection/resuspension of alkenones in driving $U^{K'}_{37}$ changes, and thus records must be carefully considered with this in mind. The choice of $U^{K'}_{37}$ calibration is also an important consideration in high-temperature paleoclimate records, as our results indicate a considerably lower sensitivity of $U^{K'}_{37}$ to temperature (0.022 $U^{K'}_{37}$ units/°C) above 26 °C than suggested by the most widely applied global calibrations of *Müller et al.* [1998] or *Conte et al*. [2006] (> 0.03 $U^{K'}_{37}$ units / °C), which could generate differences in the magnitude of deglacial temperature changes in paleoclimate records of more than 1 °C. It is also possible that $U^{K'}_{37}$ based SSTs are underestimated in the highest temperature regions where the $U^{K'}_{37}$ reaches unity for at least part of the year, and thus the magnitude of SST change from the deglacial to present day may also be underestimated in regions where modern temperatures exceed ~29 °C.

Mg/Ca temperature estimates from the West Pacific do not provide such a clear spatial pattern as $U^{K'}_{37}$ estimates, and appear to be biased by secondary factors including the [CO_3^{2-}] effect as demonstrated most strongly in core top samples from the South China Sea. Combined proxy-model approaches [e.g. *Wang et al.*, 2013; *Timmermann et al*., 2014] that have attempted to account for past variations in seasonality have shown that differences between the Mg/Ca and $U^{K'}_{37}$ paleothermometers can be well replicated by the different seasonal-weighting of temperature signals. In the context of our results, this is surprising as we find that

there are no consistent seasonal differences between the two proxies, with some regions recording $U^{K'}_{37}$ and Mg/Ca signals in-phase with each other, whilst in other regions signals are biased towards opposite seasons. Suggestions of a summer bias in Mg/Ca temperatures, and winter bias in $U^{K'}_{37}$ temperatures in the West Pacific as proposed by *Timmermann et al.* [2014] is also not borne out by our modern core top relationships (Figure 4.6). The inclusion of further parameters into proxy-model comparisons, in particular the influence of salinity, into both core top and paleo-records may therefore yield further insights into these discrepancies.

Throughout this study we note that core top compilations are prone to large uncertainties due to inter-laboratory methodological and analytical differences. In particular, Mg/Ca measurements are impacted by cleaning procedures, where non-reductively cleaned samples may overestimate temperature by >1.5 °C when compared to reductively cleaned samples. This may lead to considerable errors in calculations of Mg/Ca-SST relationships. Based on this, we recommend that Mg/Ca and $U^{K'}_{37}$ core top datasets used for calibration should be measured in single laboratories, or include a number of paired samples measured in multiple laboratories to allow some quantification of inter-laboratory offsets. Furthermore, a consistent analytical procedure should be followed between laboratories for (e.g. using the same size fractions of foraminifera, using the same cleaning techniques) for both modern and paleoclimate temperature reconstructions.

References

Anand, P., Elderfield, H., and Conte, M. H. (2003). Calibration of Mg/Ca

thermometry in planktonic foraminifera from a sediment trap time series. Paleoceanography, 18(2).

Arbuszewski, J., deMenocal, P., Kaplan, A., and Farmer, E. C. (2010). On the fidelity of shell-derived $\delta^{18}O_{seawater}$ estimates. Earth and Planetary Science Letters, 300(3), 185-196.

Behrenfeld, M. J., O'Malley, R. T., Siegel, D. A., McClain, C. R., Sarmiento, J. L., Feldman, G. C., Milligan, A. J., Falkowski, P. G., Letelier, R. M., and Boss, E. S. (2006). Climate-driven trends in contemporary ocean productivity. Nature, 444(7120), 752-755.

Bentaleb, I., Fontugne, M., and Beaufort, L. (2002). Long-chain alkenones and $U^{K'}_{37}$ variability along a south–north transect in the Western Pacific Ocean. Global and Planetary Change, 34(3), 173-183.

Brassell, S. C., Eglinton, G., Marlowe, I. T., Pflaumann, U., and Sarnthein, M. (1986). Molecular stratigraphy: a new tool for climatic assessment. Nature, 320(6058), 129-133.

Chen, Y. L. L., Chen, H. Y., and Chung, C. W. (2007). Seasonal variability of coccolithophore abundance and assemblage in the northern South China Sea. Deep Sea Research Part II: Topical Studies in Oceanography, 54(14), 1617-1633.

Chou, W. C., Sheu, D. D., Lee, B. S., Tseng, C. M., Chen, C. T. A., Wang, S. L., and Wong, G. T. F. (2007). Depth distributions of alkalinity, TCO_2 and $\delta^{13}C_{TCO2}$ at SEATS time-series site in the northern South China Sea. Deep Sea Research Part II: Topical Studies in Oceanography, 54(14), 1469-1485.

Conte, M. H., Sicre, M. A., Rühlemann, C., Weber, J. C., Schulte, S., Schulz- Bull, D., and Blanz, T. (2006). Global temperature calibration of the alkenone unsaturation index (UK′ 37) in surface waters and comparison with surface sediments. Geochemistry, Geophysics, Geosystems, 7(2).

Dekens, P. S., Lea, D. W., Pak, D. K., and Spero, H. J. (2002). Core top calibration of Mg/Ca in tropical foraminifera: Refining paleotemperature estimation. Geochemistry, Geophysics, Geosystems, 3(4), 1-29.

de Garidel- Thoron, T., Rosenthal, Y., Beaufort, L., Bard, E., Sonzogni, C., and Mix, A. C. (2007). A multiproxy assessment of the western equatorial Pacific hydrography during the last 30 kyr. Paleoceanography, 22(3).

de Villiers, S., Greaves, M., and Elderfield, H. (2002). An intensity ratio calibration method for the accurate determination of Mg/Ca and Sr/Ca of marine carbonates by ICP- AES. Geochemistry, Geophysics, Geosystems, 3(1).

Elderfield, H., Vautravers, M., and Cooper, M. (2002). The relationship between shell

size and Mg/Ca, Sr/Ca, $\delta^{18}O$, and $\delta^{13}C$ of species of planktonic foraminifera. Geochemistry, Geophysics, Geosystems, 3(8), 1-13.

Fraser, N., Kuhnt, W., Holbourn, A., Bolliet, T., Andersen, N., Blanz, T., Beaufort, L. (2014), Precipitation variability within the West Pacific Warm Pool over the past 120 ka: evidence from the Davao Gulf, southern Philippines, *Paleoceanography*, 29, doi:10.1002/2013PA002599.

Goñi, M. A., Hartz, D. M., Thunell, R. C., and Tappa, E. (2001). Oceanographic considerations for the application of the alkenone-based paleotemperature $U^{K'}_{37}$ index in the Gulf of California. Geochimica et Cosmochimica Acta, 65(4), 545-557.

Grimalt, J. O., Calvo, E., and Pelejero, C. (2001). Sea surface paleotemperature errors in $U^{K'}_{37}$ estimation due to alkenone measurements near the limit of detection. Paleoceanography, 16(2), 226-232.

Grottoli, A. G., Adkins, J. F., Panero, W. R., Reaman, D. M., and Moots, K. (2010). Growth rates, stable oxygen isotopes ($\delta^{18}O$), and strontium (Sr/Ca) composition in two species of Pacific sclerosponges (Acanthocheatetes wellsi and Astrosclera willeyana) with $\delta^{18}O$ calibration and application to paleoceanography. Journal of Geophysical Research: Oceans (1978–2012), 115(C6).

Hönisch, B., Allen, K. A., Lea, D. W., Spero, H. J., Eggins, S. M., Arbuszewski, J., deMenocal, P., Rosentahl, Y., Russell, A. D., and Elderfield, H. (2013). The influence

of salinity on Mg/Ca in planktic foraminifers–Evidence from cultures, core top sediments and complementary $\delta^{18}O$. Geochimica et Cosmochimica Acta, 121, 196-213.

Jansen, H., Zeebe, R. E., and Wolf- Gladrow, D. A. (2002). Modeling the dissolution of settling CaCO3 in the ocean. Global Biogeochemical Cycles, 16(2), 11-1.

Kawahata, H., Nishimura, A., and Gagan, M. K. (2002). Seasonal change in foraminiferal production in the western equatorial Pacific warm pool: evidence from sediment trap experiments. Deep Sea Research Part II: Topical Studies in Oceanography, 49(13), 2783-2800.

Kienast, M., Steinke, S., Stattegger, K., and Calvert, S. E. (2001). Synchronous tropical South China Sea SST change and Greenland warming during deglaciation. Science, 291(5511), 2132-2134.

Kienast, M., MacIntyre, G., Dubois, N., Higginson, S., Normandeau, C., Chazen, C., and Herbert, T. D. (2012). Alkenone unsaturation in surface sediments from the eastern equatorial Pacific: Implications for SST reconstructions. Paleoceanography, 27(1).

Kisakürek, B., Eisenhauer, A., Böhm, F., Garbe-Schönberg, D., and Erez, J. (2008). Controls on shell Mg/Ca and Sr/Ca in cultured planktonic foraminiferan *Globigerinoides ruber* (white). Earth and Planetary Science Letters, 273(3), 260-269.

Kuhnt, W., et al. (2005). Cruise report SONNE-185: Variability of the Indonesian Throughflow and Australasian climate history of the last 150000 years (VITAL), report, Inst. für Geowiss., Christian-Albrechts-Univ. zu Kiel, Kiel, Germany.

Kuhnt, W. et al. (2011). Cruise report SONNE-217: Variability of the Indonesian Throughflow within the Makassar-Java passage (MAJA). Report, Inst. für Geowiss., Christian-Albrechts-Univ. zu Kiel, Kiel, Germany.

Laepple, T., and Huybers, P. (2013). Reconciling discrepancies between Uk37 and Mg/Ca reconstructions of Holocene marine temperature variability. Earth and Planetary Science Letters, 375, 418-429.

Lea, D. W., Mashiotta, T. A., and Spero, H. J. (1999). Controls on magnesium and strontium uptake in planktonic foraminifera determined by live culturing. Geochimica et Cosmochimica Acta, 63(16), 2369-2379.

Lea, D. W., Pak, D. K., and Spero, H. J. (2000). Climate impact of late Quaternary equatorial Pacific sea surface temperature variations. Science, 289(5485), 1719-1724.

Lewis, E., Wallace, D., and Allison, L. J. (1998). Program developed for CO2 system calculations (p. 38). Carbon Dioxide Information Analysis Center, managed by Lockheed Martin Energy Research Corporation for the US Department of Energy.

Locarnini, R. A., A. V. Mishonov, J. I. Antonov, T. P. Boyer, H. E. Garcia, O. K. Baranova, M. M. Zweng, C. R. Paver, J. R. Reagan, D. R. Johnson, M. Hamilton, and D. Seidov, 2013. World Ocean Atlas 2013, Volume 1: Temperature. S. Levitus, Ed., A. Mishonov Technical Ed.; NOAA Atlas NESDIS 73, 40 pp.

Martin, P. A., and Lea, D. W. (2002). A simple evaluation of cleaning procedures on fossil benthic foraminiferal Mg/Ca. Geochemistry, Geophysics, Geosystems, 3(10), 1-8.

Mix, A. C. (2006). Running hot and cold in the eastern equatorial Pacific. Quaternary Science Reviews, 25(11), 1147-1149.

Mohtadi, M., Steinke, S., Groeneveld, J., Fink, H. G., Rixen, T., Hebbeln, D., ... and Herunadi, B. (2009). Low- latitude control on seasonal and interannual changes in planktonic foraminiferal flux and shell geochemistry off south Java: A sediment trap study. Paleoceanography, 24(1).

Mohtadi, M., Lückge, A., Steinke, S., Groeneveld, J., Hebbeln, D., and Westphal, N. (2010). Late Pleistocene surface and thermocline conditions of the eastern tropical Indian Ocean. Quaternary Science Reviews, 29(7), 887-896.

Mohtadi, M., Oppo, D. W., Lückge, A., DePol- Holz, R., Steinke, S., Groeneveld, J., Hemme, N., and Hebbeln, D. (2011). Reconstructing the thermal structure of the

upper ocean: Insights from planktic foraminifera shell chemistry and alkenones in modern sediments of the tropical eastern Indian Ocean. Paleoceanography, 26(3).

Morimoto, M., Abe, O., Kayanne, H., Kurita, N., Matsumoto, E., and Yoshida, N. (2002). Salinity records for the 1997–98 El Nino from Western Pacific corals. Geophysical Research Letters, 29(11), 35-1.

Müller, P. J., Kirst, G., Ruhland, G., von Storch, I., and Rosell-Melé, A. (1998). Calibration of the alkenone paleotemperature $U^{K'}_{37}$ index based on core tops from the eastern South Atlantic and the global ocean (60° N - 60° S). Geochimica et Cosmochimica Acta, 62(10), 1757-1772.

Ni, Y., Foster, G. L., Bailey, T., Elliott, T., Schmidt, D. N., Pearson, P., Haley, B., and Coath, C. (2007). A core top assessment of proxies for the ocean carbonate system in surface- dwelling foraminifers. Paleoceanography, 22(3).

Nürnberg, D., Bijma, J., and Hemleben, C. (1996). Assessing the reliability of magnesium in foraminiferal calcite as a proxy for water mass temperatures. Geochimica et Cosmochimica Acta, 60(5), 803-814.

Pelejero, C., and Grimalt, J. O. (1997). The correlation between the $U^{K'}_{37}$ index and sea surface temperatures in the warm boundary: The South China Sea. Geochimica et Cosmochimica Acta, 61(22), 4789-4797.

Pelejero, C., Grimalt, J. O., Heilig, S., Kienast, M., and Wang, L. (1999). High- resolution UK 37 temperature reconstructions in the South China Sea over the past 220 kyr. Paleoceanography, 14(2), 224-231.

Pelejero, C., and Calvo, E. (2003). The upper end of the UK′ 37 temperature calibration revisited. Geochemistry, Geophysics, Geosystems, 4(2).

Prahl, F. G., and Wakeham, S. G. (1987). Calibration of unsaturation patterns in long-chain ketone compositions for palaeotemperature assessment. Nature, 330, 367-369.

Prahl, F. G., Muehlhausen, L. A., and Zahnle, D. L. (1988). Further evaluation of long-chain alkenones as indicators of paleoceanographic conditions. Geochimica et Cosmochimica Acta, 52(9), 2303-2310.

Prahl, F. G., Rontani, J. F., Zabeti, N., Walinsky, S. E., and Sparrow, M. A. (2010). Systematic pattern in–Temperature residuals for surface sediments from high latitude and other oceanographic settings. Geochimica et Cosmochimica Acta, 74(1), 131-143.

Regenberg, M., Nürnberg, D., Steph, S., Groeneveld, J., Garbe- Schönberg, D., Tiedemann, R., and Dullo, W. C. (2006). Assessing the effect of dissolution on planktonic foraminiferal Mg/Ca ratios: Evidence from Caribbean core tops. Geochemistry, Geophysics, Geosystems, 7(7).

Regenberg, M., Steph, S., Nürnberg, D., Tiedemann, R., and Garbe-Schönberg, D. (2009). Calibrating Mg/Ca ratios of multiple planktonic foraminiferal species with $\delta^{18}O$-calcification temperatures: Paleothermometry for the upper water column. Earth and Planetary Science Letters, 278(3), 324-336.

Regenberg, M., Nielsen, S. N., Kuhnt, W., Holbourn, A., Garbe-Schönberg, D., and Andersen, N. (2010). Morphological, geochemical, and ecological differences of the extant menardiform planktonic foraminifera *Globorotalia menardii* and *Globorotalia cultrata*. Marine Micropaleontology, 74(3), 96-107.

Regenberg, M., Regenberg, A., Garbe- Schönberg, D., and Lea, D. W. (2014). Global dissolution effects on planktonic foraminiferal Mg/Ca ratios controlled by the calcite- saturation state of bottom waters. Paleoceanography, 29(3), 127-142.

Reynolds, R. W., Smith, T. M., Liu, C., Chelton, D. B., Casey, K. S., and Schlax, M. G. (2007). Daily high-resolution-blended analyses for sea surface temperature. Journal of Climate, 20(22), 5473-5496.

Rincón- Martínez, D., Lamy, F., Contreras, S., Leduc, G., Bard, E., Saukel, C., Blanz, T., Mackensen, A., and Tiedemann, R. (2010). More humid interglacials in Ecuador during the past 500 kyr linked to latitudinal shifts of the equatorial front and the Intertropical Convergence Zone in the eastern tropical Pacific. Paleoceanography, 25(2).

Rosell-Melé, A., and Prahl, F. G. (2013). Seasonality of UK′ 37 temperature estimates as inferred from sediment trap data. Quaternary Science Reviews, 72, 128-136.

Rosenthal, Y., and Lohmann, G. P. (2002). Accurate estimation of sea surface temperatures using dissolution- corrected calibrations for Mg/Ca paleothermometry. Paleoceanography, 17(3), 16-1.

Rosenthal, Y., Oppo, D. W., and Linsley, B. K. (2003). The amplitude and phasing of climate change during the last deglaciation in the Sulu Sea, western equatorial Pacific. Geophysical Research Letters, 30(8).

Rosenthal, Y., et al. (2004). Interlaboratory comparison study of Mg/Ca and Sr/Ca measurements in planktonic foraminifera for paleoceanographic research. Geochemistry, Geophysics, Geosystems, 5(4).

Saher, M. H., Rostek, F., Jung, S. J. A., Bard, E., Schneider, R. R., Greaves, M., Ganssen, G. M., Elderfield, H., and Kroon, D. (2009). Western Arabian Sea SST during the penultimate interglacial: A comparison of $U^{K'}_{37}$ and Mg/Ca paleothermometry. Paleoceanography, 24(2).

Schneider, B., Leduc, G., and Park, W. (2010). Disentangling seasonal signals in Holocene climate trends by satellite- model- proxy integration. Paleoceanography,

25(4).

Sikes, E. L., and Volkman, J. K. (1993). Calibration of alkenone unsaturation ratios ($U^{K'}_{37}$) for paleotemperature estimation in cold polar waters. Geochimica et Cosmochimica Acta, 57(8), 1883-1889.

Sonzogni, C., Bard, E., Rostek, F., Lafont, R., Rosell-Mele, A., and Eglinton, G. (1997). Core top calibration of the alkenone index vs sea surface temperature in the Indian Ocean. Deep Sea Research Part II: Topical Studies in Oceanography, 44(6), 1445-1460.

Sonzogni, C., Bard, E., Rostek, F., Dollfus, D., Rosell-Melé, A., and Eglinton, G. (1997b). Temperature and salinity effects on alkenone ratios measured in surface sediments from the Indian Ocean. Quaternary Research, 47(3), 344-355.

Steinke, S., Kienast, M., Groeneveld, J., Lin, L. C., Chen, M. T., and Rendle-Bühring, R. (2008). Proxy dependence of the temporal pattern of deglacial warming in the tropical South China Sea: toward resolving seasonality. Quaternary Science Reviews, 27(7), 688-700.

Steph, S., Regenberg, M., Tiedemann, R., Mulitza, S., and Nürnberg, D. (2009). Stable isotopes of planktonic foraminifera from tropical Atlantic/Caribbean core tops: Implications for reconstructing upper ocean stratification. Marine Micropaleontology, 71(1), 1-19.

Stott, L., Poulsen, C., Lund, S., and Thunell, R. (2002). Super ENSO and global climate oscillations at millennial time scales. Science, 297(5579), 222-226.

Stott, L., Timmermann, A., and Thunell, R. (2007). Southern hemisphere and deep-sea warming led deglacial atmospheric CO2 rise and tropical warming. science, 318(5849), 435-438.

Tanaka, Y., and Kawahata, H. (2001). Seasonal occurrence of coccoliths in sediment traps from West Caroline Basin, equatorial West Pacific Ocean. Marine Micropaleontology, 43(3), 273-284.

Timmermann, A., Sachs, J., and Elison Timm, O. (2014). Assessing divergent SST behavior during the last 21 ka derived from alkenones and G. ruber- Mg/Ca in the Equatorial Pacific. Paleoceanography.

Tyrrell, T., and Merico, A. (2004). Emiliania huxleyi: bloom observations and the conditions that induce them. In Coccolithophores (pp. 75-97). Springer Berlin Heidelberg.

Villanueva, J., and Grimalt, J. O. (1996). Pitfalls in the chromatographic determination of the alkenone $U^{K'}_{37}$ index for paleotemperature estimation. Journal of Chromatography A, 723(2), 285-291.

Visser, K., Thunell, R., and Stott, L. (2003). Magnitude and timing of temperature change in the Indo-Pacific warm pool during deglaciation. Nature, 421(6919), 152-155.

Wang, Y. V., Leduc, G., Regenberg, M., Andersen, N., Larsen, T., Blanz, T., and Schneider, R. R. (2013). Northern and southern hemisphere controls on seasonal sea surface temperatures in the Indian Ocean during the last deglaciation. Paleoceanography, 28(4), 619-632.

Wiesner, M. G., Zheng, L. F., Wong, H. K., Wang, Y. F., and Chen, W. (1996). Fluxes of particulate matter in the South China Sea. Particle Flux in the Ocean, 293-312.

Xu, J., Kuhnt, W., Holbourn, A., Regenberg, M., and Andersen, N. (2010). Indo- Pacific Warm Pool variability during the Holocene and Last Glacial Maximum. Paleoceanography, 25(4).

4.6 Auxiliary Material

Auxiliary Material Table 4.1 - Summary of compiled new and previously published $U^{K'}_{37}$ and Mg/Ca measurements

Sample	Latitude (°N)	Longitude (°E)	Water depth (m)	Region[a]	*G. ruber* Mg/Ca (mmol/mol)[b]	*G. ruber* Mg/Ca_{cor} (mmol/mol)[c]	$\Delta[CO_3^{2-}]$[d]	$U^{K'}_{37}$[e]	Alkenone conc. (ng/g)	maSST[f] (°C)
SO95 17922	15.42	117.46	4221	NSCS	-	-	-	0.940	-	28.39
SO95 17924	19.41	118.85	3438	NSCS	-	-	-	0.929	-	27.21
SO95 17925	19.85	119.05	2979	NSCS	-	-	-	0.930	-	27.13
SO95 17926	19.00	118.73	3761	NSCS	-	-	-	0.925	-	27.32
SO95 17928	18.27	119.75	2486	NSCS	-	-	-	0.930	-	28.06
SO95 17930	20.33	115.78	629	NSCS	4.78	4.78	25.69	-	-	26.44
SO95 17931	20.10	115.96	1005	NSCS	4.19	4.19	17.51	-	-	26.58
SO95 17932	19.95	116.04	1365	NSCS	3.84	3.84	13.76	-	-	26.66
SO95 17933	19.53	116.23	1972	NSCS	3.89	3.89	6.89	-	-	26.81
SO95 17934	19.03	116.46	2665	NSCS	-	-	-	0.918	-	26.98
SO95 17935	18.88	116.53	3143	NSCS	-	-	-	0.926	-	27.04
SO95 17936	18.77	117.12	3809	NSCS	-	-	-	0.928	-	27.15
SO95 17937	19.50	117.67	3428	NSCS	-	-	-	0.921	-	26.98
SO95 17938	19.79	117.54	2840	NSCS	-	-	-	0.930	-	26.88
SO95 17941	21.52	118.48	2201	NSCS	3.86	3.86	4.59	-	-	26.63
SO95 17943	18.95	117.55	917	NSCS	3.85	3.85	18.51	0.920	-	27.13
SO95 17944	18.66	113.64	1219	NSCS	4.02	4.02	14.80	-	-	26.93
SO95 17945	18.13	113.78	2404	NSCS	3.55	3.55	1.68	0.918	-	27.11
SO95 17946	18.13	114.25	3464	NSCS	-	-	-	0.915	-	27.17
SO95 17947	18.47	116.03	3765	NSCS	-	-	-	0.910	-	27.10
SO95 17948	16.71	114.90	2855	NSCS	-	-	-	0.937	-	27.65
SO95 17949	17.35	115.17	2195	NSCS	3.80	3.80	4.60	0.927	-	27.46
SO95 17950	16.09	112.90	1868	NSCS	3.65	3.65	7.81	0.938	-	27.70
SO95 17951	16.29	113.41	2340	NSCS	3.64	3.64	2.55	0.934	-	27.70

Sample	Latitude (°N)	Longitude (°E)	Water depth (m)	Region[a]	*G. ruber* Mg/Ca (mmol/mol)[b]	*G. ruber* Mg/Ca_{cor} (mmol/mol)[c]	$\Delta[CO_3^{2-}]$[d]	$U^{K'}_{37}$[e]	Alkenone conc. (ng/g)	maSST[f] (°C)
SO95 17952	16.67	114.47	2882	NSCS	-	-	-	0.938	-	27.66
SO95 17954	14.80	111.53	1517	NSCS	3.72	3.72	12.27	0.933	-	27.71
SO95 17955	14.12	112.18	2404	NSCS	3.87	3.87	1.68	0.933	-	27.84
SO95 17956	13.85	112.59	3387	NSCS	-	-	-	0.936	-	27.88
SO95 17957	10.90	115.30	2197	SSCS	3.96	3.96	4.60	0.968	-	28.62
SO95 17958	11.62	115.08	2581	SSCS	3.93	3.93	-3.77	0.969	-	28.56
SO95 17959	11.14	115.29	1957	SSCS	3.92	3.92	6.98	0.968	-	28.64
SO95 17960	10.12	115.56	1707	SSCS	4.25	4.25	9.24	0.966	-	28.72
SO95 17961	8.51	112.33	1795	SSCS	4.00	4.00	8.45	0.956	-	28.50
SO95 17962	7.18	112.08	1970	SSCS	3.99	3.99	6.89	0.956	-	28.62
SO95 17963	6.17	112.67	1233	SSCS	4.40	4.40	14.72	0.963	-	28.72
SO95 17964	6.16	112.21	1556	SSCS	3.92	3.92	11.23	0.961	-	28.73
SO95 17965	6.16	112.55	889	SSCS	4.32	4.32	18.91	0.972	-	28.72
GeoB10008	-0.95	98.26	934	SUM	5.68	4.94	31.32	0.992	-	29.50
GeoB10010	-1.17	97.98	2937	SUM	4.99	4.34	3.58	-	-	29.45
GeoB10014	1.68	96.98	1158	SUM	6.29	5.47	26.46	-	-	29.84
GeoB10016	1.59	96.66	1900	SUM	5.28	4.59	15.61	-	-	29.78
GeoB10022	-0.50	98.85	706	SUM	6.28	5.46	39.46	-	-	29.68
GeoB10024	-0.77	99.27	1381	SUM	5.33	4.63	22.56	-	-	29.71
GeoB10025	-0.67	99.12	1149	SUM	5.50	4.78	26.63	-	-	29.71
GeoB10026	-0.94	99.52	1641	SUM	5.14	4.47	18.90	0.994	-	29.66
GeoB10027	-0.80	99.65	875	SUM	5.34	4.64	33.00	-	-	29.68
GeoB10028	-0.70	99.76	522	SUM	6.33	5.50	55.23	-	-	29.68
GeoB10029	-1.49	100.13	974	SUM	5.45	4.74	30.26	-	-	29.62
GeoB10033	-1.56	99.95	1756	SUM	4.92	4.28	17.40	0.987	-	29.63
GeoB10034	-4.16	101.50	995	SUM	5.32	4.63	29.71	-	-	29.16
GeoB10036	-5.34	103.66	1502	SUM	5.41	4.70	20.81	0.990	-	28.87
GeoB10038	-5.94	103.25	1891	SUM	4.78	4.16	15.72	0.978	-	28.73

Sample	Latitude (°N)	Longitude (°E)	Water depth (m)	Region[a]	*G. ruber* Mg/Ca (mmol/mol)[b]	*G. ruber* Mg/Ca_{cor} (mmol/mol)[c]	$\Delta[CO_3^{2-}]$[d]	Alkenone $U^{K'}_{37}$[e]	Alkenone conc. (ng/g)	maSST[f] (°C)
GeoB10039	-5.86	103.29	1799	SUM	5.53	4.81	16.84	-	-	28.76
GeoB10040	-6.47	102.86	2605	SUM	5.39	4.69	7.43	-	-	28.57
GeoB10041	-6.27	103.01	1540	SUM	4.94	4.30	20.27	-	-	28.61
GeoB10042	-7.11	104.64	2457	SUM	5.14	4.47	9.14	0.983	-	28.55
GeoB10044	-8.50	109.02	3346	JAV	5.21	4.53	-1.53	0.959	-	28.01
GeoB10047	-9.31	109.02	1780	JAV	4.68	4.07	17.09	0.970	-	27.88
GeoB10049	-8.78	110.50	1289	JAV	4.49	3.90	24.01	0.969	-	27.84
GeoB10050	-9.47	110.45	1221	JAV	4.22	3.67	25.24	0.971	-	27.84
GeoB10058	-8.68	112.64	1113	JAV	5.30	4.61	27.33	-	-	27.64
GeoB10059	-8.68	112.87	1370	JAV	4.71	4.10	22.73	0.953	-	27.68
GeoB10061	-9.73	113.02	2170	JAV	4.84	4.21	12.41	0.974	-	27.82
GeoB10063	-9.64	118.15	2501	JAV	5.34	4.64	8.64	0.980	-	28.22
GeoB10064	-9.53	118.30	2033	JAV	5.14	4.47	13.99	-	-	28.21
GeoB10065	-9.22	118.89	1284	JAV	4.86	4.23	24.09	0.980	-	28.09
GeoB10068	-9.59	121.15	2010	JAV	4.43	3.85	14.27	0.986	-	28.41
GeoB10069	-9.59	120.92	1249	JAV	5.03	4.37	24.70	0.984	-	28.38
SO189/2_002	-5.48	103.01	1972	SUM	5.42	4.71	14.73	-	-	28.82
SO189/2_003	-4.70	101.96	1707	SUM	5.91	5.14	18.04	0.972	-	29.04
SO189/2_009	-4.16	101.64	1128	SUM	5.56	4.83	27.04	0.976	-	29.16
SO189/2_011	-3.83	101.23	911	SUM	5.53	4.81	31.92	-	-	29.24
SO189/2_027	-1.88	99.61	1002	SUM	5.92	5.15	29.54	-	-	29.49
SO189/2_028	-1.67	99.68	1758	SUM	5.66	4.92	17.38	-	-	29.60
SO189/2_031	-1.30	99.72	1734	SUM	5.10	4.43	17.69	0.946	-	29.64
SO189/2_032	-1.62	100.00	1751	SUM	5.84	5.08	17.47	-	-	29.64
SO189/2_034	-1.46	100.23	560	SUM	5.87	5.10	48.27	-	-	29.59
SO189/2_035	-0.87	99.80	755	SUM	5.77	5.02	37.39	-	-	29.67
SO189/2_038	-0.79	99.91	517	SUM	6.03	5.24	55.86	-	-	29.68
SO189/2_041	0.34	98.13	674	SUM	5.96	5.18	40.95	0.991	-	29.78

Sample	Latitude (°N)	Longitude (°E)	Water depth (m)	Region[a]	*G. ruber* Mg/Ca (mmol/mol)[b]	*G. ruber* Mg/Ca_{cor} (mmol/mol)[c]	$\Delta[CO_3^{2-}]$[d]	$U^{K'}_{37}$[e]	Alkenone conc. (ng/g)	maSST[f] (°C)
SO189/2_048	0.95	98.13	457	SUM	6.11	5.31	63.63	0.986	-	29.83
SO189/2_053	1.00	98.03	82	SUM	6.33	5.50	167.95	-	-	29.82
SO189/2_059	1.15	98.07	479	SUM	6.38	5.55	60.02	-	-	29.82
SO189/2_060	1.45	98.05	551	SUM	5.70	4.96	49.78	0.990	-	29.86
SO189/2_072	2.83	96.39	913	SUM	5.78	5.03	31.87	-	-	29.86
SO189/2_076	2.82	96.61	1108	SUM	5.79	5.03	27.43	-	-	29.89
SO189/2_080	2.95	96.50	1088	SUM	6.06	5.27	27.83	0.959	-	29.86
SO189/2_084	2.99	96.22	861	SUM	6.03	5.24	33.45	-	-	29.83
SO189/2_089	2.78	96.42	916	SUM	5.96	5.18	31.79	0.972	-	29.86
SO189/2_097	2.56	96.76	1136	SUM	5.79	5.03	26.88	0.991	-	29.84
SO189/2_101	2.49	97.12	767	SUM	5.52	4.80	36.90	-	-	29.87
SO189/2_104	3.20	96.78	1013	SUM	5.57	4.84	29.33	-	-	29.92
SO189/2_112	3.87	96.01	81	SUM	6.74	5.86	168.37	-	-	29.82
SO189/2_114	3.49	95.33	1535	SUM	5.72	4.97	20.34	0.978	-	29.69
SO189/2_118	3.52	96.31	804	SUM	5.69	4.95	35.39	-	-	29.87
SO189/2_121	3.28	96.15	1031	SUM	5.53	4.81	28.97	-	-	29.85
SO189/2_139	1.76	96.77	1854	SUM	6.30	5.48	16.17	-	-	29.82
SO189/2_147	-0.69	98.07	1052	SUM	5.68	4.94	28.55	-	-	29.51
SO185-18456	-9.53	130.43	348	ETS	4.96	4.96	81.26	0.983	1489	28.60
SO185-18457	-9.45	130.18	394	ETS	4.83	4.83	73.21	0.984	1838	28.60
SO185-18458	-9.02	129.01	2045	ETS	4.50	4.50	13.85	0.981	760	28.63
SO185-18459	-8.50	128.17	1741	ETS	4.64	4.64	17.60	0.978	347	28.54
SO185-18460	-8.79	128.64	1876	ETS	4.86	4.86	15.90	0.983	295	28.61
SO185-18462	-9.09	129.24	1455	ETS	4.42	4.42	21.47	-	-	28.64
SO185-18463	-9.10	129.28	1311	ETS	4.84	4.84	23.67	-	-	28.64
SO185-18464	-9.12	129.32	1206	ETS	4.32	4.32	25.53	-	-	28.65
SO185-18465	-9.14	129.39	1082	ETS	4.84	4.84	27.95	-	-	28.64
SO185-18466	-9.16	129.42	1004	ETS	5.06	5.06	29.50	-	-	28.64

Sample	Latitude (°N)	Longitude (°E)	Water depth (m)	Region[a]	*G. ruber* Mg/Ca (mmol/mol)[b]	*G. ruber* Mg/Ca_{cor} (mmol/mol)[c]	$\Delta[CO_3^{2-}]$[d]	Alkenone $U^{K'}_{37}$[e]	Alkenone conc. (ng/g)	maSST[f] (°C)
SO185-18467	-9.17	129.47	899	ETS	-	-	-	0.968	185	28.64
SO185-18468	-9.20	129.53	803	ETS	5.15	5.15	35.43	0.982	835	28.63
SO185-18469	-9.24	129.64	704	ETS	5.02	5.02	39.55	-	-	28.62
SO185-18470	-9.30	129.80	603	ETS	5.05	5.05	44.99	0.981	1343	28.60
SO185-18471	-9.37	129.98	485	ETS	5.14	5.14	59.25	0.973	1058	28.59
SO185-18474	-11.17	122.15	1605	JAV	4.56	4.56	19.37	-	-	28.53
SO185-18475	-11.03	121.70	1771	JAV	4.56	4.56	17.21	0.979	1551	28.45
SO185-18476	-10.95	120.99	986	JAV	4.39	4.39	29.95	0.976	666	28.39
SO185-18477	-10.83	120.62	1480	JAV	4.50	4.50	21.11	0.973	495	28.37
SO185-18478	-11.02	120.08	1769	JAV	4.34	4.34	17.23	0.972	388	28.41
SO185-18479	-12.45	121.37	2974	WTS	-	-	-	0.963	203	28.84
SO185-18480	-12.52	121.65	2295	WTS	-	-	-	0.938	85	28.86
SO185-18481	-12.56	121.84	1897	WTS	4.52	4.52	15.65	0.977	348	28.88
SO185-18482	-12.62	122.15	1508	WTS	4.84	4.84	20.72	0.976	189	28.90
SO185-18483	-12.63	122.31	1356	WTS	4.76	4.76	22.95	-	-	28.90
SO185-18484	-12.66	122.37	1247	WTS	4.81	4.81	24.74	-	-	28.90
SO185-18485	-12.67	122.41	1132	WTS	5.06	5.06	26.96	0.952	92	28.90
SO185-18488	-12.89	122.76	555	WTS	5.09	5.09	49.11	0.974	245	28.95
SO185-18489	-13.05	122.93	431	WTS	4.85	4.85	67.98	0.980	733	28.96
SO185-18490	-13.24	122.95	407	WTS	4.89	4.89	71.22	0.981	645	28.96
SO185-18491	-13.82	122.99	327	WTS	5.07	5.07	84.57	-	-	28.95
SO185-18492	-14.14	122.65	350	WTS	5.49	5.49	80.93	-	-	28.92
SO185-18493	-13.42	122.08	599	WTS	5.15	5.15	45.25	-	-	28.91
SO185-18494	-13.38	121.92	839	WTS	5.22	5.22	34.16	-	-	28.91
SO185-18495	-13.12	121.86	1609	WTS	4.96	4.96	19.32	0.970	177	28.90
SO185-18496	-12.70	121.28	2541	WTS	-	-	-	0.971	224	28.85
SO185-18497	-12.70	121.28	2535	WTS	-	-	-	0.958	349	28.85
SO185-18499	-14.91	120.57	1383	WTS	5.19	5.19	22.52	0.965	144	28.78

Sample	Latitude (°N)	Longitude (°E)	Water depth (m)	Region[a]	*G. ruber* Mg/Ca (mmol/mol)[b]	*G. ruber* Mg/Ca_{cor} (mmol/mol)[c]	$\Delta[CO_3^{2-}]$[d]	$U^{K'}_{37}$[e]	Alkenone conc. (ng/g)	maSST[f] (°C)
SO185-18500	-14.98	120.70	1167	WTS	4.71	4.71	26.28	0.970	149	28.78
SO185-18501	-15.14	120.78	742	WTS	4.98	4.98	37.93	0.977	317	28.78
SO185-18502	-15.19	120.91	564	WTS	5.25	5.25	47.60	0.977	566	28.78
SO185-18503	-15.31	121.08	354	WTS	4.84	4.84	80.28	-	-	28.75
SO185-18505	-15.79	120.20	1045	WTS	5.15	5.15	28.69	0.979	324	28.65
SO185-18506	-15.31	119.50	2410	WTS	-	-	-	0.964	53	28.64
SO185-18507	-13.85	120.00	2450	WTS	-	-	-	0.949	53	28.78
SO217-18514	-4.53	118.95	652	MAJA	4.26	4.26	42.02	0.947	597	29.25
SO217-18515	-3.63	119.37	678	MAJA	-	-	-	0.981	514	29.18
SO217-18516	-1.64	117.54	930	MAJA	-	-	-	0.983	789	29.01
SO217-18517	-1.54	117.57	699	MAJA	4.45	4.45	39.76	0.984	811	29.01
SO217-18518	-1.14	117.84	620	MAJA	4.70	4.70	43.93	-	-	29.04
SO217-18519	-0.57	118.12	1657	MAJA	4.87	4.87	18.69	0.970	528	29.09
SO217-18521	0.51	118.93	991	MAJA	4.39	4.39	29.82	-	-	29.08
SO217-18522	1.40	119.09	986	MAJA	4.94	4.94	29.95	0.976	581	28.89
SO217-18523	0.18	119.44	2175	MAJA	5.22	5.22	12.35	0.963	173	29.16
SO217-18524	-1.66	118.91	1561	MAJA	4.47	4.47	19.98	-	-	29.41
SO217-18525	-2.56	118.64	1822	MAJA	5.50	5.50	16.56	-	-	29.38
SO217-18526	-3.62	118.17	1523	MAJA	5.03	5.03	20.51	0.989	860	29.09
SO217-18527	-3.97	117.82	1617	MAJA	5.48	5.48	19.22	0.988	722	29.11
SO217-18528	-4.76	117.89	1785	MAJA	4.90	4.90	17.03	0.982	763	29.19
SO217-18529	-4.66	118.03	1915	MAJA	4.35	4.35	15.43	0.984	487	29.21
SO217-18530	-5.24	117.34	872	MAJA	4.94	4.94	33.09	-	-	29.02
SO217-18531	-5.17	117.45	1085	MAJA	4.54	4.54	27.89	0.989	1063	29.05
SO217-18532	-5.93	116.83	628	MAJA	4.45	4.45	43.43	-	-	28.89
SO217-18534	-7.52	116.27	563	MAJA	4.43	4.43	47.76	0.983	459	28.85
SO217-18535	-7.14	117.22	506	MAJA	4.52	4.52	57.16	0.989	1431	28.76
SO217-18536	-7.47	118.24	835	MAJA	4.89	4.89	34.29	-	-	28.70

Sample	Latitude (°N)	Longitude (°E)	Water depth (m)	Region[a]	*G. ruber* Mg/Ca (mmol/mol)[b]	*G. ruber* Mg/Ca_{cor} (mmol/mol)[c]	$\Delta[CO_3^{2-}]$[d]	$U^{K'}_{37}$[e]	Alkenone conc. (ng/g)	maSST[f] (°C)
SO217-18537	-7.60	118.25	930	MAJA	4.49	4.49	31.42	-	-	28.75
SO217-18538	-7.60	118.27	908	MAJA	-	-	-	0.989	321	28.75
SO217-18539	-6.95	119.37	853	MAJA	4.46	4.46	33.71	-	-	28.61
SO217-18540	-6.88	119.59	1201	MAJA	4.56	4.56	25.63	0.933	225	28.60
SO217-18541	-6.78	119.41	739	MAJA	4.42	4.42	38.06	0.983	886	28.56
SO217-18542	-5.87	119.07	925	MAJA	4.80	4.80	31.55	0.981	768	28.48
SO217-18544	-4.53	118.59	2010	MAJA	-	-	-	0.969	307	29.30
SO217-18545	-5.10	118.73	714	MAJA	4.70	4.70	39.12	-	-	29.06

[a] Scheme of different regions is shown in Figure 5.2 .
[b] Raw Mg/Ca values, prior to correction. Data compiled from Regenberg et al. (2014), Mohtadi et al. (2011), and new measurements of this study.
[c] Mg/Ca values with 15 % correction (following Rosenthal et al., 2014) applied to samples from Mohtadi et al. (2011) to account for differences in cleaning methodology.
[d] $\Delta[CO_3^{2-}]$ calculated using SouthEast Asian Time Series (SEATS) stations (Chou et al., 2007) and World Ocean Circulation Experiment (WOCE) stations. See Section 5.5.6.
[e] $U^{K'}_{37}$ data compiled from Pelejero and Grimalt (1997), Mohtadi et al. (2011) and new measurements of this study.
[f] maSST derived from Advanced Very High Resolution Radiometer (AVHRR) satellite SST estimations (Reynolds et al., 2007

Chapter 5

Conclusions and Outlook

In this thesis, I examined the relationship between bottom water temperature and benthic Mg/Ca ratios and potential biases affecting this geochemical proxy commonly used for paleotemperature reconstructions. I additionally integrated new benthic Mg/Ca temperature reconstructions with geochemical and sedimentological proxy data to investigate changes in the hydrology of the Timor Strait over the past 134 ka. These findings provide new insights on the long-term evolution of the ITF deeper component over the last glacial – interglacial cycle, and improve knowledge of past climate dynamics in a region that plays a fundamental role in modulating global and local climate.

A modern core top study based on new and published *C. wuellerstorfi* and *H. elegans* Mg/Ca ratios indicates a geographical distribution of Mg/Ca ratios in relation to BWT. *Cibicidoides wuellerstorfi* shows Mg/Ca sensitivity to BWT of 19% increase in Mg/Ca per °C for the Atlantic Ocean and of 16% per °C for the Indian and Pacific Oceans. *Hoeglundina elegans* shows Mg/Ca sensitivity to BWT of 16% per °C in the Atlantic Ocean, and of 14% per °C for the Indo-Pacific Ocean. However, as the Atlantic Ocean dataset consists of only nine samples, more *H. elegans* Mg/Ca measurements are needed to better define the relationship between Mg/Ca and BWT for this area. The carbonate ion effect on *C. wuellerstorfi* Mg/Ca ratios is negligible for the BWT range of 0 to 6 °C, when samples from the Nordic seas are excluded from the Atlantic Ocean data set. In contrast, for the Indian and Pacific Oceans, the carbonate ion effect on *C. wuellerstorfi* Mg/Ca ratios could not be quantified due to the relatively high standard error associated with the basin-specific temperature equation. This higher standard error relates to the scarcity of *C. wuellerstorfi* Mg/Ca measurements above 2 °C, and future studies should focus on increasing the number of Mg/Ca measurements at the warmer end of this temperature calibration to

minimize the associated error and to enable reliable estimations of the carbonate ion effect on *C. wuellerstorfi* Mg/Ca ratios. The carbonate ion effect on *H. elegans* Mg/Ca ratios is negligible over the $\Delta[CO_3^{2-}]_{aragonite}$ range from -40 to 65 μmol kg^{-1} and over the BWT range from 2 to 12 °C for the selected Indo-Pacific data, excluding samples from shallow and warm waters (BWT >15 °C). Above 15 °C, depletion in Mg/Ca ratios occurred in the Indo-Pacific samples and it is unclear whether these measurements are representative of Mg/Ca natural variability or are affected by other factors. Future studies should concentrate on the warmer end of this temperature calibration to verify whether or not Mg depletion occurs at higher temperatures in *H. elegans* tests.

Cibicidoides wuellerstorfi Sr/Ca ratios show high potential to record past changes in carbonate ion saturation, as $\Delta[CO_3^{2-}]_{calcite}$ appears to drive *C. wuellerstorfi* Sr/Ca variability. Distinct *C. wuellerstorfi* Sr/Ca-$\Delta[CO_3^{2-}]_{calcite}$ relationships are found for the Atlantic, Indian and Pacific basins, which may be due to the higher "corrosiveness" of Indian and Pacific waters. Although *C. wuellerstorfi* Sr/Ca variability appears to be driven by $\Delta[CO_3^{2-}]_{calcite}$, limitations apply to the use of this ratio as a carbonate ion saturation proxy in paleoclimate reconstructions, as it is unclear to what extent this relationship remained constant in the past, due to the uncertainties related to seawater Sr/Ca variability over time. *Hoeglundina elegans* Sr/Ca variability appears to be driven by BWT, most likely because of the aragonitic mineralogy of this benthic foraminiferal species. No geographical trend in the distribution of *H. elegans* Sr/Ca ratios in relation to BWT is apparent between the Atlantic and Indo-Pacific Oceans, possibly because of the limited number of Sr/Ca measurements in the Atlantic Ocean dataset. The same limitations to the use of *C. wuellerstorfi* Sr/Ca ratios as a carbonate ion saturation proxy apply to the use of *H.*

elegans Sr/Ca ratios as a paleotemperature proxy.

Based on the same core top samples, the relationships between SST and *G. ruber* Mg/Ca ratios and the $U^{K'}_{37}$ alkenone unsaturation index were examined. Lower $U^{K'}_{37}$ sensitivity to SST was found above 26 °C in contrast to previous global calibrations. Furthermore, variations in seasonal productivity appear to control $U^{K'}_{37,}$ with temperature estimates biased towards low-productivity months in region of highly variable production regimes, such as upwelling areas. The combination of new *G. ruber* Mg/Ca ratios with previously published data is complicated by the usage of different cleaning techniques (oxidative vs. reductive cleaning), which lead to systematic offsets of more than 1.5 °C and high scatter, when Mg/Ca ratios were plotted versus SST. This suggests that other mechanisms unrelated to seasonal temperature changes may influence *G. ruber* Mg/Ca variability. Although the carbonate ion effect on *G. ruber* Mg/Ca ratios could not be quantified, it seems to have a significant influence on Mg/Ca variability below 21.3 μmol kg^{-1}. Furthermore, changes in salinity and pH should be also considered as potential second-order forcings driving *G. ruber* Mg/Ca variability. Recent proxy-model approaches have reported success in using seasonal-weighting of modeled temperatures in explaining discrepancies between Mg/Ca-based and $U^{K'}_{37}$-derived SST estimates over the last glacial period and the Holocene. However, these model studies did not include other variables, such as salinity and pH, to provide more insights into the discrepancies associated with the use of different temperature proxies.

Hydrological changes related to variations in the ITF vertical structure, monsoon variability and shelf dynamics during the last 134 ka were investigated through a multi-proxy analysis of sediment core SO18471, retrieved at the southern edge of the Timor Strait, close to the Sahul Shelf. Grain size records based on XRF-

derived log(Zr/Rb) and proportion of coarse (>63µm) material show that during sea level highstands sediment winnowing intensified due to the development of a strong ITF outflow in the Timor Sea, and the opposite occurred during sea level lowstands. However, during the later part of Termination II and MIS 5e, sediment winnowing did not increase suggesting an intensification of the local wet monsoon, also reflected in the more terrigenous sediment composition of core SO18471. Surface and lower thermocline temperature and $\delta^{18}O_{sw}$ records show a glacial – interglacial trend: the surface is generally warmer (on average by ~2 °C) and saltier during globally warm periods (MIS 5a-d and 1), whereas the lower thermocline is generally cooler (on average by ~1.4 °C) and fresher than during globally cold periods (from MIS 4 to MIS 2). This most likely reflects the intensification and expansion of a cool and fresh thermocline ITF during sea level highstands, resulting in generally cool and fresh bottom waters at the core location. An exception to this glacial – interglacial trend is evident during early MIS 5e and the early Holocene, as transient warming events of the thermocline were recorded at the core location. At this time, Northern Hemisphere summer insolation was high, warming the ITF source waters at higher latitudes, which were eventually transferred at intermediate depth in the tropics. High-resolution paleoclimate records focusing on deeper ocean variability are necessary to reconstruct ocean intermediate circulation and their impact on regional and global climate evolution. In particular, it remains a major challenge to evaluate temporal changes in the ocean's heat content in order to better understand the role of the ocean as a thermal buffer. The Indonesian seas are an ideal location for this endeavor, as they represent a major crossroad for water masses originating from both northern and southern high latitudes.

Appendix A

Hoeglundina elegans Mg/Ca ratios were measured with laser ablation in 28 selected samples from sediment core SO18471, retrieved in the Timor Sea close to the Sahul Shelf (9° 21.9870’ S, 129° 58.9830’E; 485 m water depth; 13.5 m length). Two different morphotypes of *H. elegans* were found in one restricted interval of core SO18471 (400 – 750 cm) and it was crucial to verify whether or not these different morphotypes have comparable geochemical characteristic before using them as paleotemperature proxy (Fig. A1a). We decided to perform laser ablation instead of wet chemistry, as the abundance of *H. elegans* specimens within the above-mentioned interval was overall low.

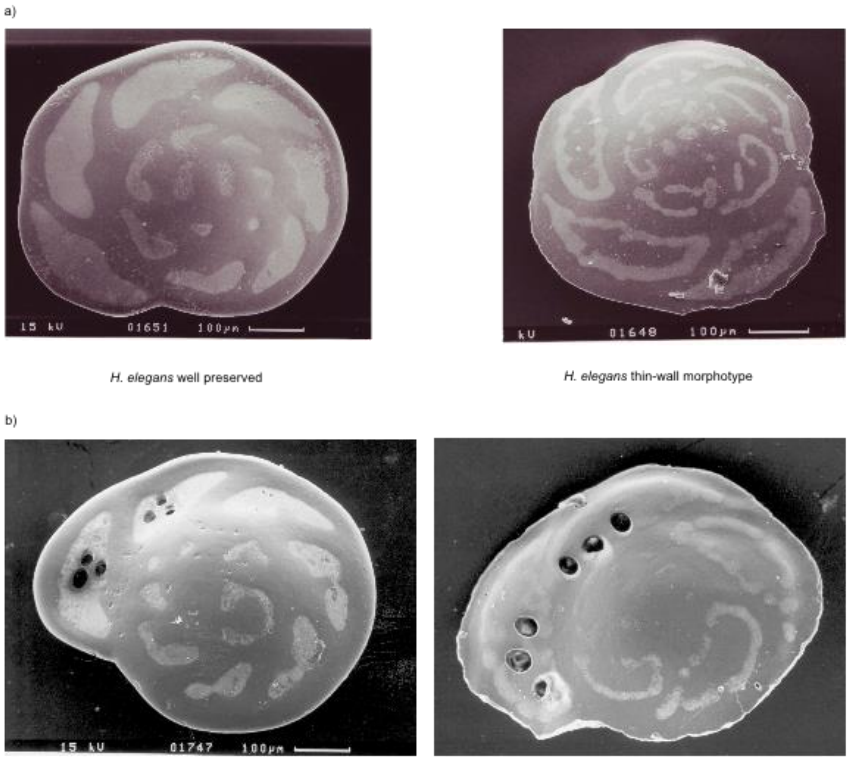

Fig. A1. SEM micrographs. **a)** Well preserved *H. elegans*, representative of the majority of specimens in core SO18471; thin-walled morphotype of *H. elegans* preferentially found in the interval between 400 and 750 cm. **b)** Ablated *H. elegans* tests of well preserved and thin-walled specimens, respectively.

Hoeglundina elegans Mg/Ca measurements

Hoeglundina elegans specimens were mounted with adhesive pads onto glass slides and arranged within a two-volume ablation cell (Zurich LDHCLAC ablation cell, [*Fricker et al*., 2011]) without any cleaning procedure. However, only well-preserved and clean tests were picked (Fig. A. 1b). We ablated for each specimen two chambers by drilling three craters per each chamber. Foraminifera were ablated using an ArF excimer laser operating at 193 nm (GeoLas Plus, Coherent/Lambda Physik, Germany). Ablation was performed in helium atmosphere (1 L/min) that was mixed with argon (0.8 L/min) before entering the ICP-MS (Inductively Coupled Plasma-Mass Spectrometry). We used a pulse repetition rate of 5 Hz with an energy density at the sample surface of 5 J cm^{-2} producing ablation craters with 20 μm diameter. The ablated particles were analysed with ICP-MS using an Agilent 7500s with Ni interface. The integration time was 20 ms per m/z in transient mode and calibration was performed against NIST 612 (National Institute of Standards and Technology, [*Jochum et al*., 2011]), with ^{44}Ca as an internal standard for quantification. A pressed powder tablet of ECRM 752 [*Greaves et al.*, 2008] was analyzed with each sample batch at the beginning and end of each session as an unknown sample. Element concentrations were measured using ^{24}Mg, ^{27}Al, ^{44}Ca, ^{55}Mn, ^{85}Rb, ^{88}Sr. Integration of time-resolved data was performed using the GLITTER software package (Macquarie University), and the signal from the first seconds of ablation was discarded to avoid non-stoechiometric laser sampling and surface contamination of the foraminifera tests.

To infer about variability within the same chamber (intra-chamber variability) and within chambers (inter-chamber variability), we ablated in 11 tests of *H. elegans* the final chamber (F), in 18 tests the penultimate chamber (F-1), in 9 tests the third to

last chamber (F-2), in 7 tests the forth to last chamber (F-3), in 4 tests the fifth to last chamber (F-4), in 2 samples the sixth two last chamber (F-5) and in one sample the seventh to last chamber (F-6). In two specimens of *H. elegans* was not possible to identify which chamber was ablated because tests got completely destroyed during ablation (Table 1).

Results and Discussion

Two different morphotype of *H. elegans*

Four paired samples containing both morphotypes of *H. elegans* showed no specific pattern in Mg/Ca variability, being the average difference in Mg/Ca between the two morphotypes 0.08±0.25 mmol mol^{-1} (Fig. A2a). Therefore we did not discriminate between the two morphotype to reconstruct temperature.

Intra-chamber variability

Hoeglundina elegans Mg/Ca ratios vary between 0.41 and 1.57 mmol mol^{-1} in core SO18471 and overall little variability is shown within the same chambers (Fig. A2b). We calculated the standard deviation between measurements performed within the same chamber and it varies between ±0.01 and ±0.26 mmol mol^{-1}, being on average ±0.07 mmol mol^{-1}. These values are comparable with the reproducibility of ±0.19 mmol mol^{-1} found for *H. elegans* Mg/Ca ratios measured using wet chemistry in core SO18471 [*Lo Giudice Cappelli et al.*, submitted]. Table 1 shows more into detail the reproducibility of measurements performed within the same chamber. For the final chamber we found an average reproducibility of ±0.12 mmol mol^{-1}, for the penultimate and for the forth to last chambers of ±0.07 mmol mol^{-1}, for the third to

last chamber of ±0.05 mmol mol^{-1}, and for the fifth and sixth to last chambers of ±0.06 mmol mol^{-1} (Fig. A2b). The last chamber appears to show the highest Mg/Ca variability.

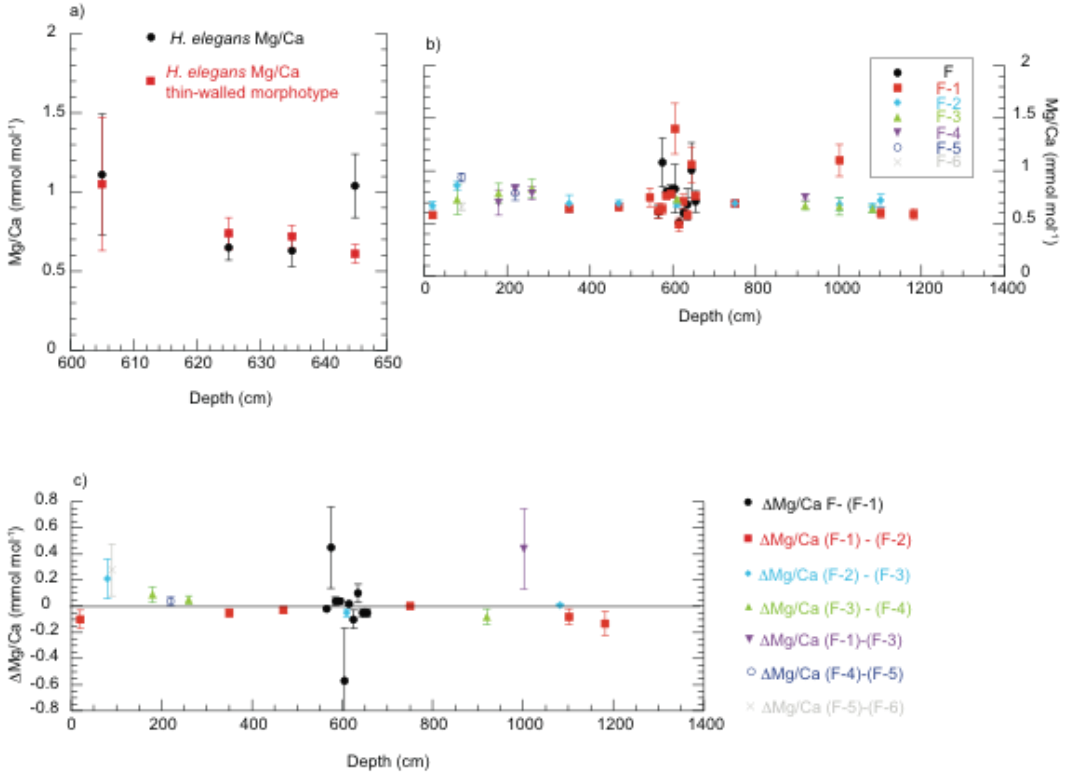

Fig. A2. a) Comparison of Mg/Ca ratios measured in both morphotypes of *H. elegans* from the same foraminiferal samples. **b)** Mg/Ca intra-chamber variability. **c)** Mg/Ca inter-chamber variability.

Inter-chamber variability

The inter-chamber variability is also relatively low (Fig. A2c). To better describe Mg/Ca variability between chambers, we grouped our samples accordingly to which pair of chambers was drilled.

Final and penultimate chambers (11 samples)

The difference (ΔMg/Ca) between Mg/Ca ratios measured in the final chamber and in the penultimate chamber does not show any specific trend, varying between -0.57 and 0.45 mmol mol^{-1}, being on average -0.01 ±0.25 mmol mol^{-1} (Fig. A2c). These measurements show the highest inter chamber Mg/Ca heterogeneity.

Penultimate and third to last chambers (6 samples)

Mg/Ca ratios measured in the penultimate chamber are always slightly lower that Mg/Ca ratios measured in the third to last chamber. However the difference (ΔMg/Ca) is very low, varying between -0.13 and 0 mmol mol^{-1}, being on average -0.06 ±0.05 mmol mol^{-1} (Fig. A2c).

Penultimate and forth to last chambers (1 sample)

The difference (ΔMg/Ca) between Mg/Ca ratios measured in these two chambers is relatively high 0.44 mmol mol^{-1} (Fig. A2c). However, only one sample was measured and therefore it is not yet clear if this high Mg/Ca heterogeneity is real or a bias due to sample contamination.

Third to last and forth to last chambers (3 samples)

The difference (ΔMg/Ca) between Mg/Ca ratios measured in the third and forth to last chambers does not show any specific trend, varying between -0.05 and 0.21 mmol mol^{-1}, being on average -0.06 ±0.14 mmol mol^{-1} (Fig. A2c).

Forth to last and fifth to last chambers (3 samples)

The difference (ΔMg/Ca) between Mg/Ca ratios measured in the forth and fifth to last chambers does not show any specific trend, varying between -0.08 and 0.09 mmol mol^{-1}, being on average 0.02 ±0.09 mmol mol^{-1} (Fig. A2c).

Fifth to last and sixth to last chambers (1 samples)

The difference (ΔMg/Ca) between Mg/Ca ratios measured in these two chambers is 0.04 mmol mol^{-1} (Fig. A2c).

Sixth to last and seventh to last chambers (1 samples)

The difference (ΔMg/Ca) between Mg/Ca ratios measured in these two chambers is 0.28 mmol mol^{-1} (Fig. A2c).

Conclusion

We laser ablated *H. elegans* tests in 28 selected samples from sediment core SO18471, as in one interval of the core SO18471 (400 -750 cm) two morphotype of *H. elegans* occurred and their overall abundance was low. The two morphotypes of *H. elegans* show a similar geochemical composition of their tests (comparable Mg/Ca ratios), allowing using both morphotype indiscriminately to reconstruct BWT variability over the last 134 ka in core SO18471.

Intra and inter chamber variability in *H. elegans* tests is overall low and comparable to the reproducibility found for *H. elegans* Mg/Ca ratios based on wet chemistry measurements. Nevertheless, measurements performed in *H. elegans* final chamber show the highest intra chamber variability as well as the highest inter

chamber heterogeneity with Mg/Ca measurements performed in the penultimate chamber.

Table 1

Sample name	Depth in core	Age	Chamber	Mg/Ca, Drill1	Mg/Ca, Drill 2	Mg/Ca, Drill 3	Average Mg/Ca	Standard deviation
036O5651	565	51.119	F	0.67	0.59	0.56	**0.61**	0.06
051O5751	575	51.684	F	0.92	1.34	0.99	**1.08**	0.23
066O5851	585	51.967	F	0.77	0.82	0.82	**0.80**	0.03
081O5951	595	52.816	F	0.78	0.80	0.88	**0.82**	0.05
105N6051	605	53.382	F	0.66	0.99	-	**0.83**	0.23
126O6151	615	53.947	F	0.53	0.50	0.51	**0.51**	0.01
150N6251	625	54.513	F	0.65	0.57	0.59	**0.60**	0.04
171N6351	635	55.078	F	0.79	-	0.58	**0.68**	0.15
201N6451	645	55.644	F	1.15	1.18	0.72	**1.01**	0.26
222N6551	655	56.21	F	0.83	0.65	0.66	**0.71**	0.10
Average								**0.12**
178H201	20	7.1807	F-1	0.58	0.55	0.61	**0.58**	0.03
065H3501	350	38.957	F-1	0.65	0.65	0.62	**0.64**	0.02
050H4701	470	45.745	F-1	0.69	0.68	0.62	**0.66**	0.04
013O5453	545	49.987	F-1	0.69	0.85	0.71	**0.75**	0.09
039O5652	565	51.119	F-1	0.58	0.71	0.58	**0.62**	0.07
054O5752	575	51.684	F-1	0.63	0.69	0.59	**0.64**	0.05
069O5852	585	51.967	F-1	0.78	0.76	0.76	**0.76**	0.01
084O5952	595	52.816	F-1	0.82	0.75	0.78	**0.78**	0.04
108N6052	605	53.382	F-1	-	1.57	1.22	**1.40**	0.24
129O6152	615	53.947	F-1	0.55	0.41	0.52	**0.49**	0.07
153N6252	625	54.513	F-1	0.72	0.76	0.63	**0.71**	0.07
174N6352	635	55.078	F-1	0.57	0.62	0.54	**0.58**	0.04
204N6452	645	55.644	F-1	1.09	1.21	0.88	**1.06**	0.17
225N6552	655	56.21	F-1	0.80	0.74	0.74	**0.76**	0.03
100H7501	750	61.866	F-1	0.67	0.71	-	**0.69**	0.02
130H1001	1002	93.972	F-1	1.06	0.97	1.27	**1.10**	0.15
073H1101	1102	108.42	F-1	0.54	0.64	0.61	**0.60**	0.05
058H1181	1182	123.31	F-1	0.57	0.55	0.63	**0.59**	0.05
Average								**0.07**
181H202	20	7.1807	F-2	0.64	0.72	0.67	**0.67**	0.04
163H801	80	17.789	F-2	0.87	0.90	0.82	**0.86**	0.04
068H3502	350	38.957	F-2	0.70	0.60	0.75	**0.69**	0.08
053H4702	470	45.745	F-2	0.73	0.67	0.67	**0.69**	0.03
010H6101	610	53.664	F-2	0.66	0.68	0.69	**0.68**	0.02
103H7502	750	61.866	F-2	0.74	0.69	0.65	**0.69**	0.04
88H1081	1082	102.05	F-2	0.60	0.69	0.66	**0.65**	0.04
076H1102	1002	108.42	F-2	0.66	0.64	0.75	**0.68**	0.06
061H1182	1102	123.31	F-2	0.71	0.66	0.77	**0.72**	0.06
Average								**0.05**
166H802	80	17.789	F-3	0.89	0.67	0.63	**0.73**	0.14
041H1801	180	28.417	F-3	0.88	0.79	0.69	**0.79**	0.09
010H2601	260	33.866	F-3	0.77	-	0.90	**0.83**	0.09
013H6102	610	53.664	F-3	0.75	0.72	0.71	**0.73**	0.02
115H9201	920	84.223	F-3	0.71	0.65	0.65	**0.67**	0.04
133H1002	1002	93.972	F-3	0.75	0.60	0.63	**0.66**	0.08
91H1082	1082	102.05	F-3	0.61	0.66	0.65	**0.64**	0.03
Average								**0.07**
044H1802	180	28.417	F-4	0.83	0.64	0.62	**0.70**	0.12
027H2201	220	31.603	F-4	0.83	0.79	0.87	**0.83**	0.04
013H2602	260	33.866	F-4	0.82	0.81	0.72	**0.79**	0.06
118H9202	920	84.223	F-4	0.77	-	0.73	**0.75**	0.03
Average								**0.06**
148H901	90	18.847	F-5	0.96	0.90	0.96	**0.94**	0.04
030H2202	220	31.603	F-5	0.74	0.76	0.87	**0.79**	0.07
Average								**0.06**
151H902	90	18.847	F-6	0.70	0.67	0.62	**0.66**	0.04
Total Average								***0.07***

References

Fricker, M. B., D. Kutscher, B. Aeschlimann, J. Frommer, R.Dietiker, J. Bettmer, and D. Günther (2011), High spatial resolution trace element analysis by LA-ICP-MS using a novel ablation cell for multiple or large samples, *Int. J. Mass Spectrom*., **307**, 39–45.

Greaves, M., et al. (2008), Interlaboratory comparison study of calibration standards for foraminiferal Mg/Ca thermometry, *Geochemistry Geophysics, Geosystems*, **9**, Q08010, doi:10.1029/2008GC001974.

Jochum, K. P., U. Weis, B. Stoll, D. Kuzmin, Q. Yang, I. Raczek, D. E. Jacob, A. Stracke, K. Birbaum, D. A. Frick, D. Günther, and J. Enzweiler (2011), Determination of reference values for NIST SRM 610–617 glasses following ISO guidelines. *Geostandards Geoanalytical Res*., **35**, 397–429. doi: 10.1111/j.1751-908X.2011.00120.x.

A DIVERSE PATCH REEF FROM TURBID HABITATS IN THE MIDDLE MIOCENE (EAST KALIMANTAN, INDONESIA)

Source: PALAIOS, 30(1):128-149.
Published By: Society for Sedimentary Geology
URL: http://www.bioone.org/doi/full/10.2110/palo.2013.047

PALAIOS
Emphasizing the impact of life on Earth's history

PALAIOS, 2015, v. 30, 128–149
Research Article
DOI: http://dx.doi.org/10.2110/palo.2013.047

A DIVERSE PATCH REEF FROM TURBID HABITATS IN THE MIDDLE MIOCENE (EAST KALIMANTAN, INDONESIA)

NADIEZHDA SANTODOMINGO,[1] VIBOR NOVAK,[2] VEDRANA PRETKOVIĆ,[3] NATHAN MARSHALL,[4] EMANUELA DI MARTINO,[1] ELENA LO GIUDICE CAPELLI,[5] ANJA RÖSLER,[3] SONJA REICH,[2] JUAN CARLOS BRAGA,[3] WILLEM RENEMA,[2] AND KENNETH G. JOHNSON[1]

[1]*Natural History Museum, Department of Earth Sciences, Cromwell Road, SW7 5BD, London, UK*
[2]*Naturalis Biodiversity Center, Department of Geology, P.O. Box 9517, 2300 RA Leiden, The Netherlands*
[3]*Universidad de Granada, Departamento de Estratigrafía y Paleontología, Campus Fuente Nueva s/n, 18002 Granada, Spain*
[4]*Utrecht University, Department of Earth Sciences, Budapestlaan 17, 3584 CD Utrecht, The Netherlands*
[5]*Institute of Geosciences, Marine Micropaleontology, Ludewig-Meyn-Str. 14, D-24118 Kiel, Germany*
e-mail: n.santodomingo@nhm.ac.uk

ABSTRACT: **The Kutai Basin (East Kalimantan, Indonesia) contains a rich and well-preserved Miocene fossil record of small patch reefs that developed under the influence of high siliciclastic input associated with the progradation of the Mahakam Delta. In this study, we reconstruct the biodiversity and paleoenvironments on one of these delta-front, mixed carbonate-siliciclastic systems that developed at the Serravallian–Tortonian boundary near the city of Samarinda. In two newly exposed sections, we analyzed the sedimentology and distribution of the main fossil biota including corals, foraminifers, coralline algae, and bryozoans. Seven facies are herein defined, including two dominated by platy corals and two by larger benthic foraminifera. Facies distributions were driven by changes in depth and variations in terrigenous input within a range of delta-front habitats. Despite the turbid conditions, fossil assemblages are highly diverse, including 69 coral species and 28 bryozoan species that occur in coral-dominated facies. Crustose coralline algae were mainly associated with the coral-dominated facies. Larger benthic foraminifera showed broader ecological tolerance within the range represented in the studied sections and thus are common in most facies. These diverse patch reef ecosystems were able to cope with high siliciclastic input during the early development of the Miocene coral reef biota.**

INTRODUCTION

Coral reefs are declining worldwide as a result of human activities (Hughes et al. 2003; Hoegh-Guldberg 2011). Anthropogenic stressors include local activities such as overfishing and water pollution from urban areas, and at broader scale, global warming and declining pH (Bellwood et al. 2004; Hughes et al. 2007). Global warming has changed rainfall patterns (Xie et al. 2010) that, in combination with coastal expansion and deforestation around river basins, have led to increased discharges of sediments into the oceans. As a consequence, many coral reefs have undergone phase shifts into systems tolerant of sediment input (Hughes et al. 2007; Hoegh-Guldberg et al. 2007).

Understanding the dynamics of coral reefs living under terrigenous input contributes to a better understanding of the ecological processes that support reef resilience. Terrigenous influx is a key control on the development of coral reefs, because (1) it leads to increased water turbidity, reducing light available for light-dependent organisms; and (2) smothering of biota due to high sedimentation regimes (Rogers 1990; Nugues and Roberts 2003; Fabricius 2005). Numerous studies have shown that prolonged exposure to sediment discharge from rivers has a negative impact on corals and other reef biota leading to decreased coral reef health (Rogers 1990; Katwijk et al. 1993; Stafford-Smith 1993; Fabricius and De'ath 2001; Fabricius 2005). There is also a generally accepted view that coral diversity tends to be low in reefs that are substantially influenced by siliciclastic input (Van Woesik et al. 1999; DeVantier et al. 2006; De'ath and Fabricius 2010). In contrast, other studies challenge the idea of a negative effect of high rates of sedimentation on reef development (Kleypas et al. 1999; Larcombe et al. 2001; Perry et al. 2012; Browne et al. 2012). Indeed, Perry et al. (2012) found that periods of most rapid accretion over the past ~ 700 years coincide with phases of reef development dominated by fine-grained terrigenous sediment accumulation.

Paleoecological studies are key to understanding the dynamics of the environmental parameters that drive coral reef development and diversity at broader temporal and spatial scales (Perry et al. 2009; Roff et al. 2013). In the geological record there are numerous examples of coral assemblages developing in turbid-water environments since at least the Late Triassic (Rosen et al. 2002) in the Mediterranean (Hayward 1982; Braga et al. 1990; Morsilli et al. 2011; Pomar et al. 2012) and the Caribbean (McNeill et al. 2000; Klaus et al. 2008). In fact, the fossil record of Southeast Asia, the region that hosts today the most diverse marine ecosystems on Earth (commonly referred to as the Coral Triangle; Bellwood et al. 2005; Hoeksema 2007), is rich in well-preserved coral assemblages that mainly developed under high sediment influx (Gerth 1923; Umbgrove 1929; Wilson 2005; Novak et al. 2013).

Sedimentology and carbonate dynamics of Miocene reefs in the Coral Triangle have been studied in a regional context (Wilson and Lokier 2002; Wilson 2005), revealing the potential high diversity of patch reefs that formed in mixed carbonate-siliciclastic deposits (Wilson 2005). Still, little is known about the species composition, development, and detailed paleoecology of those Miocene turbid environments. Due to urban

Published Online: February 2015
 0883-1351/15/030-128/$03.00

development in the area, numerous new outcrops are exposed regularly, increasing the number of sections through patch reefs beyond those available for study by Wilson (2005).

In the current study, we characterize a new example of coral-rich facies that occur within mixed carbonate-siliciclastic systems in the region referred to as the Stadion coral carbonates (Stadion CC) as they are exposed on the highway leading to *Stadion Utama Kaltim*, which opened in 2008. The main goals of this study are: (1) to describe the assemblages of corals, benthic foraminifera, coralline algae, bryozoans, and mollusks occurring in the Stadion CC sections; (2) to perform a paleoenvironmental reconstruction based on the analyses of the sedimentology and biota; (3) to describe the developmental stages of the Stadion CC sections; and (4) to discuss the importance of terrigenous input as a controlling factor for modern coral reefs.

GEOLOGICAL SETTING

The study area is located within the Kutai Basin in East Kalimantan (Fig. 1), a depositional basin that originated during the middle Eocene when the Makassar Straits and Philippine Sea opened (Cloke et al. 1999; Wilson and Moss 1999). Throughout the Miocene, large amounts of clastic sediments formed rapidly prograding deltas (Hall and Nichols 2002). In particular, during the middle Miocene more than 4 km of shelf to fluvial sediments were deposited as the Mahakam Delta system prograded to its current position (Wilson and Moss 1999; Hall and Nichols 2002; Marshall et al. 2015). The modern Mahakam Delta is located on a low wave-energy coast. Its dynamics are tide dominated so that the deltaic sediments are characterized by high silt and clay contents as little sand is sorted by longshore currents (Allen and Chambers 1998; Storms et al. 2005).

The Miocene Mahakam Delta succession (Fig. 2A) begins with shale-dominated shelf deposits and includes several carbonate intervals that are exposed as prominent ridges such as the Batu Putih patch reefs (Moss and Chambers 1999; Wilson 2005; Lokier et al. 2009; Marshall et al. 2015). Stratigraphically above the Batu Putih patch reefs, deltaic sedimentation takes place and sandstone progressively becomes the dominant lithology, often directly above coal beds. Based on magnetostratigraphic analyses that correlate the Samarinda polarity pattern and the geomagnetic polarity timescale, an average sedimentation rate of ~ 75 cm/kyr has been estimated throughout the Samarinda sequence (Marshall et al. 2015). The Stadion CC is a second set of fossiliferous carbonates (Fig. 2). Within 20 m above the Stadion CC, fluvial sedimentation resumes as thick sandstone and nonfossiliferous shale (Marshall et al. 2015).

The age of the Stadion locality has been placed close to the Serravallian–Tortonian boundary (11.6 Ma) using integrated magnetostratigraphy and biostratigraphy (Marshall et al. 2015). Thus, the Stadion CC is younger than other Samarinda carbonate sections previously studied by Wilson (2005).

Terminology

Facies descriptions in this work follow the nomenclature and characterizations developed by Insalaco (1998). These terms are an extension of the boundstone category applied by Dunham (1962) to facies that are dominated by *in situ* bioconstructors (corals, sponges, bryozoans, etc.) in growth position that may or may not form a true framework. From this approach, the term growth fabric is used to describe the structure of coral facies. The term framework, *sensu stricto*, is applied when a degree of rigidity, wave resistance, and intergrowth can be inferred for the growth fabric (Insalaco 1998). The Insalaco nomenclature is based on the growth form of scleractinian corals as the primary descriptor. Thus, a facies dominated (> 60%) by branching corals is named a pillarstone, by platy to tabular corals (width to height ratio ≤ 30 to ~ 3:1) is a platestone, by thin-platy to sheet-like corals (width to height ratio > 30:1) is a sheetstone, by domal massive corals is a domestone, and finally, by a variety of coral growth morphologies is a mixstone. Regarding the geometry of the bioconstructions, the term biostrome is applied to bioclastic accumulations that are distinctly bedded and do not thicken into lenses so that their upper and lower surfaces are flat and parallel. In contrast, bioherm is used to define rigid structures that caused modification of seabed topography and therefore are likely to have distinct ecological zonation (Cummings 1932).

Although extensively used in paleoenvironmental interpretations, the terms reef and patch reef have countless contradictory and ambiguous definitions (see review in Fagerstrom 1987; Rosen 1990). Therefore, we constrain our direct comparisons to previous studies in Kalimantan region (Moss and Chambers 1999; Wilson and Lokier 2002; Wilson 2005, 2008; Lokier et al. 2009; Novak et al. 2013). In East Kalimantan, the term patch reef has been applied to modern coral communities characterized as small isolated assemblages, which develop in shallow waters on the delta front, eight kilometers from the mouth of the Berau River (Tomascik et al. 1997). A similar approach was used for the interpretation of Miocene fossil coral assemblages located in the delta front of the Mahakam delta, in which the term patch reef has been applied to carbonate structures that "developed in shallow waters, form low-relief coral buildups, lack rigid frameworks, and had gently sloping margins of a few degrees" (Wilson 2005). It is important to note that Wilson's definition implies the use of the term reef in a broad sense due to the "lack of rigid framework" of the carbonate structures. Likewise, in the present study, the term patch reef is used in concordance with Wilson (2005), to describe coral carbonates regardless of the lack or presence of rigid frameworks (Moss and Chambers 1999; Wilson and Lokier 2002; Wilson 2008; Lokier et al. 2009; Novak et al. 2013).

From our descriptive approach, we use the word biostrome independently from the term coral carpets as proposed by Riegl and Piller (2000a, 2002), because the use of coral carpets implies an environmental interpretation by analogy with modern coral settings. While coral carpets can be preserved as biostromes, not all biostromes have been interpreted as coral carpet successions (e.g., algal biostromes, Bosence 1983; Benisek et al. 2009; bryozoan biostromes, Taylor and Zaborski 2002). These concepts provide the background for further interpretations of the different facies within the Stadion CC.

METHODS

The Stadion CC are exposed in two outcrops: Stadion CC-1 located at 0.585° S, 117.120° E (Fig. 1C); and Stadion CC-2 at 0.586° S, 117.120° E (Fig. 1D). These outcrops are 150 m apart, at the crossroad of the stadium highway and a local coal mine road. The two studied sections are 8–10 m thick (Figs. 1C–D), with an eastward dip of 55°. Both consist of lateral exposure of a few tens of meters but are partially covered by vegetation (Figs. 1C–D). Both sections were logged and sampled to identify lithological units, sedimentary structures, relative abundance of carbonaceous content, sediments, and fossil components, and main taphonomic features. Photographs were taken to describe morphology and lateral variation and the units were correlated and summarized in two logs (Fig. 2B). Annotated photographs with shaded facies overlays are provided in Figure 3. Lithological samples were collected from each unit for further microfacies analysis utilizing 21 standard thin sections (28 × 48 mm). Lithology and facies descriptions follow Folk (1980) for siliciclastics, and Dunham (1962) and Insalaco (1998) for carbonates.

The carbonate content of the sediment matrix was determined using Total Inorganic Carbon (TIC) analysis. Fifty mg of each sample was ground and then analyzed with the front-end acid digestion instrument CM 5240, which converts inorganic carbonate into CO_2. The CO_2 was transported into a UIC Inc. CM 5014 Coulometer that measures the TIC

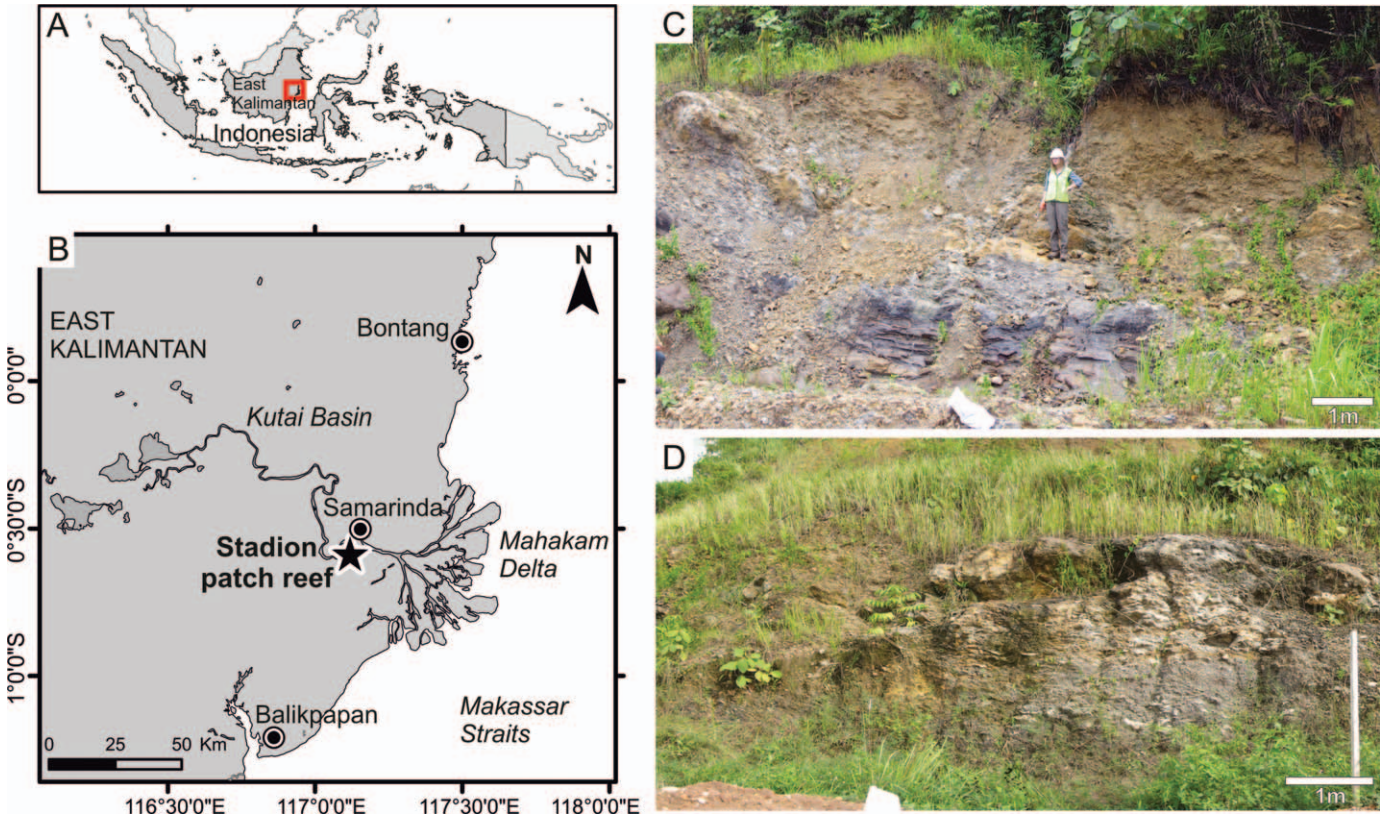

FIG. 1.—Location of the Stadion patch reef. **A**) Location of East Kalimantan in Indonesia. **B**) Location of Samarinda city and the Stadion patch reef, east of the present-day Mahakam Delta. **C**) Outcrop photograph of locality Stadion CC-1. **D**) Outcrop photograph of locality Stadion CC-2.

percentage from which the $CaCO_3$ percentage was calculated. A 12% carbon standard was used for the instrument calibration.

Fossil Content

The Stadion CC sections preserve a diverse assemblage that includes corals, foraminifers, coralline algae, bryozoans, and mollusks. In addition, some echinoid spines, serpulid tubes, small brachiopods, and crustacean chelae were found within the sediments or cemented to coral surfaces. In this study, only the former five main groups are discussed based primarily on the relative abundance of these taxa. The primary datasets used to describe the distributions of these five main taxa within the study interval include field observations, hand specimens and bulk samples collected from the fossiliferous units, and thin sections. Bulk samples were collected randomly within each unit and also along 4–5-m-long line transects. Transects were placed at each observed change of composition within each unit, thus nine transects were measured at Stadion CC-1 and seven equivalent transects at Stadion CC-2 (Fig. 3).

Bulk samples consisted of approximately 5 to 7 kg mix of sediment and fossil material obtained from each outcrop unit. The bulk samples were soaked in water, washed, and sieved through 5 mm, 2 mm, 500 μm, and 125 μm sieves in the laboratory.

Fossil specimens were identified to the lowest taxonomic grade possible, according to their preservation and the taxonomic framework available for each group. Some taxa were left in open nomenclature pending detailed taxonomic description that is beyond the scope of this study. Representative specimens of corals, bryozoans, and mollusks are deposited at the Natural History Museum (London), larger benthic foraminifera at the Naturalis Biodiversity Center (Leiden), and coralline algae at the Departamento de Estratigrafía y Paleontología at the University of Granada.

Corals were studied from 53 bulk samples as well as specimens individually collected from the outcrop surface. High taxonomic richness and the lack of a rigorous regional taxonomic framework for Miocene reef corals restricted our ability to identify taxa in the field, so transects were used to estimate percentages of the different types of coral growth forms, including massive, branching (ramose and phaceloid), solitary, and platy, the latter subclassified as thin platy and platy tabular (Insalaco 1998; Rosen et al. 2002). The relative abundance of sediment and corals in each unit was estimated along each transect. Specimens recovered from bulk samples were counted and weighed, and relative abundances were estimated as a percentage of each taxon per unit (see Supplementary Data, Appendix A). External morphological characters of corals, such as colony forms and calice features, were used for taxonomic identifications in the laboratory and taxa names were assigned following the recent revision on Indo-Pacific fossil corals by Johnson et al. (2015). *Acropora* specimens were placed within "species groups" (Wallace 1999). Well-preserved corals, which had weathered out of the outcrop, were also collected to enhance taxonomic lists and identifications.

Larger benthic foraminifera were examined in 11 thin sections (28 × 48 mm) and as specimens picked from 14 bulk samples (500 μm to 2 mm fractions; ~ 300 foraminifera per sample). Taxon abundances were estimated relative to the total number of foraminifera identified in each sample or thin section (see Supplementary Data, Appendix B). A semiquantitative approach was applied to evaluate benthic foraminiferal assemblages within the 125–500 μm fraction from each sample. In each sample, ~ 100 specimens were sorted, identified, and scored as abundant if they represented more than 40%, common between 15% and 40%, frequent from 5% to 15%, and rare if less than 5%. The percentage of planktonic/benthic foraminifera was also calculated (see Supplementary Data, Appendix C).

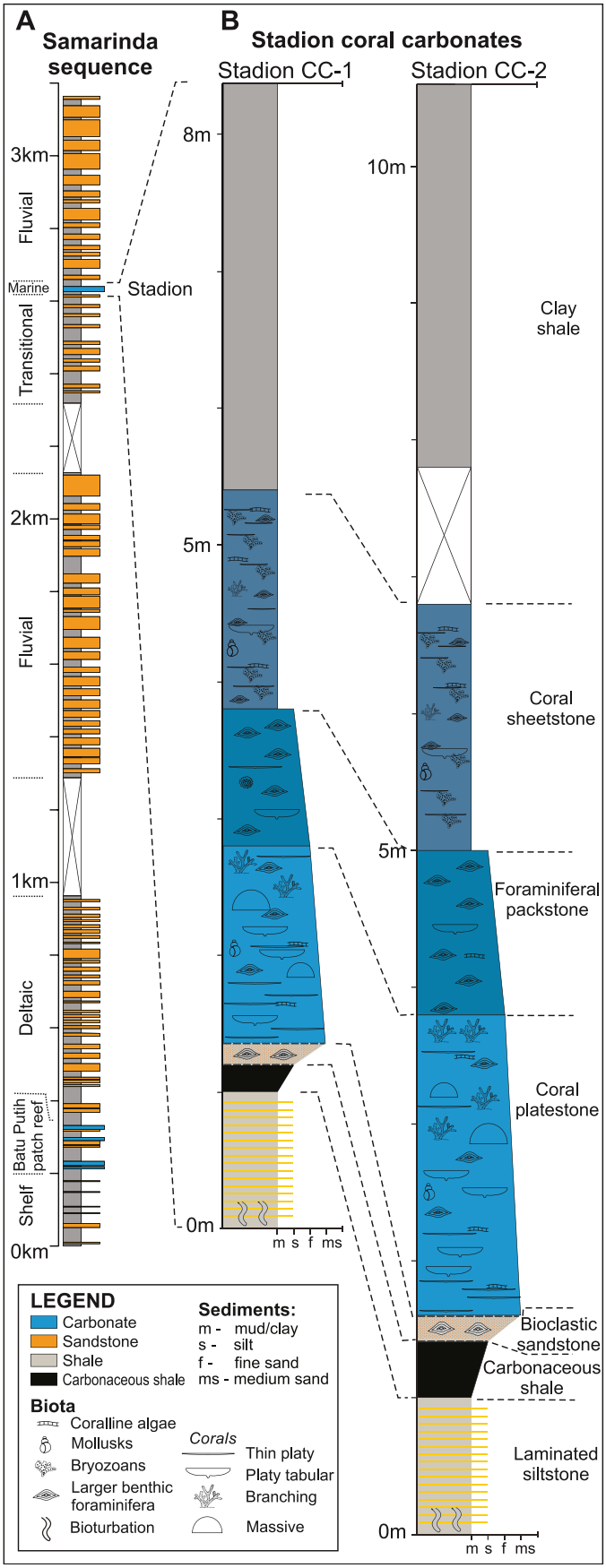

Coralline algae were selectively collected in the field and subsequently studied in a total of 32 ultra-thin sections (10–15 µm thick). Relative abundances of taxa of coralline algae were estimated by measuring the proportional cross-sectional area occupied by each taxon in relation to the total coverage of coralline algae (Perrin et al. 1995). Structures built by coralline algae such as crusts, rhodoliths, and foralgaliths, which are compact nodules with foraminifers (Prager and Ginsburg 1989), were recognized in hand specimens and in thin sections. Growth forms were described using the terms of Woelkerling et al. (1993).

Bryozoans were found encrusting the bases of platy corals and coral branches, and as colony fragments picked from sediment fractions larger than 500 µm from ten bulk samples. Bryozoan specimens were identified to the genus or family level. Relative abundances of taxa were estimated by counting the number of encrusting colonies on the corals and fragments of erect species scattered in the sediments. The proportion of corals encrusted by bryozoans was also estimated by comparing the number of coral specimens and/or fragments encrusted by bryozoans and the total number of coral specimens and/or fragments contained in the bulk samples. Colony growth forms of bryozoans included two main categories, encrusting and erect, and their respective proportions were calculated in terms of both species richness and specimen abundance.

Statistical Analysis

To assess changes in the community composition among facies and between the two sections, nonmetric multidimensional scaling (NMDS) ordinations were produced for corals and larger benthic foraminifera. Coral abundances were estimated as weight percentages standardized using the "Wisconsin double standardization" where species are first standardized by maxima, and then site by site totals (Oksanen et al. 2013). NMDS plots based on transformed data from percentages of the number of fragments and/or colonies showed a similar pattern of clustering to that obtained from their respective weight percentages; hence the former plots are not included here. Analyses of similarity (ANOSIM) were used to test for intergroup differences, and similarity of percentages analysis (SIMPER) was used to identify species that were most responsible for the discrimination between facies and outcrops. Statistical analyses were performed using the vegan package (Oksanen et al. 2013) within the R statistical software environment (R-Core Team 2013)

RESULTS

Seven main lithological units were recognized and correlated across both sections (Fig. 2B). Each of the lithofacies extended laterally at least 150 m, as along-strike exposures were identified no farther than 50 m north from Stadion CC-1 and 300 m south from Stadion CC-2. Thus the horizontal size of the structure is interpreted to be larger than 150 m and less than 300 m.

Facies Types

A combined analysis of the sedimentary composition and main fossil contents of the seven lithological units showed that each unit corresponds to a distinctive facies type (Figs. 2B, 3–4). Table 1 provides a summary of the most relevant characteristics of the facies and their respective fossil contents.

←

FIG. 2.—Measured sections. **A**) Composite section through the Samarinda sequence which preserves the Miocene progradation of the Mahakam Delta System. **B**) Detailed sections through the Stadion patch reef showing correlations between units. Details of lithology indicated alongside. For paleoenvironmental interpretations see Figure 11.

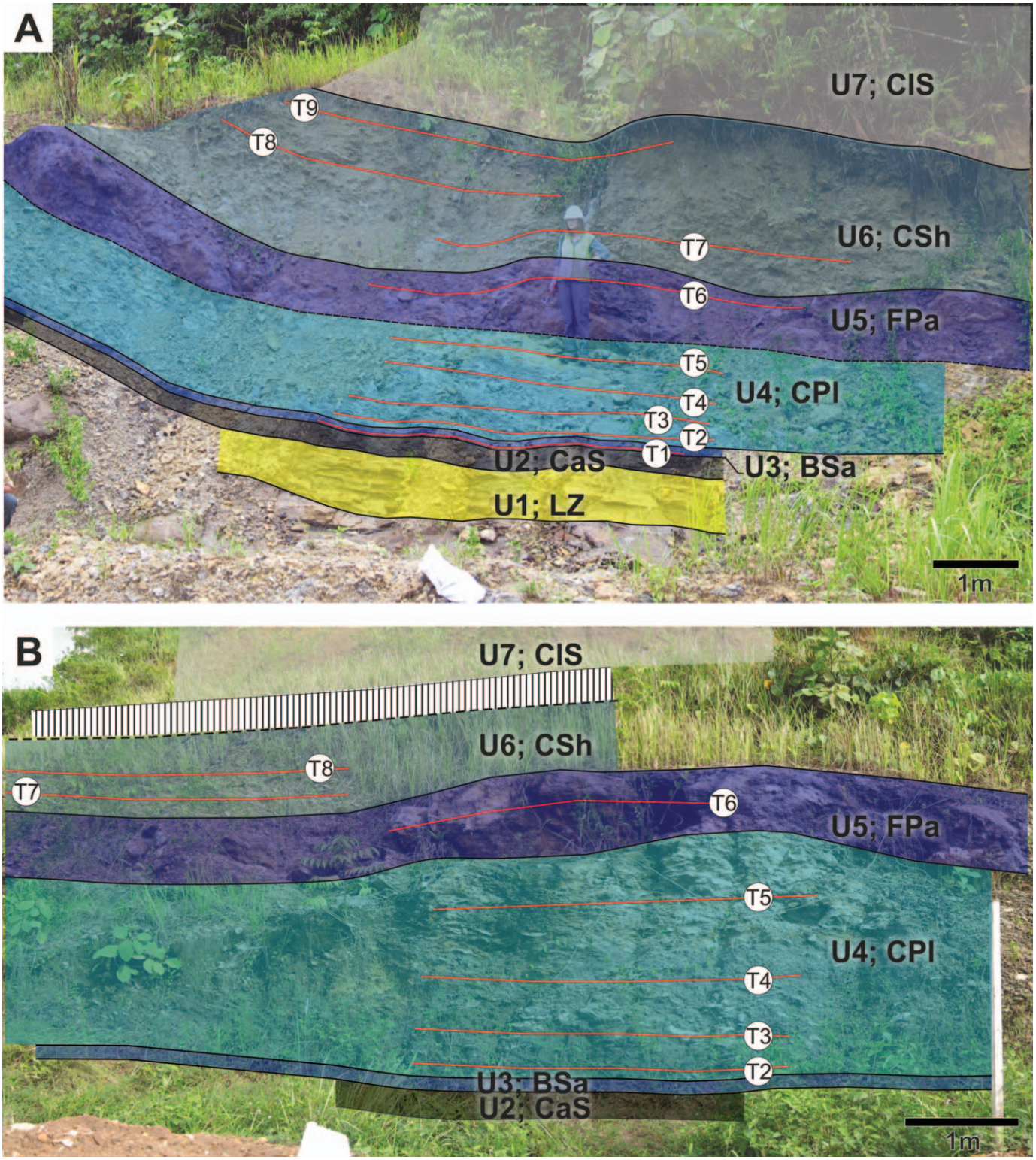

FIG. 3.—Outcrops of the Stadion coral carbonate sections showing lithological units (U1 to U7) and facies. **A**) Locality Stadion CC-1. **B**) Locality Stadion CC-2. Laminated siltstone = LZ; carbonaceous shale = CaS, bioclastic sandstone = BSa, coral platestone = CPl, foraminiferal packstone = FPa; coral sheetstone = CSh; clay shale = ClS. Red contours indicate line transects (T1 to T9).

Laminated Siltstone Facies.—This facies is characterized by a laminated siltstone with thin mudstone layers (3–10 mm) and occasional ripple marks (Fig. 4A). The laminated siltstone facies can be recognized in lithological Unit 1. The lower part of the unit is intensely bioturbated. Toward the top, the siltstone alternates with fine-grained sandstone beds and thin carbonaceous shale layers (< 1 cm). Invertebrate fossils are absent. The exposed facies is about 1 m thick in both sections, with its base covered.

TABLE 1.—*Principal characteristics of the Stadion coral carbonates, including facies types, lithologies, and main fossil groups.*

Unit	Facies type	Lithology	Foraminifers	Corals	Coralline algae	Bryozoans	Mollusks
7	ClS	Fossil barren clay-shale	Absent	Absent	Absent	Absent	Absent
6	CSh	Coral sheetstone within a clay-rich matrix	Dominance of elongated forms of *Lepidosemicyclina bifida* (37%), followed by *Amphistegina* (30%) and *Nephrolepidina* (29%). *Operculina*, *Cibicidoides*, and *Elphidium* common in finer fraction; Planktonic foraminifera increase from base to top (<1 to 11%)	Main carbonate-forming group. Highly diverse, 56 species, and well-preserved specimens. Mainly thin-platy corals of *Porites* sp. 1 (41%), and the agariciids *Leptoseris* spp. (17%). Most colonies are 1 to 5 mm thick; n=3042	Very abundant crusts, mainly *Neogoniolithon* spp. (80%) and other mastophoroids, encrusting corals, some protuberant, and some forming foralgaliths; n=25	Twenty-eight species. Mostly encrusting (78%) the under surfaces of platy corals as large colonies, up to 10 cm width; *Steginoporella* sp. (27%) is the most common species. Among the erect forms (22%), with *Vincularia* spp. (11%) as the most common species; n=695	Two fragments of oysters and one gastropod *Angaria* sp. Poorly preserved specimens; n=3
5	FPa	Foraminifera packstone	Main carbonate-forming group. *Nephrolepidina* (63%) dominate. Subordinate *Amphistegina* (19%) and *Lepidosemicyclina* (12%). *Cycloclypeus* present, but in low abundances (3.5%); Planktonic foraminifera absent	Low abundance, very recrystallized, and low species richness, mainly represented by the genus *Porites* in massive (44%), ramose (30.5%) and platy (10%) forms; n=16	Low abundance, very recrystallized, hard to identify, some *Lithophyllum pseudoamphiroa*; n=4	Absent	Absent
4	CPl	Coral platestone	High diversity. Dominance of *Nephrolepidina* (45%) and *Amphistegina* (39%). Some *Lepidosemicyclina* (13%); No planktonic foraminifera	Main carbonate-forming group. Forty-eight species in 43 genera. Thin-platy forms decreased from the base (82%) to the top (27%); in the middle part, platy-tabular *Porites* sp.1 (24%) and *Progyrosmilia* sp. 2 (23%), and small massive *Porites* sp. 3 (33%) dominate. At the top, phaceloid *Galaxea* spp. (15%) and ramose *Porites* sp. 2 (10%) become more abundant; n= 1471	*Neogoniolithon sp.*, *Hydrolithon sp.* and thick crusts of *Spongites* encrusting corals, partly with forams; n=6	Absent	Eighteen taxa, including 14 genera. Mostly herbivore gastropods (52%), followed by suspension feeders (28%). Poorly preserved specimens, yet identifiable; n=79
3	BSa	Bioclastic packstone	Low diversity. Smaller and robust forms of *Amphistegina* (47%) and *Nephrolepidina* (39%) dominate. A few *Lepidosemicyclina* (12%); Planktonic foraminifera present (2%)	Absent	Absent	Absent	Gastropods, including ?*Calliostoma* sp. Poorly preserved; n=4
2	CaS	Carbonaceous shale	Absent	Absent	Absent	Absent	Absent
1	LZ	Laminated siltstone interbedded with mudstone	Absent	Absent	Absent	Absent	Absent

Carbonaceous Shale Facies.—This facies is characterized by dominance of carbonaceous shale with occasional thin clay and silt layers (Fig. 4B). The carbonaceous shale of Unit 2 is 20 cm thick in Stadion CC-1 and 40 cm thick in Stadion CC-2. This unit has a sharp contact with the laminated siltstone facies at the base and a gradual change into the mixed siliciclastic-carbonate facies toward the top. The carbonaceous content decreases upward as clay and silt content increases. Small pieces of amber were observed in the lower part of this unit.

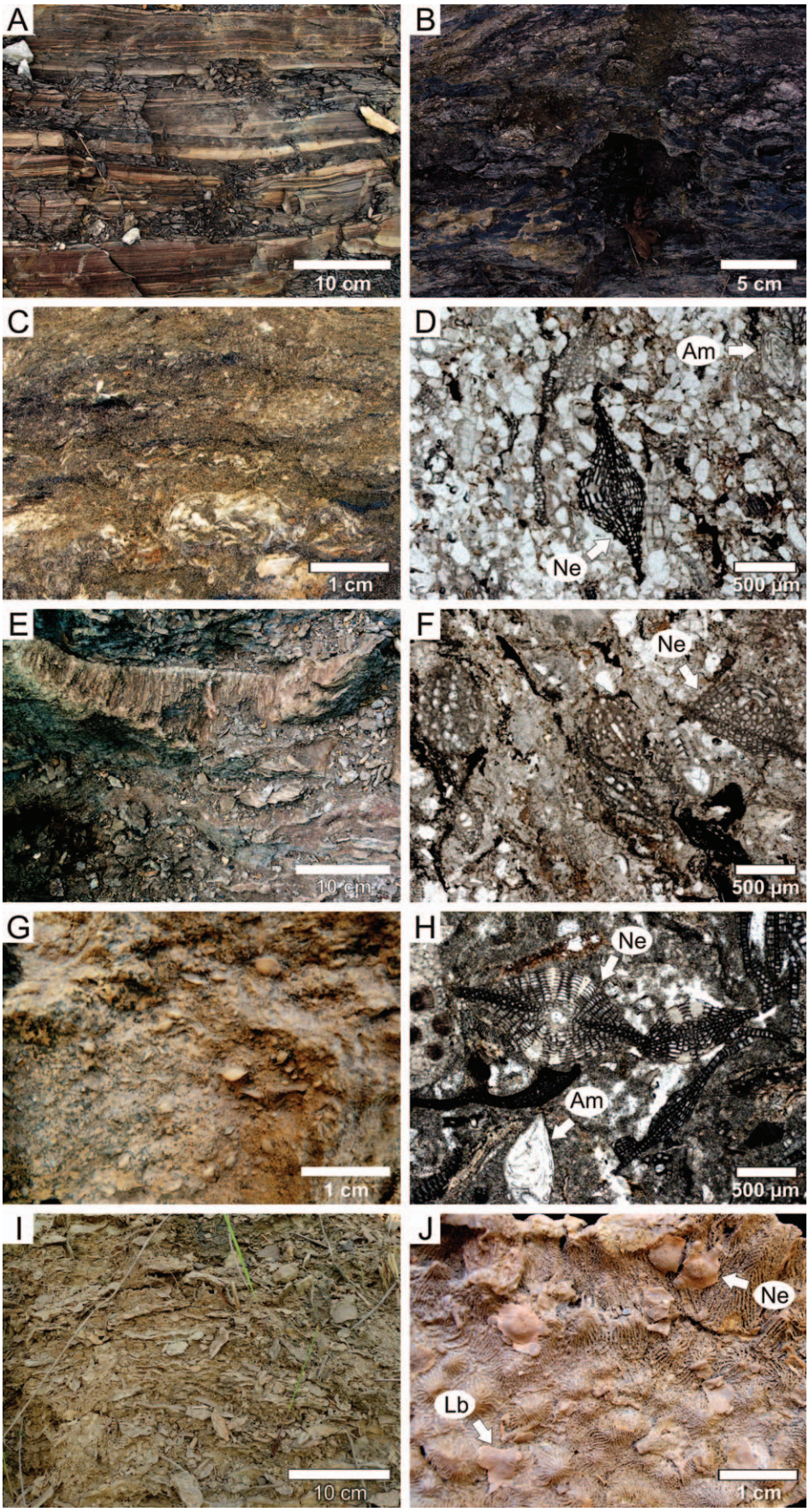
A
10 cm
B
5 cm
C
1 cm
D
Am
Ne
500 µm
E
10 cm
F
Ne
500 µm
G
1 cm
H
Ne
Am
500 µm
I
10 cm
J
Ne
Lb
1 cm

Bioclastic Sandstone Facies.—This facies is characterized by larger benthic foraminifera and mollusk bioclasts in a predominantly moderate to well-sorted fine sand matrix, composed of a mix of subangular to subrounded fine-grained quartz. This facies occurs in Unit 3, which is a 20-cm-thick transitional bed of mixed siliciclastic and bioclastic carbonate components (Fig. 4C). Contacts at the base and the top are gradual. Compared to the underlying facies, the carbonaceous content is lower (<10%) while the average carbonate content is higher (36%). Larger benthic foraminifers comprise about 15% of the sediment (Fig. 4D). A few planktonic foraminifers were observed in the finer fractions (2%).

Coral Platestone Facies.—This mixed carbonate and siliciclastic facies is characterized by a coral framework with thick-platy corals that develop a platestone growth fabric (*sensu* Insalaco 1998). This facies can be recognized in Unit 4, where corals and other bioclasts occur in a gray matrix with an average of 45% $CaCO_3$ (Figs. 4E–F). The thickness of this unit is 1.1 m at the Stadion CC-1 and 3 m at the Stadion CC-2. The transition from the underlying bioclastic sandstone facies is gradual from sand to a silt-rich sediment matrix with abundant fossils. Corals constitute the main carbonate-forming component of this unit (60%–70%, Fig. 5). Most corals are densely packed in growth position, with their calicular surfaces facing upward and bioclastic sediment in the interstices (Fig. 4E). Relative abundances of the different coral growth forms change from the base to the top of the unit (Fig. 5). Corals first appear in transect 2 (Fig. 5), mainly as thin-platy forms (1 to 7 mm thick) and delicate ramose corals (1 to 6 mm in diameter). More robust forms are abundant in the middle of this unit, including ramose corals (up to 16 mm in diameter), platy-tabular (4 to 7 cm thick), and small massive forms (10 to 15 cm high). At the upper part of the unit, the growth fabric consists of relatively similar proportions of small massive (21.2%), phaceloid (17%), and platy-tabular corals (16.4%) (Fig. 5). Larger benthic foraminifers appear as a subordinate component (10%) within the siliciclastic matrix. Coralline algae occur in low abundances (5%), mainly as encrusting plants. The majority of mollusks recovered from the Stadion CC belong to this unit. Some echinoid spines were also observed within the sediments.

Foraminiferal Packstone Facies.—This facies is characterized by packstone dominated by larger benthic foraminifers (Figs. 4G–H). It occurs in Unit 5 with relatively uniform thickness of 1 m at Stadion CC-1 and 1.2 m at Stadion CC-2. It has the highest carbonate content (72%). The contacts with the units below and above are sharp. Corals were observed as a subordinate component (15%), preserved in growth position, and evenly distributed among thin-platy, massive, tabular, and ramose forms. From the base to the top, no changes in the fossil assemblages were observed. Coralline algae, *Halimeda* fragments, echinoid spines, and entirely recrystallized gastropods occur as minor components.

Coral Sheetstone Facies.—This facies is characterized by dominant thin-platy corals forming a sheetstone fabric (*sensu* Insalaco 1998). It occurs in Unit 6 where corals are the main component (40%–60%) of this mixed carbonate-siliciclastic bed (Fig. 4I). The thickness is 1.6 m at Stadion CC-1 and 1.8 m at Stadion CC-2. Carbonate content within the sediment matrix averages 30%, decreasing from 40% to 11% upsection. The upper part of the unit is characterized by a decline in coral abundance. Among the corals, thin-platy forms dominate (65%–95%). These thin-platy corals are mostly 1–5 mm thick, and densely packed in growth position. Platy-tabular corals (30%) up to 3 cm thick were also observed, mainly toward the top of the bed, and some clusters of branching corals were sparsely distributed along the transects. The siliciclastic sediment matrix is yellow and clay-rich with abundant larger benthic foraminifers (20%–30%). Crustose coralline algae occur in low proportions (5%), mainly encrusting corals together with foraminifers (Fig. 4J). Bryozoans are commonly found encrusting the under surfaces of thin-platy corals, colonizing 27% of the corals. Sparse cidaroid echinoid spines, gastropods, and fragments of bivalves also occur.

Clay-Shale Facies.—This facies is dominanted by clay and devoid of fossils. It occurs in the uppermost exposure of Unit 7 at the Stadion CC sections. Although the top of the outcrop is covered by vegetation with no other deposits exposed, several hundred meters of thick deltaic sandstones are visible further up the section (Cibaj 2009).

Fossil Assemblages

Rich fossiliferous biofacies are characteristic in the four middle facies of the Stadion sections, including the coral-dominated facies (coral platestone and sheetstone) and foraminifer-dominated facies (bioclastic sandstone and foraminiferal packstone). The other facies are barren in fossils. Percentages of abundance for the five main fossil groups studied in the Stadion sections are illustrated in Figure 5 and principal taxa are summarized in Table 1. Most fossil taxa recovered from the Stadion CC sections have complete or partial calcitic skeletons with higher potential of preservation, such as coralline algae (Bosence 1991), foraminifera (Lowenstam and Weiner 1983), octocoral sclerites (Bayer and Macintyre 2001), echinoderm spines (Su et al. 2000), and polychaete tubes (Vinn et al. 2009), among others. Even though scleractinian corals deposit aragonitic skeletons, those were recrystallized and transformed from original aragonite into secondary calcite as it is commonly found in corals older than Pleistocene age (Constantz 1986; Mcgregor and Gagan 2003; Reuter et al. 2005).

Corals.—A high richness of coral species was recorded from the studied sections (Table 1; Fig. 6). A total of 69 species belonging to 41 genera were identified from the 4686 studied specimens. They include 66 species from 38 genera of scleractinians. Other taxa were the hydrozoan *Millepora* sp., and the octocorals *Heliopora* sp. (Fig. 6G) and *Isis* sp. (see Supplementary Data, Appendix A). A few octocoral sclerites (3–5 mm long) were also recovered. A small percentage of the specimens (<1%) could not be identified. The 157 specimens collected from the outcrop surface only yielded two additional taxa, *Leptoseris* aff. *mycetoseroides* and *Lobophyllia* sp. The latter two taxa could not be assigned to any specific facies so were left out of the statistical analyses.

Statistical ordinations showed that the coral assemblages were significantly different between the coral sheetstone and coral platestone facies (Fig. 7; ANOSIM R = 0.278, p-value = 0.022) but not between the Stadion CC-1 and Stadion CC-2 sections (R = 0.078, p-value = 0.206). External morphological features of corals were well preserved in the coral platestone facies allowing taxonomic identifications. Internal microstructures of coral skeletons were highly recrystallized and some specimens have a friable consistency. The reconstruction of the coral succession

←

FIG. 4.—Lithofacies characteristic of the Stadion patch reef. **A**) Laminated siltstone. **B**) Carbonaceous shale. **C**) Bioclastic sandstone. **D**) Micrograph of bioclastic sandstone thin section showing well sorted fine-sand and larger benthic foraminifera. **E**, **F**) Coral platestone. **E**) Large tabular colony of *Progyrosmilia* sp. **F**) micrograph of thin section showing *Nephrolepidina ferreroi*. **G**, **H**) Foraminiferal packstone. **H**) Micrograph of thin section showing *Nephrolepidina* and *Amphistegina*. **I**, **J**) Coral sheetstone showing multiple stacks of thin platy coral colonies. **J**) Detail of larger benthic foraminifera encrusting on coral surface of a *Pavona* sp. Common larger benthic foraminifera include *Nephrolepidina* = Ne, *Amphistegina* = Am, and *Lepidosemicyclina bifida* = Lb.

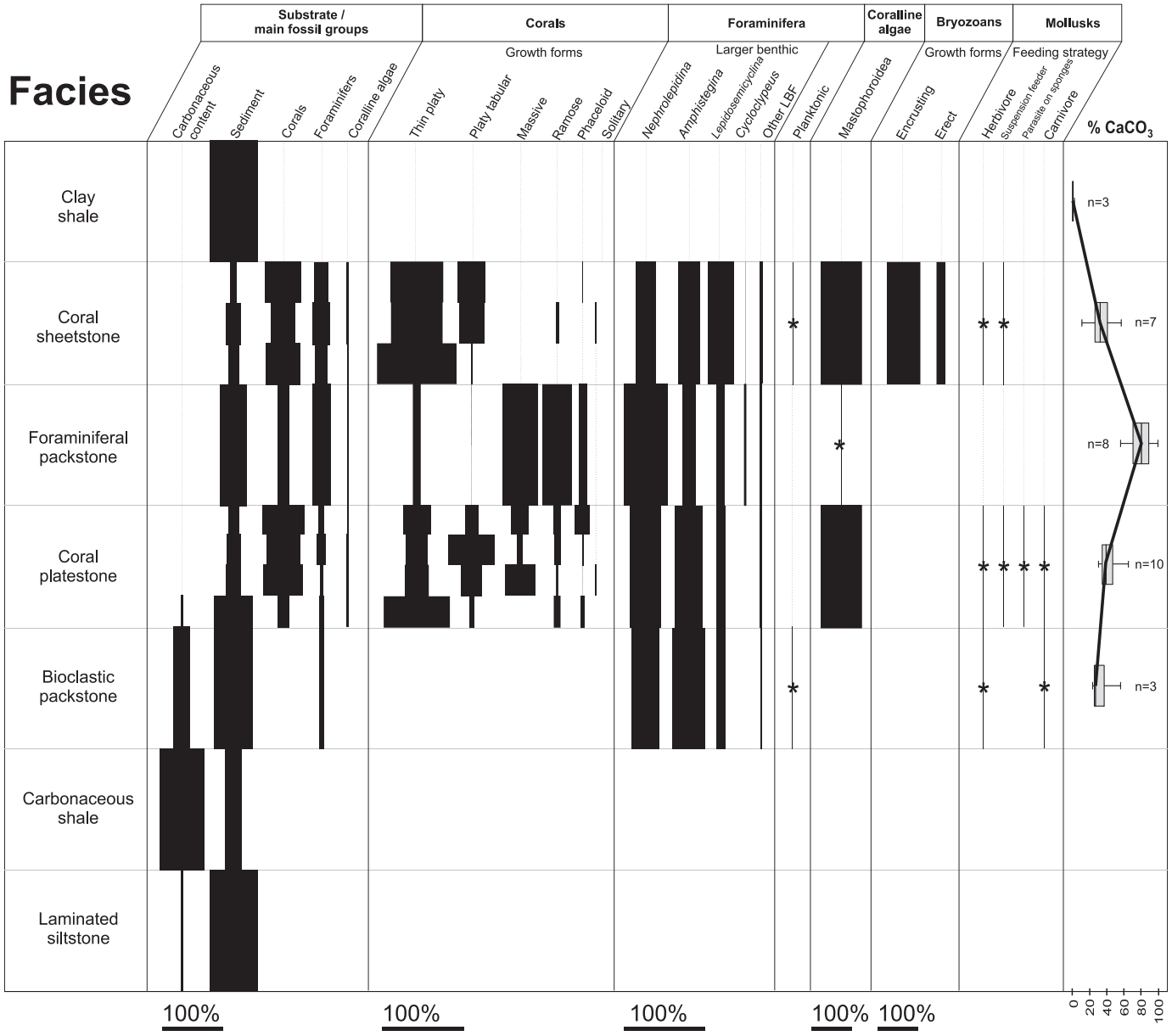

FIG. 5.—Lithofacies characteristics of the Stadion patch reef, including percentages of the main substrate components and fossil groups. Biotic distribution and abundance of corals, foraminifers, coralline algae, bryozoans, and mollusks are illustrated, including the main growth forms, taxa, or feeding strategy, accordingly. Asterisks (*) indicate the occurrence of the fossil group but preservation issues hampered the estimation of its abundance within the facies. Percentages of calcium carbonate ($CaCO_3$) in the marine facies are shown in the last column.

shows that the first corals appear at the base of the coral platestone facies in transect 2, about 20 cm above the carbonaceous shale, including *Porites* sp. 1 (Fig. 6A), *Leptoseris* sp. 7, and *Heliopora* sp. Coral abundances and richness increase to 22 in transects 3 and 5, reaching its maximum number of 31 species in transect 4. Within this facies, platy tabular forms of *Progyrosmilia* sp. 2 (Fig. 6C) and *Astreopora* spp. were dominant in the Stadion CC-2, while small massive colonies of *Porites* sp. 3 (Fig. 6E) were typical in the Stadion CC-1. At the top of the coral platestone facies, the phaceloid taxa *Galaxea* spp. (Fig. 6F) and ramose *Porites* sp. 2 and *Dictyaraea* sp. were more abundant. In total for the coral platestone facies, 48 species from 30 genera were identified, with 24 species common to both sections.

Corals were poorly preserved in the foraminiferal packstone facies and highly cemented into the matrix. No new taxa were found in this facies, and 43 coral species that were present in the previous coral platestone facies did not occur in this facies. Only five species were identified from samples collected in transect 6, from which massive *Porites* sp. 3 (44%), ramose *Porites* sp. 2 (30.5%), and platy *Porites* sp. 1 (9.8%) were the most abundant corals.

With a total of 56 species, the highest coral richness and the best-preserved specimens were observed in the coral sheetstone facies, mainly dominated by thin-platy forms of *Porites* sp. 1, the agariciids *Leptoseris* spp. (e.g., Fig. 6J) and *Pavona* spp. (e.g., Fig. 6L), the merulinid *Cyphastrea* spp. (e.g., Fig. 6M), and the siderastreid *Psammocora* sp. (e.g., Fig. 6N). Twenty-three coral species were present in the upper part of coral sheetstone facies, including *Porites* sp. 1, *Cyphastrea* cf. *imbricata*, and other agariciids. Thirty-seven species were shared with the coral platestone facies. Except for the small massive *Porites* sp. 3, all

species from the underlying foraminiferal packstone facies were present in the coral sheetstone facies.

Foraminifera.—In the coarser fractions (0.5–2 mm and >2 mm), assemblages of larger benthic foraminifera varied among the lithofacies (Table 1, Fig. 5; Supplementary Data, Appendix B). Ordination analyses showed two distinctive groups (Fig. 7B), a first one preserved in the bioclastic sandstone, coral platestone, and foraminiferal packstone facies and a second group found in the coral sheetstone facies (ANOSIM R = 0.706, p-value = 0.001). No significant differences were found between the two Stadion CC sections (ANOSIM R = 0.461, p-value < 0.001). Small and robust forms of *Amphistegina* and *Nephrolepidina* (Fig. 8A) dominated in the bioclastic sandstone facies, with rare occurrences of thin and flatter *Lepidosemicyclina*. In the coral platestone facies richness increased slightly, with *Amphistegina* and *Nephrolepidina* still dominant, albeit with increased abundance of *Lepidosemicyclina*, and subordinate *Operculina*. Although very abundant, they were less rich in the foraminiferal packstone facies than in the coral platestone facies, and again contained abundant *Amphistegina*, with subordinate *Nephrolepidina* and *Lepidosemicyclina.* In the uppermost fossiliferous unit, the coral sheetstone facies, there was an abrupt change in larger benthic foraminifera composition as *Lepidosemicyclina bifida* (Fig. 8C) became the most abundant taxon with subordinate *Nephrolepidina* (e.g., Fig. 8A), *Amphistegina* and *Operculina*, and rare occurrences of flat discoidal *Cycloclypeus annulatus* (Fig. 8B).

Among the 125 μm fractions recovered from the bulk samples, benthic foraminifera were present in the bioclastic sandstone, coral platestone, and coral sheetstone facies, but absent from the clay-shale facies (see Supplementary Data, Appendix C). In general, foraminiferal tests were poorly preserved and taxonomic identifications were only possible at the genus level. Six taxa were identified, from which *Amphistegina* spp. (Fig. 8D) were the most abundant, followed by *Operculina* spp. (Fig. 8E), *Elphidium* spp. (Fig. 8G), and *Cibicidoides* spp. (Fig. 8H). Small differences could be noticed among the facies types: abundances of *Cibicidoides* and *Elphidium* increased from frequent at bioclastic sandstone and coral platestone facies, to common in coral sheetstone facies. Similarly, miliolids (Fig. 8F) were rare in the bioclastic sandstone and coral platestone facies but common in coral sheetstone facies. Samples from the coral sheetstone facies were moderately well preserved and contained the highest benthic foraminiferal richness.

Coralline Algae.—Abundances, growth forms, and groups commonly associated with coralline algal assemblages in the successive carbonate units are shown in Table 1 and detailed data per taxon in the Supplementary Data, Appendix D. Coralline algae were present as a subordinate component in the coral platestone, foraminiferal packstone, and coral sheetstone facies. Abundances were higher in coral platestone and coral sheetstone facies, mainly encrusting corals, forming foralgaliths, and also as fragments within the matrix (Fig. 5). Assemblages and growth forms of coralline algae did not vary significantly between the coral-dominated facies, but both were characterized by abundant mastophoroids (Fig. 9), mainly *Neogoniolithon* spp. (Figs. 9A–B). In the foraminiferal packstone facies, coralline algae were less abundant and very recrystallized, limiting taxonomic identification.

Bryozoans.—Although bryozoans were restricted to the coral sheetstone facies (Table 1, Fig. 5), they included 28 species, with 3 cyclostomes, 25 cheilostomes (9 anascan-grade and 16 ascophoran-grade species), and rare ctenostome borings visible on the undersurfaces of corals (see Supplementary Data, Appendix E). Species richness and specimen abundance was very similar in the two sections: 25 species (302 specimens) at the Stadion CC-1 and 24 species (393 specimens) at the Stadion CC-2. Twenty-one of the species that occur in both sections were the most abundant taxa. In contrast, the four species found exclusively in Stadion CC-1 and the three species unique to Stadion CC-2 were represented by a few or even a single colony. The dominant taxa among erect colonies were the articulated anascan *Vincularia berningi* (11%) and the fenestrate ascophoran *Triphyllozoon* sp. (7%), both found as scattered fragments and as specimens cemented to coral surfaces and a few colony bases. Among encrusters the anascans *Steginoporella* sp. (27%; Fig. 10B), ?*Crassimarginatella* sp. (3%), *Cranosina rubeni* (Fig. 10A), *Antropora* cf. *subvespertilio* (Fig. 10D), the cribrimorph *Puellina* spp., and the ascophorans *Reptadeonella* sp. A (Fig. 10C) and *Hippopodina* cf. *feegeensis* (5%) usually developed large colonies on coral undersides; only a few specimens were observed encrusting the surfaces of ramose corals. Unidentifiable cheilostome species accounted for 33% at Stadion CC-1 and 17% at Stadion CC-2, mainly represented by fenestrate phidoloporid fragments.

Most taxa were encrusters (78%), typically two-dimensional colonies of low relief. The remaining 22% of the species were erect, mostly flexible because of jointing and anchored to a substrate by rootlets, or rigid fenestrate with a cemented base. A single ctenostome species occurs as borings in the corals. Almost the same proportions of growth forms occur in terms of specimen abundance: 81.6% of specimens were encrusters, 18.3% were fragments of erect species, and only one specimen (0.1%) was boring a coral substrate (Fig. 5).

Mollusks.—Eighty-six poorly preserved specimens were recovered, including representatives of three bivalve families and at least eleven gastropod families (see Supplementary Data, Appendix F). Aragonitic mollusks are rare and mainly represented by very small, incomplete, and highly recrystallized shells. Gastropods with an outer calcitic shell layer and/or relatively thick shells (e.g., Trochidae and Turbinidae; Gainey and Wise 1980; Beesley et al. 1998) are comparatively common in the Stadion CC sections. The majority of bivalves present at the studied sections are epifaunal taxa that aggregate calcitic foliated, and therefore relatively hard and chemically resistant shells (Kennedy et al. 1969; Taylor and Layman 1972).

Most mollusks were recovered from coral platestone facies, in which 92% of the total number of specimens were collected. Bivalves are predominately preserved as fragments and include oysters (e.g., *Lopha, sensu lato*), pectinids, and one specimen of the Lucinidae ?*Anodontia* (*Pegophysema*). The most common gastropod families are Turritellidae (n = 13), Trochidae (?*Euchelus* sp., n = 12), and Turbinidae (*Astraea* sp., n = 6; opercula of two species). Other identifiable families include Cerithiidae, Scaliolidae, Rissoidae, Iravadiidae, Triphoridae, and Pyramidellidae, each with very low abundances (n < 4). Gastropods are represented by herbivores, suspension feeders, and parasites (Fig. 5). Predatory taxa are entirely lacking, although they are dominant in modern reef-associated gastropod faunas (Taylor 1977) due to the preservation constraint.

DISCUSSION

Most of the fossils found in the Stadion sections are light-dependent benthic taxa, including zooxanthellate corals, larger benthic foraminifera, and coralline algae, that lived as distinct communities during deposition of bioclastic sandstone, coral platestone, foraminiferal packstone, and coral sheetstone facies (units 3 to 6), indicating that in those settings light reached the benthic environment. The varying composition of the communities in these facies may suggest a variation in light levels, most likely related to changes in depth and/or alterations in terrestrial input (Perrin et al. 1995; Wilson 2005, 2012; Bassi and Nebelsick 2010; Novak et al. 2013). Terrigenous input can drive the response of light-dependent biota through: (1) the amount of siliciclastic input; (2) the frequency of input (i.e., constant or episodic); (3) grain size; and (4) associated nutrient input (Sanders and Baron-Szabo 2005; Wilson 2005; Lokier et al. 2009). Disentangling the role of each factor involved with terrigenous input is difficult, as each interacts with other factors, such as depth and hydrodynamic regimes, to produce similar effects on the amount of light

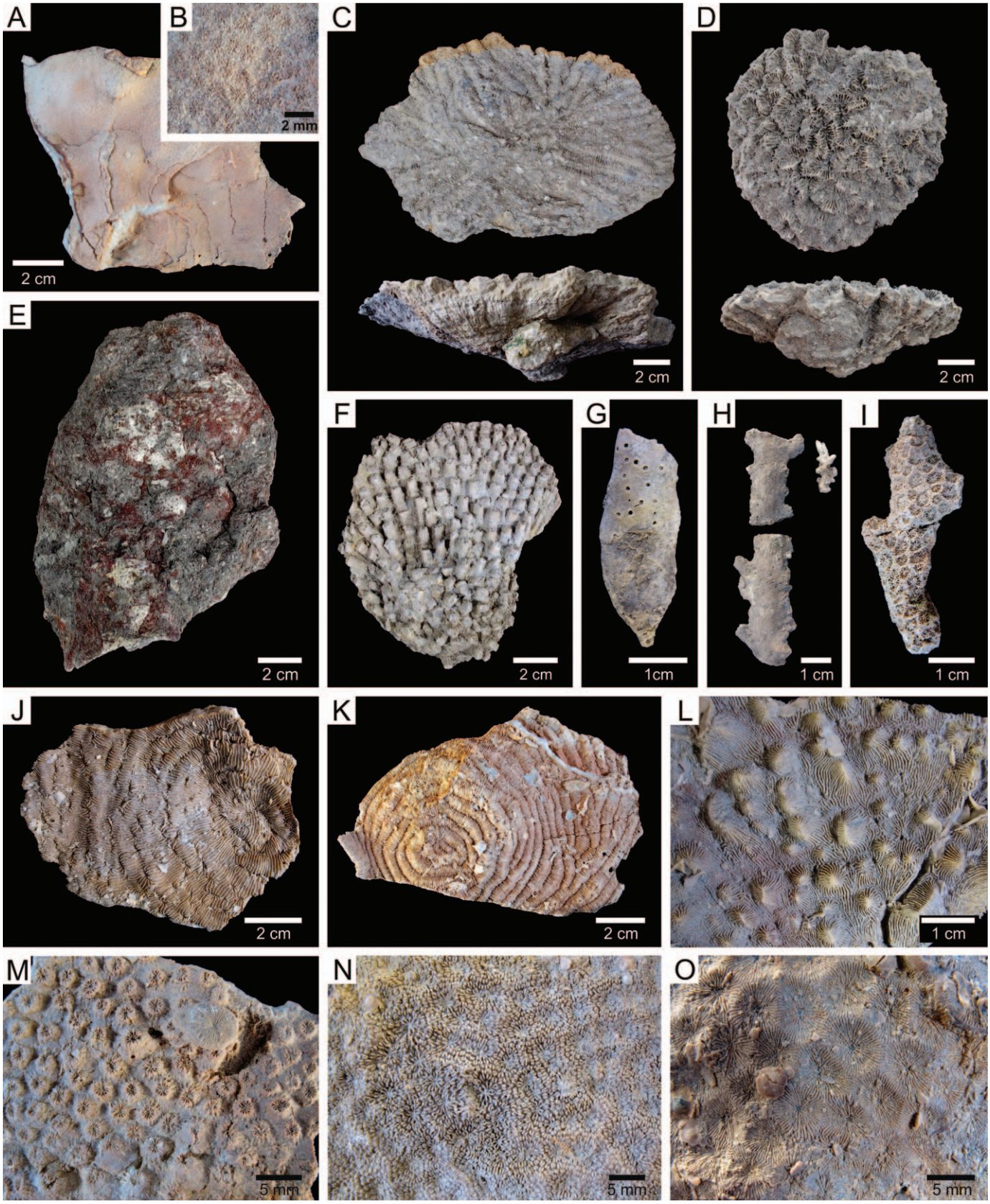
A
B
2 mm
2 cm
C
2 cm
D
2 cm
E
2 cm
F
2 cm
G
1cm
H
1 cm
I
1 cm
J
2 cm
K
2 cm
L
1 cm
M
5 mm
N
5 mm
O
5 mm

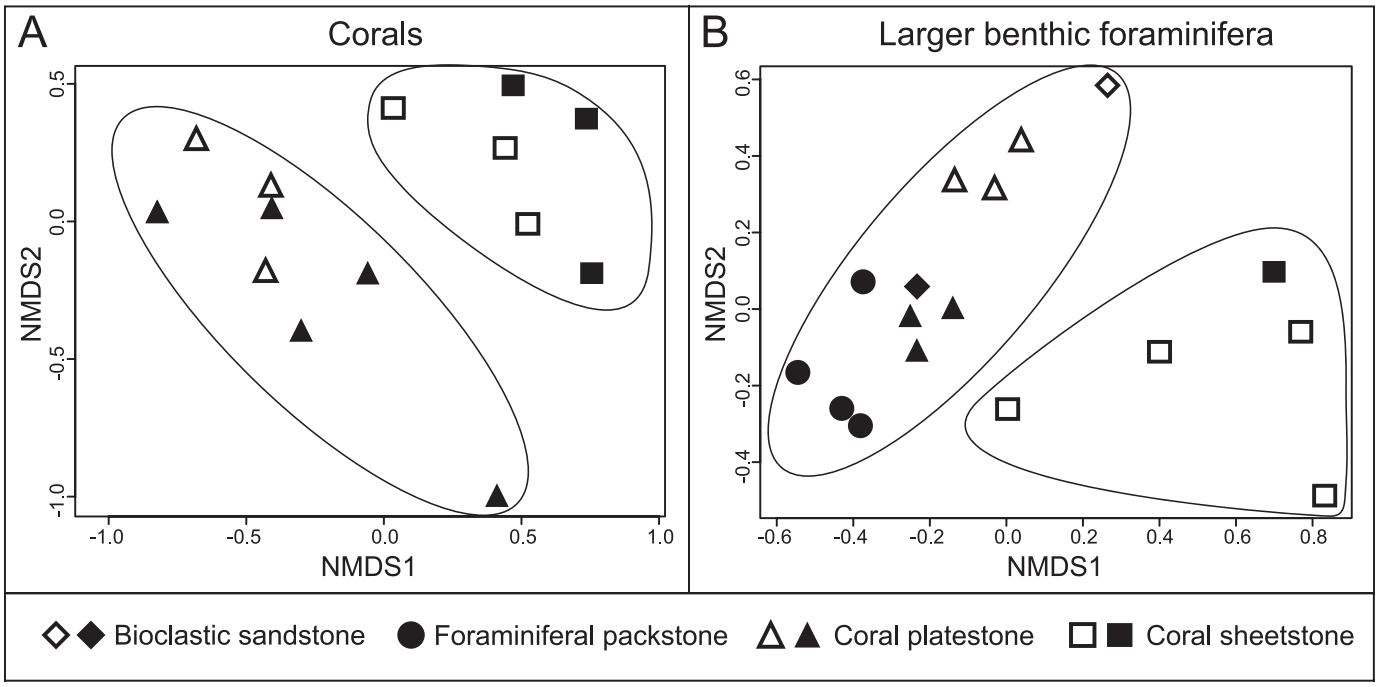

FIG. 7.—Nonmetric multidimensional scaling analysis of fossils from the study interval. **A**) Coral assemblages. **B**) Larger benthic foraminiferal assemblages. Open symbols correspond to Stadion CC-1 and filled symbols to Stadion CC-2.

available to the benthic community. Thus, paleoenvironmental interpretations based on the light-dependent components of Stadion communities are relative and require independent evidence to verify. In this study, the growth forms and taxonomic composition of fossil assemblages were analyzed because these two aspects are key to interpret paleoenvironments, as has been shown in previous studies for scleractinian corals (Perrin et al. 1995; Pandolfi 1996; Perrin 2000; Klaus et al. 2008; Johnson et al. 2009), larger benthic foraminifera (Hallock and Glenn 1986; Hottinger 1997; Hohenegger et al. 1999; Renema and Troelstra 2001), and coralline algae (Bosence 1983; Perrin et al. 1995; Braga et al. 2009).

Facies Interpretation and Paleoenvironmental Evolution

The Stadion CC were deposited during a transgressive interval within a 3-km-thick section of alternating shallow marine, deltaic, and fluvial deposits that accumulated between 16 and 11 Ma (Marshall et al. 2015). The observed geometry and lateral continuity of the deposits that extend at least 150 m between the two studied sections suggests that the Stadion CC could have developed as a low-relief patch reef (Moss and Chambers 1999; Wilson 2005). The main factors controlling this patch reef were most likely depth and episodic variation in the nature and rate of terrigenous sedimentation (Fig. 11).

At the base of the Stadion CC sections, the lack of marine fossils in the laminated and occasionally rippled siltstone and fine-grained sandstone facies suggests a low-energy depositional environment within a delta-plain setting (Allen and Chambers 1998). Increase in marine influence leading to the development of coastal swamps or estuarine mangrove environments can be inferred from the appearance of thin carbonaceous layers, first occasionally at the top of the laminated siltstone facies and becoming more abundant until they form the distinctive carbonaceous shale facies (Figs. 11A–B). The first occurrence of larger benthic foraminifera marks the transition into a fully marine environment, characterized by deposition of bioclastic sandstone (Fig. 11C). The foraminiferal assemblage in the bioclastic sandstone facies, dominated by smaller and robust specimens of *Amphistegina* and *Nephrolepidina* with subordinate miogypsinids and *Operculina*, supports the interpretation of shallow-water conditions and an increase of energy levels in the environment (Hallock and Glenn 1986). Similar communities of foraminifera occur in the subsequent coral platestone facies, although smaller and more robust forms decrease, and slightly thinner and elongated forms increase, upsection.

Corals are preserved in growth position in the coral platestone facies indicating autochthonous deposition and fully marine conditions. The platy morphology of corals has been recognized as an adaptation to low-light environments (Rosen et al. 2002; Sanders and Baron-Szabo 2005) that could have resulted as a response to terrigenous input, consistent with the silty siliciclastic matrix of the facies. Although significant, the overall siliciclastic input was low as indicated by the robustness of platy-tabular and small massive colonies (Figs. 6C–E, 11D); in addition, relatively constant sedimentation rates are likely as the corals present no signs of partial mortality during development. The subsequent appearance of phaceloid and ramose morphologies toward the top of the coral

←

FIG. 6.—Representative corals from the Stadion patch reef. **A**, **B**) *Porites* sp.1, NHMUK AZ6718, from the coral sheetstone facies. **A**) Fragment of a platy colony of *Porites* sp. 1 and B) detail of corallites. **C**–**H**) Some corals from the coral platestone facies. **C**) *Progyrosmilia* sp., NHMUK AZ6575. **D**) *Symphyllia recta*, NHMUK AZ7214. **E**) *Porites* sp. 3, NHMUK AZ7238. **F**) *Galaxea* sp., NHMUK AZ6477. **G**) *Heliopora* sp., NHMUK AZ7230. **H**) *Acropora* sp. *elegans* group, NHMUK AZ7302. **I**–**O**) Some corals from the coral sheetstone facies. **I**) *Goniopora planulata*, NHMUK AZ6606. **J**) *Leptoseris* sp., NHMUK AZ7329. **K**) *Pachyseris* sp. 4, NHMUK AZ6722. **L**) *Pavona* cf. *varians*, NHMUK AZ7351. **M**) *Cyphastrea* sp., NHMUK AZ6979. **N**) *Psammocora* sp., NHMUK AZ7159. **O**) *Coscinaraea* sp., NHMUK AZ6833.

FIG. 8.—Representative foraminifera from the Stadion patch reef. Common foraminifers from the coarse fraction (> 0.5 mm) include **A**) *Nephrolepidina martini*, **B**) *Cycloclypeus annulatus*, and **C**) *Lepidosemicyclina bifida*. Foraminifers from the fine fraction (> 125 µm to 0.5 mm) include **D**) *Amphistegina* sp., **E**) *Operculina* sp., **F**) miliolid, **G**) *Elphidium* sp., and **H**) *Cibicidoides* sp.

platestone facies can be indicative of an environment with relatively higher sedimentation rates of silt-size siliciclastics (Perrin et al. 1995; Sanders and Baron-Szabo 2005). The initial stage of the coral platestone facies was characterized by low coral abundances (< 10%) and dominance of thin-platy forms (Fig. 5), suggesting plausible constratal framework (Insalaco 1998) with corals barely exceeding the rates of siliciclastic deposition. Once this pioneer coral community was established, the framework may have become partially suprastratal as suggested by higher abundances of corals arranged with more colony intergrowth and the appearance of small massive and branching growth

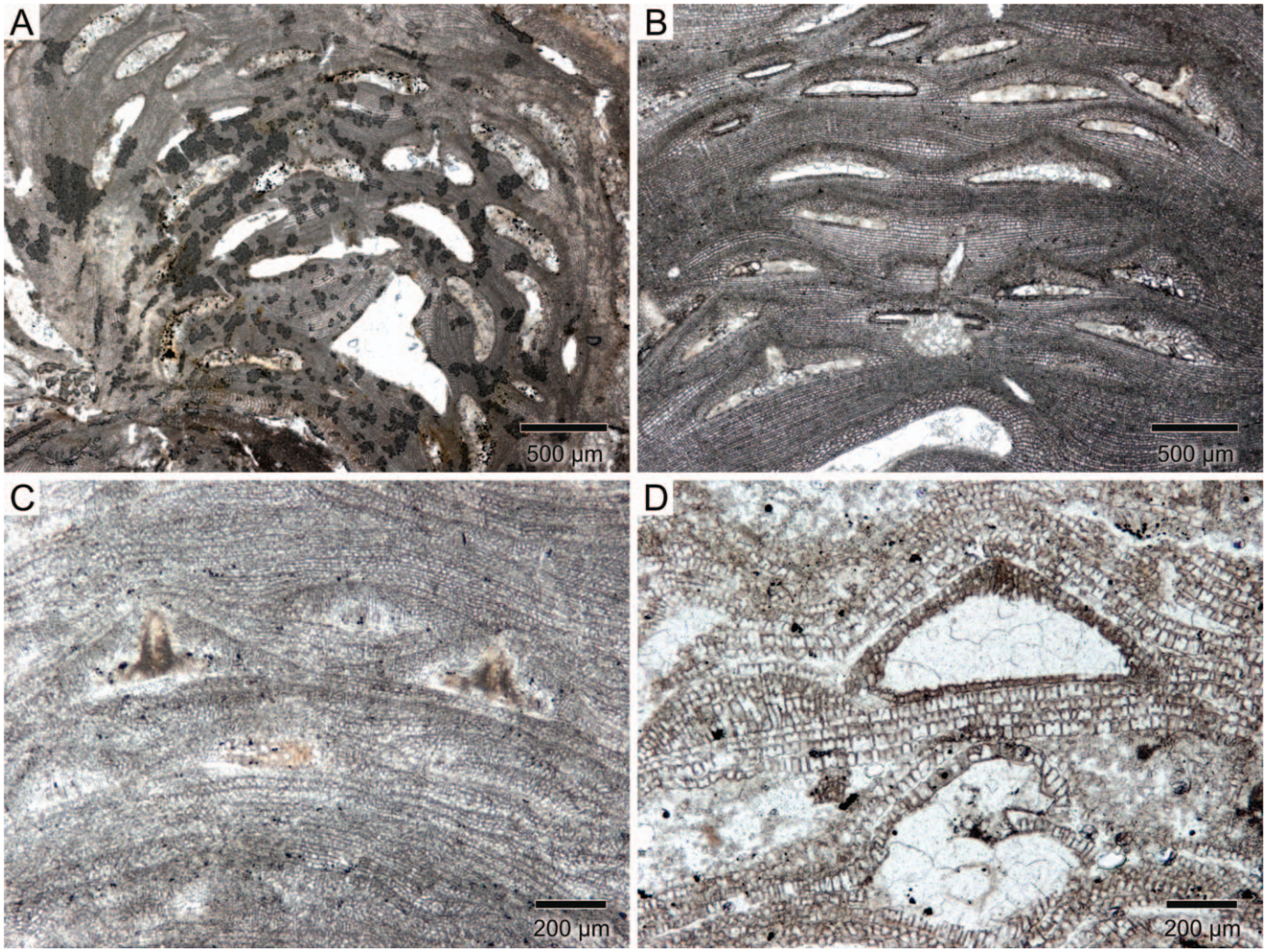

FIG. 9.—Representative crustose coralline algae of the Stadion patch reef. **A**) *Neogoniolithon* sp., AR274-3. **B**) *Neogoniolithon fosliei*, AR262-1. **C**) *Spongites* sp., AR267-1. **D**) *Lithoporella* sp., AR263D-1.

forms (Insalaco 1998). However, any growth above seafloor was limited to a few decimeters, resulting in the relatively flat parallel geometry of the bed after compaction. Gastropods from the coral platestone facies such as Turbinidae, Trochidae, Cerithiidae, and Turritellidae are typical inhabitants of reefs and other shallow marine habitats (Taylor 1968; Héros et al. 2007). The absence of encrusting bryozoans in the coral platestone facies, despite the abundant offer of coral substrates for their colonization, can be explained as a preservation issue due to the cementation of sediments on coral surfaces, as it has been suggested by Taylor and Di Martino (2014).

Coralline algal assemblages provide the most reliable signal for an interpretation of paleodepth for the coral platestone facies. Mastophoroids are well-known components of the algae communities that live on shallow parts of modern coral reefs, mainly in the first 30 m depth (Adey 1986; Minnery 1990; Verheij and Erftemeijer 1993; Iryu et al. 1995). Relatively high abundance of thick crusts of members of the subfamily Mastophoroideae (such as *Neogoniolithon* and *Spongites*) has also been well constrained to shallow-water environments in tropical Miocene reefs (Perrin et al. 1995; Braga et al. 2009, 2010). While the paleodepth interpretation of coralline algae with affinity for low light is ambiguous, the photophilic (high-light affinity) property of thick mastophoroid species constitutes an unequivocal indication of a shallow paleodepth for the coral platestone facies. High sediment input rates have characterized the Kutai Basin since its early formation (van de Weerd and Armin 1992; Allen and Chambers 1998). In the modern Mahakam delta-front system water transparency is very low, with Secchi disc estimation at maximum of 13 m depth (Budhiman et al. 2012), due to high quantities of suspended sediments (Storms et al. 2005). Therefore, by analogy to modern conditions around the Mahakam delta, the co-occurrence of mastophoroids and platy coral communities within a terrigenous-rich matrix suggests that coral development took place at a few meters depth, likely less than 10 m depth. The abrupt transition from the coral platestone facies to the foraminiferal packstone facies may indicate an increase in clastic sedimentation past the tolerance level of coral species (Fig. 11E).

In the foraminiferal packstone facies, the dominance of flatter forms of *Nephrolepidina* combined with the presence of *Cycloclypeus* suggests a decrease of light levels, most likely due to a depth increase (Hallock 1981; Hallock et al. 1986; Renema 2006). This increase in turbidity was not likely to have been caused by increased nutrient input, as elevated $CaCO_3$ content of the foraminiferal packstone facies suggests continued low terrigenous input. Corals are the secondary component within this facies, providing additional evidence for a reduction in light levels. The presence

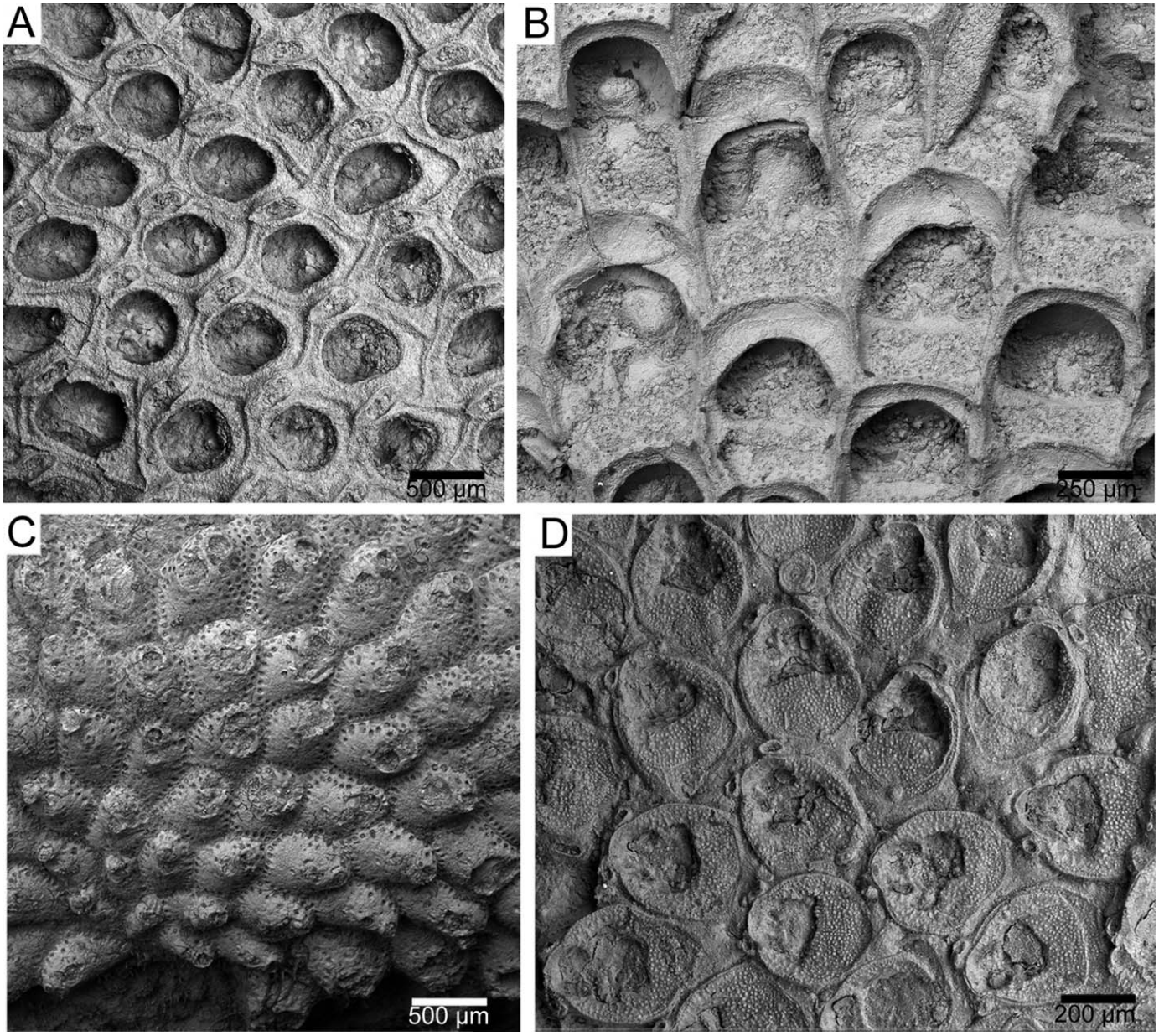

FIG. 10.—Representative bryozoans from the Stadion patch reef. **A**) *Cranosina rubeni*. **B**) *Steginoporella* sp. **C**) *Reptadeonella* sp. A. **D**) *Antropora* cf. *subvespertilio*.

of unidentifiable crustose corallines and fragments of geniculate corallines merely confirm that the foraminiferal packstone facies was deposited in the photic zone but cannot provide a more refined interpretation.

Subsequently, the recolonization of thin-platy corals in the coral sheetstone facies could be a response to a stabilized environment by larger benthic foraminifers and a change of the grain-size composition from silt to clay (Fig. 11F). Previous studies have shown that thin-platy corals are successful in turbid environments if the input contains finer fractions of sediments (Lokier et al. 2009). Flat forms are more common in the foraminiferal assemblage that is dominated by *Lepidosemicyclina bifida* and includes abundant *Amphistegina* and *Nephrolepidina*. It has been proposed that increased surface area to volume ratios provide a morphological response of foraminifera to facilitate the capture of light in low-light environments by symbionts (Hallock et al. 1986). On the other hand, corals in the coral sheetstone facies are typically thinner than 5 mm, suggesting that lower light availability occurred under conditions of clay input in comparison to the silt input that characterized the coral platestone facies. Corals growing at their tolerance limits can develop helical spiraling colony forms to maximize both light capture and ability to shed sediment (Rosen et al. 2002; Sanders and Baron-Szabo 2005). Ragged margins were observed in some thin-platy colonies (Figs. 6A, K), suggesting that episodic higher discharges of clay produced partial mortality, followed by regrowth during intervals of lower sediment stress (Sanders and Baron-Szabo 2005). Agariciids are among the most common corals of the coral sheetstone facies and provide more evidence for a turbid habitat. Agariciid corals are the principal inhabitants of many modern mesophotic reefs (Kahng et al. 2010), mainly associated with deep and clear waters in the Indo-Pacific (Maragos and Jokiel 1986), Red Sea (Fricke et al. 1987), and Caribbean (Reed 1985). In fact, *Leptoseris* species are the deepest-known zooxanthellate corals that live

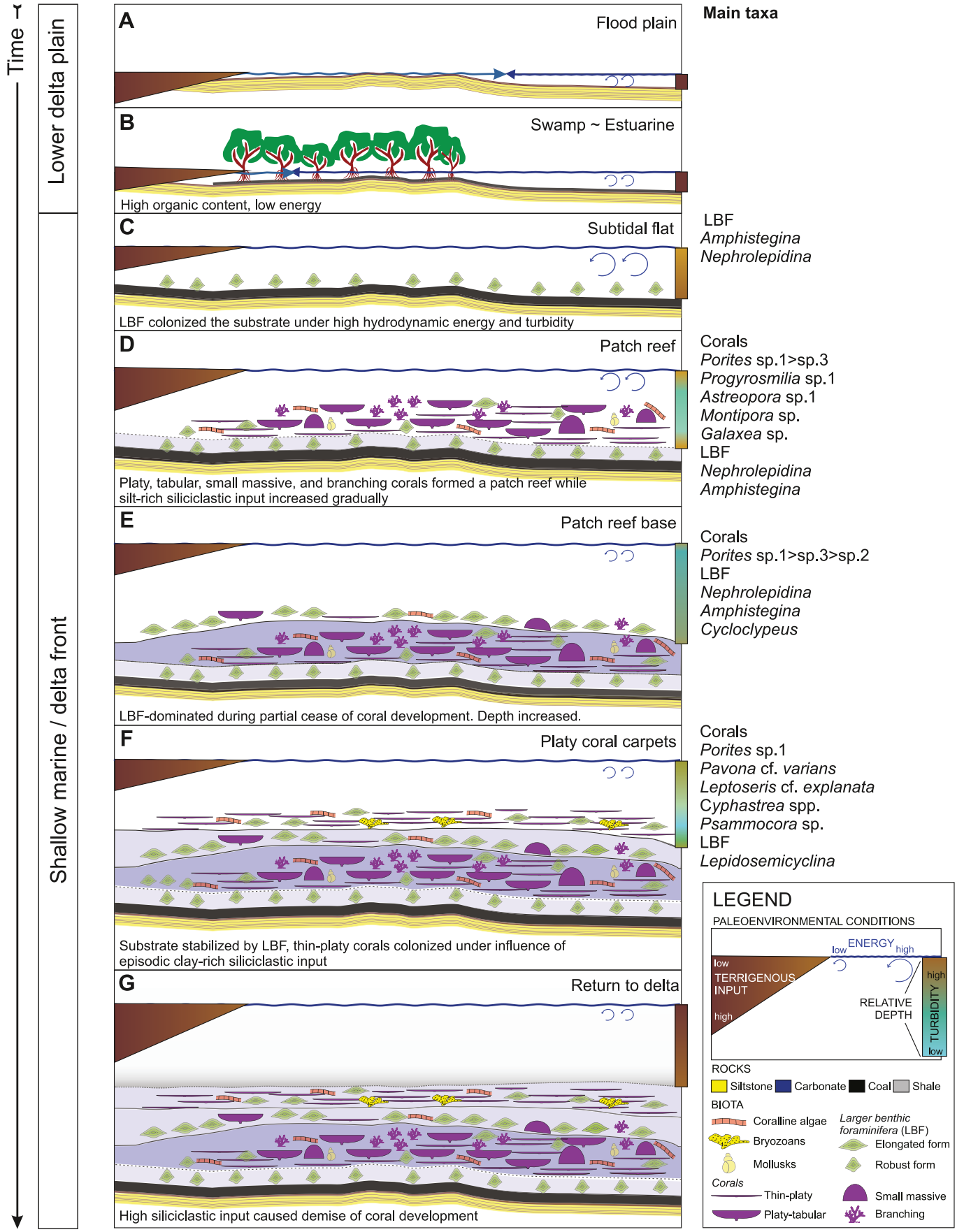

FIG. 11.—Interpretation of depositional environments of the Stadion patch reef.

today at depths of ~ 150 m (Kahng and Maragos 2006), suggesting that not only growth forms but also the taxonomic composition of coral communities in low-light environments could be analogous between turbid shallow waters, such as the Stadion CC habitats, and clear deep waters as in the modern examples. The coral community did not acquire ecological differentiation at this stage, but remained as thin veneers following the seafloor morphology, similar to coral carpets described elsewhere (Riegl and Piller 2000a, 2000b). The rich community of bryozoan epibionts preserved on the underside of agariciids and other taxa, indicates that corals may have grown suprastratally, even though the sheetstone facies was built almost entirely of thin-platy corals. Abundant larger benthic foraminifera and crustose coralline algae were observed partially overgrowing the calicular surfaces of thin-platy corals, suggesting significant partial mortality of the corals before burial. For some taxa, coral growth can be enhanced in turbid habitats (Edinger et al. 2000), and rapid growth allows colonies to survive high levels of partial mortality, promoting rapid accretion of coral carbonates in turbid environments (Perry et al. 2012). Higher nutrient input associated with episodic terrigenous influx can also be inferred at this stage, based on the proliferation of large encrusting colonies of filter-feeding organisms such as bryozoans (Moissette et al. 2007).

The abundance of mastophoroid corallines indicates relatively high light levels in this shallow habitat influenced by siliciclastics. Thus, thin-platy agariciid corals, elongated foraminifera, the occurrence of mastophoroid coralline algae, and a clay-rich matrix all suggest a habitat characterized by episodic high terrigenous input in calm waters at a paleodepth of approximately 10 m. The absence of fossils and any carbonate contents in the overlying clay-shale facies suggests an environmental shift that was intolerable for coral communities (Fig. 11G).

The laminated siltstone and carbonaceous shale were likely deposited within peat swamp or mangrove estuarine environments in a deltaic flood plain setting. In contrast, the bioclastic sandstone, coral platestone, foraminiferal packstone, and coral sheetstone developed on the delta front, probably at depths <10 m, and fully marine environmental conditions. The capping clay shale records the termination of marine-dominated habitats suitable for reef biota.

Diversity of Fossil Assemblages

Species richness varied among the studied fossil assemblages. Corals were the main carbonate-forming group as well as the most diverse group. The substrate provided by corals is likely to have enhanced overall diversity in the Stadion settings by hosting bryozoans, mollusks, and coralline algae. The bryozoan community had a medium diversity in comparison to other studied localities of Miocene age in East Kalimantan (Di Martino et al. 2015), yet did not contribute significantly to carbonate accretion. The record of mollusks in the Stadion section is biased due to a lack of aragonite preservation. Mollusks are typical of other Miocene reef successions in East Kalimantan. They also occur in other modern habitats and several fossil localities (Wright et al. 2003, and references therein). Larger benthic foraminifera were present in the greater number of fossil facies due to their higher ability to tolerate terrigenous input with respect to corals (Lokier et al. 2009) and because they are efficient colonizers of soft substrates (Hohenegger et al. 1999; Renema 2008). The taxonomic richness of larger benthic foraminifera of the Stadion CC is lower than clear-water faunas but is comparable to modern low-light marine environments of Indonesia (Renema and Troelstra 2001; Renema 2008). Higher richness in clear waters is probably due to increased habitat partitioning along an extended photic gradient (Hallock 1987; Renema and Troelstra 2001; Novak and Renema 2015). In this study, analysis of larger benthic foraminifera was used mainly as a paleoenvironmental proxy rather than as a diversity indicator. Even though coralline algae are important paleodepth indicators, in the Stadion patch reef their abundance and diversity was relatively low and restricted to a few mastophoroids species and *Sporolithon* (Rösler et al. 2015). Therefore, discussion about diversity in the Stadion CC sections is focused on the richest taxa found represented by corals and bryozoans.

Corals.—The 69 coral taxa identified from these sections indicate that high coral richness could develop under turbid conditions in the Stadion CC. Of course, corals are smothered and die at high levels of terrigenous input (Van Woesik et al. 1999; Fabricius 2005), but these findings clearly show that below this lethal threshold, turbid environments can support rich coral communities over ecologically significant time scales. Likewise, the Stadion coral assemblages were not building large-scale high-relief reef structures, supporting the idea that high coral species diversity can be independent of reef development (Johnson et al. 2008). Thus, high siliciclastic input is a major control on the functioning of reef-coral communities even though a high diversity of coral species would be able to thrive under turbid conditions (Klaus et al. 2011).

The Stadion coral assemblages are the richest known for a Miocene setting in the Indo-Pacific. Previous records in the area (Wilson 2005; Lokier et al. 2009) include at least ten coral genera, one quarter the richness discovered in this study. In terms of species richness, the maximum number of species per locality recorded so far is 34 species in a middle Miocene site in Fiji (Bromfield and Pandolfi 2012), and 36 species for a Burdigalian patch reef located about 80 km to the north of the Stadion CC (Novak et al. 2013). Coral assemblages of late Oligocene age in similar mixed carbonate-siliciclastic settings in Sabah, Malaysian Borneo are also less rich, with a maximum of 37 genera per site (McMonagle et al. 2011; McMonagle 2012).

Comparisons of the Stadion patch reef assemblages with modern assemblages are complicated by the possibility of time-averaging processes inherent in any fossil assemblage (Pandolfi and Greenstein 1997; Pandolfi 2002). Although the richness of the Stadion assemblages could reflect a time-averaged effect, it is notable that the Stadion patch reef contains a similar number of species as communities living today in clear waters on the nearshore Great Barrier Reef, estimated to be around 60 species per site (Van Woesik et al. 1999), although a larger study of 135 reefs in the Great Barrier Reef system identified an average coral richness of 39.5 taxa per site (DeVantier et al. 2006). The Stadion patch reef is almost three times as diverse as coral assemblages currently growing under high river and tidal influence, in which observed average coral richness per site varied from 20 to 24 species per site (Van Woesik et al. 1999).

There are significant differences in the abundances of the dominant *Porites* species between the coral platestone and coral sheetstone facies (Fig. 7A). Studies on *Porites* species at the Great Barrier Reef have shown that colonies of this genus are able to tolerate long-term sediment input and low-light levels, in relatively calm waters for long periods of time (Stafford-Smith and Ormond 1992; Stafford-Smith 1993; Anthony 1999; Perry et al. 2009).

Acroporids are characteristic of the platestone facies, while agariciids are more common and diverse in the sheetstone facies (Table 2). Although acroporids are mainly known to prefer clear- and shallow-water habitats on modern reefs, some *Astreopora* and the *A. elegans*-group (Fig. 6H) species that are typical of the coral platestone facies are also known from low-light environments such as shallow turbid reefs and reef slopes (Wallace 1999; Veron 2000). A higher abundance and diversity of agariciids in the coral sheetstone facies, including *Pachyseris*, *Leptoseris*, and *Pavona* species, could be explained by their ability to grow and colonize disturbed habitats as observed in modern Indo-Pacific (Tomascik et al. 1997) and Caribbean reefs (Jackson and Hughes 1985). In the Leitha Limestone (Austria), middle Miocene coral assemblages dominated by a platy *Leptoseris* species developed as coral carpets with a rich associated bryozoan community that is comparable to the Stadion CC (Reuter et al. 2012). Even though both coral carpet communities have been interpreted to

TABLE 2.—*Percentage contribution by the top 24 coral species to the Bray-Curtis similarity (SIMPER analysis) in species biomass (weight in grams) at the coral platestone (= CPl) and coral sheetstone (= CSh) facies in the Stadion patch reef.*

	Coral species	Contrib	SD	Ratio	av. F4, CPl	av. F6, CSh	Cumulative
1	*Porites* sp.1	0.183	0.132	1.390	728.9	2679.9	0.214
2	*Progyrosmilia* sp.2	0.066	0.103	0.639	448.9	247.8	0.291
3	*Leptoseris* cf. *explanata*	0.063	0.101	0.621	6.6	649.7	0.364
4	*Porites* sp.3	0.056	0.099	0.569	545.5	–	0.431
5	*Cyphastrea* cf. *divaricata*	0.046	0.057	0.805	–	442.6	0.485
6	*Pavona* cf. *varians*	0.042	0.053	0.797	–	743.9	0.534
7	*Leptoseris* sp.7	0.035	0.049	0.710	328.3	–	0.575
8	*Psammocora* sp.1	0.033	0.046	0.714	–	366.4	0.614
9	*Pachyseris* sp.4	0.030	0.031	0.973	33.3	429.1	0.649
10	*Astreopora* sp.1	0.021	0.060	0.355	340.3	–	0.674
11	*Astreopora* sp.2	0.021	0.021	0.994	245.2	155.9	0.698
12	*Goniopora planulata*	0.021	0.035	0.596	1.1	288.2	0.723
13	*Montipora* cf. *venosa*	0.021	0.032	0.655	252.1	12.4	0.748
14	*Galaxea* sp.1	0.020	0.035	0.555	215.2	3.9	0.770
15	*Merulina* sp.1	0.018	0.042	0.437	–	304.8	0.792
16	*Progyrosmilia vacua*	0.017	0.030	0.547	–	303.3	0.811
17	*Fungophyllia* sp.1	0.013	0.021	0.629	37.1	88.4	0.827
18	*Cyphastrea* cf. *imbricata*	0.013	0.031	0.430	–	143.7	0.843
19	*Symphyllia* sp.1	0.010	0.014	0.717	103.2	33.7	0.855
20	*Porites* sp.2	0.010	0.012	0.825	61.6	111.6	0.866
21	*Coscinaraea* sp.1	0.009	0.020	0.473	4.4	185.6	0.877
22	*Alveopora* sp.1	0.009	0.013	0.694	100.2	1.1	0.887
23	*Stylophora* sp.1	0.009	0.017	0.502	59.6	53.7	0.897
24	*Goniopora* sp.2	0.008	0.019	0.402	64.2	26.2	0.906

occur under similar high siliciclastic environments, species richness of the Stadion in the Indo-Pacific is much higher than the one of the impoverished carpets of the Leitha Limestone in the Paratethys.

Bryozoans.—Twenty-eight bryozoan species occurred within the Stadion coral environments and these new records increase our knowledge of this poorly studied group in fossil communities of the Indo-Pacific (Di Martino and Taylor 2012, 2014). The undersides of platy corals supported a relatively rich encrusting bryozoan community. These surfaces may have formed long-lived, cryptic habitats for the settlement of bryozoan larvae, offering a large surface area for the growth of encrusting bryozoans and adequate vertical space for erect colony growth. Despite high richness, the abundance of bryozoans is due primarily to a few common encrusting species, particularly *Steginoporella* sp. and *Reptadeonella* sp. In the studied units, these two cheilostomes covered more substrate space than any other species. Furthermore, *Steginoporella* sp. often overgrows older colonies of the same species by frontal budding. Congeneric species encrusting the undersurfaces of foliaceous reef corals in Jamaica at the present day show a similar tendency to monopolize the substrate (Jackson and Winston 1982; Jackson 1984). In Jamaican successions *Steginoporella* is an extremely fast growing taxon (Jackson and Hughes 1985), whereas *Reptadeonella* grow much more slowly. *Steginoporella* colonies are much more common than *Reptadeonella* in disturbed microhabitats such as the edges of coral colonies (Jackson and Hughes 1985). Although colony fragmentation renders, it is impossible to distinguish with certainty between coral edges and inner zones. The distribution of *Steginoporella* sp. and *Reptadeonella* sp. may reflect the same pattern showed by congeneric Jamaican species.

Comparison with Coeval Regional Patch Reefs

Wilson (2005) described seven other Miocene delta-front patch reefs located in the Kutai Basin that likely developed in turbid shallow waters (≤ 10 m) with low-light penetration during lowstand to transgressive intervals. The Stadion reefs described herein developed under similar conditions but also add new elements that aid in understanding the dynamics of Miocene turbid-water coral communities. Here we compare the Stadion patch reef with the Bontang patch reef (Novak et al. 2013) and two of the seven reefs described by Wilson (2005). The Batu Putih carbonates occur about 2.3 km below the Stadion CC in the Samarinda sequence, and the Dibelakan Parliament has been considered as a lateral extension of the youngest carbonates of the Batu Putih patch reef (Wilson 2005). The Bontang patch reef (Novak et al. 2013) is about 83 km to the north and late Burdigalian in age. As with most Miocene patch reefs in the region, initial coral development in the Stadion patch reef occurred during a transgressive interval. Although disseminated leaves and carbon detritus were observed at the base of the succession in Batu Putih and Dibelakan Parliament patch reefs (Wilson 2005), the development of the patch reef on top of a carbonaceous shale makes the Stadion coral assemblages different from all previously described patch reefs of the region. Coral assemblages occurring immediately after carbonaceous deposition shows that a relatively minor change in depth could trigger coral development in the ancient Kutai Basin.

In terms of biotic composition, mastophoroid coralline algae are dominant in the Stadion CC in contrast to the dim-light Melobesioidae assemblage observed in the Batu Putih, Dibelakan Parliament, and Bontang patch reefs (Wilson 2005; Novak et al. 2013). Coral assemblages follow a relatively similar succession, which in the case of the Batu Putih patch reef has been described as ideal because it shows a change from sheet-platestone to mixstone and pillarstone (Wilson 2005; Lokier et al. 2009). In the Bontang patch reef, which exhibits a change of facies from sheetstone into platestone, this idealized succession is only partially developed (Novak et al. 2013). In the coral platestone facies of the Stadion patch reef this succession of thin-platy to tabular, small massive and branching coral growth forms occurs as a thin, "condensed succession" without sharp differentiation into distinct facies.

Common coral genera mentioned by Wilson (2005) are also present in the Bontang patch reef (Novak et al. 2013) and the Stadion patch reef, yet direct taxonomic comparisons can only be performed between the latter two. Although poritids (*Porites* and *Goniopora*) are abundant in the four settings, the Bontang patch reef hosts more common merulinid taxa

(former Faviidae), while in the Stadion CC, acroporids (*Astreopora* spp.) and agariciids are more abundant.

Thus, a spectrum of three different types of biotic assemblages within these turbid environments can be recognized: (1) the Stadion patch reef with characteristic photophilic coralline algae and "condensed succession" of coral development; (2) Batu Putih and Dibelakan Parliament patch reefs with coralline algae tolerant of a broader range of turbid low-light habitats and an "ideal" succession of reef development (Wilson 2005); and (3) the Bontang patch reef (Novak et al. 2013), also with coralline algae that can thrive in turbid low light but an incomplete succession of corals restricted to sheet and platestones. Such differences in the composition of coralline algae and corals could be interpreted as a response of the biota to slightly different levels of light within the low-light levels characteristic of these shallow turbid habitats. In particular, the Stadion patch reef developed in the upper limits of low-light regime, but the Bontang patch reef (Novak et al. 2013) developed at the lower boundaries of low-light levels. The Batu Putih and Dibelakan Parliament patch reefs (Wilson 2005) developed within the whole range of low-light levels resulting in more habitat partitioning among biota. According to Wilson (2005), turbid conditions on the delta-front limited coral development on the the Batu Putih and Dibelakan Parliament patch reefs to habitats less than 10 m deep. The lithology and fossil assemblages found in the Stadion patch reef suggest that the Stadion patch reef occupied a similar habitat. In the case of the Bontang reef, mesophotic conditions resulted from both high terrigenous input and deposition below fairweather wave base (Novak et al. 2013).

Another possible explanation for the differences found among the three fossil assemblages in question is the relative position of the patch reefs within the delta system. In deltaic environments, turbidity and light penetration are controlled primarily by position within the deltaic complex. In the modern Mahakam delta system, the maximum concentration of suspended particles is found in the mouth of the main delta lobes, while the minimum concentration is observed in the offshore region (Budhiman et al. 2012). Similarly, sand decreases in grain size in an offshore direction (Storms et al. 2005). Superimposed on these onshore-offshore trends is a north-south variation caused by the southward flow of the Indonesian Throughflow current that generally persists throughout the year (Murray and Arief 1988) and favors a higher concentration of carbonates on the northern part of the shelf (Roberts and Sydow 2003). Thus, the Stadion patch reef may have developed north of an active delta lobe, while the Bontang (Novak et al. 2013), Batu Putih, and Dibelakan Parliament patch reefs (Wilson 2005), may have been located closer to different active delta lobes. However, additional data, not available in the present study, are needed to test this hypothesis.

Shallow Turbid Reefs and Coral Diversity

The reef-coral fauna recovered from the Stadion patch reef is one of the richest Miocene assemblages yet discovered and provides a record of the transition from foraminifera- to coral-dominated carbonates (Wilson and Rosen 1998). This faunal transition is likely related to the initiation of the modern-day Indo-West Pacific biodiversity hotspot as recorded by diverse coral assemblages from the late Oligocene in Malaysian Borneo (McMonagle et al. 2011). These Oligocene faunas, and the various patch reefs that have been described from the Kutai basin, all developed in turbid habitats, yet contain significant diversity. This suggests that such habitats may well have played a stronger role in coral diversification during the Miocene than has previously been attributed to them.

CONCLUSIONS

Carbonate bodies of the Stadion CC sections in East Kalimantan, Indonesia can be interpreted as a shallow-water patch reef, in which the main controls for coral development were depth and varying levels of water turbidity related to the amount, frequency, and grain size of siliciclastic input. Evidence gathered in this study supports a paleodepth interpretation for the Stadion patch reef within turbid waters at a maximum of 10 m depth. Different facies were most likely deposited following a proposed deepening sequence comprising: (1) laminated siltstone; (2) carbonaceous shale; (3) bioclastic packstone; (4) coral platestone; (5) foraminiferal packstone; (6) coral sheetstone; and (7) clay shale.

Larger benthic foraminifera were present in all fossiliferous facies, supporting their role as the most siliciclastic-tolerant group. Although the environmental conditions for coral development within the Samarinda sequence were ephemeral, the Stadion patch reef had a rich coral assemblage that could cope with changing terrigenous input. Yet their demise was due to increased siliciclastic input exceeding the tolerance of any coral species. Corals enhanced the overall diversity in these turbid settings by hosting bryozoans, coralline algae, mollusks, and echinoderms.

Comparisons to coeval patch reefs in East Kalimantan show that platy corals are dominant in these environments, with some taxa found in most sites but other taxa more unevenly distributed among habitats. Communities of larger benthic foraminifera tend to be similar among all patch reefs, but calcareous coralline algal assemblages vary significantly according to light availability, with characteristic assemblages in lower and higher light habitats within the Samarinda turbid settings during the Miocene. Bryozoans are diverse and their presence in the studied fossil record is usually associated with thin platy coral assemblages. Mollusks are poorly preserved in platy-coral dominated settings. Large, ecologically sampled collections and multitaxa analysis of fossil assemblages are important to the better understanding of paleoenvironmental conditions. The high diversity of coral species in the Stadion patch reef highlights the importance of marginal turbid habitats as a reservoir of diversity during the origins of the Coral Triangle hotspot.

ACKNOWLEDGMENTS

This manuscript is part of a series of papers produced by the Throughflow Project, in a collaborative effort to provide detailed information about biodiversity during the Miocene of East Kalimantan. This research was funded by the Marie Curie Actions Plan, Seventh Framework Programme of the European Union (grant no. 237922). Fieldwork was possible thanks to the collaboration of Jon Todd, Lil Stevens, Jeremy Young, Aries Kusworo, Untung Margono, and Asep S. Erawatna. Safe access to the roadcut outcrops was provided by staff of the KTC Coal Mining and Energy Group. Brian Rosen is greatly acknowledged for his help on coral identifications and fruitful discussions regarding ancient coral environments and interpretations. Paul D. Taylor, Frank Wesselingh, and Ann Holborn assisted with the taxonomic identification of bryozoans, mollusks, and foraminifera, respectively. Ann F. Budd and Carden Wallace are thanked for their advice on coral identifications of Merulinidae and *Acropora*, respectively. Jill Darrell and Lyndsey Douglas assisted with the curation of specimens at the Natural History Museum, London (NHM), and we gratefully acknowledge the enthusiastic support of Ali Thomas and the NHM "V-Factor" volunteers for exhaustive sample processing. This study was conducted under research license 0266/SIP/FRP/XI/2010 issued by RISTEK (Kementerian Riset Dan Teknologi Republik Indonesia) with special thanks (*terima kasih*) to Professor Fauzie Hasibuan of the Indonesian Geological Agency–Center for Geology Survey, for his support of this work. Christine Perrin, Wolfgang Müller, John-Paul Zonneveld, and one anonymous reviewer are acknowledged for their constructive suggestions, which helped in improving this manuscript.

SUPPLEMENTAL MATERIAL

Data is available from the PALAIOS Data Archive: http://www.sepm.org/pages.aspx?pageid=332.

REFERENCES

Adey, W.H., 1986, Coralline algae as indicators of sea-level, *in* Plassche, O. van de, ed., Sea-Level Research: A Manual for the Collection and Evaluation of Data: Amsterdam, Free University of Amsterdam, p. 229–279.

Allen, G.P., and Chambers, J.L.C., 1998, Sedimentation in the Modern and Miocene Mahakam Delta: Jakarta, Indonesia, Indonesian Petroleum Association, 236 p.

Anthony, K.R.N., 1999, Coral suspension feeding on fine particulate matter: Journal of Experimental Marine Biology and Ecology, v. 232, p. 85–106, doi: 10.1016/S0022-0981(98)00099-9.

Bassi, D., and Nebelsick, J.H., 2010, Components, facies and ramps: redefining upper Oligocene shallow water carbonates using coralline red algae and larger foraminifera (Venetian area, northeast Italy): Palaeogeography, Palaeoclimatology, Palaeoecology, v. 295, p. 258–280, doi: 10.1016/j.palaeo.2010.06.003.

Bayer, F.M., and Macintyre, I.G., 2001, The mineral component of the axis and holdfast of some gorgonacean octocorals (Coelenterata: Anthozoa), with special reference to the family Gorgoniidae: Biological Society of Washington, Proceedings, v. 114, p. 309–345.

Beesley, P.L., Ross, G.J.B., and Wells, A.E., 1998, Mollusca: The southern synthesis. Fauna of Australia. Part A. XVI: Melbourne, Australia, CSIRO Publishing, 563 p.

Bellwood, D.R., Hughes, T.P., Folke, C., and Nyström, M., 2004, Confronting the coral reef crisis: Nature, v. 429, p. 827–833.

Bellwood, D.R., Hughes, T.P., Connolly, S.R., and Tanner, J., 2005, Environmental and geometric constraints on Indo-Pacific coral reef biodiversity: Ecology Letters, v. 8, p. 643–651, doi: 10.1111/j.1461-0248.2005.00763.x.

Benisek, M.-F., Betzler, C., Marcano, G., and Mutti, M., 2009, Coralline-algal assemblages of a Burdigalian platform slope: implications for carbonate platform reconstruction (northern Sardinia, western Mediterranean Sea): Facies, v. 55, p. 375–386, doi: 10.1007/s10347-009-0183-7.

Bosence, D.W.J., 1983, Coralline algal reef frameworks: Journal of the Geological Society, v. 140, p. 365–376, doi: 10.1144/gsjgs.140.3.0365.

Bosence, D.W.J., 1991, Coralline algae: mineralization, taxonomy, and palaeoecology, *in* Calcareous Algae and Stromatolites: Springer, Berlin Heidelberg, p. 98–113.

Braga, J.C., Martin, J.M., and Alcala, B., 1990, Coral reefs in coarse-terrigenous sedimentary environments (upper Tortonian, Granada Basin, southern Spain): Sedimentary Geology, v. 66, p. 135–150, doi: 10.1016/0037-0738(90)90011-H.

Braga, J.C., Vescogni, A., Bosellini, F.R., and Aguirre, J., 2009, Coralline algae (Corallinales, Rhodophyta) in western and central Mediterranean Messinian reefs: Palaeogeography, Palaeoclimatology, Palaeoecology, v. 275, p. 113–128, doi: 10.1016/j.palaeo.2009.02.022.

Braga, J.C., Bassi, D., and Piller, W.E., 2010, Palaeoenvironmental significance of Oligocene-Miocene coralline red algae: a review, *in* Mutti, M., Piller, W.E., and Betzler, C., eds., Carbonate Systems during the Oligocene-Miocene Climatic Transition: IAS Special Publications 42, p. 165–182.

Bromfield, K., and Pandolfi, J.M., 2012, Regional patterns of evolutionary turnover in Neogene coral reefs from the central Indo-West Pacific Ocean: Evolutionary Ecology, v. 26, p. 375–391, doi: 10.1007/s10682-011-9483-9.

Browne, N.K., Smithers, S.G., and Perry, C.T., 2012, Coral reefs of the turbid inner-shelf of the Great Barrier Reef, Australia: an environmental and geomorphic perspective on their occurrence, composition and growth: Earth-Science Reviews, v. 115, p. 1–20, doi: 10.1016/j.earscirev.2012.06.006.

Budhiman, S., Salama, M.S., Vekerdy, Z., and Verhoef, W., 2012, Deriving optical properties of Mahakam Delta coastal waters, Indonesia using in situ measurements and ocean color model inversion: ISPRS Journal of Photogrammetry and Remote Sensing, v. 68, p. 157–169, doi: 10.1016/j.isprsjprs.2012.01.008.

Cibaj, I., 2009, A fluvial series in the middle Miocene of Kutei Basin: a major shift from Proto-Mahakam shallow marine to the continental environment, *in* AAPG Hedberg Conference "Variations in Fluvial-Deltaic and Coastal Reservoirs Deposited in Tropical Environments", Jakarta, Indonesia: American Association of Petroleum Geologists (AAPG) Search and Discover Article #90102, p. 1–11.

Cloke, I.R., Moss, S.J., and Craig, J., 1999, Structural controls on the evolution of the Kutai Basin, East Kalimantan: Journal of Asian Earth Sciences, v. 17, p. 137–156.

Constantz, B.R., 1986, The primary surface area of corals and variations in their susceptibility to diagenesis, *in* Schroeder, J.H. and Purser, B.H., eds., Reef Diagenesis: New York, Springer, p. 53–76.

Cummings, E.R., 1932, Reefs or bioherms?: Geological Society Of America Bulletin, v. 43, p. 331–352.

De'ath, G., and Fabricius, K.E., 2010, Water quality as a regional driver of coral biodiversity and macroalgae on the Great Barrier Reef Water as a driver of coral quality biodiversity regional on the Great Barrier Reef: Ecological Applications, v. 20, p. 840–850.

DeVantier, L.M., De'ath, G., Turak, E., Done, T.J., and Fabricius, K.E., 2006, Species richness and community structure of reef-building corals on the nearshore Great Barrier Reef: Coral Reefs, v. 25, p. 329–340, doi: 10.1007/s00338-006-0115-8.

Di Martino, E., and Taylor, P.D., 2012, Systematics and life history of Antoniettella exigua, a new genus and species of cribrimorph bryozoan from the Miocene of East Kalimantan (Indonesia): Bollettino della Società Paleontologica Italiana, v. 51, p. 99–108, doi: 10.4435/BSPI.2012.11.

Di Martino, E., and Taylor, P.D., 2014, Miocene Bryozoa from East Kalimantan, Indonesia. Part I: Cyclostomata and Cheilostomata "Anasca:" Scripta Geologica, v. 146, p. 17–126.

Di Martino, E., Taylor, P.D., and Johnson, K.G., 2015, Bryozoan diversity in the Miocene of the Kutai Basin, East Kalimantan, Indonesia: PALAIOS, v. 30, p. 109–115.

Dunham, R.J., 1962, Classification of carbonate rocks according to depositional texture, *in* Ham, W.E., ed., Classification of Carbonate Rocks: American Association of Petroleum Geologists Memoir: p. 108–121.

Edinger, E.N., Limmon, G.V, Jompa, J., Widjatmoko, W., Heikoop, J.M., and Risk, M.J., 2000, Normal coral growth rates on dying reefs: Are coral growth rates good indicators of reef health?: Marine Pollution Bulletin, v. 40, p. 404–425, doi: 10.1016/S0025-326X(99)00237-4.

Fabricius, K.E., 2005, Effects of terrestrial runoff on the ecology of corals and coral reefs: review and synthesis: Marine Pollution Bulletin, v. 50, p. 125–146, doi: 10.1016/j.marpolbul.2004.11.028.

Fabricius, K.E., and De'ath, G., 2001, Environmental factors associated with the spatial distribution of crustose coralline algae on the Great Barrier Reef: Coral Reefs, v. 19, p. 303–309, doi: 10.1007/s003380000120.

Fagerstrom, J.A., 1987, The evolution of reef communities: New York, John Wiley & Sons, 600 p.

Folk, R.L., 1980, Petrology of Sedimentary Rocks: Austin, Texas, Hemphill Publishing Company, 184 p.

Fricke, H.W., Vareschi, E., and Schlichter, D., 1987, Photoecology of the coral Leptoseris fragilis in the Red Sea twilight zone (an experimental study by submersible): Oecologia, v. 73, p. 371–381.

Gainey, L.F., and Wise, S.W., 1980, Convergent shell morphology in intertidal gastropods: Journal of Molluscan Studies, v. 46, p. 192–207.

Gerth, H., 1923, Die Anthozoenfauna des Jungtertiärs von Borneo [Anthozoa from the upper Tertiary of Borneo]: Sammlungen des Geologischen Reichs-Museums in Leiden, Serie 1, v. 10, p. 37–136, 9 plates.

Hall, R., and Nichols, G., 2002, Cenozoic sedimentation and tectonics in Borneo: climatic influences on orogenesis, *in* Jones, S.J. and Frostick, L., eds., Sediment Flux to Basins: Causes, Controls and Consequences: Geological Society, London, Special Publications, p. 5–22.

Hallock, P., 1981, Production of carbonate sediments by selected large benthic foraminifera on two Pacific coral reefs: Journal of Sedimentary Petrology, v. 51, p. 467–474.

Hallock, P., 1987, Fluctuations in the trophic resource continuum: A factor in global diversity cycles?: Paleoceanography, v. 2, p. 457–471.

Hallock, P., and Glenn, E.C., 1986, Larger benthic foraminifera: A tool for paleoenvironmental analysis of Cenozoic carbonate depositional facies: PALAIOS, v. 1, p. 55–64.

Hallock, P., Forward, L.B., and Hansen, H.J., 1986, Influence of environment on the test shape of Amphistegina: The Journal of Foraminiferal Research, v. 16, p. 224–231, doi: 10.2113/gsjfr.16.3.224.

Hayward, A.B., 1982, Coral reefs in a clastic sedimentary environment: Fossil (Miocene, S.W. Turkey) and modern (recent, Red Sea) analogues: Coral Reefs, v. 1, p. 109–114, doi: 10.1007/BF00301692.

Héros, V., Lozouet, P., Maestrati, P., Cosel, R. Von, Brabant, D., and Bouchet, P., 2007, Mollusca of New Caledonia, *in* Payri, C. and Forges, R de, eds., Compendium of Marine Species of New Caledonia, Documents Scientifique et Techniques II, 7: Institut de recherche pour le développement, Centre de Nouméa, p. 199–254.

Hoegh-Guldberg, O., 2011, Coral reef ecosystems and anthropogenic climate change: Regional Environmental Change, v. 11, p. S215–S227, doi: 10.1007/s10113-010-0189-2.

Hoegh-Guldberg, O., Mumby, P.J., Hooten, A.J., Steneck, R.S., Greenfield, P., Gomez, E., Harvell, C.D., Sale, P.F., Edwards, A.J., Caldeira, K., Knowlton, N., Eakin, C.M., Iglesias-Prieto, R., Muthiga, N., Bradbury, R.H., Dubi, A., and Hatziolos, M.E., 2007, Coral reefs under rapid climate change and ocean acidification: Science, v. 318, p. 1737–1742, doi: 10.1126/science.1152509.

Hoeksema, B.W., 2007, Delineation of the Indo-Malayan Centre of Maximum Marine Biodiversity: The Coral Triangle, *in* Renema, W., ed., Biogeography, Time, and Place: Distributions, Barriers, and Islands: Springer, Netherlands, p. 117–178.

Hohenegger, J., Yordanova, E., Nakano, Y., and Tatzreiter, F., 1999, Habitats of larger foraminifera on the upper reef slope of Sesoko Island, Okinawa, Japan: Marine Micropaleontology, v. 36, p. 109–168.

Hottinger, L., 1997, Shallow benthic foraminiferal assemblages as signals for depth of their deposition and their limitations: Bulletin de la Société Géologique de France, v. 168, p. 491–505.

Hughes, T.P., Baird, A.H., Bellwood, D.R., Card, M., Connolly, S.R., Folke, C., Grosberg, R., Hoegh-Guldberg, O., Jackson, J.B.C., Kleypas, J.A., Lough, J.M., Marshall, P., Nyström, M., Palumbi, S.R., Pandolfi, J.M., Rosen, B., and Roughgarden, J., 2003, Climate change, human impacts, and the resilience of coral reefs: Science, v. 301, p. 929–933, doi: 10.1126/science.1085046.

Hughes, T.P., Rodrigues, M.J., Bellwood, D.R., Ceccarelli, D., Hoegh-Guldberg, O., McCook, L.J., Moltschaniwskyj, N., Pratchett, M.S., Steneck, R.S., and Willis, B., 2007, Phase shifts, herbivory, and the resilience of coral reefs to climate change: Current Biology: CB, v. 17, p. 360–365, doi: 10.1016/j.cub.2006.12.049.

Insalaco, E., 1998, The descriptive nomenclature and classification of growth fabrics in fossil scleractinian reefs: Sedimentary Geology, v. 118, p. 159–186.

Iryu, Y., Nakimori, T., Matsuda, S., and Abe, O., 1995, Distribution of marine organisms and its geological significance in the modern reef complex of the Ryukyu Islands: Sedimentary Geology, v. 99, p. 243–258.

Jackson, J.B.C., 1984, Ecology of cryptic coral reef communities. III. Abundance and aggregation of encrusting organisms with particular reference to Cheilostome Bryozoa: Journal of Experimental Marine Biology and Ecology, v. 75, p. 37–57.

Jackson, J.B.C., and Hughes, T.P., 1985, Adaptive strategies of coral-reef invertebrates: American Scientist, v. 73, p. 265–274.

Jackson, J.B.C., and Winston, J.E., 1982, Ecology of cryptic coral reef communities. I. Distribution and abundance of major groups of encrusting organisms: Journal of Experimental Marine Biology and Ecology, v. 57, p. 135–147.

Johnson, K.G., Jackson, J.B.C., and Budd, A.F., 2008, Caribbean reef development was independent of coral diversity over 28 million years: Science, v. 319, p. 1521–1523, doi: 10.1126/science.1152197.

Johnson, K.G., Sánchez-Villagra, M.R., and Aguilera, O.A., 2009, The Oligocene-Miocene transition on coral reefs in the Falcon Basin (NW Venezuela): PALAIOS, v. 24, p. 59–69, doi: 10.2110/palo.2008.p08-004r.

Johnson, K.G., Renema, W., Rosen, B.R., and Santodomingo, N., 2015, Old data for old questions: what can the historical collections really tell us about the Neogene origins of really tell us about reef-coral diversity in the Coral Triangle: PALAIOS, v. 30, p. 94–108.

Kahng, S.E., and Maragos, J.E., 2006, The deepest, zooxanthellate scleractinian corals in the world?: Coral Reefs, v. 25, p. 254–254, doi: 10.1007/s00338-006-0098-5.

Kahng, S.E., Spalding, H.L., Brokovich, E., Wagner, D., Weil, E., Hinderstein, L., and Toonen, R.J., 2010, Community ecology of mesophotic coral reef ecosystems: Coral Reefs, v. 29, p. 255–275, doi: 10.1007/s00338-010-0593-6.

Katwijk, M.M. Van, Meier, N.F., Loon, R. Van, Hove, E.M. Van, Giesen, W.B.J.T., Velde, G. Van Der, and Hartog, C. Den, 1993, Sabaki River sediment load and coral stress: correlation between sediments and condition of the Malindi-Watamu reefs in Kenya (Indian Ocean): Marine Biology, v. 117, p. 675–683.

Kennedy, W.J., Taylor, J.D., and Hall, A., 1969, Environmental and biological control on bivalve shell mineralogy: Biological Reviews, v. 44, p. 499–530.

Klaus, J.S., Mcneill, D.F., Budd, A.F., and Johnson, K.G., 2008, Assessing community change in Miocene to to Pliocene coral assemblages of the Northern Dominican Republic, *in* Nehm, R.H. and Budd, A.F., eds., Evolutionary Stasis and Change in the Dominician Republic Neogene: Springer Science + Business Media B.V., Netherlands, p. 193–223.

Klaus, J.S., McNeill, D.F., Budd, A.F., and Coates, A.G., 2011, Neogene reef coral assemblages of the Bocas del Toro region, Panama: The rise of Acropora palmata: Coral Reefs, v. 31, p. 191–203, doi: 10.1007/s00338-011-0835-2.

Kleypas, J.A., McManus, J.W., and Meñez, L.A.B., 1999, Environmental limits to coral reef development: Where do we draw the line?: American Zoologist, v. 39, p. 146–159.

Larcombe, P., Costen, A., and Woolfe, K.J., 2001, The hydrodynamic and sedimentary setting of nearshore coral reefs, central Great Barrier Reef shelf, Australia: Paluma Shoals, a case study: Sedimentology, v. 48, p. 811–835.

Lokier, S.W., Wilson, M.E.J., and Burton, L.M., 2009, Marine biota response to clastic sediment influx: A quantitative approach: Palaeogeography, Palaeoclimatology, Palaeoecology, v. 281, p. 25–42, doi: 10.1016/j.palaeo.2009.07.007.

Lowenstam, H.A., and Weiner, S., 1983, Mineralization by organisms and the evolution of biomineralization, *in* Westbroek, P. and DeJong, E.W., eds., Biomineralization and Biological Metal Accumulation: Dordrecht, Reidel Publishing Company, p. 191–203.

Maragos, J.E., and Jokiel, P.L., 1986, Reef corals of Johnston Atoll: One of the world's most isolated reefs: Coral Reefs, v. 4, p. 141–150.

Marshall, N., Novak, V., Cibaj, I., Krijgsman, W., Renema, W., Young, J., Fraser, N., Limbong, A., and Morley, R., 2015, Dating Borneo's Deltaic Deluge: middle Miocene progradation of the Mahakam Delta: PALAIOS, v. 30, p. 7–25.

Mcgregor, H.V., and Gagan, M., 2003, Diagenesis and geochemistry of Porites corals from Papua New Guinea: implications for Paleoclimate reconstruction: Geochimica et Cosmochimica Acta, v. 67, p. 2147–2156.

McMonagle, L.B., 2012, A diverse assemblage of corals from the late Oligocene of eastern Sabah, Borneo: pre-Miocene origins of the Indo-West Pacific marine biodiversity hotspot [Unpublished M.Phil. thesis]: Durham University, UK, 445 p.

McMonagle, L.B., Lunt, P., Wilson, M.E.J., Johnson, K.G., Manning, C., and Young, J., 2011, A re-assessment of age dating of fossiliferous limestones in eastern Sabah, Borneo: implications for understanding the origins of the Indo-Pacific marine biodiversity hotspot: Palaeogeography, Palaeoclimatology, Palaeoecology, v. 305, p. 28–42, doi: 10.1016/j.palaeo.2011.02.009.

Mcneill, D.F., Coates, A.G., Budd, A.F., and Borne, P.F., 2000, Integrated paleontologic and paleomagnetic stratigraphy of the upper Neogene deposits around Limon, Costa Rica: a coastal emergence record of the Central American Isthmus: Geological Society of America Bulletin, v. 112, p. 963–981, doi: 10.1130/0016-7606(2000)112<963.

Minnery, G.A., 1990, Crustose coralline algae from the Flower Garden Banks, northwestern Gulf of Mexico: controls on distribution and growth morphology: Journal of Sedimentary Petrology, v. 60, p. 992–1007.

Moissette, P., Dulai, A., Escarguel, G., Kázmér, M., Müller, P., and Saint Martin, J.-P., 2007, Mosaic of environments recorded by bryozoan faunas from the middle Miocene of Hungary: Palaeogeography, Palaeoclimatology, Palaeoecology, v. 252, p. 530–556, doi: 10.1016/j.palaeo.2007.05.010.

Morsilli, M., Bosellini, F.R., Pomar, L., Hallock, P., Aurell, M., and Papazzoni, C.A., 2011, Mesophotic coral buildups in a prodelta setting (late Eocene, southern Pyrenees, Spain): a mixed carbonate–siliciclastic system: Sedimentology, v. 59, p. 766–794, doi: 10.1111/j.1365-3091.2011.01275.x.

Moss, S.J., and Chambers, J.L.C., 1999, Tertiary facies architecture in the Kutai Basin, Kalimantan, Indonesia: Journal of Asian Earth Sciences, v. 17, p. 157–181.

Murray, S.P., and Arief, D., 1988, Throughflow into the Indian Ocean through the Lombok Strait, January 1985–January 1986: Nature, v. 333, p. 444–447, doi: 10.1038/333444a0.

Novak, V., and Renema, W., 2015, Larger foraminifera as environmental discriminators in Miocene mixed carbonate-siliciclastic systems: PALAIOS, v. 30, p. 40–52.

Novak, V., Santodomingo, N., Rösler, A., Di Martino, E., Braga, J.C., Taylor, P.D., Johnson, K., and Renema, W., 2013, Environmental reconstruction of a late Burdigalian (Miocene) patch reef in deltaic deposits (East Kalimantan, Indonesia): Palaeogeography, Palaeoclimatology, Palaeoecology, doi: 10.1016/j.palaeo.2013.01.009.

Nugues, M.M., and Roberts, C.M., 2003, Coral mortality and interaction with algae in relation to sedimentation: Coral Reefs, v. 22, p. 507–516, doi: 10.1007/s00338-003-0338-x.

Oksanen, J., Blanchet, F.G., Kindt, R., Legendre, P., Minchin, P.R., O'Hara, R.B., Simpson, G.L., Solymos, P., Henry, M., Stevens, H., and Wagner, H., 2013, Vegan: Community ecology package. Ordination methods, diversity analysis and other functions for community and vegetation ecologists, http://vegan.r-forge.r-project.org/, Checked April 2013.

Pandolfi, J.M., 1996, Limited membership in Pleistocene reef coral assemblages from the Huon Peninsula, Papua New Guinea: constancy during global change: Paleobiology, v. 22, p. 152–176.

Pandolfi, J.M., 2002, Coral community dynamics at multiple scales: Coral Reefs, v. 21, p. 13–23, doi: 10.1007/s00338-001-0204-7.

Pandolfi, J.M., and Greenstein, B.J., 1997, Taphonomic alteration of reef corals: effects of reef environment and coral growth form. I. The Great Barrier Reef: PALAIOS, v. 12, p. 27–42.

Perrin, C., 2000, Changes of palaeozonation patterns within Miocene coral reefs, Gebel Abu Shaar, Gulf of Suez, Egypt: Lethaia, v. 33, p. 253–268, doi: 10.1080/002411600750053826.

Perrin, C., Bosence, D.W.J., and Rosen, B.R., 1995, Quantitative approaches to palaeozonation and palaeobathymetry of corals and coralline algae in Cenozoic reefs: Geological Society Special Publication, p. 181–229, doi: 10.1144/GSL.SP.1995.083.01.10.

Perry, C.T., Smithers, S.G., and Johnson, K.G., 2009, Long-term coral community records from Lugger Shoal on the terrigenous inner-shelf of the central Great Barrier Reef, Australia: Coral Reefs, v. 28, p. 941–948, doi: 10.1007/s00338-009-0528-2.

Perry, C.T., Smithers, S.G., Gulliver, P., and Browne, N.K., 2012, Evidence of very rapid reef accretion and reef growth under high turbidity and terrigenous sedimentation: Geology, v. 40, p. 719–722, doi: 10.1130/G33261.1.

Pomar, L., Bassant, P., Brandano, M., Ruchonnet, C., and Janson, X., 2012, Impact of carbonate producing biota on platform architecture: insights from Miocene examples of the Mediterranean region: Earth-Science Reviews, v. 113, p. 186–211, doi: 10.1016/j.earscirev.2012.03.007.

Prager, E.J., and Ginsburg, R.N., 1989, Carbonate nodule growth on Florida's outer shelf and its implications for fossil interpretations: PALAIOS, v. 4, p. 310–317.

R-Core Team, 2013, R: a language and environment for statistical computing, http://www.r-project.org. Checked March 2013.

Reed, J.K., 1985, Deepest distribution of Atlantic hermatypic corals discovered in the Bahamas: Fifth International Coral Reef Symposium, Proceedings, v. 6, p. 249–254.

Renema, W., 2006, Large benthic foraminifera from the deep photic zone of a mixed siliciclastic-carbonate shelf off East Kalimantan, Indonesia: Marine Micropaleontology, v. 58, p. 73–82, doi: 10.1016/j.marmicro.2005.10.004.

Renema, W., 2008, Habitat selective factors influencing the distribution of larger benthic foraminiferal assemblages over the Kepulauan Seribu: Marine Micropaleontology, v. 68, p. 286–298, doi: 10.1016/j.marmicro.2008.06.002.

Renema, W., and Troelstra, S.R., 2001, Larger foraminifera distribution on a mesotrophic carbonate shelf in SW Sulawesi (Indonesia): Palaeogeography, Palaeoclimatology, Palaeoecology, v. 175, p. 125–146, doi: 10.1016/S0031-0182(01)00389-3.

Reuter, M., Brachert, T.C., and Kroeger, K.F., 2005, Diagenesis of growth bands in fossil scleractinian corals: identification and modes of preservation: Facies, v. 51, p. 146–159, doi: 10.1007/s10347-005-0064-7.

Reuter, M., Piller, W.E., and Erhart, C., 2012, A middle Miocene carbonate platform under silici-volcaniclastic sedimentation stress (Leitha Limestone, Styrian Basin, Austria): depositional environments, sedimentary evolution and palaeoecology: Palaeogeography, Palaeoclimatology, Palaeoecology, v. 350–352, p. 198–211, doi: 10.1016/j.palaeo.2012.06.032.

Riegl, B., and Piller, W.E., 2000a, Biostromal coral facies: a Miocene example from the Leitha Limestone (Austria) and its actualistic interpretation: PALAIOS, v. 15, p. 399–413, doi: 10.1669/0883-1351(2000)015<0399:BCFAME>2.0.CO;2.

Riegl, B.M., and Piller, W.E., 2000b, Reefs and coral carpets in the northern Red Sea as models for organism-environment feedback in coral communities and its reflection in growth fabrics: Geological Society, London, Special Publications, v. 178, p. 71–88, doi: 10.1144/GSL.SP.2000.178.01.06.

Riegl, B.M., and Piller, W.E., 2002, Reefs and coral carpets in the Miocene paratethys (Badenian, Leitha Limestone, Austria): 9th International Coral Reef Symposium, Bali, Indonesia, Proceedings, v. 1, p. 211–216.

Roberts, H.H., and Sydow, J., 2003, Late Quaternary stratigraphy and sedimentology of the offshore Mahakam Delta, East Kalimantan (Indonesia), *in* Sidi, F.H., Nummedal, D., Imbert, P., Darman, H., and Posamentier, H.W., eds., Tropical Deltas of Southeast Asia: Sedimentation, Stratigraphy and Petroleum Geology: Society for Sedimentary Geology (SEPM) Special Publication, v. 76, p. 125–145.

ROFF, G., CLARK, T.R., REYMOND, C.E., ZHAO, J., FENG, Y., MCCOOK, L.J., DONE, T.J., AND PANDOLFI, J.M., 2013, Palaeoecological evidence of a historical collapse of corals at Pelorus Island, inshore Great Barrier Reef, following European settlement: The Royal Society, Proceedings: Biological Sciences, v. 280, p. 1–10, doi: 10.1098/rspb.2012.2100.

ROGERS, C.S., 1990, Responses of coral reefs and reef organisms to sedimentation: Marine Ecology Progress Series, v. 62, p. 185–202.

ROSEN, B.R., 1990, Reefs and carbonate build-ups, *in* Briggs, D.E.G., and Crowther, P.R., eds., Palaeobiology: A Synthesis: Oxford, UK, Blackwell Scientific Publications, p. 341–346.

ROSEN, B.R., AILLUD, G.S., BOSELLINI, F.R., CLACK, N.J., AND INSALACO, E., 2002, Platy coral assemblages: 200 million years of functional stability in response to the limiting effects of light and turbidity: 9th International Coral Reef Symposium, Bali, Indonesia, Proceedings, p. 255–264.

RÖSLER, A., PRETKOVIĆ, V., NOVAK, V., RENEMA, W., AND BRAGA, J.C., 2015, Coralline algae from the Miocene Mahakam Delta (East Kalimantan, Southeast Asia): PALAIOS, v. 30, p. 83–93.

SANDERS, D., AND BARON-SZABO, R.C., 2005, Scleractinian assemblages under sediment input: their characteristics and relation to the nutrient input concept: Palaeogeography, Palaeoclimatology, Palaeoecology, v. 216, p. 139–181, doi: 10.1016/j.palaeo.2004.10.008.

STAFFORD-SMITH, M.G., 1993, Sediment-rejection efficiency of 22 species of Australian scleractinian corals: Marine Biology, v. 115, p. 229–243.

STAFFORD-SMITH, M.G., AND ORMOND, R.F.G., 1992, Sediment-rejection Mechanisms of 42 Species of Australian Scleractinian Corals: Australian Journal of Marine and Freshwater Research, v. 43, p. 683–705.

STORMS, J.E.A., HOOGENDOORN, R.M., DAM, R.A.C., HOITINK, A.J.F., AND KROONENBERG, S.B., 2005, Late-Holocene evolution of the Mahakam delta, East Kalimantan, Indonesia: Sedimentary Geology, v. 180, p. 149–166, doi: 10.1016/j.sedgeo.2005.08.003.

SU, X., KAMAT, S., AND HEUER, A.H., 2000, The structure of sea urchin spines, large biogenic single crystals of calcite: Journal of Materials Science, v. 35, p. 5545–5551.

TAYLOR, J.D., 1968, Coral reef and associated invertebrate communities (mainly molluscan) around Mahé, Seychelles: Royal Society of London, Philosophical Transactions, Series B: Biological Sciences, v. 254, p. 129–206.

TAYLOR, J.D., 1977, Food and habitats of predatory gastropods on coral reefs: Report of the Underwater Association, New Series, v. 2, p. 155–193.

TAYLOR, P.D., AND DI MARTINO, E., 2014, Why is the tropical Cenozoic fossil record so poor for bryozoans?: Bryozoan Studies - Studi Trentini di Scienze Naturali, v. 94, p. 249–257.

TAYLOR, J.D., AND LAYMAN, M., 1972, The mechanical properties of bivalve (Mollusca) shell structures: Palaeontology, v. 15, p. 73–87.

TAYLOR, P.D., AND ZABORSKI, P.M., 2002, A late Cenomanian bryozoan biostrome from north-eastern Nigeria: Cretaceous Research, v. 23, p. 241–253, doi: 10.1006/cres.2002.0308.

TOMASCIK, T., MAH, A.J., NONTJI, A., AND MOOSA, M.K., 1997, The Ecology of the Indonesian Seas: Hong Kong, Periplus, 752 p.

UMBGROVE, J.H.F., 1929, Anthozoa van N. O. Borneo: Wetenschappelijke Mededelingen van de Dienst van de Mijnbouw in Nederlands Indië, v. 9, p. 46–76, pl. 1–5.

VAN DE WEERD, A.A., AND ARMIN, R.A., 1992, Origin and evolution of the Tertiary hydrocarbon-bearing basins in Kalimantan (Borneo), Indonesia: American Association of Petroleum Geologists Bulletin, v. 79, p. 1778–1803.

VAN WOESIK, R., TOMASCIK, T., AND BLAKE, S., 1999, Coral assemblages and physico-chemical characteristics of the Whitsunday Islands: evidence of recent community changes: Marine Freshwater Research, v. 50, p. 427–440.

VERHEIJ, E., AND ERFTEMEIJER, P.L.A., 1993, Distribution of seagrasses and associated macroalgae in South Sulawesi, Indonesia: Blumea, v. 38, p. 45–64.

VERON, J.E.N., 2000, Corals of the World: Townsville, Australia, Australian Institute of Marine Science, v. 1-3, 463, 429, 490 p.

VINN, O., KIRSIMÄE, K., AND TEN HOVE, H.A., 2009, Tube ultrastructure of Pomatoceros americanus (Polychaeta, Serpulidae): implications for the tube formation of serpulids: Estonian Journal of Earth Sciences, v. 58, p. 148–152, doi: 10.3176/earth.2009.2.05.

WALLACE, C.C., 1999, Staghorn Corals of the World: A Revision of the Coral Genus Acropora (Scleractinia; Astrocoeniina; Acroporidae) Worldwide, with Emphasis on Morphology, Phylogeny and Biogeography: Collingwood, Australia, CSIRO Publishing, 438 p.

WILSON, M.E.J., 2005, Development of equatorial delta-front patch reefs during the Neogene, Borneo: Journal of Sedimentary Research, v. 75, p. 114–133, doi: 10.2110/jsr.2005.010.

WILSON, M.E.J., 2008, Global and regional influences on equatorial shallow-marine carbonates during the Cenozoic: Palaeogeography, Palaeoclimatology, Palaeoecology, v. 265, p. 262–274, doi: 10.1016/j.palaeo.2008.05.012.

WILSON, M.E.J., 2012, Equatorial carbonates: an earth systems approach: Sedimentology, v. 59, p. 1–31, doi: 10.1111/j.1365-3091.2011.01293.x.

WILSON, M.E.J., AND LOKIER, S.W., 2002, Siliciclastic and volcaniclastic influences on equatorial carbonates: insights from the Neogene of Indonesia: Sedimentology, v. 49, p. 583–601.

WILSON, M.E.J., AND MOSS, S.J., 1999, Cenozoic palaeogeographic evolution of Sulawesi and Borneo: Palaeogeography, Palaeoclimatology, Palaeoecology, v. 145, p. 303–337.

WILSON, M.E.J., AND ROSEN, B.R., 1998, Implications of paucity of corals in the Paleogene of SE Asia: Plate tectonics or centre of origin?, *in* Hall, R., and Holloway, J.D., eds., Biogeography and Geological Evolution of SE Asia: Leiden, The Netherlands, Backburys Publisher, p. 165–195.

WOELKERLING, W.J., IRVINE, L.M., AND HARVEY, A.S., 1993, Growth-forms in non-geniculate coralline red algae (Corallinales, Rhodophyta): Australian Systematic Botany, v. 6, p. 277–293.

WRIGHT, P., CHERNS, L., AND HODGES, P., 2003, Missing molluscs: field testing taphonomic loss in the Mesozoic through early large-scale aragonite dissolution: Geology, v. 31, p. 211–214, doi: 10.1130/0091-7613(2003)031<0211.

XIE, S.-P., DESER, C., VECCHI, G.A., MA, J., TENG, H., AND WITTENBERG, A.T., 2010, Global warming pattern formation: sea surface temperature and rainfall: Journal of Climate, v. 23, p. 966–986, doi: 10.1175/2009JCLI3329.1.

Received 21 May 2013; accepted 16 March 2014.